A Charge-Recycling Scheme and Ultra Low Voltage Self-Startup Charge Pump for Highly Energy Efficient Mixed Signal Systems-On-A-Chip

A Dissertation
Presented for the
Doctor of Philosophy Degree

The University of Tennessee, Knoxville

Chandradevi Ulaganathan
December 2012

Copyright © 2012 by Chandradevi Ulaganathan

All rights reserved

To my parents

& AT

Acknowledgements

I would like to express my sincere gratitude to my advisor Dr. Benjamin J. Blalock whose constant support, guidance and patience helped me in completing this dissertation. I'm thankful to him for providing me with employment at the Integrated Circuits and Systems Laboratory (ICASL) for the past 6 years. Dr. Blalock's tireless efforts to secure funding for cutting-edge research are very much appreciated. I also thank him for fostering a collaborative atmosphere in the lab and for giving me the freedom to pursue my interests.

I'm grateful to Dr. Charles L. Britton for his valuable advice, help and for being a source of inspiration during this research. I wish to thank Dr. Jeremy Holleman and Dr. Xiaobing Feng for serving on my committee and providing me with helpful suggestions and encouragement throughout this work. I thank Dr. Bimal K. Bose for his support and mentoring during my graduate studies. I'm grateful to Ryan Lind, Clif Jones and the Home Audio Amplifiers group at TI for their support.

I would like to thank all my current and former colleagues in ICASL for their support. It has been a great pleasure working with you. I'm grateful to Drs. Neena Nambiar, Suheng Chen and Robert Greenwell for their encouragement, friendship and support. In addition, I would like to thank Pollob, Junjie and Kai for their help with the chip submissions. I wish to thank the administrative and the IT staff at the Department of Electrical Engineering and Computer Science for all their help.

I wish to express my deepest gratitude to my friends Aparna Thyagarajan, Ezhilarasi Manickavasagam, Sukanya Iyer, Sangeetha Swaminathan, Srivatsan Sundararajan, Ankit Master and Anton D'Silva. I'm grateful to Lalitha Aunty for her unconditional love and support.

Most importantly, I wish to thank my parents Mrs. Saroja and Mr. Ulaganathan, and my sisters Arthi and Vaishnavi, for their unconditional love, support and faith in me. I'm eternally grateful to you for all the difficult decisions that you have made to help me realize my dreams.

Abstract

The advent of battery operated sensor-based electronic systems has provided a pressing need to design energy-efficient, ultra-low power integrated circuits as a means to improve the battery lifetime. This dissertation describes a scheme to lower the power requirement of a digital circuit through the use of charge-recycling and dynamic supply-voltage scaling techniques. The novel charge-recycling scheme proposed in this research demonstrates the feasibility of operating digital circuits using the charge scavenged from the leakage and dynamic load currents inherent to digital design. The proposed scheme efficiently gathers the "ground-bound" charge into storage capacitor banks. This reclaimed charge is then subsequently recycled to power the source digital circuit.

The charge-recycling methodology has been implemented on a 12-bit Gray-code counter operating at frequencies of less than 50 MHz. The circuit has been designed in a 90-nm process and measurement results reveal more than 41% reduction in the average energy consumption of the counter. The total energy savings including the power consumed for the generation of control signals aggregates to an average of 23%. The proposed methodology can be applied to an existing digital path without any design change to the circuit but with only small loss to the performance. Potential applications of this scheme are described, specifically in wide-temperature dynamic power reduction and as a source for energy harvesters.

The second part of this dissertation deals with the design and development of a self-starting, ultra-low voltage, switched-capacitor (SC) DC-DC converter that is essential to an energy harvesting system. The proposed charge-pump based SC-converter operates from 125-mV input and thus enables battery-less operation in ultra-low voltage energy harvesters. The charge pump does not require any external components or expensive post-fabrication processing to enable low-voltage operation. This design has been implemented in a 130-nm CMOS process. While the proposed charge pump provides significant efficiency enhancement in energy harvesters, it can also be incorporated within charge recycling systems to facilitate adaptable charge-recycling levels.

In total, this dissertation provides key components needed for highly energy-efficient mixed signal systems-on-a-chip.

Contents

CHAPTER 1 INTRODUCTION.....1

1.1 Motivation 1

1.2 Research Goals 3

1.3 Dissertation Overview 4

CHAPTER 2 LITERATURE REVIEW 6

2.1 Introduction 6

2.2 Power Consumption 6

2.3 Scaling Trends for CMOS Technologies 8

2.4 Low Energy Design Techniques 10

2.4.1 Power Supply Voltage Scaling 10

2.4.2 Leakage power reduction 12

2.4.3 Charge-recycling systems 13

2.5 Conclusion 19

CHAPTER 3 DESIGN AND ANALYSIS OF THE PROPOSED CHARGE RECYCLING SCHEME.....21

3.1 Introduction 21

3.1.1 Switching or Dynamic Power dissipation 22

3.1.2 Optimum power supply voltage 27

3.1.3 Feasibility of Charge Recycling 28

3.2 Proposed Charge-Recycling Methodology 29

3.3 Design of the proposed charge-recycling system 31

3.3.1 Charge-Recycling Process – Design and Control 31

3.3.2 Estimation of the Charge-Recycling Capacitor Size 33

3.3.3 Low-Power Comparator 34

3.4 Analysis of Energy Consumption in the Charge-Recycling Scheme 38

3.4.1 Estimation of Virtual Power Supply Voltage levels and CR cycle39

3.4.2 Estimation of Energy Saved using CR Scheme 45
3.5 Implementation of the charge-recycling methodology 51
3.5.1 Design Methodology 52
3.5.2 Physical Implementation 55
3.6 Simulation Results and Performance Analysis 58
3.6.1 Energy Saving 59
3.6.2 Effect on Circuit's Speed and Delay 61
3.6.3 Leakage Current Reduction 63
3.7 Summary and Conclusions 63

CHAPTER 4 CHARACTERIZATION OF THE CHARGE-RECYCLING GRAY-CODE COUNTER 65

4.1 Test Setup 65
4.1.1 Power Supply Generation and Partitions on PCB 65
4.1.2 On-board Supply Regulators 67
4.1.3 Digital Buffers on PCB 68
4.1.4 Reset signal generation 68
4.2 Test Procedure 69
4.3 Measurement Results 72
4.3.1 Energy Reduction due to Charge-recycling 75
4.3.2 Efficiency of Charge-recycling scheme 81
4.4 Techniques to improve the proposed CR scheme 84
4.5 Summary and Conclusion 86

CHAPTER 5 DESIGN & ANALYSIS OF THE ULTRA-LOW VOLTAGE DC-DC CONVERTER 88

5.1 Introduction and Motivation 88
5.2 Literature Review 90
5.2.1 Switched Capacitor Charge Pump topologies 90
5.2.2 Low voltage self-startup in converters 99
5.2.3 Ultra-low voltage SC converters 100

5.3 Design of the proposed low-voltage, self-starting DC-DC converter ...106
5.3.1 Architecture of the Converter ...106
5.3.2 Choice of CP topology ...108
5.3.3 Design of Ring Oscillator ...109
5.3.4 Design of Non-Overlapping (NOV) phase generator ...114
5.3.5 Design of the Proposed Linear Charge Pump (LCP) ...115
5.4 Efficiency of the Proposed Charge Pump ...135
5.4.1 Output voltage of the Charge Pump ...135
5.4.2 Input current consumption of the Charge Pump ...140
5.4.3 Conversion Efficiency of the Charge Pump ...141
5.5 Implementation of the DC-DC Converter ...142
5.6 Simulation Results ...143
5.6.1 LCP simulation results ...145
5.6.2 Performance of the Proposed CP topology with increase in number of CP stages ...150
5.7 Summary ...152

CHAPTER 6 CHARACTERIZATION OF LOW-VOLTAGE SELF-STARTUP CHARGE PUMP ...153

6.1 Test Setup ...153
6.1.1 Power Supply Partition & Generation on the PCB ...153
6.1.2 Ring Oscillator control signal generation ...156
6.2 Test Procedure ...156
6.3 Prototype Characterization ...157
6.3.1 Ring Oscillator ...157
6.3.2 Charge Pump Output Voltage ...160
6.3.3 Charge Pump Startup Voltage ...164
6.3.4 Charge Pump Drive Capability ...166
6.3.5 Charge Pump Efficiency ...168
6.4 Techniques to improve efficiency ...171
6.4.1 Adaptive Frequency control ...172

6.4.2 Charge Recycling 172
6.5 Summary and Conclusion 172
CHAPTER 7 CONCLUSION 175
7.1 Original contributions 176
7.2 Directions for future work 176
7.2.1 Charge recycling based low power digital operation 176
7.2.2 Charge pump 177
REFERENCES 179
VITA 187

List of Figures

Figure 2.1 Inverter illustrating current paths during operation 7
Figure 2.2 Energy-delay optimization and tradeoff in digital circuit design [7], [8] 11
Figure 2.3 Charging and discharging action in switch [16] 13
Figure 2.4 Charging and discharging action in switch [16], [17] 15
Figure 2.5 Charge recycling system based on vertically-stacked logic cells [24] 16
Figure 2.6 Conceptual schematic of the charge recycling scheme [26]. 18
Figure 2.7 Conceptual schematic of charge-recycling scheme [28] 19
Figure 3.1 Block level schematic of FO4 inverter stages 24
Figure 3.2 NanoSim simulation results of power consumption across V_{DD} variation in the FO4 buffer 25
Figure 3.3 Normalized power, delay and power-delay product across V_{DD} variation in the FO4 buffer 26
Figure 3.4 Block level schematic of the charge-recycling scheme 30
Figure 3.5 Schematic illustrating operation during charge-accumulation phase 31
Figure 3.6 Schematic illustrating operation during charge-recycling phase 32
Figure 3.7 Schematic of the low-power comparator 35
Figure 3.8 Histogram of comparator's offset voltage distribution from Monte-Carlo simulations 36
Figure 3.9 Comparator schematic illustrating the leakage paths to be investigated 37
Figure 3.10 Virtual power supply voltage levels in the charge-recycling scheme 40
Figure 3.11 Duration of CR cycle as a function of C_{CR}/C_L across number of stages (N) 45
Figure 3.12 Virtual power supply voltage levels and power consumption in the CR system 46
Figure 3.13 Percentage energy saved by employing the proposed charge recycling technique 50
Figure 3.14 Functional schematic of partially-self powered charge-recycling system 51
Figure 3.15 Schematic illustrating time-multiplexed virtual V_{DD} generation 52
Figure 3.16 Alternate implementation of CR scheme to support multiple target blocks 53
Figure 3.17 Simplified schematic of the analog buffer used to monitor the virtual supply nodes 55
Figure 3.18 Input referred offset voltage of the analog buffer across the input voltage range of interest 56

Figure 3.19 Layout of Gray-code counter with CR scheme in 90-nm process.....57
Figure 3.20. Layout of Gray-code counter with CR scheme in 0.5-µm process 57
Figure 3.21 Transient simulation results of CR counter in 90-nm process 58
Figure 3.22 Simulated power consumption of the CR Gray-code counter.....59
Figure 3.23 Power consumption in the 12-bit Gray code counter in 90-nm implementation 60
Figure 4.1 Die photo of the charge-recycling Gray-code counter in 90-nm process.....66
Figure 4.2 Layout of test board to characterize charge-recycling Gray-code counter (90-nm process) 66
Figure 4.3 Cross-section of the test board showing the layer stack-up 67
Figure 4.4 Schematic of LDO voltage-regulator circuit on the test board [65].....68
Figure 4.5 12-bit Gray-code output from the charge recycling counter 70
Figure 4.6 Transient measurement results demonstrating power reduction in the counter 71
Figure 4.7 Measured input offset voltage of analog buffers.....72
Figure 4.8 Transient measurement results illustrating virtual supply rails in the CR counter.....73
Figure 4.9 Measured energy reduction in the charge-recycling Gray-code counter (Chip # 1) 75
Figure 4.10 Measured energy reduction in the charge-recycling Gray-code counter, including power dissipated by the control logic (Chip # 1).....76
Figure 4.11 Measured energy reduction in the charge-recycling Gray-code counter (Chip # 2) 77
Figure 4.12 Measured energy reduction in the charge-recycling Gray-code counter, including power dissipated by the control logic (Chip # 2).....78
Figure 4.13 Measured energy reduction in the charge-recycling Gray-code counter (Chip # 3) 79
Figure 4.14 Measured energy reduction in the charge-recycling Gray-code counter, including power dissipated by the control logic (Chip # 3).....79
Figure 4.15 Measured energy reduction in the charge-recycling Gray-code counter (Chip # 4) 80
Figure 4.16 Measured energy reduction in the charge-recycling Gray-code counter, including power dissipated by the control logic (Chip # 4).....81
Figure 4.17 Normalized energy in Counter versus normalized delay due to CR scheme 82
Figure 4.18 Normalized energy (including CR logic) versus normalized delay due to CR scheme .82
Figure 4.19 Normalized energy versus normalized delay as a result of reduction in V_{DD}.....83

Figure 5.1 Simplified schematic of a three-stage linear charge pump with charge transfer switch (CTS) implementations (a) CMOS diode CTS (b) CTS with gate control generator and (c) Bootstrapped CTS. 92
Figure 5.2 Simplified schematic of a three-stage Fibonacci charge pump (a) Φ_1 is active (b) Φ_2 is active. 95
Figure 5.3 Simplified schematic of exponential charge pump (a) Φ_1 is active (b) Φ_2 is active 96
Figure 5.4 Simplified schematic of linear charge pump's stage illustrating reverse current loss. 98
Figure 5.5 Schematic of the low-voltage charge pump in [46] 100
Figure 5.6 Simplified schematic of the low-voltage charge pump in [45] 101
Figure 5.7 Simplified schematic of the low-voltage charge pump in [49] 102
Figure 5.8 Simplified schematic of the low-voltage exponential charge pump in [50] 104
Figure 5.9 Topology of the proposed self-starting converter 107
Figure 5.10 Model of inverter-based ring oscillator 109
Figure 5.11 RO's startup voltage across device ratio for typical process corner 112
Figure 5.12 RO's voltage across device ratio for worst-case process corners 113
Figure 5.13 Schematic of the 5-stage ring oscillator 114
Figure 5.14 Schematic of the non-overlapping phase generator 115
Figure 5.15 Simplified schematic of the proposed LCP 117
Figure 5.16 Schematic of the level-shifter used to generate the CTS control in the proposed LCP 118
Figure 5.17 Simplified schematic of the proposed LCP along with the GC generation 119
Figure 5.18 Schematic of the proposed self-starting linear charge pump 122
Figure 5.19 Schematic illustrating control signals and charge transfer in the first stage of LCP 124
Figure 5.20 Schematic illustrating control signals and charge transfer in the second stage of LCP 125
Figure 5.21 Schematic illustrating control signals and charge transfer in the third stage of LCP 126
Figure 5.22 Schematic illustrating control signals and charge transfer in the last stage of LCP 127
Figure 5.23 Schematic of the proposed improved self-starting charge pump - version 2 129
Figure 5.24 Schematic illustrating control signals and charge transfer in the second stage of LCP V2 130
Figure 5.25 Schematic illustrating control signals and charge transfer in the 2^{nd}-to3^{rd} stage of LCP V2 132

Figure 5.26 Voltage across charge pump capacitors during charging (Φ_C) and discharging (Φ_D) phase of operation for (a) First stage CP capacitor, (b) *i*-th stage CP capacitor, (c) Last or *N*-th stage CP capacitor, and (d) the output capacitor 137
Figure 5.27 Layout of the low-voltage charge pump V1 in 130-nm process 142
Figure 5.28 Layout of the low-voltage charge pump V2 in 130nm process.....143
Figure 5.29 Ring oscillator's output frequency across input voltage variations.....144
Figure 5.30 Ring oscillator's output frequency control with delay network 144
Figure 5.31 Post-layout simulation showing startup of the LCP V1 146
Figure 5.32 Post-layout simulation showing startup of the LCP V2 147
Figure 5.33 Plot of LCP's output voltage across varying input voltages for different load conditions.....148
Figure 5.34 Plot of LCP's conversion gain across varying input voltages for different load conditions.....148
Figure 5.35 Plot of charge pumps' efficiency across varying input voltages and different load conditions.....149
Figure 5.36 Seven-stage LCP V2's output voltage across varying input voltages for different load conditions.....150
Figure 5.37 Seven-stage LCP V2's efficiency across varying input voltages and different load conditions.....151
Figure 5.38 Plot of LCP V2's output voltage across varying number of pumping stages (*N*) 151
Figure 5.39 Plot of LCP V2's efficiency across varying number of pumping stages (*N*) 152
Figure 6.1 Microphotograph of the fabricated die 154
Figure 6.2 Test board to characterize low-voltage charge pumps 154
Figure 6.3 Cross-section of the test board showing the layer stack-up 155
Figure 6.4 Schematic of LDO voltage-regulator circuit on the test board [65].....156
Figure 6.5 Measured charge pump output voltage across frequency of operation (V_{IN} at 0.33 V)....158
Figure 6.6 Measured charge pump efficiency across frequency of operation, normalized to 158
Figure 6.7 Frequency tuning in ring oscillator (a) simplified schematic of RO illustrating delay cells, (b) Realized RO schematic, and (c) Required RO schematic, across different delay (switch) settings.....159

Figure 6.8 Simulated RO's output frequency, normalized to the free-running frequency, across delay settings for V_{IN} at 0.125 V and 0.33 V. 160
Figure 6.9 Measured charge pump output voltage across variations in input voltage and DC load current for Chip 1 161
Figure 6.10 Measured charge pump output voltage across variations in input voltage and DC load current for Chip 2 161
Figure 6.11 Measured charge pump output voltage across variations in input voltage and DC load current for Chip 3 162
Figure 6.12 Measured charge pump output voltage across low input voltages at different DC load current conditions for Chip 1 163
Figure 6.13 Measured charge pump output voltage across low input voltages at different DC load current conditions for Chip 2 163
Figure 6.14 Measured charge pump output voltage across low input voltages at different DC load current conditions for Chip 3 164
Figure 6.15 LCP V1's conversion gain across low input voltages and load conditions.....165
Figure 6.16 LCP V2's conversion gain across low input voltages and load conditions.....165
Figure 6.17 Output voltage of LCP across varying load conditions for chip 1 167
Figure 6.18 Output voltage of LCP across varying load conditions for chip 2 167
Figure 6.19 Output voltage of LCP across varying load conditions for chip 3 168
Figure 6.20 Measured end-to-end efficiency of the DC-DC converter (LCP V1) across varying load conditions 169
Figure 6.21 Measured end-to-end efficiency of the DC-DC converter (LCP V2) across varying load conditions 170
Figure 6.22 Simulated LCP V2 efficiency and end-to-end converter efficiency (LCP V2).....170

List of Tables

Table 2.1 Comparison of the state-of-the-art Charge-recycling based low power techniques 20
Table 3.1 Partially Self-Powered Circuit's performance with and without Charge-Recycling at 50 MHz 61
Table 3.2 Energy reduction of system with and without Charge-Recycling at 100MHz (90-nm design) 62
Table 3.3 Propagation delay with and without Charge-Recycling 62
Table 4.1 Offset voltage of the comparators used in CR control logic 74
Table 4.2 Comparison of the state-of-the-art Charge-recycling based low power techniques 87
Table 5.1 Summary of the state-of-art low-voltage DC-DC converters with startup mechanisms ...105
Table 6.1 Charge pump startup voltage across different load conditions 166
Table 6.2 Performance comparison of the proposed charge pump with state-of-the-art converters .173

Chapter 1 Introduction

1.1 Motivation

The fast-paced growth of the semiconductor industry has facilitated the development of highly integrated electronic systems with sophisticated functionalities. Our dependence on these ubiquitous, pervasive electronic systems and the increasing concerns over global warming has placed efficient energy consumption as a significant topic of research. The International Technology Roadmap for Semiconductors (ITRS) [1] has identified power consumption and leakage power consumption as focus topics for research for the next 15 years [2]. Also, reducing the power consumption of the integrated circuits (ICs) in portable electronics is critical for long battery life between recharge cycles and thus to the performance of the system. Energy efficiency is important in wired applications as well, where low power consumption directly translates to lower utility bills and improved reliability due to lower heat generation.

With this pressing need for efficient power utilization, many low-power IC design techniques have been put forth over the past two decades. Foremost among these digital design techniques are supply and threshold voltage scaling [11], [21], sub-threshold operation [7], body-biasing [20], power-gating [19], and adiabatic computation [13], [16]. Each of these techniques has a different power-performance tradeoff and has been successfully used in microprocessors along with power management systems. Sensor-based mixed-signal circuits represent a niche class of systems that requires low-cost, highly energy efficient operation. Often, the generation of multiple supply voltages or the use of sophistication power management ICs presents a large overhead on these systems. In such applications, highly aggressive low-power design with efficient, integrated power management scheme is required to meet the power constraints of the system.

Additionally, the CMOS device scaling trend has resulted in the degradation of analog device performance at Ultra-Deep-Submicron (UDSM) scale processes. This has necessitated the use of digital assist techniques to improve the overall system performance, improve reproducibility, and provide a simple and powerful interface [1]. With the increasing dependence

on such digital housekeeping circuits for otherwise straightforward analog implementations, a power reduction technique that encompasses these power-constrained UDSM circuits would be very valuable.

It is the opinion of the author that adaptive voltage scaling techniques would be the potentially most effective way to achieve energy efficiency, especially in the presence of process and temperature variations. The Adaptive Voltage Scaling (AVS) technique automatically adjusts the power supply voltage to achieve energy efficient operation at a required performance level, across variations in the operating conditions. Majority of voltage-scaling based energy reduction techniques focus on the methods to reduce energy consumption by employing multiple supply voltages, but do not account for the generation of these multiple supply voltage levels. While the energy expended for the generation of multiple supply levels is validated by the significant energy savings achieved in large computation systems, it presents a major overhead to severely power-constrained, mixed-signal systems. Hence, this research addresses the challenge of adopting VS techniques in these small mixed-signal systems.

This dissertation focuses on the design and implementation of charge-recycling (CR) based voltage-scaling (VS) schemes to improve the efficiency of power-constrained mixed-signal circuits. Furthermore, the proposed scheme can be easily adapted to AVS scheme. As with any VS technique, reduction in power comes at the expense of some performance degradation [3]. The power-reduction and performance-loss tradeoff in the system is analyzed in this work.

The realization of charge-recycling scheme with an adjustable power-supply voltage that compensates for performance or temperature variations requires a low-voltage DC-DC converter that functions as the power delivering unit. Further, power autonomy can be achieved with a self-starting DC-DC converter that is powered by the recycled charge (or harvested energy) to generate the output power-supply voltage. Additionally, ultra-low voltage charge pumps are widely exploited in energy harvesting systems, sensor nodes, as well as in smart power management ICs. Hence, the second part of this dissertation explores the design of an ultra-low voltage, self-starting charge pump which is an essential component in ultra-low voltage DC-DC conversion. Furthermore, unassisted self-startup capability in the ultra-low voltage regime

provides significant efficiency enhancements in micro-energy harvesters and thus presents a very attractive challenge for research.

1.2 Research Goals

The goals of this research can be summarized as follows:

- To investigate the feasibility of recycling charge from switching and leakage currents that are inherent to digital operation.
- To explore energy-efficient means to use the reclaimed charge.
- To design and implement a charge-recycling (CR) methodology that lowers the total power consumption of digital circuits in a mixed-signal system. Further, the proposed CR technique should be easily adaptable to existing digital circuits and independent of the process technology employed.
- To study the performance-power design trade-off as a result of implementing the proposed CR scheme.
- To investigate ultra-low voltage DC-DC conversion topologies that enable power autonomy, and offer variable conversion gains depending on the input voltage.
- To design and implement an unassisted self-starting, ultra-low voltage charge pump which forms an integral component in micro-energy harvesters.
- To characterize the startup voltage and the performance of the proposed charge pump.
- To determine possible applications of the proposed CR scheme and the ultra-low voltage charge pump.

To meet these goals, the state-of-the-art low-power designs have been studied and the various factors that limit power reduction have been understood. To investigate charge-recycling as a means to lower energy consumption, a methodology is proposed to analyze existing digital cells and the best possible way to adopt CR is studied. A prototype has been designed and implemented in 90-nm CMOS and 0.5-µm SiGe BiCMOS processes. The energy reduction for

one cycle of operation in these test prototypes has been characterized and the performance of the proposed CR scheme has been discussed.

In the second part of this dissertation, the factors that affect self-startup and operation of DC-DC converters at ultra-low voltages have been analyzed. A self-starting, switched-capacitor charge pump has been designed and implemented in a 130-nm CMOS process. The performance of the fabricated prototypes has been characterized across varying input and load conditions. Further, the performances of the designed prototypes have been compared with the current state-of-the-art designs in order to study the effectiveness of the proposed circuits.

1.3 Dissertation Overview

Chapter 2 reviews trends in CMOS technology and the challenges of low-power design. A literature survey of state-of-the-art power reduction techniques is presented. Chapter 3 provides an in-depth look at charge-recycling based dynamic voltage scaling in digital cells. The design considerations and methodology to optimize power consumption are presented. Further, an estimate of the percentage energy reduction due to charge-recycling is derived. The physical design and implementation of the proposed CR scheme for a 12-bit Gray-code counter are described. Furthermore, to show its effectiveness, the CR scheme has also been ported to a 0.5-μm SiGe BiCMOS process and the efficiency of the two systems has been compared with simulation results.

Chapter 4 describes the test-board design and the procedure employed to characterize the energy savings in the test chips. Further, the design trade-offs and the realized energy savings in the system are analyzed in detail. Directions for future work with techniques to improve the proposed CR scheme are discussed. The chapter concludes with the performance comparison of the proposed CR scheme with the current state-of-the-art low-power designs. The applications of the CR technique are also explored in this chapter.

Chapter 5 reviews the current state-of-the-art self-starting DC-DC converters and establishes the design goals for this research. The proposed switched-capacitor-based, self-starting DC-DC converter topology is introduced and its design is presented. Next, the operational losses and their effect on the efficiency of the converter are analyzed. Further, an

output voltage equation that accurately models the CP's operational losses is derived. Finally, the improvements obtained using the proposed topologies are illustrated with the simulation results.

Chapter 6 presents the test-board design and the methodology employed to verify the operation of the proposed self-starting charge pumps. The startup voltage and the performance of the proposed low-voltage charge pumps are characterized and compared with the current state-of-the-art designs.

Chapter 7 provides a summary and conclusion to this work. The original contributions made in this research are presented. Finally, the possible directions for future work are discussed.

Chapter 2 Literature Review

2.1 Introduction

Traditionally, digital design optimization was targeted at improving the computation speed until the advent of battery operated systems which necessitated power and energy optimization techniques to extend the lifetime of the battery. For more than a decade, energy optimization has been one of the actively researched areas in IC design. A literature review of the various low-power design techniques along with an analysis of the implementation challenges helps to illustrate the contribution of this dissertation research to the state of the art low power methodologies. Section 2.2 presents a brief overview of the different sources of power dissipation that are inherent to digital operation. Section 2.3 discusses the role of CMOS technology scaling in the design of energy-efficient mixed-signal ICs. Low-power, energy-efficient design techniques and their challenges are explored in Section 2.4. Finally, Section 2.5 summarizes and concludes this chapter.

2.2 Power Consumption

The average power consumption in a conventional CMOS digital circuit is given by

$$P_{average} = \frac{1}{T}\int_0^T I_{VDD}(t)\cdot V_{DD}\cdot dt \qquad (2.1)$$

where V_{DD} is the power supply voltage, and $I_{VDD}(t)$ the instantaneous supply current consumed by the circuit in the time period, T. To examine the different components of power dissipation, consider the CMOS inverter schematic shown in Figure 2.1. At equilibrium state, only one of the transistors is ON thereby eliminating any conductive path between the supply rails. Hence, $I_{VDD}(t)$ current is primarily drawn from the supply only during a transition (or switching) of the output logic state. The load capacitance (C_L) at the output node is charged to V_{DD} during a LOW-to-HIGH transition or discharged to ground during a HIGH-to-LOW logic transition. A charge of $C_L V_{DD}$ is thus moved from V_{DD} to C_L through the pull-up network (PMOS transistor) or from C_L to ground by the pull-down network (NMOS transistor) for the respective transitions. Thus, the energy expended for a digital transition is given by $(1/2)C_L V_{DD}^2$. This switching current

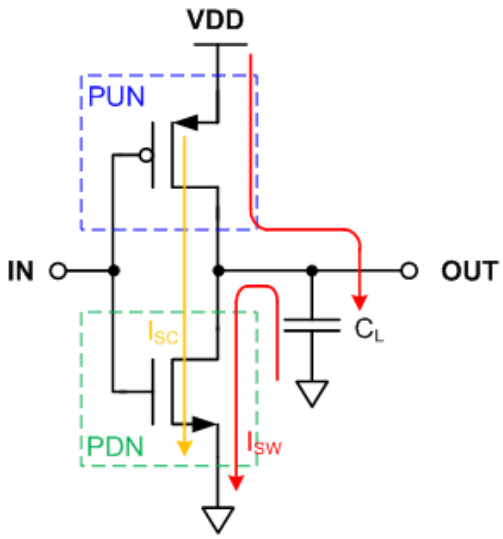


Figure 2.1 Inverter illustrating current paths during operation

component which is essential for digital operation represents one of the dynamic components of power dissipation. The dynamic power dissipated per switching cycle can be approximated as [3]

$$P_{dyn,switching} = \alpha\left(C_L \cdot V_{DD}{}^2 \cdot 1/t\right) \tag{2.2}$$

where α is the probability of a switching transition and $1/t$ is the frequency of operation. The load capacitance at the output node comprises of the reverse-biased diffusion capacitances of the driving circuit, gate capacitance of the fanout load, interconnection wire capacitance, and any external load capacitance connected to the output node.

Furthermore, during the switching transitions, when one transistor is being turned ON, the other is being switched OFF. Therefore, there exists a short period of time when both the transistors are ON, resulting in a short-circuit current (I_{SC}) through the direct conductive path from V_{DD} to ground. This undesirable current component is dependent on the slope of input transition and can be controlled by proper transistor sizing and fanout ratios. However, this I_{SC} forms a small percentage of the total dynamic power required for digital operation.

Additionally, in current UDSM technologies, there exists a static component of power consumption that is caused by the small static leakage currents that flow through the transistors even in the OFF state. This static component of power dissipation is primarily determined by the

subthreshold leakage and the gate leakage currents in UDSM processes [5]. Thus the total average power dissipated for digital operation can be summarized as [3]

$$P_{total,avg} = \alpha\left(C_L \cdot V_{DD}{}^2 \cdot f_{CLK}\right) + I_{SC} \cdot V_{DD} + I_{Lkg} \cdot V_{DD} \tag{2.3}$$

where the first two terms summarize the dynamic power dissipation, representing the switching and the short-circuit components while the static power dissipation due to leakage currents is represented by the last term. Typically, the switching component of dynamic power approximates the total power consumed and thus forms the target for most power reduction techniques.

2.3 Scaling Trends for CMOS Technologies

The consistent scaling of CMOS process technologies has been driven by the ever-increasing need for low power, high performance and high packing density. With constant-field CMOS scaling, the device dimensions (width W, length L), gate-oxide thickness (t_{ox}), threshold voltage (V_{TH}), along with the power supply voltage (V_{DD}) are scaled by a factor of S (about $\sqrt{2}$) for every process node. However, material parameters such as silicon bandgap and built-in junction potential do not scale with reduced voltages or dimensions and thus present challenges in device design [6]. So, the modern processes follow the generalized scaling model, where the device dimensions are scaled by S but the V_{DD}, V_{TH} and doping follow a different scaling factor (U) which is smaller than S [3].

To gauge the effects of scaling on energy efficiency, the critical digital design parameters of intrinsic delay and power are considered in this section. The intrinsic delay associated with long-channel MOSFET (with $V_{GS} = V_{DD}$) is given by [3]

$$\tau = \frac{C_G \cdot V_{DD}}{I_{DSAT}} = \frac{C_{OX} \cdot WL \cdot V_{DD}}{\frac{1}{2}\mu C_{OX} W/L \left(V_{DD} - V_{TH}\right)^2} = \frac{2L^2}{\mu} \cdot \frac{V_{DD}}{\left(V_{DD} - V_{TH}\right)^2} \tag{2.4}$$

where C_G is the gate capacitance, C_{OX} is the gate-oxide capacitance per unit area, I_{DSAT} is the saturation drain current at $V_{GS}=V_{DD}$ and μ is MOSFET mobility. As seen in (2.4) the delay scales with the device length as L^2 and thus device scaling results in quadratic increase in the maximum achievable speed (performance) for a given V_{DD} and V_{TH}. However, in modern UDSM processes, the small device length presents undesirable short-channel effects such as carrier velocity

saturation, drain-induced barrier lowering (DIBL) and severe channel-length modulation. For nominal supply voltages, the electric field across short-channel lengths is high enough to cause velocity saturation and thus it is safe to assume that all modern logic devices are affected by short-channel effects. Once velocity saturation occurs, the saturation drain current I_{DSAT} has a linear dependence on the V_{GS} and can be approximated as [3]

$$I_{DSAT} = \mu C_{OX} W/L \cdot V_{DSAT}\left(V_{GS} - V_{TH} - V_{DSAT}/2\right) \tag{2.5}$$

where V_{DSAT} is the drain-source voltage at which velocity saturation occurs, and is usually less than V_{GS}-V_{TH} for short-channel devices. The saturated carrier velocity v_{sat} is given by $(V_{DSAT} \cdot \mu)/L$. Now, the intrinsic delay τ for short-channel devices can be derived similar to (2.4) and is linearly dependent on L as shown below:

$$\tau = \frac{C_{OX} \cdot WL \cdot V_{DD}}{\mu C_{OX} W/L \cdot V_{DSAT}\left(V_{DD} - V_{TH} - V_{DSAT}/2\right)} = \frac{L}{v_{sat}} \cdot \frac{V_{DD}}{\left(V_{DD} - V_{TH} - V_{DSAT}/2\right)} \tag{2.6}$$

where v_{sat} is constant above V_{DSAT}. Thus there is a linear increase in the maximum attainable switching frequency (performance) with device scaling in short-channel length devices.

For most digital applications with $V_{DD} >> V_{TH}$, the switching power dissipation approximates the total power consumption and is proportional to the product of load capacitance C_L and V_{DD}^2 as in (2.2). The dynamic power dissipation associated with the maximum operating frequency for short-channel devices can be written using (2.6) as

$$P_{Dyn,Swt} = \alpha C_L V_{DD}^{\ 2} \cdot 1/\tau = \alpha \frac{C_{OX}}{S} \cdot \frac{V_{DD}^{\ 2}}{U^2} \cdot \frac{v_{sat} S}{L} \cdot \frac{\left(V_{DD} - V_{TH} - V_{DSAT}/2\right)}{V_{DD}} \tag{2.7}$$

where α is the switching activity factor. The power consumption scales quadratically with the power supply reduction. For a fixed frequency of operation, choosing a smaller feature size results in much lower active power which is scaled by $1/(SU^2)$, where S is the t_{ox} (dimension) scaling factor and U is the V_{DD} scaling factor. Also, from (2.6) and (2.7), the energy per operation (i.e. power-delay product) is reduced by scaling technology. Further, the UDSM processes also provide different flavors of devices with varying V_{TH} to cater to low-operating power (LOP), low-standby power (LSP), or high-performance (HP) circuit applications. Thus,

depending on the application, the choice of technology and the available device types can be exploited to design for low energy consumption. Specifically, the excess performance offered by technology scaling can be exchanged for energy-efficient computation.

2.4 Low Energy Design Techniques

Design techniques to lower computation energy have been implemented at different levels such as device level, logic level and at architectural level. Device level techniques employ threshold scaling, supply-voltage scaling or frequency scaling in order to lower the circuit's power dissipation by varying the operating conditions of the devices. At the logic level, the choice of circuit topology and the logic implementation, such as dynamic versus static logic, true single phase clocking (TSPC) logic etc., is employed. Architectural level techniques include parallel-computing, time-multiplexed, or pipelined system architecture to improve the system performance when operating at low power levels [3]. Since this work applies to device level optimization techniques, this literature study is limited to device level techniques.

2.4.1 Power Supply Voltage Scaling

As evident from (2.3), V_{DD} scaling presents a straight-forward and an effective method to lower power consumption in digital systems. The extent of V_{DD} scaling depends on the performance and energy-efficiency requirements in these circuits. However, the reduction in V_{DD} results in an increase in the propagation delay and thus lowers the maximum frequency of operation. Hence, there exists a power-performance, power-delay or energy-delay tradeoff with supply-voltage scaling. Figure 2.2 [7], [8] illustrates the energy-delay tradeoff in digital circuits. The energy-delay curve represents the optimal operating point to achieve a given performance with minimal energy consumption, or to operate at the maximum speed possible within a fixed energy constraint. The optimal energy-delay curve is derived for a system based on a set of design parameters such as activity level, transistor size, and V_{TH} levels. Thus any change in these design parameters would cause a shift in the energy-delay curve [8].

An unoptimized design's energy-efficiency can be improved by operating with minimum energy dissipation that corresponds to (E_{min},D_{max}) co-ordinates in Figure 2.2, by relaxing the performance requirement, or by speeding up the system to operate at (E_{max}, D_{min}) point by

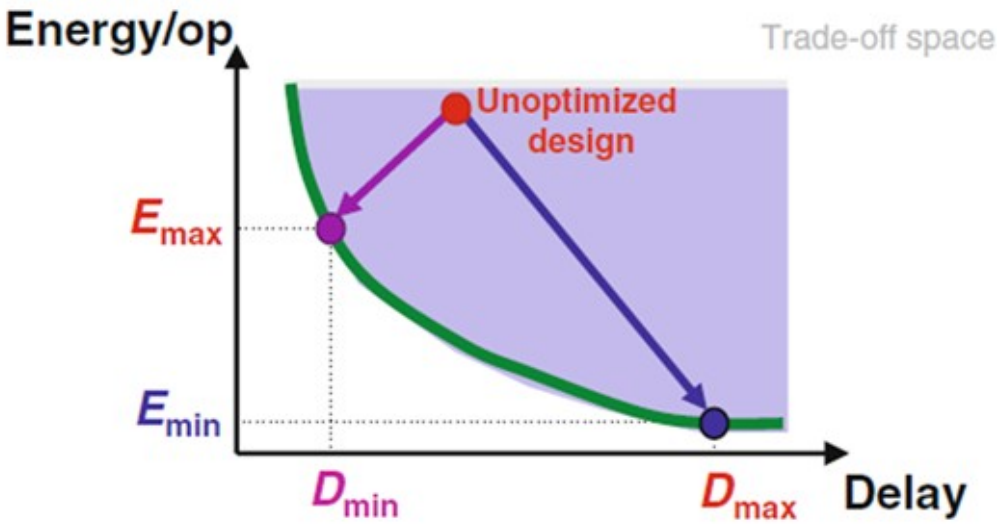


Figure 2.2 Energy-delay optimization and tradeoff in digital circuit design [7], [8]

increasing the power consumption. Thus, V_{DD} scaling techniques operate at an optimum V_{DD} voltage for a required performance such that the power-delay product i.e. the energy per operation is at a minimum level [3], [7].

2.4.1.1 Multiple V_{DD} schemes

Supply voltage islands or multiple V_{DD} are commonly used to optimize the energy consumption across a chip [9], [10]. Circuits that have high activity, i.e. large switching power component, use low V_{TH} devices and are biased at low V_{DD}. Similarly, low activity circuits that have appreciable leakage power are biased at high V_{DD} and employ high V_{TH} devices. Generation of multiple supply-voltages results in an increase in the total chip power and area.

2.4.1.2 Dynamic & Adaptive V_{DD} schemes

Conventional dynamic voltage scaling (DVS) schemes vary the supply voltage to establish low power levels for the required frequency of operation [9], [10]. The critical path's delay associated with V_{DD} is monitored using ring-oscillator or FO4-based logic, and then a look-up-table is used to specify the optimum V_{DD} voltage that provides the required performance at the given temperature.

Some adaptive V_{DD} techniques employ closed-loop control systems to preserve minimum energy operation with V_{DD} variations. In [11], the authors present a control circuit that automatically adjusts both the V_{DD} and V_{TH} such that minimum power consumption is maintained across process and temperature variations. The control circuit determines the body bias voltage needed to obtain the optimum V_{TH} so that the ratio of the dynamic switching current to the static leakage current remains at a fixed level. In another V_{DD} adaptive low-power design work [12], the transistor gate-size ratio is varied with change in V_{DD} in order to maintain minimum energy point across different operating regions of the gate. This ensures that the large transistor sizes required for subthreshold operation does not increase the power when V_{DD} is set above the threshold voltage. A 6X reduction in the power-delay product was obtained.

2.4.2 Leakage power reduction

Highly energy-constrained applications such as energy harvesters that operate at ultra-low voltages (ULV), low-speeds use subthreshold digital operation to achieve energy efficiency. While low-voltage operation reduces the dynamic switching power, the static leakage of the devices increases. Thus the minimum energy point (MEP) in these applications is primarily set by the supply voltage for which the switching power is equal to the leakage power [18]. Since the static leakage currents in ULV operation form a considerable percent of the total power, techniques to reduce the leakage currents are necessary.

At stand-by mode of operation, the power dissipated by static leakage currents can be eliminated by power gating [19]. Pass-transistors are used to connect the circuit to the power supply or ground terminal. When the system is in idle state, the pass-transistors are switched off and thereby disconnecting the circuit from the supply terminal. Now, the power consumption is mainly due to the leakage current flowing through the pass-transistor.

Transistor stacking technique uses stacked transistor gates to reduce the subthreshold leakage current. When both the transistors are switched “off”, the gate-to-source voltage of the top transistor is negative and the increase in V_{TH} due to body effect results in lower subthreshold leakage currents [19] .

Several dynamic/adaptive body biasing techniques that vary the device V_{TH} have been effectively used to reduce leakage current [20], [21]. To minimize the stand-by power, the V_{TH} of

devices are adaptively increased by varying levels of reverse body-bias. Some recent works have shown that simultaneous supply voltage scaling and bidirectional body is effective in achieving high performance in standby as well as active mode of operation.

2.4.3 Charge-recycling systems

Charge-recycling (*CR*) or energy-recovery refers to the low-power design approach that recovers some of the charge stored in the load capacitances (C_L). Figure 2.3 shows a simple *RC* circuit that models an inverter's switching action (charge-discharge of C_L) with *R* representing the on-resistance (*Ron*) of the active device and *C* is the load capacitance. A digital transition from *LOW* to *HIGH* requires that the load capacitance is charged to V_{DD}. The energy expended by the power supply, for this transition, is $C_L V_{DD}^2$ and the energy stored in the load capacitance is $C_L V_{DD}^2/2$ while the switch (*Ron*) dissipates the remaining energy. A switching transition of *HIGH* to *LOW* discharges the load capacitor to ground and this process dissipates the energy stored ($C_L V_{DD}^2/2$) in the capacitor. Thus, for one clock cycle of operation, the energy dissipated by the power supply is $C_L V_{DD}^2$ and the charge supplied is $C_L V_{DD}$. While adiabatic computing techniques work on reducing the actual energy expended ($C_L V_{DD}^2$) by the power supply, charge-recycling techniques aim at recovering the stored charge ($C_L V_{DD}$) from one computation and reusing for subsequent computations. Note that the entire charge from the load capacitor can potentially be recycled in the charge-recovery process.

Several implementations of charge-recycling or energy-recovery systems have been reported as in [13]-[17], [22]-[27]. Some of the energy recovery systems are discussed with

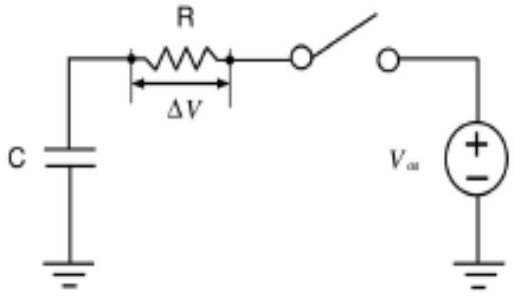


Figure 2.3 Charging and discharging action in switch [16]

reference to adiabatic computing. The latter part of this section focuses on charge-recycling approaches that use the recovered charge to supply power for other computations, and are directly relevant to this research effort.

2.4.3.1 Adiabatic Energy-recovery Logic

The principle behind energy-efficient adiabatic logic is to dissipate very low energy during charging of load capacitances and recovering most of the energy back to the power-supply during the discharge phase. This is accomplished by the use of clocked power-supply that is derived from the clock signal. The energy recovery process and the power supply waveform are illustrated in Figure 2.4. With controlled, slow edge-transitions, the voltage drop across the PMOS transistors is small and the output voltage follows the slope of the power-supply clock. This results in lower peak charging-current and thus low energy dissipation during the charge of C_L. During the hold phase of the power supply clock, the output voltage is sampled or evaluated in the subsequent stage. During the recovery phase, the power-supply transitions to zero and the charge stored in the load capacitor is transferred back to the supply. The total energy dissipated by adiabatic switching is approximately

$$E_{DISS} = \frac{RC}{T_S} CV_{DD}^2 \tag{2.8}$$

where R is the effective "on" resistance of the gate, C is the load capacitance, T_S is the edge transition time of the power supply clock and V_{DD} the power supply voltage. Ideally with very slow clock transitions, the energy expended per operation can be made very low. Multiple clock phases are employed to synchronize the stages such that the hold time of a stage falls during the evaluate phase of the subsequent stage. Four-phase clock with 90º phase shift is recommended for effective energy saving [17].

The main challenge in adiabatic computing is the generation of efficient power supply sources that transfer bidirectional energy to and from the circuit [17]. The transition time of the power-clock which needs to be large enough to reduce the energy consumption also results in large propagation delay in the path. Additionally, the circuitry overhead associated with the energy-recovery process would reduce the overall efficiency.

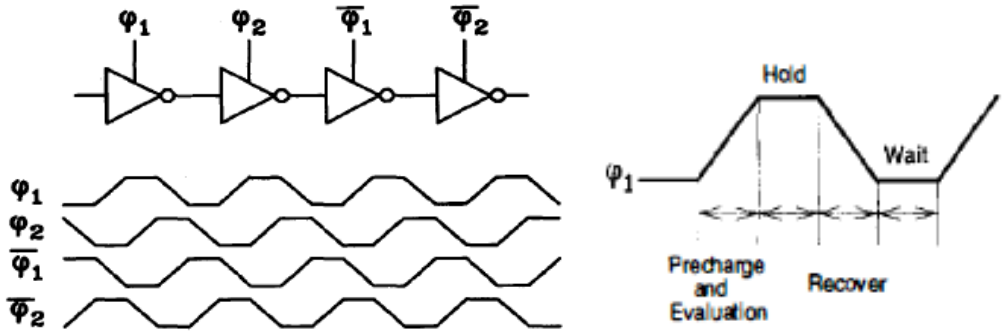


Figure 2.4 Charging and discharging action in switch [16], [17]

2.4.3.2 Vertically-stacked V_{DD} techniques

The charge-recycling technique based on vertically-stacked computation logics has been explored by *Rajapandian et al.* [22]-[24] and *Gu et al.* [25]. Implicit charge-recycling is accomplished by vertically stacking identical logic units such that the ground-bound charge from a digital *HIGH* to *LOW* transition in upper tier (domain) logic cells can be reused for a *LOW* to *HIGH* transition in the lower stack (domain). Thus this scheme is effective for large computation systems that are made of several identical logic unit blocks with similar energy consumption, performance and concurrent operation.

The goal of *Rajapandian's* work was to achieve energy-efficient on-chip dc-dc conversion to supply power for digital circuits using *CR*. Figure 2.5 shows the charge-recycling prototype presented in [24]. A 16x16 carry-save array multiplier is split into 16 logic partitions (granules) and connected in vertical stacks with different supply voltages. A linear push-pull regulator controls the ground reference voltage of the upper domain which is also the power supply voltage of the lower domain granules. Additionally, the regulator monitors the transient current consumption of both the domains. When perfectly matched, the entire current demand of the lower domain granules is supplied by the upper domain. An imbalance between domains would require the regulator to supply the current difference. When a current source-sink imbalance of more than a permissible amount is detected between the domains, the granule switching control logic randomly chooses a granule from the appropriate domain and switches it over to the other domain. This automatic charge (current)-balancing scheme between the logic

domains improves the energy-efficiency of the system and a measured efficiency of 85% was reported for $V_{DD}/2$ conversion [24].

Vertical voltage-stacking (logic-domain) reduces the total current flowing in each power supply route by 50% (without *CR*) for the same supply voltage levels. With charge-recycling between domains, the external (off-chip) current requirement is further decreased. The amount of current reduction depends on the number of logic domains employed and the switching activity in the domains. A direct consequence of lower supply current is a significant reduction in the *IR* and *Ldi/dt* noise associated with each supply. Furthermore, the current requirements on the linear regulator and thus the size of the pass transistor and on-chip decoupling capacitor are reduced. Hence, charge-recycling based V_{DD} stacking proves to be an effective method of power delivery through dc-dc down conversion.

Another implementation of multi-story logic based charge-recycling has been presented by *Gu and Kim* [25]. Their approach is similar to *Rajapandian et al.* [22]-[24] in the use of stacked logic to reuse the charge discarded by upper domain for computations in the lower domain. Their implementation differs in the current balancing technique where digital voltage

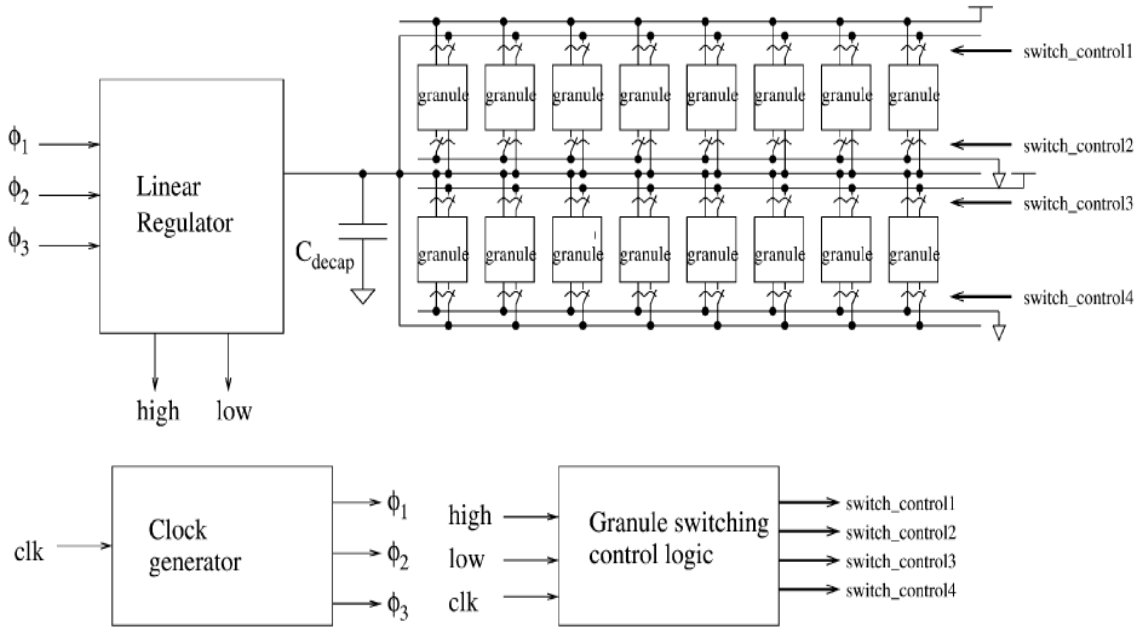


Figure 2.5 Charge recycling system based on vertically-stacked logic cells [24]

regulation is achieved by adjusting the switching activity of the functional units in all the logic stacks. This is accomplished by sensing the supply voltage variation and by controlling the digital inputs to the functional units such that the supply voltage is regulated. The focus of their efforts was to use logic stacking as a means of low-noise, power supply delivery. Ring oscillators, 16-bit LFSR and ALUs were used to evaluate the effectiveness of this scheme. Simulation results were presented to quantify the *IR* noise reduction to be 66% and *Ldi/dt* noise reduction of 67% with total power savings of 5% [25].

The main drawback of the stacked V_{DD} technique is that the current balancing between the logic stacks is critical to ensure the charge from higher stacks is efficiently recycled in the lower domain stacks. A current monitoring mechanism that regulates the current consumption across the stacked domains would dissipate power and might not be a viable option for all mixed signal systems. Voltage-level converters that are necessary to communicate between the different power domains would also consume power. Additionally, in order to avoid severe body-effect or possible device breakdown, the body connections of NMOS transistors in the upper voltage domains need to be isolated and tied to their respective ground reference voltages. So, silicon-on-insulator (SOI) or triple-well processes would be essential for logic domain (V_{DD}) stacking to work.

2.4.3.3 Charge-pump based charge-recycling Schemes

A charge-pump based recycling scheme using virtual supply and virtual ground has been published by *Manne et al.* [26]. This scheme works on the principle of collecting the ground-bound charge during the discharge of load capacitance. Once the virtual ground reaches a threshold voltage, the charge is boosted by a charge pump to V_{DD} and is then used as a supply voltage. Figure 2.6 shows the architecture of this recycling scheme.

To improve the energy efficiency, the charge pump uses adiabatic charge boosting techniques where the charge transfer to the charge-pump's output capacitor happens in voltage increments. This energy conscious charge-pump action presents an inherent delay to boost the virtual V_{DD} node to the required supply voltage. This delay is overlapped with the computational delays within the digital system. Hence, the application of this method is constrained to digital systems with considerable computation time and pipelined operation. Also, the generation of

control signals, the threshold voltages and the incremental voltages for adiabatic charge pump action would consume finite power that would reduce the system's energy efficiency. This design was implemented in digital signal processing (DSP) circuits to reduce the energy consumption by as much as 18% (on average of 9.9%) without perceptible loss in performance [26].

A modified version of this recycling scheme that reduces the power required to generate the control signals for monitoring the various virtual nodes was published by *Keung et al.* [28]. A single-stage charge pump along with a DC voltage source boosts the recycled charge to V_{DD}. Figure 2.7 presents the conceptual schematic of the memory slice along with the virtual ground modules. This system uses two time-multiplexed charge accumulation capacitors to recycle charge. Once the capacitor reaches a fixed threshold voltage, it is disconnected from the "producer" slice and the stored voltage is pumped up to the required power supply voltage of the "consumer" slice. Energy savings of 25% was reported on SRAM L2 caches based on SPICE simulations.

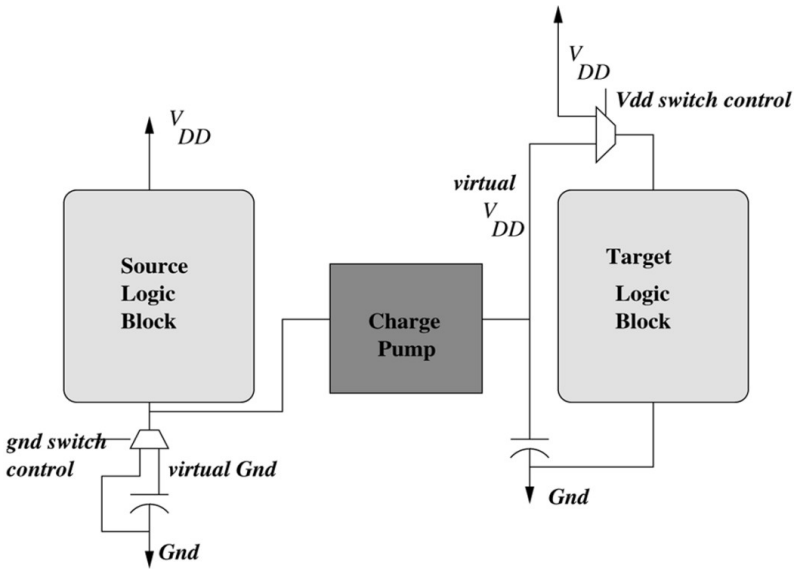


Figure 2.6 Conceptual schematic of the charge recycling scheme [26].

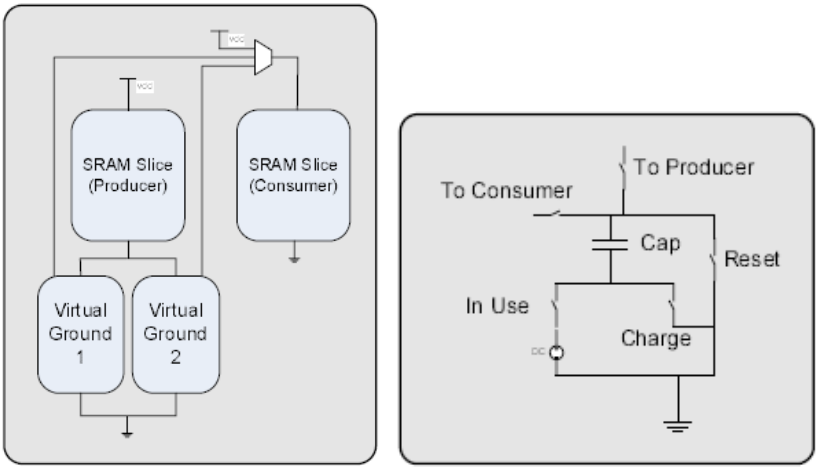


Figure 2.7 Conceptual schematic of charge-recycling scheme [28]

2.5 Conclusion

The literature review is not a comprehensive discussion of all the reported low-power digital design techniques but includes design methodologies relevant to this work. The above discussed techniques have been targeted for large computational digital systems such as microprocessors, DSP chips, memories etc. For a small mixed-signal system, such as an ADC where digital control circuits consume appreciable amount of power, techniques that integrate the advantages of these low-power design techniques are required to accomplish energy-efficient computations. Also, low-power technique that achieves energy-efficient, low-cost operation across wide operating range offers significant advantage. Hence, this research employs continuous voltage scaling as well as charge-recycling methodologies as a means of lowering power consumption in mixed-signal systems.

Table 2.1 presents a comparison of the state-of-the-art charge-recycling based methodologies that reduce the power dissipated in digital systems. While the vertical stacking of digital blocks [24] provides large power reduction, it is not conducive to mixed-signal systems where matching of current consumption might not be possible. While the single-stage charge-pump design [28] require external charge pump clock, the three-stage charge-pump based voltage boosting design [26] also requires a considerable startup time that is masked within the

logic paths. The literature study has thus directed this research effort to address these keys concerns in order to extend the application of charge-recycling techniques to mixed-signal systems.

Table 2.1 Comparison of the state-of-the-art Charge-recycling based low power techniques

Reference	***% Power Saving***	***Features***	***Comments***
[24]	33 % (V_{DD} stacks) 85 % ($V_{DD}/2$ conversion)	V_{DD} stacks	Current balancing critical
[25]	5 % (dual V_{DD} stacks)	V_{DD} stacks	About 66 % reduction in noise
[26]	10 %	Adiabatic Charge pump	External, multiple phase CP clock required
[28]	25 %*	Single-stage Charge pump	External boost voltage required

* Simulation results

Chapter 3 Design and Analysis of the Proposed Charge Recycling Scheme

This chapter is revised based on the paper published by Chandradevi Ulaganathan et al. [32]:

C. Ulaganathan, C. L. Britton, Jr., J. Holleman, and B. J. Blalock, "A Novel Charge Recycling Approach to Low-Power Circuit Design," *Intl. Conference on Mixed Design of Integrated Circuits and Systems*, pp. 208–213, May 2012.

My primary contribution to this paper include (i) identification of the scope of research, (ii) compilation of a literature review of previously published work, (iii) design of the proposed solution, (iv) analysis of simulation results, and (v) preparation of the manuscript.

The objectives of this research include:

- To investigate the feasibility of charge-recycling (CR) based low-power design
- To propose a novel CR methodology that overcomes the limitations of the state-of-the-art CR designs.
- To insure that the proposed scheme should be easily adaptable to existing digital circuits and independent of the process technology employed.

3.1 Introduction

An important figure-of-merit in energy efficient systems is the minimization of energy per cycle of operation, E_{TOT}. E_{TOT} is the total power-delay product, given by $P_{TOT} \bullet T_{clk}$, which is the power (P_{TOT}) consumed to perform all required computations within one clock cycle (T_{clk}). The minimization of E_{TOT} maximizes the energy efficiency [4]. In this section, the factors governing digital power consumption, and the path or propagation delay are examined to explore the feasibility of charge-recycling based energy reduction techniques.

3.1.1 Switching or Dynamic Power dissipation

As discussed in chapter 2, the power consumption in a digital circuit can be approximated as

$$P_{total} = \alpha\left(C_L \cdot {V_{DD}}^2 \cdot f_{CLK}\right) + I_{SC} \cdot V_{DD} + I_{Lkg} \cdot V_{DD} \quad (3.1)$$

The switching component of total power dissipation can be reduced by minimizing the load capacitance C_L that is charged or discharged at each logic transition, or by reducing the logic voltage level (i.e. the power-supply voltage V_{DD}), or by lowering the frequency of the logic transitions (i.e. frequency of operation f_{CLK}). The impact of these design parameters on power reduction and their tradeoffs will be examined in this section.

As evident in (3.1), the node capacitance (C_L) and V_{DD} determine the amount of charge drawn from the power supply for each digital transition. Hence, minimization of C_L helps in reducing the power consumption. The load capacitance encompasses the diffusion and gate-drain (Miller) capacitances at the driver output, gate capacitance of the load, interconnect (wire) capacitance, and any external capacitance connected to that node. The device capacitances are in turn determined by the transistor sizing that is controlled by the drive-strength requirement (i.e. fanout) of the path, power and area specifications. Minimum-sized gates have the lowest diffusion and gate capacitances, and thus the least C_L, are suitable for low-power, area-efficient designs. However, larger PMOS ratios are often essential to have symmetric rise and fall transitions, and good noise margin for robust circuit operation. The general design methodology is to optimize the sizing ratio of the transistors in order to achieve a given performance, area, energy or power specification [29].

A CMOS buffer is used to illustrate how device sizing affects the power consumption and the performance of the circuit. The propagation delay of an inverter is given by

$$t_{pd} = \frac{t_{pHL} + t_{pLH}}{2} = 0.69 \cdot C_L \left(\frac{R_{eqN} + R_{eqP}}{2} \right) \quad (3.2)$$

where C_L is the load capacitance at the output node and R_{eqN}, R_{eqP} are the equivalent "*ON*" resistances of the NMOS and PMOS transistors. The load capacitance at the output is given by [29]

$$C_L = C_{dn1} + \beta C_{dn1} + C_{gn2} + \beta C_{gn2} + C_w \tag{3.3}$$

where β is the sizing ratio of the PMOS to NMOS transistors, C_{dn1} includes the diffusion and gate-drain Miller capacitance of the driver, C_{gn2} is the gate capacitance of the load, and C_w is the interconnect capacitance. The equivalent "*ON*" resistance of the transistor can be approximated as [29]

$$R_{eq} \approx \frac{3}{4}\frac{V_{DD}}{I_{DSAT}} \; where \; I_{DSAT} = K' \frac{W}{L}\left((V_{GS} - V_{TH})V_{DSAT} - \frac{V_{DSAT}^2}{2} \right) \tag{3.4}$$

where I_{DSAT} is the saturation current, K' is the process dependent transconductance parameter, V_{GS} is the gate-to-source voltage, and V_{DSAT} is the drain-to-source saturation voltage. From (3.4), the device sizing ratio, β, that achieves symmetric logic transitions at the output (i.e. $t_{pHL} = t_{pLH}$) can be deduced using the relationship of $\frac{R_{eqN}}{R_{eqP}} = \frac{\beta}{\mu_n / \mu_p}$.

Substituting (3.3) and (3.4) into (3.2) results in propagation delay of

$$t_{pd} = 0.69\left((1+\beta)(C_{dn1} + C_{gn2}) + C_w \right)\frac{R_{eqN}}{2}\left(1 + \frac{\mu_n / \mu_p}{\beta} \right) \tag{3.5}$$

The optimum sizing ratio (β_{opt}) for best performance (minimum t_{pd}) can be found by equating $dt_{pd}/d\beta$ to zero which yields [29],

$$\beta_{opt} = \sqrt{\mu_n / \mu_p \cdot \left(1 + \frac{C_w}{C_{dn1} + C_{gn2}} \right)} \tag{3.6}$$

The β_{opt} for the 90-nm process is simulated to be close to 3.6. This value represents the ratio of PMOS to NMOS transistor-sizing that is required for the best performance (i.e. least delay), and to have equal rise and fall times i.e. equal t_{pLH} and t_{pHL} values. Increasing the size beyond β_{opt} would increase the strength of PMOS to reduce the t_{pLH}, but would also increase the load capacitance to be driven by the NMOS and thus increase the t_{pHL}. Therefore, beyond the calculated β_{opt}, the increase in load capacitance would dictate an increase in the propagation

delay due to self-loading. Additionally, if the wire capacitance is significant compared to the device capacitances, a larger value of β_{opt} would result.

For ratios just below β_{opt}, the performance is slightly degraded, but circuit's power consumption is reduced due to lower C_L. The optimal transistor sizing for minimum energy consumption can be found for a required performance by following an approach similar to that of sizing for performance. The normalized energy of the inverter with respect to a reference circuit that is optimized for performance is derived in [29] as

$$\frac{E}{E_{ref}} = \left(\frac{V_{DD}}{V_{DD,ref}}\right)^2 \cdot \left(\frac{2+2\beta+F}{4+F}\right) \tag{3.7}$$

where, β is the sizing ratio and F is the overall effective fanout of the circuit, which is the ratio of external load capacitance to gate capacitance of the node. From (3.7), it can be inferred that the energy consumption can be reduced by device sizing and power supply voltage reduction for F greater than 1. The device sizing ratio $\beta_{opt,energy}$ is smaller than the $\beta_{opt,performance}$ [29].

The optimum fanout (F) for best performance (minimum delay) is technology dependent and is approximately 2.7 to 5. Using an optimum fanout ensures that the path delay is within 5% of the minimum delay [31]. Hence the buffer used to study the power-performance tradeoff is designed with a fanout-of-4 (FO4) load at each stage. Four FO4 inverter stages are used as shown in Figure 3.1. The first inverter is used to shape the input signal, the second and third inverters form the buffer under study, while the last inverter is used to ensure a FO4-load for the buffer output. Further, load capacitor C_L is placed at the output such that it presents a fanout-of-4

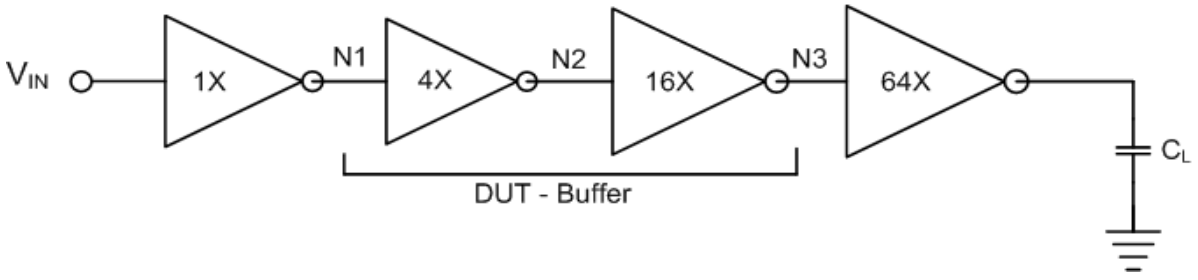


Figure 3.1 Block level schematic of FO4 inverter stages

load to the last stage and thus minimize Miller effect from gate-drain capacitances of the last stage to the node *N3*. Although the transistor sizing ratio of 3.6 that corresponds to $\beta_{opt,performance}$ is not power efficient, it serves as a good case study to illustrate the design tradeoffs. The effect of supply voltage reduction on power and performance characteristics of the FO4 buffer stages is analyzed at a frequency of 200 MHz.

Figure 3.2 shows the achievable reduction in power consumption by operating at lower supply voltages. Synopsys's NanoSim tool was used to simulate the FO4 inverter stages. As seen in the figure, the dynamic power, i.e. the switching power component dominates the total power consumption. The total wasted power which is contributed by the dynamic short-circuit current and the static leakage currents is insignificant in the total power consumption. The lowering of supply voltage results in a quadratic reduction in total power consumption since the circuit nodes charge and discharge to a lower V_{DD} voltage. Notice that for power supply voltage below 0.6 V, there is a sharp increase in the total wasted power with a large drop in the total power consumption of the inverter. The V_{DD} of below 0.6 V marks the transition into the subthreshold region of operation where the devices operate with lower peak currents and large propagation

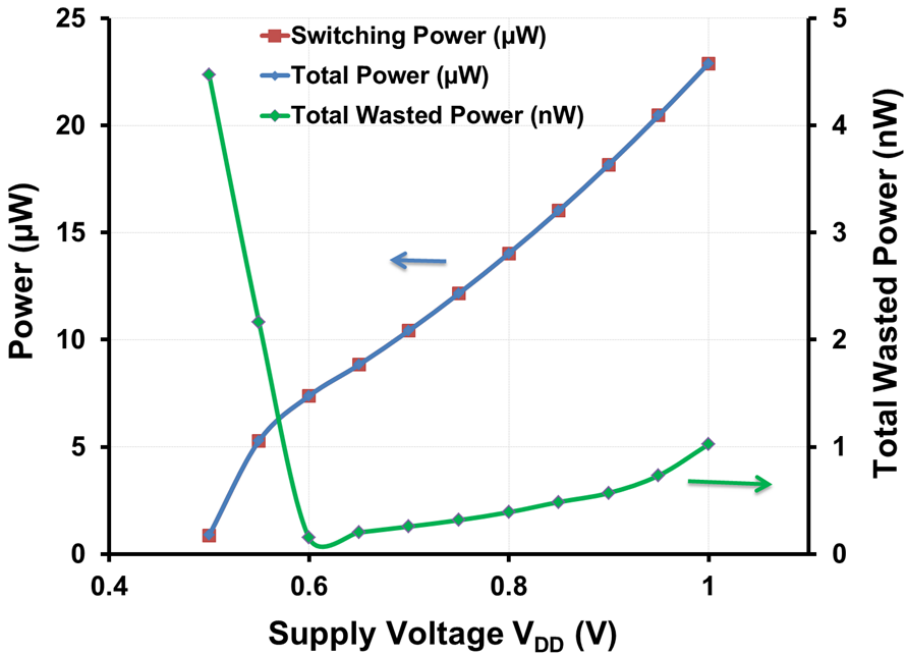


Figure 3.2 NanoSim simulation results of power consumption across V_{DD} variation in the FO4 buffer

delays. Thus, there is an increase in the dynamic short-circuit current component of the total wasted power and a sharp reduction of the total switching component of power. At V_{DD} of 0.5 V, the switching component of power is still the dominant component of the total power consumption. Further reduction in the V_{DD} would result in deep subthreshold operation where the total wasted power becomes comparable to the total switching component of power consumption.

Power reduction by lowering V_{DD} comes with the penalty of degradation in circuit performance due to increased path delay. The propagation delay of the buffer increases due to the increase in "*ON*" resistance of the transistors as a result of lower I_{DSAT} as shown in (3.4). Figure 3.3 presents the simulation results of normalized power, normalized delay and power-delay product of the FO4 buffer at different V_{DD} voltages. As evident in Figure 3.3, the normalized power and the energy per computation can be considerably reduced, while the normalized delay steeply increases with reduction in the circuit's power supply voltage. From (3.2), one approach to lower the propagation delay is to minimize C_L by using smallest device

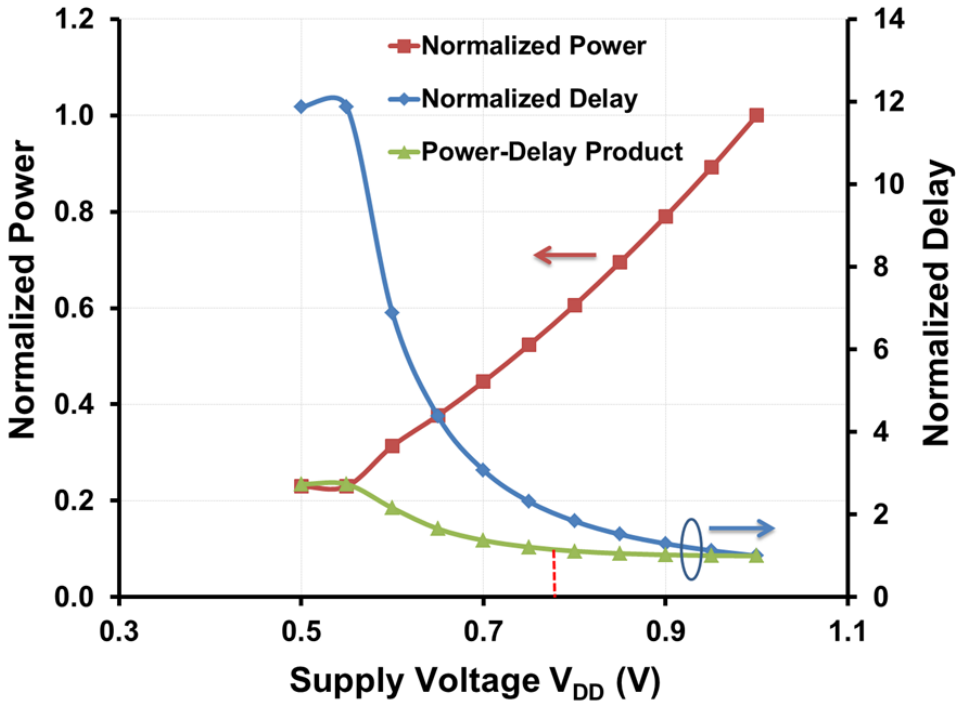


Figure 3.3 Normalized power, delay and power-delay product across V_{DD} variation in the FO4 buffer

size (β_{opt}) possible, and to reduce the "*ON*" resistance (R_{eq}) by increasing the *W/L* ratio. However, the degree of performance improvement gained by increasing *W/L* is very small, since beyond the optimum device sizing, the device capacitances cause self-loading to increase the propagation delay. Hence, for achieving low-power operation, lowering the V_{DD} presents a realistic approach only if the performance requirements can be met.

The normalized power-delay product (PDP) and the corresponding energy-delay product (EDP) quantify the operational efficiency of the circuit with variation in V_{DD} (Section 2.4.1 , Figure 2.2). Further, the PDP or EDP curves exhibit a minimum close to 0.8 V of V_{DD} which is slightly more than $2V_{TH}$ of the devices. This V_{DD} offers the optimal point of operation if energy and delay are given equal importance in this DUT (buffer).

The optimal energy-delay curve is derived for a system based on a set of design parameters such as activity level, transistor size, and V_{TH} levels. Thus, any change in these design parameters would cause a shift in the energy-delay curve [8]. Note that using a different device sizing ratio would shift the normalized power and delay values but the circuit would still exhibit the similar power-delay tradeoff. Therefore, the PDP or EDP curve can be employed to arrive at the minimum possible energy consumption to meet a given speed (delay) requirement. Similarly, for a given energy constraint, the maximum possible performance can be deduced. Thus, for a given performance requirement, the reduction of V_{DD} along with optimum device sizing presents an attractive but a challenging design path to minimize the circuit's energy consumption.

3.1.2 Optimum power supply voltage

The optimum power supply voltage for a circuit depends on various factors such as performance, power consumption, and reliability requirements. Operation at the nominal V_{DD} offers the best possible performance with good timing margins in the logic paths, but the power consumption is non-optimal. Hence, for a given performance requirement, the power supply voltage that guarantees optimum operating point based on the energy-delay product can be employed. The energy-delay product can be approximated as [29]

$$EDP = PDP \cdot t_p = \frac{C_L V_{DD}^2 \cdot t_p}{2} \tag{3.8}$$

where t_p is the minimum propagation delay which defines the maximum frequency of operation. For short channel devices operating in velocity saturation, the propagation delay can be approximated as [29]

$$t_p \approx \frac{\alpha C_L V_{DD}}{V_{DD} - V_{TH} - V_{DSAT}/2} \tag{3.9}$$

where α is a technology parameter. Substituting (3.9) in (3.8) yields [29]

$$EDP = \frac{\alpha C_L^2 V_{DD}^3}{2\left(V_{DD} - V_{TH} - V_{DSAT}/2\right)} \tag{3.10}$$

The optimum supply voltage can be derived from (3.10) by differentiating it with respect to V_{DD} and equating to 0. The optimum V_{DD} is

$$V_{DD,opt} = \frac{3}{2}\left(V_{TH} - V_{DSAT}/2\right) \tag{3.11}$$

Hence, operating at a reduced supply voltage of $V_{DD,opt}$ results in the optimum operating point that corresponds to minimum energy expended to operate at the required performance (minimum EDP).

3.1.3 Feasibility of Charge Recycling

The power-performance analysis of the FO4 buffer demonstrates the fact that the power consumption of digital circuits, operating at nominal power-supply voltage of the process, is dominated by the switching current required to charge and discharge the internal load or gate capacitances. Hence, reducing the switching component would decrease the power consumption in the circuit. The charge required by a node for every digital transition from logic *LOW* (i.e. ground) to logic *HIGH* (i.e. V_{DD}), or logic *HIGH* to *LOW* is given by

$$Q_{S/W} = C_L \cdot V_{DD} \tag{3.12}$$

where C_L is the load capacitance at the switching node. Thus for each clock cycle, charge $Q_{S/W}$ is either drawn from the V_{DD} supply to increase a node voltage to logic *HIGH*, or discharged from a node to ground to reduce that node voltage to logic *LOW*. The transition to logic *LOW*, which results in the loss of charge $Q_{S/W}$ to the ground, presents an opportunity to recycle this ground-bound charge. The readily available ground-bound switching-charge along with the possibility of

energy-efficient operation at lower V_{DD} voltages inspires charge-recycling in digital circuits. The design of the proposed charge-recycling scheme to reduce power consumption in medium-speed digital circuits will be discussed in the next section.

3.2 Proposed Charge-Recycling Methodology

This research focuses on lowering power consumption in digital circuits by recycling charge from the ground-bound switching currents. This is achieved by actively accumulating the ground-bound charge using a storage capacitor bank. In this procedure, the available power supply level to the circuit is lowered. If the reduced supply voltage is monitored to be close to the optimum V_{DD} that is required to realize a given performance, then the system's energy-efficiency would be considerably improved. The advantage of this approach is that energy-efficiency and power-consumption are enhanced by both charge-recycling (CR), as well as supply-voltage reduction methodology. Furthermore, adopting the CR scheme to provide power supply, eliminates the need to use voltage regulators to generate the required multiple V_{DD} levels.

A block level schematic of the proposed charge-recycling scheme [32] is shown in Figure 3.4. The source logic block and the target logic block could be different components of a digital system or the same logic circuit. Identification of potential blocks in a system is essential to maximize charge-recycling and power reduction. The choice of the source block is governed by the rate of switching activity in the logic and also by the ease with which the system can be separated into functional blocks. Also, it is critical to ensure that the required circuit performance is achieved with the reduced supply voltage resulting from charge-recycling.

The charge-recycling scheme operates in two-phased cycles, namely charge-accumulation phase and charge-recycling phase. During the charge-accumulation phase the source logic is powered up from V_{DD} to a virtual ground (V_{VGND}) to enable the collection of ground-bound charge by the charge-recycling or storage (CR) capacitor bank connected to the V_{VGND} node. The V_{VGND} node is monitored to ensure the functionality of the circuit is not degraded by the continuous reduction in the available power supply voltage. Once the V_{VGND} node reaches a predetermined reference voltage, V_{RG}, the CR control signals initiate the charge-recycling phase.

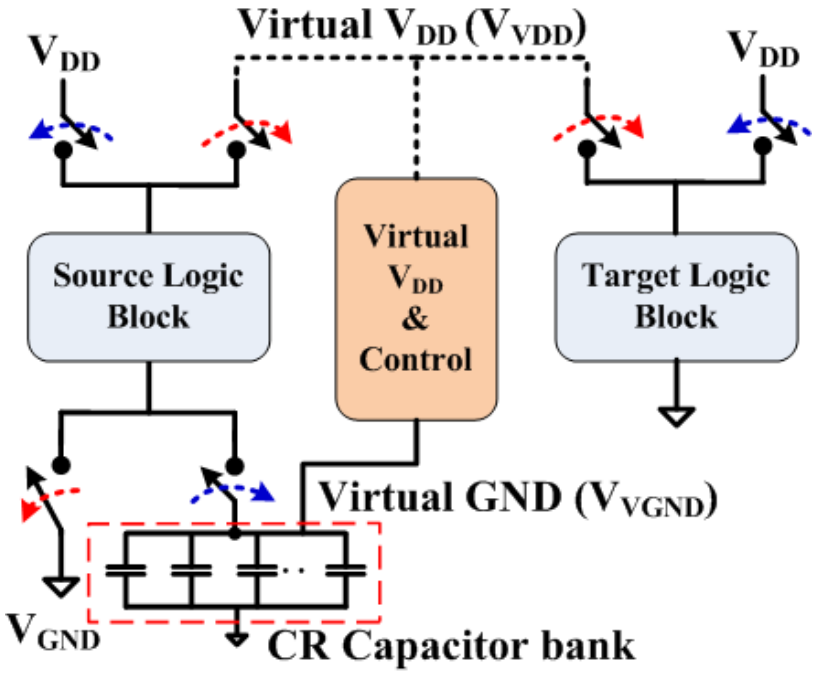


Figure 3.4 Block level schematic of the charge-recycling scheme

The charge-recycling phase begins with the boosting of the voltage across storage capacitors to the virtual V_{DD} (V_{VDD}) level. This is achieved by vertically stacking the capacitors that are charged to V_{VGND} in order to generate the required V_{VDD}. The target logic block is then powered up from V_{VDD} to ground, V_{GND}. Similar to the charge-accumulation phase, the V_{VDD} node is monitored to prevent the supply voltage from discharging below a reference voltage level, V_{RD}, to ensure the circuit's performance.

The proposed architecture offers the advantage of power reduction without any design change to pre-existing digital circuits. An added advantage of power supply scaling by employing virtual supply nodes is the reduction in the leakage currents. This reduction is the result of increased threshold voltages due to body biasing, and also lower drain-to-source voltages that cause a reduction in the Drain-Induced Barrier Lowering (DIBL) component of leakage current [26]. The peak short-circuit current is also reduced with lower supply voltages. Additionally, the charge-recycling capacitors also accumulate charge from short-circuit currents

and leakage currents. Thus, the proposed charge-recycling scheme lowers the power consumption due to dynamic as well as static power dissipation components in (3.1) by dynamically varying the supply voltage, and recycling the ground-bound charge to further reduce the energy consumption in digital circuits.

3.3 Design of the proposed charge-recycling system

The design of the CR system along with the generation of control signals are discussed in this section.

3.3.1 Charge-Recycling Process – Design and Control

The schematic during the charge-accumulation phase is shown in Figure 3.5. A low-power comparator generates the control signals to enable the charging of the capacitors until the V_{VGND} node reaches the maximum allowed voltage, V_{RG}. V_{RG} is determined such that the circuit's

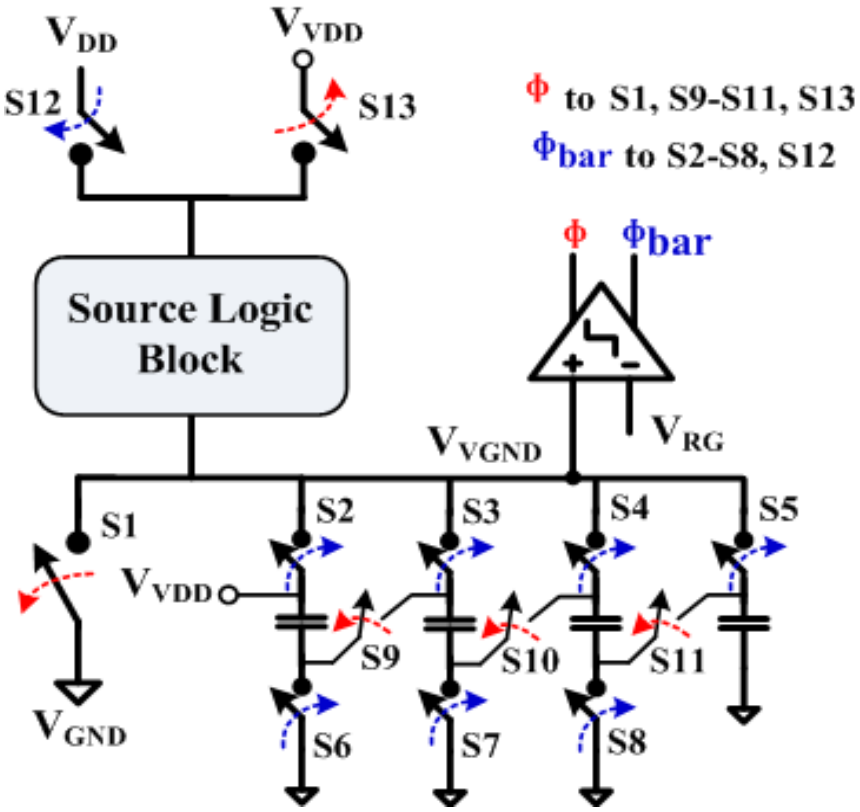


Figure 3.5 Schematic illustrating operation during charge-accumulation phase

performance requirements are met at the reduced virtual supply voltage, even in the presence of comparator offset. This voltage in turn sets the number of CR capacitors (N) required to obtain V_{VDD}. For this implementation, a moderate value of $V_{DD}/3$ is chosen such that three equal-sized CR capacitors (N=3) are placed in series to provide the virtual supply V_{VDD}.

When V_{VGND} reaches the fixed voltage V_{RG}, the comparator output, ϕ goes high and the switches (S2-S8) connecting the CR capacitors to V_{VGND} are opened and the circuit is directly connected to V_{GND} through S1. This configuration defines the beginning of charge-recycling phase. Since the switches connect from ground to a sufficiently low voltage, NMOS-only switches have been employed for switches S1 to S8.

Figure 3.6 illustrates the switch settings of the capacitive stack necessary to establish the V_{VDD} voltage. Switches S9 to S11 connect the top and bottom plates of adjacent capacitors.

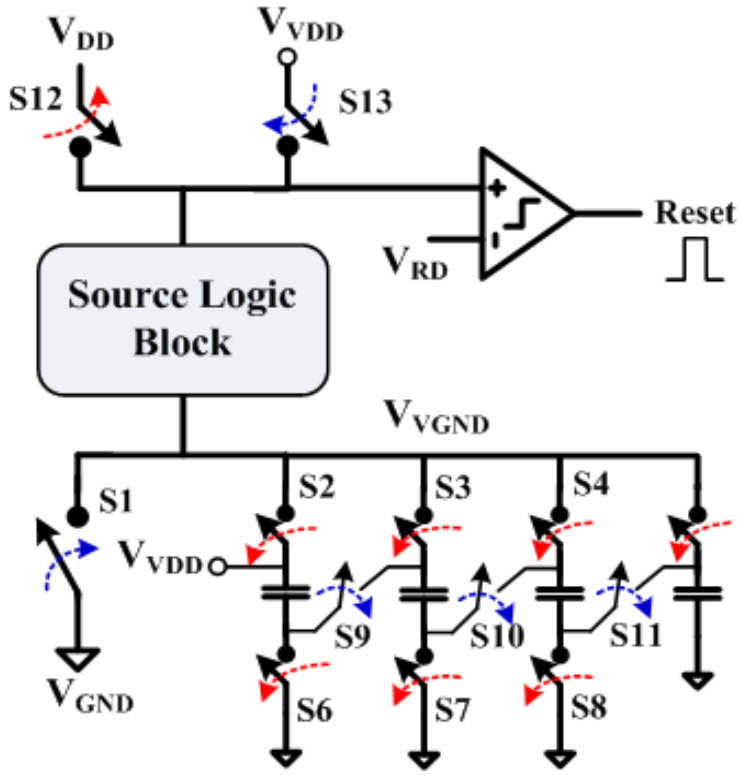


Figure 3.6 Schematic illustrating operation during charge-recycling phase

Transmission gate switches are used here to provide low resistance as the voltages change due to the transfer of charge from V_{VDD} to sustain the target circuit's operation. The V_{DD} switches, S12 and S13, are PMOS-only versions. Once the comparator detects the V_{VDD} voltage to be less than or equal to V_{RD}, a reset pulse is generated and the circuit reverts to the V_{DD} power rail. Also, the CR capacitors are returned to the accumulation phase configuration, as in Figure 3.5. The end of the charge-recycling phase initiates the charge-accumulation phase and the cycle repeats. The value of V_{RD} is set between $2V_{DD}/3$ to $3V_{DD}/4$.

The first cycle of the charge-accumulation phase consumes more time when compared to subsequent cycles. This is due to the initial need to charge from ground to V_{RG} while the following cycles only need an incremental charge from V_{RD}/N to V_{RG}. The system repeats the charge-accumulation and charge-recycling phases as long as the clock to the source block is enabled, i.e. until the source block goes to idle mode or is powered OFF.

3.3.2 Estimation of the Charge-Recycling Capacitor Size

The charge-recycling capacitors need to be large enough to supply the energy required by the target logic blocks and maintain a virtual supply voltage of more than V_{RD} to deliver power to the target block. Conventional CMOS logic cells consume energy of $C_L V_{DD}^2$ to charge a load capacitor C_L to V_{DD}. A worst case estimate of the required charge can be given by $C_L V_{DD}^2$ times the number of PMOS transistors in the target design [26], [33]. So the CR capacitors that form the virtual V_{DD} need to be large enough to sustain the worst case energy requirements of the target logic.

Another design parameter that needs to be studied for the capacitor sizing is the frequency of charge-accumulation and charge-recycling phases versus the power-reduction efficiency of the proposed scheme. The frequency of the recycling phases depends on the energy available for reuse in the CR capacitors as well as the activity factor and the power consumption of the source and target blocks. Since the control logic would also dissipate energy for generating the control signals, operating at a high cycle rate would mean more energy dissipation and lower energy efficiency. However, increasing the accumulation-recycle time implies large CR capacitors and longer charging times. Hence, an optimum value of CR capacitors and accumulation-recycle time is chosen to permit maximum energy efficiency.

A reasonable estimate of the average power consumed by the digital cell is used to determine the effective size of the CR capacitors. Since the topology employs stacking of CR capacitors, the effective capacitance decreases with the number of stacks, N. Hence, the individual capacitors are sized by N times the required value. The price paid for eliminating charge-pump induced delay (as in [26]) between the accumulation and recycle phase is an increase in chip area needed for the CR capacitors.

3.3.3 Low-Power Comparator

The low-power dynamic comparator used in this design is a regenerative latch that is commonly used as a sense amplifier in SRAM cells [29], [30]. The schematic of the high-speed, low-power comparator is presented in Figure 3.7. The positive regenerative action of the cross-coupled inverter pairs provides the high-gain necessary for accurate comparison.

The control signals of $\phi 1$ and $\phi 1b$ are derived from the input clock of the source logic block, thus enabling the comparator to run at the same frequency as the source digital block. During the sample/reset phase, $\phi 1$ is low and transistors MBN, MBP are OFF, thus disabling the latch. In this phase input switches S1 and S2 are closed and the inputs (V_{VGND} and V_{RG} for virtual GND comparison, V_{VDD} and V_{RD} for monitoring virtual V_{DD}) are sampled at the high impedance nodes V_1 and V_2. Next, in the regeneration/active phase, $\phi 1$ goes high to activate the regenerative action and to open the input switches to isolate the nodes V_1 and V_2 from the input. The voltage difference between the sampled input signals is amplified and the output is available at the V_1 and V_2 nodes.

In order to ensure low power dissipation in the nano-Watt range, the transistors MBN and MBP are sized to limit the maximum current available for regeneration. Further, the cross-coupled input pairs are sized with minimum lengths to keep the power consumption as low as possible. This design path results in random mismatch between the input pairs and thus higher input offset voltage. Two comparators are employed in the system to monitor the virtual ground and virtual V_{DD} voltages. The outputs from the comparators are used to generate the control signals to switch between the charge-accumulation and charge-recycle phases.

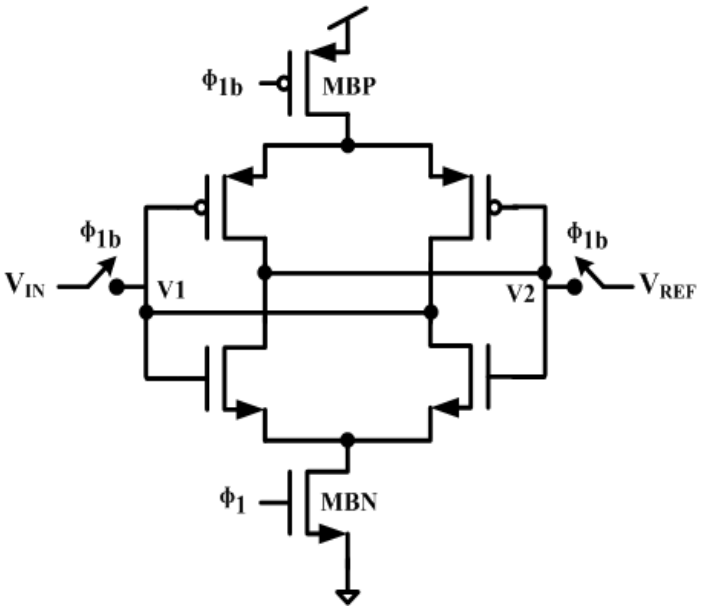
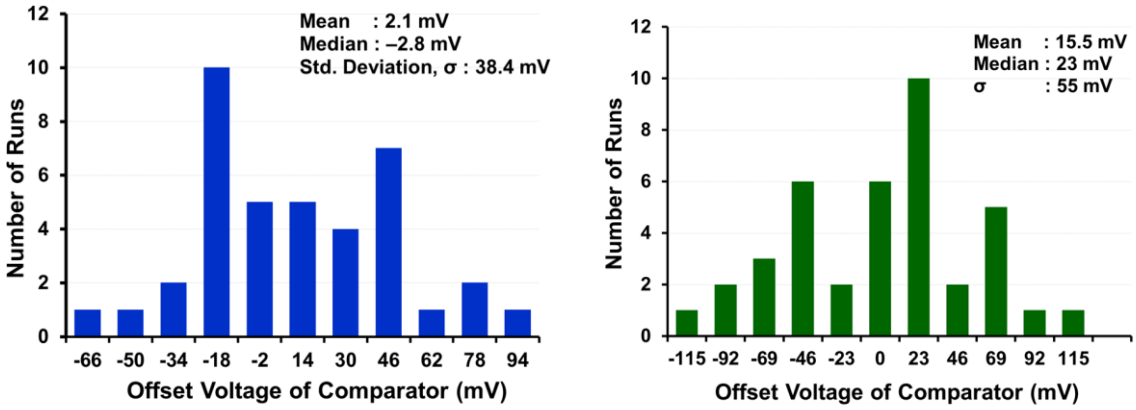


Figure 3.7 Schematic of the low-power comparator

Monte-Carlo simulations with three-sigma variations were performed to study the effect of matching and process variations on the comparators' offset voltage. The histograms showing the offset distribution for the virtual ground and virtual V_{DD} comparators, across 40 Monte-Carlo runs, are presented in Figure 3.8. Though the comparators exhibit a large offset voltage change across process and mismatch variations, the accuracy of the comparators is not as critical as their speed and power consumption. The power consumption needs to be kept low in order to limit total power dissipated by the control logic, and also to minimize the charge drained from the virtual supply nodes during the comparison. The simulated average power consumption of the comparator is less than 25 nW at 25 MHz clock frequency. Further, there is no quiescent current consumption with this topology. Hence, with this comparator implementation, accuracy is traded-off in order to lower power consumption with increased speed of operation.

Analysis of Leakage Paths in the comparator

The existence of leakage paths in the comparator needs to be checked in order to minimize undesirable effects of current flow and charge sharing between the power supply voltage (V_{DD}), reference voltage (V_{RG} or V_{RD}), and the virtual supply (V_{VGND} or V_{VDD}) nodes. The leakage current paths from V_{DD} or V_{RG} to V_{VGND} would increase the V_{VGND} and thus the charge accumulated by



(a) (b)

Figure 3.8 Histogram of comparator's offset voltage distribution from Monte-Carlo simulations

(a) Virtual Ground comparator (b) Virtual V_{DD} comparator

the CR capacitors would not be entirely from the ground-bound charge. In the virtual V_{DD} comparator, leakage from V_{VDD} to V_{RD} or ground (V_{SS}) would result in additional losses and reduce the efficiency of the system. Since the existence of leakage currents impacts the efficiency of the CR scheme, the comparators and the control signals were designed to eliminate the leakage paths.

High threshold voltage (HVT) devices, with threshold voltages of –490 mV for PMOS and 540 mV for NMOS, were employed to keep the subthreshold leakage low. Further, the body connections of the input devices were connected to V_{DD} (PMOS) and V_{SS} (NMOS), so as to exploit body-effect to increase the threshold voltages. In order to operate at high-speeds, the comparator has very small devices with minimum gate lengths and thereby reduces the amount of parasitic capacitance within the comparator.

Figure 3.9 presents the virtual ground comparator with leakage paths that if present would corrupt the virtual ground node. The path P1 represents the leakage path from V_{RG} through MN1 and MN2 to V_{VGND} while path P2 is the corresponding path from V_{RG} through PMOS devices to V_{VGND}. Since the maximum reference voltage is below 350 mV, the NMOS devices are always biased below their threshold voltages during the sampling phase. Further, as illustrated in Figure

3.9, when V_{VGND} is close to ground, MN1 will be OFF. For the case when V_{VGND} is close to V_{RG} (330 mV), the leakage current through P1 cannot flow to V_{VGND} since the common source node cannot be greater than 0.33 V. Next, considering the path P2 with PMOS devices, the worst case leakage scenario is when V_{VGND} is close to ground. The V_{GS} of MP1 can be close to threshold voltage but V_{GS} of MP2 is well below threshold. Hence, leakage from reference voltage to virtual ground through paths P1 and P2 is not possible with this setup. Employing HVT devices also minimizes the short circuit current flow from V_{DD} to V_{VGND} and V_{DD} to V_{SS} during the transition from sampling to regenerative phase.

The analysis for the virtual V_{DD} comparator is similar to the virtual ground comparison. The minimum reference voltage of close to 0.7 V is well below the threshold voltage of the PMOS devices while close to those of NMOS devices. However, there cannot be any leakage current path through the NMOS devices since one of them will have a very low V_{GS}. Further, during transition from the sampling to regenerative phase, there can be a very small amount of

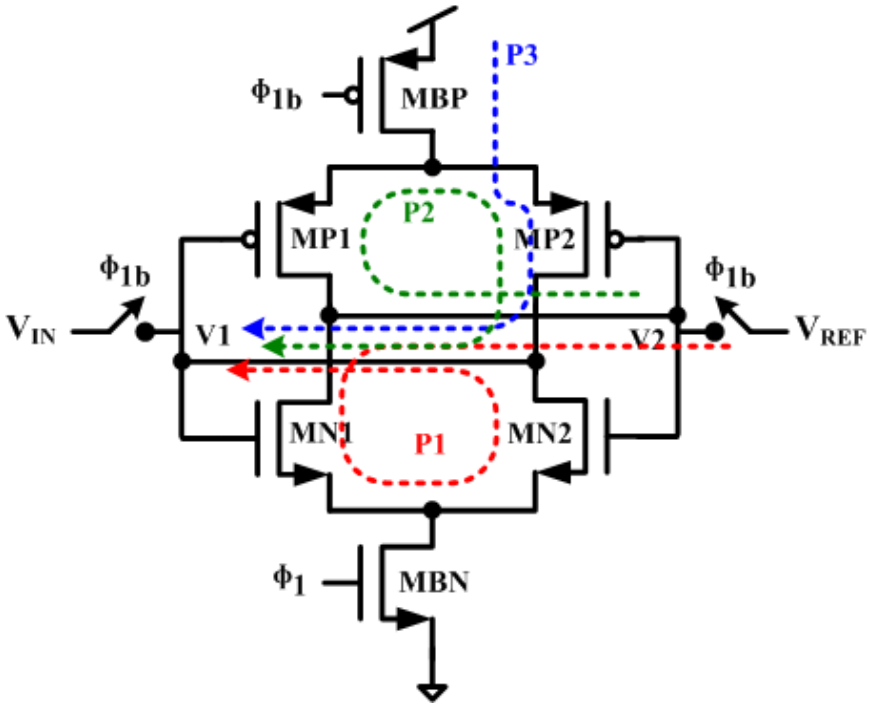


Figure 3.9 Comparator schematic illustrating the leakage paths to be investigated

short-circuit current flowing from the inputs to the ground. The rise and fall times of the transitions are in the order of a few tens of picoseconds and the peak current is severely limited by the high threshold voltages, thus the short-circuit current does not cause any appreciable change at the virtual supply node.

3.4 Analysis of Energy Consumption in the Charge-Recycling Scheme

To evaluate the efficiency of the system, it is important to analyze the energy consumption and energy savings in the charge-recycling scheme. The total energy E_{IN} stored by the CR capacitors at the end of the accumulation phase is given by

$$E_{IN} = \left(\frac{1}{2} N \cdot C_{CR} V_{RG}^{\,2}\right) N \tag{3.13}$$

where $N \cdot C_{CR}$ is the individual charge-recycling capacitance, V_{RG} is the maximum voltage at the virtual ground and N is the number of CR capacitors in parallel ($V_{DD} = N \cdot V_{RG}$). Without the CR scheme, this energy E_{IN} would have been lost as discharge to ground.

Let $E_{T,AVG}$ be the average energy consumed per computation by the target block. During the charge-accumulation phase, $E_{T,AVG}$ is provided by V_{DD}, whereas during the charge-recycling phase the CR capacitors furnish the required $E_{T,AVG}$. As long as the available energy, E_{IN}, is greater than the required, $E_{T,AVG}$, the recycling system provides energy to the target block provided V_{VDD} is above V_{RD}. Thus, only a portion of the total recovered charge is used in each accumulation-recycle phase while the rest of the charge resides on the CR capacitors. Note that from the second cycle onwards, the CR capacitors need to recover only the difference in charge required to reach to V_{RG} and so energy recovered can be written as

$$E_{IN}' = \frac{1}{2} C_{CR}\left(V_{DD}^{\,2} - V_{RD}^{\,2}\right) \tag{3.14}$$

Let the energy consumed by the control logic in the CR scheme be given by E_{DISS} which encompasses the energy dissipated by the clock to drive the switches, energy consumed by the comparators, control signal generation and also the resistive loss within the switches. The process-related leakage currents and parasitic coupling to the substrate also add to E_{DISS}. Note that $E_{T,AVG}$ determines the size of CR capacitors and switches. Now, the actual recycled energy E_{RCYC} is given by

$$E_{RCYC} = E_{T,AVG} \cdot N_{T,RCYC} = E_{IN}' - E_{DISS} \tag{3.15}$$

where $N_{T,RCYC}$ is the number of clock cycles in the target logic during the charge-recycling phase. Thus, the system's energy efficiency is maximized by reducing E_{DISS}. The percentage energy saved in the target block by charge-recycling is approximately given by

$$E_{SAVED} = \frac{E_{RCYC}}{E_{T,AVG}} \cdot 100\% \tag{3.16}$$

The efficiency of the charge-recycling scheme is given by

$$\eta_{RCYC} = \frac{E_{RCYC}}{E_{IN}'} \cdot 100\% \tag{3.17}$$

The total energy reduction in the system is the sum of energy saved in the source block as a result of dynamic voltage scaling during the charge-accumulation phase, and the energy saved in the target block (E_{SAVED}) due to charge-recycling phase.

3.4.1 Estimation of Virtual Power Supply Voltage levels and CR cycle

To estimate the amount of energy savings using the CR scheme, the dynamic virtual power supply level is first examined. With this designed charge-recycling scheme of N stages, $N \cdot C_{CR}$ is the size of individual charge-recycling capacitors. The maximum virtual ground voltage is set by the ground reference voltage of V_{RG} ($V_{RG} = V_{DD}/N$), while the minimum virtual V_{DD} voltage is the virtual V_{DD} reference of V_{RD} which is $V_{DD}–V_{RG}$. Figure 3.10 (a) and (b) illustrate the transient virtual V_{DD} (V_{VDD}) and virtual ground (V_{VGND}) levels during the charge-accumulation (CA-phase) and charge-recycle phases (CR-phase). As seen in Figure 3.10 (b), the charge-accumulation phase begins with an initial voltage of V_{RD}/N since the recycle phase does not reuse the entire charge stored in the CR capacitors. The virtual supply level seen by the charge-recycling circuit (source and target blocks are the same in this case) is shown in Figure 3.10 (c), which is the difference between V_{VDD} and V_{VGND}. The power delivered by the external power supply source is shown in Figure 3.10 (d). During the CR-phase, the power supply does not furnish any current to the circuit and so the power delivered is zero, neglecting the insignificant subthreshold leakage current through the power switch.

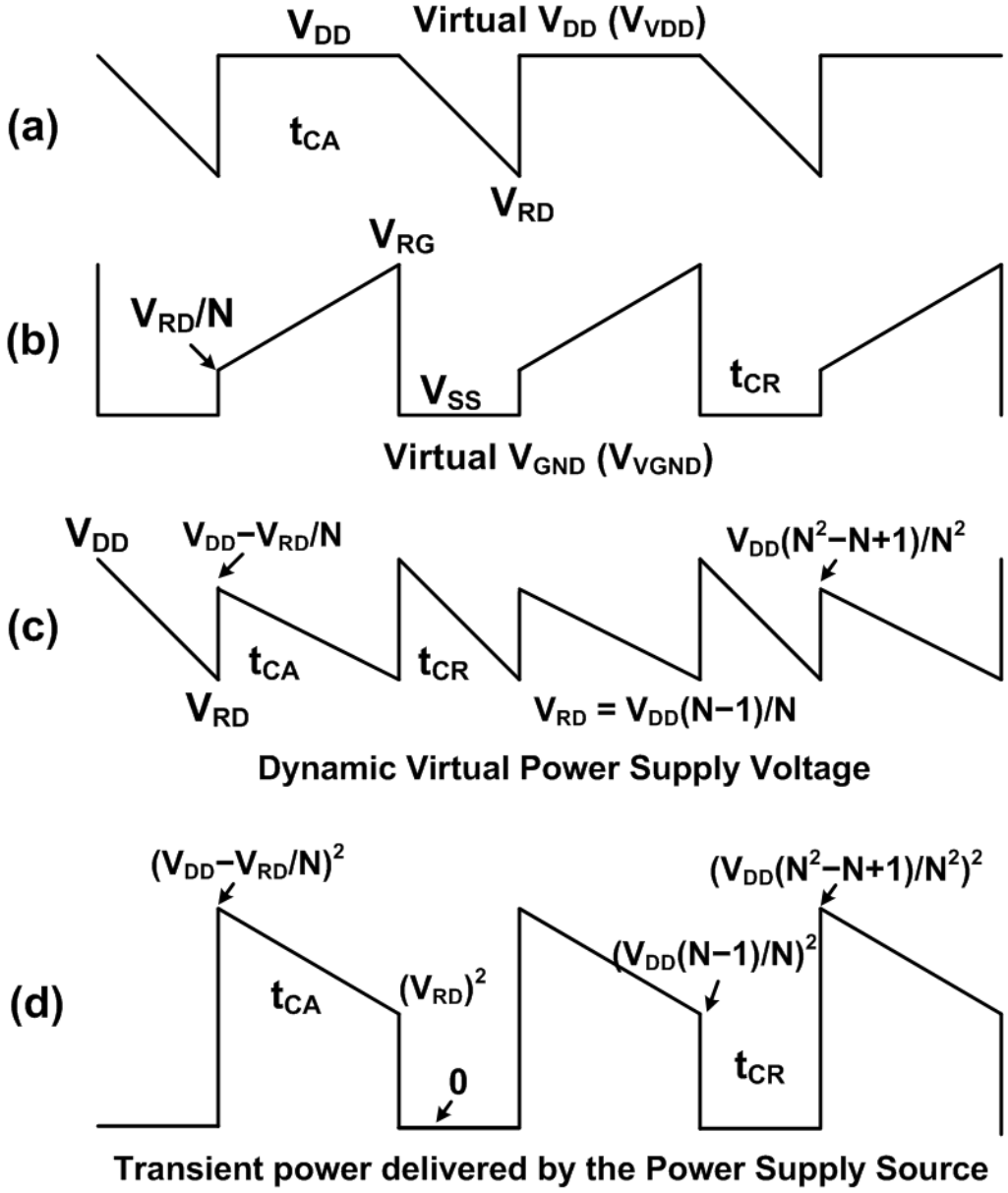


Figure 3.10 Virtual power supply voltage levels in the charge-recycling scheme
(a) virtual V_{DD} (V_{VDD}), (b) virtual ground (V_{VGND}), (c) $V_{VDD-}V_{VGND}$, and
(d) power delivered by the power supply source, $\alpha \cdot C_L(V_{VDD-}V_{VGND})^2 f$

To estimate the energy saved in one cycle of operation, the time taken to collect ground-bound charges (t_{CA}) and the time (t_{CR}) during which the target block is powered by the recycled charge are calculated. The rate of charging the CR capacitors during CA-phase depends on the activity factor, α, which is the probability of a *HIGH-to-LOW* (V_{DD}-*to-0*) transition. Also, the size of charge-recycling capacitors relative to the effective load capacitance (C_L) of the source block defines the increase in V_{VGND} with each clock cycle (t_{CLK}). Hence, the increase in V_{VGND} due to ground-bound switching charges, after each clock cycle, can be approximated as

$$\Delta V_{VGND}(t) = \frac{Q(t)}{NC_{CR} \cdot N} = \frac{\alpha \cdot C_L (V_{DD} - V_{VGND}(t))}{NC_{CR} \cdot N} = S \cdot (V_{DD} - V_{VGND}(t)) \tag{3.18}$$

where $V_{VGND}(t)$ represents the virtual ground voltage at the clock event, and the CR capacitor bank has N stages of $N \cdot C_{CR}$ capacitors connected in parallel from V_{VGND} to V_{SS}. Short-circuit and subthreshold leakage currents represent the other sources of charge to increase the V_{VGND}. The contribution from these current components can be approximated as

$$\Delta V_{VGND}(t) = \frac{Q_{LKG}(t)}{NC_{CR} \cdot N} = \frac{C_{LKG,SC} (V_{DD} - V_{VGND}(t))}{NC_{CR} \cdot N} = L \cdot (V_{DD} - V_{VGND}(t)) \tag{3.19}$$

where $C_{LKG,SC}$ is the effective capacitance that represents the leakage currents. The total increase in the virtual ground voltage is the sum of (3.18) and (3.19). The loss of charge from the CR capacitor bank to charge the logic-ground (*LOW*) nodes within the source block from $V_{VGND}(t\text{-}1)$ to the current $V_{VGND}(t)$ value is very small. Further, in order to limit the analysis to the significant contributing factors, the charge lost from CR-bank to the internal ground nodes is not included. Thus, the increase in V_{VGND} due to ground-bound switching and leakage current components after each clock cycle can be approximated as

$$\Delta V_{VGND}(t) = (S + L) \cdot (V_{DD} - V_{VGND}(t)) = K \cdot (V_{DD} - V_{VGND}(t)) \tag{3.20}$$

The virtual ground voltage can now be written as

$$V_{VGND}(t) = V_{VGND}(t-1) + \Delta V_{VGND}(t-1) \tag{3.21}$$

$$V_{VGND}(t) = V_{VGND}(t-1) \cdot \left[1 - \frac{\alpha \cdot C_L}{N^2 C_{CR}} - \frac{C_{LKG,SC}}{N^2 C_{CR}} \right] + V_{DD} \cdot \left[\frac{\alpha \cdot C_L}{N^2 C_{CR}} + \frac{C_{LKG,SC}}{N^2 C_{CR}} \right] \tag{3.22}$$

Simplifying (3.22) gives

$$V_{VGND}(t) = V_{VGND}(t-1)\cdot[1-K]+K\cdot V_{DD} \tag{3.23}$$

The boundary conditions can now be included to calculate the charge-accumulation time, t_{CA}. During the first cycle of charge-accumulation, the initial V_{VGND} is at V_{SS}, while from the next cycle onwards the initial V_{VGND} is at V_{RD}/N. At time t_{CA}, the final V_{VGND} voltage is at V_{RG}. So, the boundary conditions can be incorporated as

$$V_{VGND}(0) = \frac{V_{RD}}{N} = \frac{N-1}{N^2}\cdot V_{DD} \tag{3.24}$$

$$V_{VGND}(t_{CA}) = V_{RG} = \frac{V_{DD}}{N} \tag{3.25}$$

The V_{VGND} voltage at a time t can be visualized as made of small packets of charge flowing to the CR bank at a period of t_{CLK}. Thus, the charge-accumulation time has t_{CA}/t_{CLK} number of charge flow cycles and is represented as 'a'. Using (3.23) and (3.24), the V_{VGND} can now be written as

$$V_{VGND}(1) = \frac{N-1}{N^2}\cdot V_{DD}(1-K)+K\cdot V_{DD} \tag{3.26}$$

$$V_{VGND}(2) = \frac{N-1}{N^2}\cdot V_{DD}(1-K)^2 + K(1-K)\cdot V_{DD} + K\cdot V_{DD} \tag{3.27}$$

where, the numbers 1 and 2 represent the number of clock periods, i.e. $V_{VGND}(2)=V_{VGND}(2\cdot t_{CLK})$. The general equation for V_{VGND} at the i^{th} clock period is given by

$$V_{VGND}(i) = \frac{N-1}{N^2}\cdot V_{DD}(1-K)^i + K\cdot V_{DD}\left[1+(1-K)+(1-K)^2+\ldots+(1-K)^{i-1}\right] \tag{3.28}$$

The solution for the geometric series in the second term can be integrated to result in

$$V_{VGND}(i) = \frac{N-1}{N^2}\cdot V_{DD}(1-K)^i + V_{DD}\cdot\left[1-(1-K)^{i-1}\right] \tag{3.29}$$

The final boundary condition can be used to obtain $t_{CA} = a\cdot t_{CLK}$ as

$$V_{VGND}(a) = \frac{V_{DD}}{N} = \frac{N-1}{N^2}\cdot V_{DD}(1-K)^a + V_{DD}\cdot\left[1-(1-K)^{a-1}\right] \tag{3.30}$$

$$1 = \frac{N-1}{N}(1-K)^a + N\cdot\left[1-(1-K)^{a-1}\right] \tag{3.31}$$

Thus, for a given number of charge-recycling capacitor stages (N), the time taken ($a \cdot t_{CLK}$) to reach the virtual ground reference voltage (V_{RG}) depends on K which is the ratio of $\alpha \cdot C_L + C_{LKG,SC}$ to $N^2 \cdot C_{CR}$. For the very first CA-phase (with initial voltage at *0*), the first term in (3.29) and (3.31) are zero, thus t_{CA0} is N times longer than in the subsequent cycles.

The charge-recycling time (t_{CR}) can be derived using a similar approach as the t_{CA}. The initial V_{VDD} voltage starts at V_{DD} and subsequently decreases to V_{RD} in time t_{CR} that is equal to $r \cdot t_{CLK}$. The rate of discharging in CR-phase depends on the activity factor, κ which is the probability of a *LOW-to-HIGH* (*0-to-*V_{DD}) transition. The relative sizes of charge-recycling capacitors and the effective load capacitance (C_{LT}) of the target block define the reduction in V_{VDD} with each clock cycle (t_{CLK}). Hence, the decrease in V_{VDD} due to *LOW-to-HIGH* transitions, short-circuit and leakage currents, after each clock cycle, can be approximated as

$$\Delta V_{VDD}(t) = \frac{Q(t)}{C_{CR}} = \frac{(\kappa \cdot C_{LT} + C_{LKG,SC}) V_{VDD}(t)}{C_{CR}} = B \cdot V_{VDD}(t) \tag{3.32}$$

where the effective charge-recycling capacitance reduces to C_{CR} due to vertical stacking of the capacitors in the CR-phase. The virtual supply voltage can now be written as

$$V_{VDD}(t) = V_{VDD}(t-1) - \Delta V_{DD}(t-1) \tag{3.33}$$

$$V_{VDD}(t) = V_{VDD}(t-1) \cdot \left[1 - \frac{\kappa \cdot C_{LT}}{C_{CR}} - \frac{C_{LKG,SC}}{C_{CR}} \right] = V_{VDD}(t-1) \cdot (1-B) \tag{3.34}$$

The boundary conditions are given by

$$V_{VDD}(0) = V_{DD} \quad ; \quad V_{VDD}(t_{CR}) = V_{RD} = \frac{N-1}{N} \cdot V_{DD} \tag{3.35}$$

The general equation for V_{VDD} at the i^{th} clock period is now given by

$$V_{VDD}(i) = V_{DD}(1-B)^i \tag{3.36}$$

The final boundary condition can be used to obtain $t_{CR} = r.t_{CLK}$ as

$$V_{VDD}(r) = \frac{N-1}{N} \cdot V_{DD} = V_{DD}(1-B)^r \tag{3.37}$$

$$\frac{N-1}{N} = (1-B)^r \tag{3.38}$$

Thus, for a given number of charge-recycling capacitor stages (N), the time taken ($r \cdot t_{CLK}$) to reach the virtual supply reference voltage (V_{RD}) depends on B which is the ratio of $\kappa \cdot C_{LT} + C_{LKG,SC}$ to C_{CR}.

Short-circuit and leakage current components are generally close to 20% of the switching current consumption. However, with the effective supply voltage reduction (reduced DIBL) and body effect, short-circuit and leakage currents are reduced. Hence, assuming an average of 10% for the leakage factors results in $C_{LKG,SC}$ equal to $0.1\alpha \cdot C_L$. Further, for the same source and target blocks, the probabilities for *HIGH-to-LOW* and *LOW-to-HIGH* transitions, and the effective load capacitances can be assumed to be equal ($\alpha = \kappa$ and $C_L = C_{LT}$). Thus, equal amounts of charge is accumulated or recycled from the CR capacitor bank during each clock transition. Solving (3.31) with $N = 3$, $\alpha = 0.5$, capacitance ratio of $C_{CR}/C_L = 50$, the value of 'a' is 305 for the first CA-phase, and 117 for the subsequent CA cycles. Solving (3.38) with the same set of values results in the value of 'r' at 33. Thus, t_{CR} (i.e. r) is approximately equal to t_{CA}/N^2 for the first cycle while from the second cycle onwards the ratio is $1/N$. Figure 3.11 presents the duration of CR cycle which is the derived from (3.31) and (3.38) as a function of C_{CR}/C_L, for different number of CR capacitor stages (N). This plot provides an insight into the design parameters of area that is defined by C_{CR}/C_L, and the amount of energy reduction which is influenced by the duration of CR cycle (i.e. $a+r$).

These results can be also be intuitively arrived by examining the amount of voltage change, per clock period, in the two phases. The total charge that is accumulated in CA-phase is equal to the charge recycled during the CR-phase. The amount of accumulated charge is given by

$$\Delta Q_{CA} = N^2 \cdot C_{CR}(V_{RG} - \frac{V_{RD}}{N}) = V_{RG} N \cdot C_{CR} \tag{3.39}$$

The recycled charge amounts to

$$\Delta Q_{CR} = C_{CR}(V_{DD} - V_{RD}) = V_{RG} \cdot C_{CR} \tag{3.40}$$

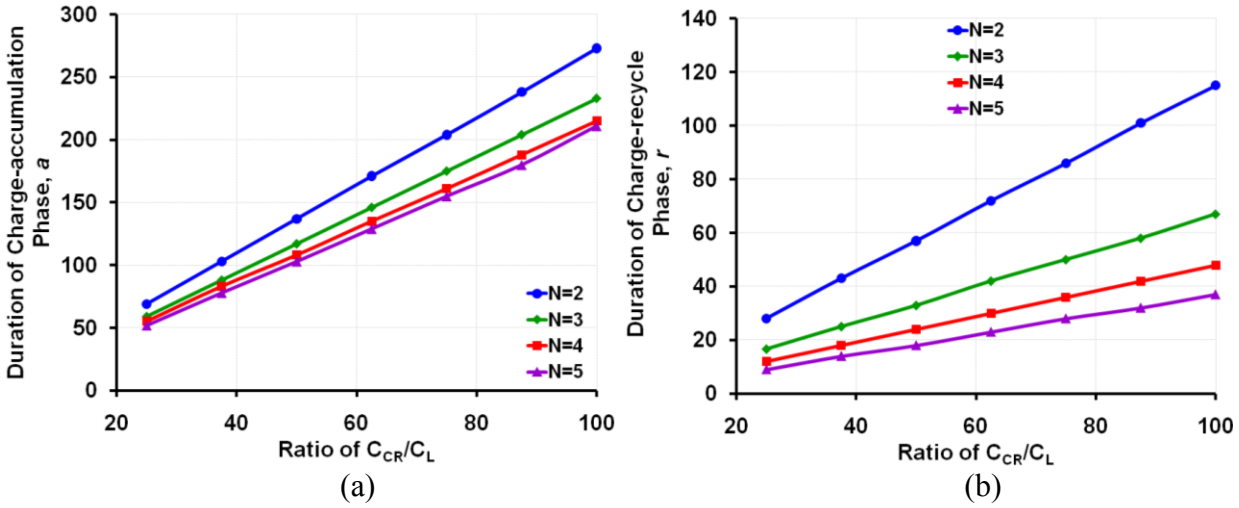


Figure 3.11 Duration of CR cycle as a function of C_{CR}/C_L across number of stages (N)
(a) duration of charge-accumulation phase, and (b) duration of charge-recycle phase

As evident from (3.39) and (3.40), with equal amounts of charge drawn per clock period, the CA-phase would be N times longer than the CR-phase. This result is valid only when equal amounts of charge flow during each clock period, which was assumed from using the same source and target blocks with equal $\alpha \cdot C_L + C_{LKG,SC}$ and $\kappa \cdot C_{LT} + C_{LKG,SC}$. For different source and target blocks, the ratios of $(\alpha \cdot C_L + C_{LKG,SC})/(N^2 C_{CR})$ and $(\kappa \cdot C_{LT} + C_{LKG,SC})/C_{CR}$ define the respective times.

3.4.2 Estimation of Energy Saved using CR Scheme

The energy consumed by the CR system can be estimated from the instantaneous virtual supply voltage levels. The instantaneous power can be approximated as

$$Power(t) = \gamma \cdot C_L (V_{VDD}(t) - V_{VGND}(t))^2 \cdot f_{CLK} \qquad (3.41)$$

where γ is the probability of a switching transition and f_{clk} is the frequency of operation. For convenient reference, the instantaneous virtual supply and power levels at the circuit are included again as Figure 3.12 (a) and (b). The circuit's power consumption follows the curve in Figure 3.12 (b) while, the external power supply actually furnishes power only during the charge accumulation phase, as depicted in Figure 3.12 (c). The energy expended by the circuit for one cycle of operation (T) can be approximated as

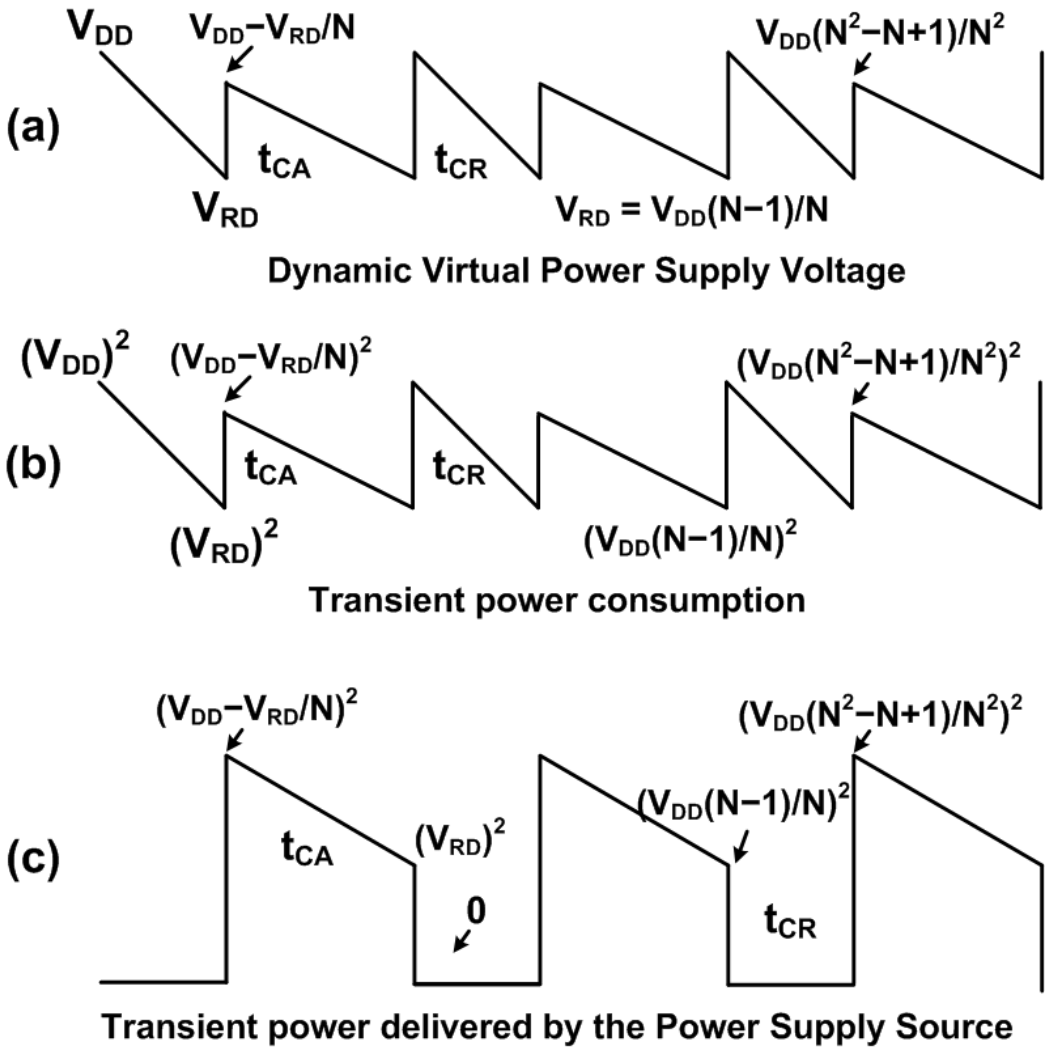


Figure 3.12 Virtual power supply voltage levels and power consumption in the CR system (a) V_{VDD}-V_{VGND}, (b) transient power consumption, $\gamma \cdot C_L(V_{VDD-}V_{VGND})^2 f$, and (c) transient power delivered by power supply source, $\gamma \cdot C_L(V_{VDD-}V_{VGND})^2 f$

$$Energy = \int_0^T power(t) \cdot dt = \int_0^T \gamma \cdot C_L \cdot \left(V_{VDD}(t) - V_{VGND}(t)\right)^2 dt \tag{3.42}$$

As seen in Figure 3.12 (b), the transient power is cyclic with a period of $t_{CA}+t_{CR}$. From the previous discussion on virtual supply levels, it is reasonable to assume that the virtual supply voltage decreases linearly by ΔV, which is equal to (3.20) in CA and (3.32) in CR, with each clock period, t_{CLK}. The transient virtual supply voltage is derived separately for the two phases of operation in order to estimate the energy consumption and savings. The energy dissipated by the circuit is given by

$$Energy = M \cdot \int_0^{t_{CA}} power, CA(t) \cdot dt + M \cdot \int_0^{t_{CR}} power, CR(t) \cdot dt \tag{3.43}$$

where $M=T/(t_{CA}+t_{CR})$. The power is estimated using the virtual supply values at the start and end of each phase. The energy spent during the CA-phase is

$$Energy, CA = M \cdot \int_0^{t_{CA}} \gamma \cdot C_L f_{CLK} \cdot \left[\frac{V_{DD}^2}{N^2} \left[(N-1)^2 - \frac{\left(N^2 - N + 1\right)^2}{N^2} \right] \cdot \frac{t}{t_{CA}} + \frac{V_{DD}^2}{N^4} \left(N^2 - N + 1\right)^2 \right] \cdot dt \tag{3.44}$$

$$Energy, CA = M \cdot \gamma \cdot \frac{C_L}{t_{CLK}} \cdot \left[\frac{V_{DD}^2}{N^2} \left[(N-1)^2 - \frac{\left(N^2 - N + 1\right)^2}{N^2} \right] \cdot \frac{t_{CA}}{2} + \frac{V_{DD}^2}{N^4} \left(N^2 - N + 1\right)^2 \cdot t_{CA} \right] \tag{3.45}$$

Substituting $t_{CA}=a \cdot t_{CLK}$ and simplifying (3.45) gives

$$Energy, CA = M \cdot \gamma \cdot C_L \cdot \left[\frac{a \cdot V_{DD}^2}{2N^2} \left[(N-1)^2 + \frac{\left(N^2 - N + 1\right)^2}{N^2} \right] \right] \tag{3.46}$$

Note that γ is the probability of any switching transition, and not α which is the probability of a HIGH-to-LOW transition during CA-phase, is included in the power estimation. The probability

factor α defines the slope of the virtual power supply in CA-phase and is integrated into (3.46) by the factor '*a*'.

The energy expended by the circuit during the CR-phase can be calculated by following a similar approach.

$$Energy, CR = M \cdot \int_0^{t_{CR}} \gamma \cdot C_L f_{CLK} \cdot \left[\frac{V_{DD}^2}{N^2}(-2N+1) \cdot \frac{t}{t_{CR}} + V_{DD}^2 \right] dt \tag{3.47}$$

$$Energy, CR = M \cdot \gamma \cdot \frac{C_L}{t_{CLK}} \cdot \left[\frac{V_{DD}^2}{N^2}(-2N+1) \cdot \frac{t_{CR}}{2} + V_{DD}^2 \cdot t_{CR} \right] \tag{3.48}$$

Substituting $t_{CR}=r \cdot t_{CLK}$ and simplifying (3.48) gives

$$Energy, CR = M \cdot \gamma \cdot C_L \cdot \left[\frac{r \cdot V_{DD}^2}{2N^2} \cdot (2N^2 - 2N + 1) \right] \tag{3.49}$$

The total energy consumption is the sum of those from the two phases and is

$$Energy = M \cdot \gamma \cdot C_L \cdot \left[\begin{array}{l} \frac{a \cdot V_{DD}^2}{2N^2} \left[(N-1)^2 + \frac{(N^2 - N + 1)^2}{N^2} \right] + \\ \left[\frac{r \cdot V_{DD}^2}{2N^2} \cdot (2N^2 - 2N + 1) \right] \end{array} \right] \tag{3.50}$$

The energy consumed by the circuit operating with a fixed $V_{DD,}$ i.e without charge recycling is

$$Energy, ckt = \int_0^T \gamma \cdot C_L \cdot V_{DD}^2 \cdot \frac{1}{t_{CLK}} dt \tag{3.51}$$

Using the relationship $T=M \cdot (a+r) \cdot t_{CLK}$ to simplify the equation, results in

$$Energy, ckt = M \cdot (a+r) \cdot \gamma \cdot C_L \cdot V_{DD}^2 \tag{3.52}$$

The percentage reduction in the energy consumption can now be determined using

$$\%\, Energy\ Saved = \left(1 - \frac{Energy\ with\ CR\ scheme}{Energy\ without\ CR\ scheme} \right) \cdot 100\% \tag{3.53}$$

$$\%\ Energy\ Saved\ = \left(\begin{array}{l} 1 - \dfrac{a}{(a+r)\cdot 2N^2}\left[(N-1)^2 + \dfrac{(N^2-N+1)^2}{N^2} \right] \\ -\left(\dfrac{r}{(a+r)} \right) \dfrac{(2N^2-2N+1)}{2N^2} \end{array} \right) \cdot 100\% \qquad (3.54)$$

Simplifying using the result $r \approx a/N$ arrived by solving (3.31) and (3.38), gives

$$\%Engy\ Svd = \left(1 - \frac{1}{2N(N+1)}\left[(N-1)^2 + \frac{(N^2-N+1)^2}{N^2} + \frac{(2N^2-2N+1)}{N} \right] \right) \cdot 100\% \qquad (3.55)$$

Equation (3.50) presents the total energy consumption of the charge-recycling circuit. Since a percentage of this energy is being supplied by the recycled charges, the actual energy delivered by the external power source corresponds to the energy dissipated during the CA-phase. Thus, the percentage energy consumed by the charge-recycling circuit from the external power source is the ratio of (3.50) by (3.52), which is

$$Normalized\ Energy = \left[\frac{a}{(a+r)\cdot 2N^2}\left[(N-1)^2 + \frac{(N^2-N+1)^2}{N^2} \right] \right] \qquad (3.56)$$

The percentage reduction in the energy supplied by the power supply source is

$$\%\ Energy\ \ Saved = \left(1 - \frac{a}{2N^2(a+r)}\left[(N-1)^2 + \frac{(N^2-N+1)^2}{N^2} \right] \right) \cdot 100\% \qquad (3.57)$$

This result can be simplified using the approximation $r \approx a/N$ to give

$$\%\ Energy\ \ Saved = \left(1 - \frac{1}{2N(N+1)}\left[(N-1)^2 + \frac{(N^2-N+1)^2}{N^2} \right] \right) \cdot 100\% \qquad (3.58)$$

Thus, equation (3.54) represents the percentage of energy saved by the dynamic voltage scaling, while (3.57) provides the percentage energy saved by integrating both dynamic voltage scaling and charge recycling from the proposed charge-recycling scheme. The energy savings can be estimated for a given number of CR stages, N, by calculating the values of 'a' and 'r' from

equations (3.31) and (3.38). For $N=3$, the values of 'a' and 'r' are 117 and 33 respectively, for C_{CR}/C_L of 50. Substituting these values in (3.54) results in a 43% reduction in the energy consumption, while the energy furnished by power supply reduced to 59% from (3.57).

Equations (3.55) and (3.58) provide a quick approximation to the percentage energy saved as a function of N. Figure 3.13 presents a plot with the estimated energy savings that can be achieved using the charge-recycling scheme (equations (3.55) and (3.58)), across different number of stages, N. This relationship holds true for the case with the same circuit block used as the source and as the target. For different configurations, the equations should be modified to include the appropriate energy components from the circuits. Also, the energy consumed by the charge-recycling control generation block is not included in (3.55) and (3.58). Hence, the total energy saved in the system would be offset from (3.58) by the percentage of energy consumed by CR control block to the energy dissipated by the system without CR.

In summary, equations necessary to estimate the achievable energy reduction using the

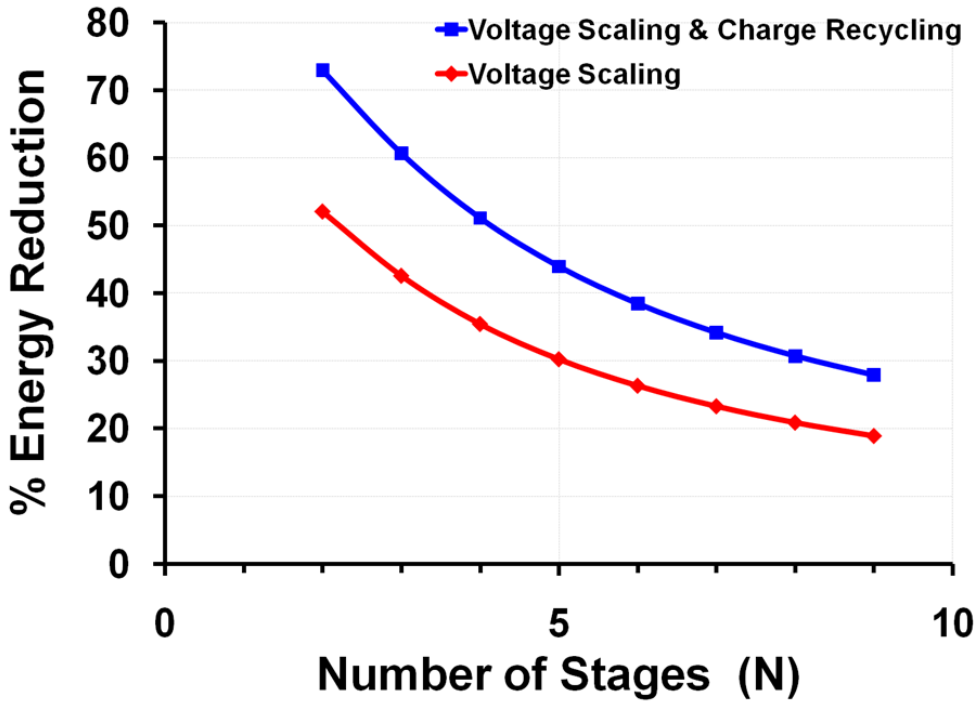


Figure 3.13 Percentage energy saved by employing the proposed charge recycling technique

proposed charge-recycling scheme have been derived in this section. Also, the design equations that define the energy-reduction-to-area-increase tradeoff have been derived in order to optimize the CR implementation.

3.5 Implementation of the charge-recycling methodology

Different implementations of the proposed scheme are possible that depend on the requirements of the application. The charge-recycling approach can be employed at the circuit-level or at the system-level. At the circuit-level, since the charge recovered from the source circuit is immediately boosted to virtual V_{DD}, it is possible to use this V_{VDD} to furnish power to the source circuit and thus realize a partially self-powered circuit. Figure 3.14 presents the functional schematic of the CR scheme applied at circuit-level in the system.

At the system level, a time multiplexing approach may be employed wherein multiple CR banks can be used to provide continuous virtual V_{DD} to the target blocks. Figure 3.15 presents a time-multiplexed CR system that can achieve power-autonomy in the target block by operating

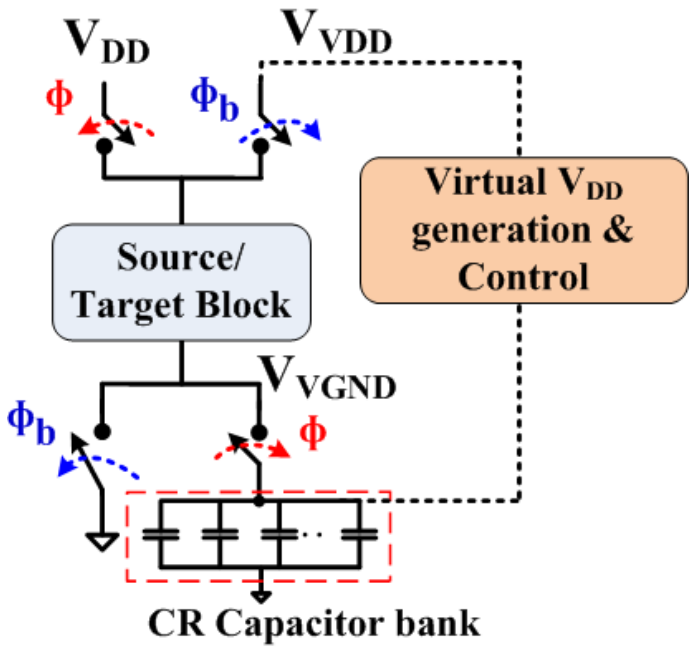


Figure 3.14 Functional schematic of partially-self powered charge-recycling system

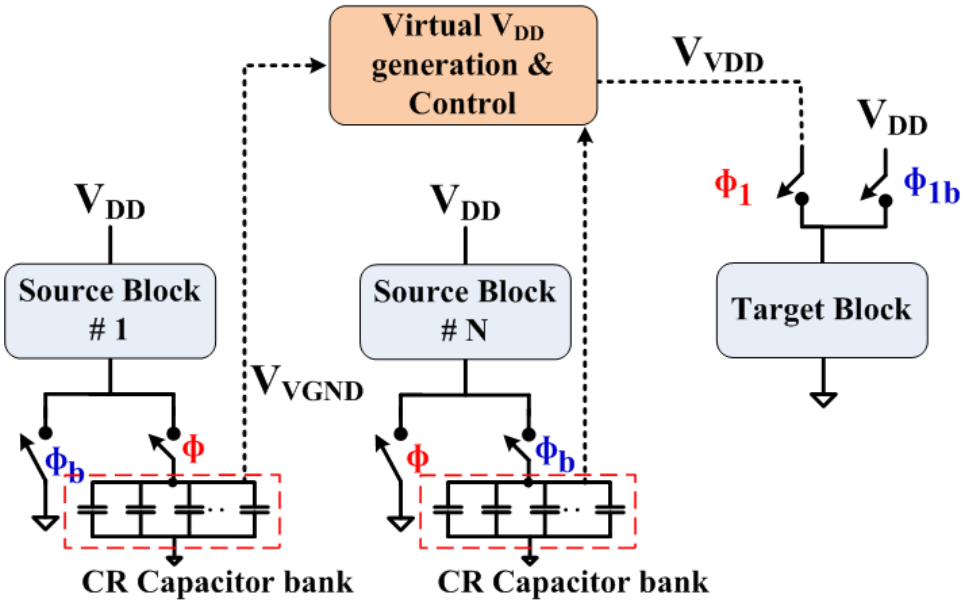


Figure 3.15 Schematic illustrating time-multiplexed virtual V_{DD} generation

entirely from recycled power and not the power supply voltage. Further, based on the energy requirements, alternate topologies can be devised to employ one virtual V_{DD} bank to furnish power to different target blocks, as illustrated in Figure 3.16. Thus, the target application defines the best strategy for implementing the proposed charge-recycling scheme.

3.5.1 Design Methodology

This section provides an overview of the design and implementation methodology of the CR scheme in mixed-signal systems. The design parameters that influence the energy-efficiency in this CR scheme include the reference voltages of V_{RG} and V_{RD}, number of stages N and size of CR capacitor (C_{CR}).

3.5.1.1 Determination of virtual supply voltage levels and number of stages *N*

The source logic block and the target logic block could be different components of a digital system or the same logic circuit. Identification of potential blocks in a system is essential to maximize charge-recycling and power reduction. The choice of the source and target blocks is governed by the rate of switching activity in the logic and also by the ease with which the system

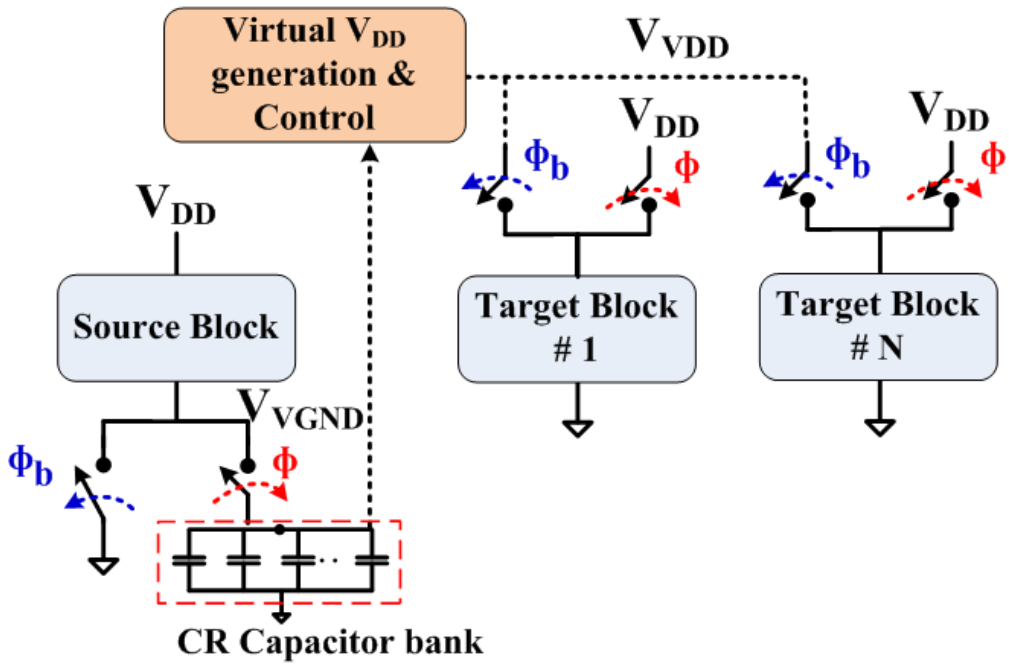


Figure 3.16 Alternate implementation of CR scheme to support multiple target blocks

can be separated into functional blocks. The dynamic virtual supply scaling as result of charge-recycling causes a decrease in the performance of the system. Thus, the critical factor that determines the successful implementation is the energy-efficiency or performance requirement of the application.

Depending on the application, since the reduction in performance of functional blocks in the non-critical delay path does not affect the overall system performance, these blocks can be exploited for charge-recycling. Characterization of the source and target blocks with reduced supply voltage is essential in order to estimate the amount of charge that can be recycled, and thus the virtual supply levels. Once the minimum V_{DD} ($V_{DD,min}$) that guarantees the system's required performance has been estimated, the values of the maximum virtual ground (V_{RG}) and virtual V_{DD} (V_{RD}) references are set as V_{DD}–$V_{DD,min}$ and $V_{DD,min}$, respectively. The number of CR capacitor stages, N, is obtained from the voltage boosting ratio of V_{DD}/V_{RG}.

Once the number of CR stages N has been obtained, an estimate of the percentage energy reduction can be obtained from the plot in Figure 3.13 or using the equations (3.55) and (3.58).

3.5.1.2 Estimation of Charge-recycling capacitor size

As discussed in section 3.3.2, the value of charge-recycling capacitor depends on the power consumption of the target block, area requirements of CR capacitors, and the duration of CR-cycle which determines the energy-efficiency of the implementation. The analysis presented in the previous section provides the vital relationship between the CR capacitor size, power consumption of the target or source block and the CR-cycle. Hence, equations (3.31) and (3.38) can be effectively used to find the optimum value of C_{CR} for the desired N. The optimum value of C_{CR} is arrived by iterative method using (3.31) and (3.38) to determine the values of 'a' and 'r', for different C_{CR} sizes. The values of 'a' and 'r' are then substituted in (3.57) to estimate the energy reduction. The optimum C_{CR} that provides best energy reduction within the planned chip-area should be used in the system.

3.5.1.3 Power Budget

The power consumption of the logic block that controls the CR system contributes to the total power consumption. Careful power budgeting is therefore required to be able to realize power or energy savings using the CR scheme. The components that influence the power consumption in the control block include the comparators, buffers and the switching losses in the control switches that connect the CR capacitors in different CR-phases. Hence, longer duration of CR-cycle implies lower switching losses and reduced power consumption in the control logic block. The power consumption of the control logic can be incorporated in the total energy consumption equation of (3.46) as

$$Energy = \left[\begin{array}{l} M \cdot \gamma \cdot C_L \cdot \left[\dfrac{a \cdot V_{DD}^2}{2N^2} \left[(N-1)^2 + \dfrac{\left(N^2 - N + 1\right)^2}{N^2} \right] \right] \\ + M(a+r) \cdot \delta \cdot C_{LCB} \cdot V_{DD}^2 \end{array} \right] \tag{3.59}$$

where δ is the probability of switching event in the control block, C_{LCB} is the effective load capacitance and V_{DD} is the nominal power supply voltage. The factor $M \cdot (a+r)$ is included to account for the fact that the control block is clocked by the same clock as the application. Thus, the power budget for the control block to ensure the required percentage energy reduction can be obtained using (3.59).

3.5.2 Physical Implementation

A 12-bit Gray-code counter within a 12-bit, 8-channel low-power Wilkinson ADC [34] designed to operate at 10 KSps, has been employed to demonstrate the effectiveness of the recycling scheme. Since the counter consumes approximately 30% of the ADC's total power [34], power reduction at the counter would be highly beneficial. The CR scheme has been implemented in a 90-nm process where leakage effects are more pronounced. Additionally, the CR Gray-code counter design has been implemented in a 0.5-µm process to study the efficiency across different process technologies. Both the designs accumulate the ground-bound charges from the Gray-code counter and subsequently reuse this charge to furnish their power-supply requirements, thereby realizing a partially self-powered Gray-code counter.

Analog buffers were integrated in order to monitor the virtual supply and ground nodes for testing purposes in the 90-nm design. The simplified schematic of the two-staged operational amplifier (opamp) used as analog buffer is presented in Figure 3.17. The buffers were designed with thick-oxide devices and powered by 2.5 V supply. This facilitates the use of the same opamp circuit to buffer both the virtual ground and virtual V_{DD} voltages. Figure 3.18 presents the offset voltages, for different inputs, from Monte-Carlo simulation results for 100 runs with three-sigma process and mismatch variations. The buffer has an average systematic offset voltage of

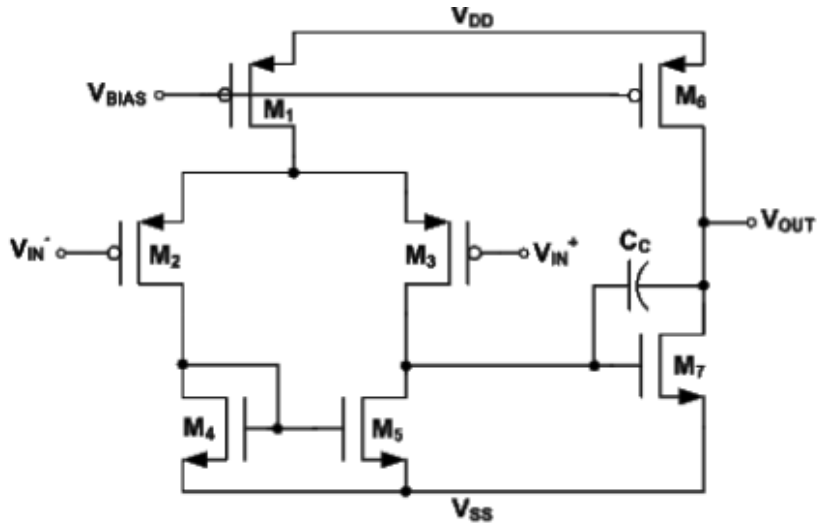


Figure 3.17 Simplified schematic of the analog buffer used to monitor the virtual supply nodes

approximately 5 mV in the range of interest. A third buffer was also integrated in order to be able to characterize the input referred offset voltage of the buffers.

Figure 3.19 and Figure 3.20 present the layouts of the CR based Gray-code counter in the 90-nm and 0.5-µm processes, respectively. The CR capacitors dominate the additional area required for the charge-recycling system. High-density, low-leakage metal-insulator-metal (MIM) on-chip capacitors were used for the CR capacitors. In the 90-nm implementation, the area of the CR system (counter, CR capacitors and control logic) is 13,500 μm^2 while the counter alone occupies an area of 7,200 μm^2. This increase is mainly due to the capacitors and they occupy an area of 6,300 μm^2 for a total of 15 pF. In the 0.5µm design, the counter alone occupies an area of 0.471 mm^2, and the 75pF total capacitance and logic take 0.077 mm^2 which is a 16% increase in the total area. Note that the source block used in this work is a simple 12-bit counter and the increase in overall area would be less substantial with a more complex source block or a system such as the ADC [30] where the area increase is only 1.3%. The power savings realized using the charge-recycling scheme justifies the increase in area.

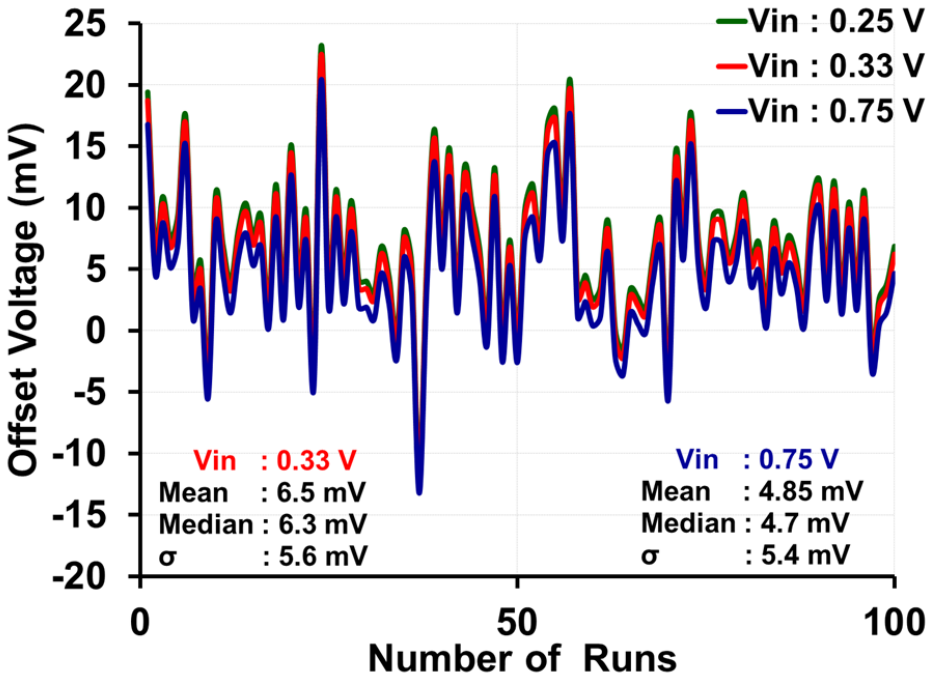


Figure 3.18 Input referred offset voltage of the analog buffer across the input voltage range of interest

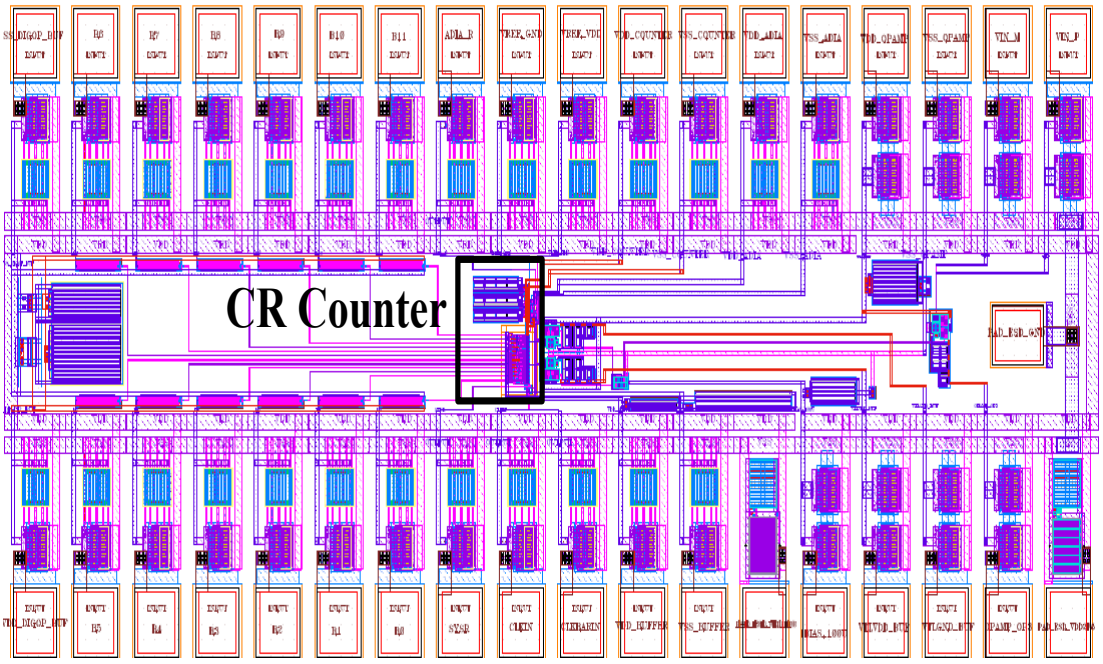


Figure 3.19 Layout of Gray-code counter with CR scheme in 90-nm process

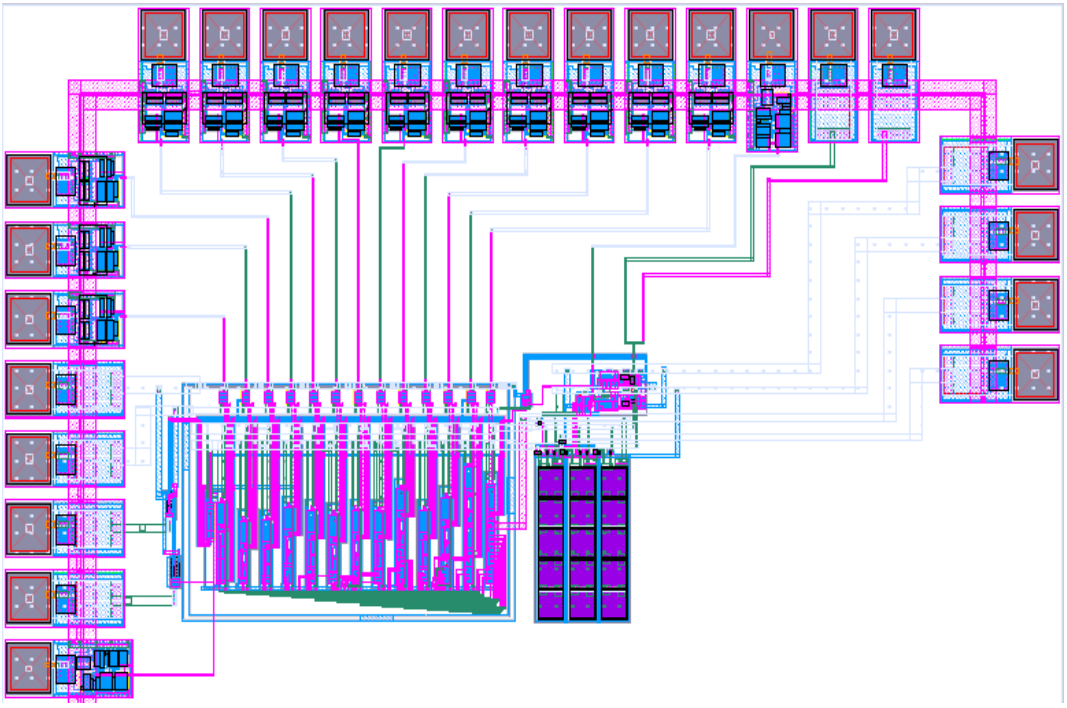


Figure 3.20. Layout of Gray-code counter with CR scheme in 0.5-μm process

3.6 Simulation Results and Performance Analysis

SPICE simulations were performed on the system to evaluate the power reduction and energy efficiency of the proposed scheme. For the 0.5-µm design, the power supply was set at 2.5 V, with the minimum virtual V_{DD} of 1.75 V. The 90-nm implementation has V_{DD} of 1 V with minimum V_{VDD} of 0.7 V. At the maximum ADC conversion rate, the Gray-code counter runs at 44 MHz. Hence the CR Gray-code counter was characterized at 50 MHz. In addition, the effectiveness of the recycling-scheme was also assessed using different target logic such as a 10-bit Binary counter and operating at a higher frequency of 100 MHz. Figure 3.21 presents the virtual V_{DD}, ground and counter output bit (before and after level-shifting) from the post-layout simulations at 50 MHz. As seen in Figure 3.21, once the V_{VGND} reaches V_{RG} of 0.3 V, the V_{VDD} is used to power up the circuit while V_{VGND} is connected to ground (seen as a drop in V_{VGND} node from V_{RG} to V_{SS}). The V_{VDD} node discharges with charge being drawn from the virtual supply for LOW-to-HIGH transitions during each clock cycle. Once the V_{VDD} reaches the V_{RD} reference of 0.7 V, the control switches over to charge-accumulation phase where V_{VGND} collects the ground-bound charge from digital transitions and leakage currents.

The transient power consumption of the charge-recycling Gray-code counter is presented

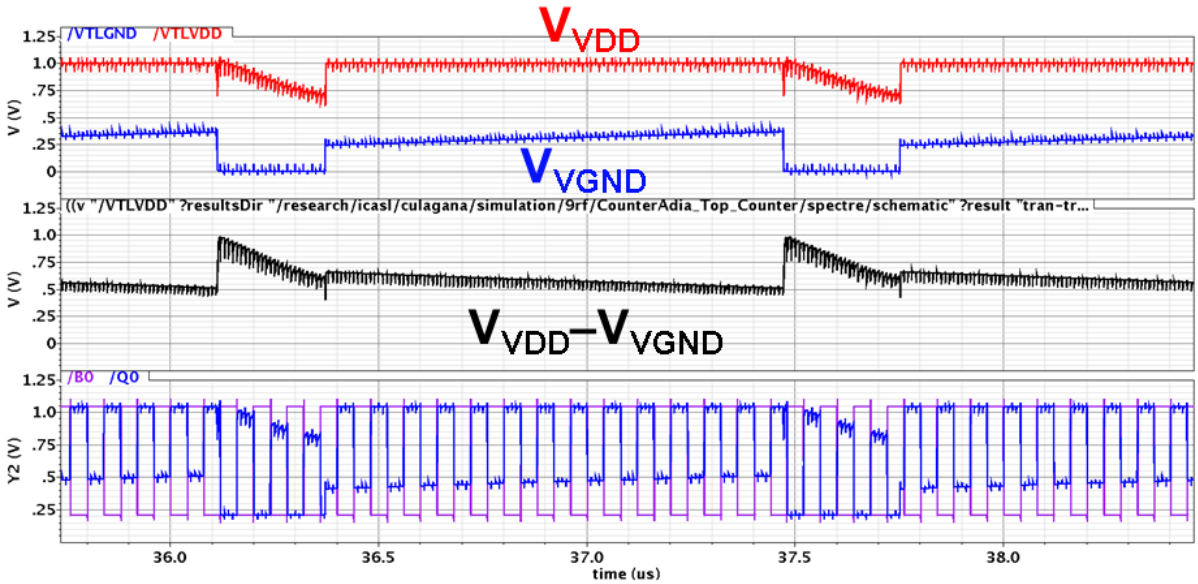


Figure 3.21 Transient simulation results of CR counter in 90-nm process

in Figure 3.22. The power consumption decreases gradually during the charge-accumulation phase due to increase in the virtual ground voltage level. During the charge-recycle phase, the virtual V_{DD} furnishes the required supply voltage and so the power delivered by the power supply is zero. The power dissipation in the recycle phase is due to the higher levels of dynamic V_{DD} (V_{DD} to V_{RD}) in the recycle phase as compared to the charge accumulation phase which has $7 \cdot V_{DD}/9$ to V_{RD} power supply voltage variation.

3.6.1 Energy Saving

The energy reduction of the partially self-powered counter was estimated by simulating at a fixed performance (at frequency of 50 MHz) with and without employing charge-recycling methodology. Figure 3.23 presents the power consumed by individual blocks in the counter and the amount of power savings achieved by charge-recycling scheme in the 90-nm implementation. The charge-recycling scheme reduces the power consumed by the Gray-code counter by 52%

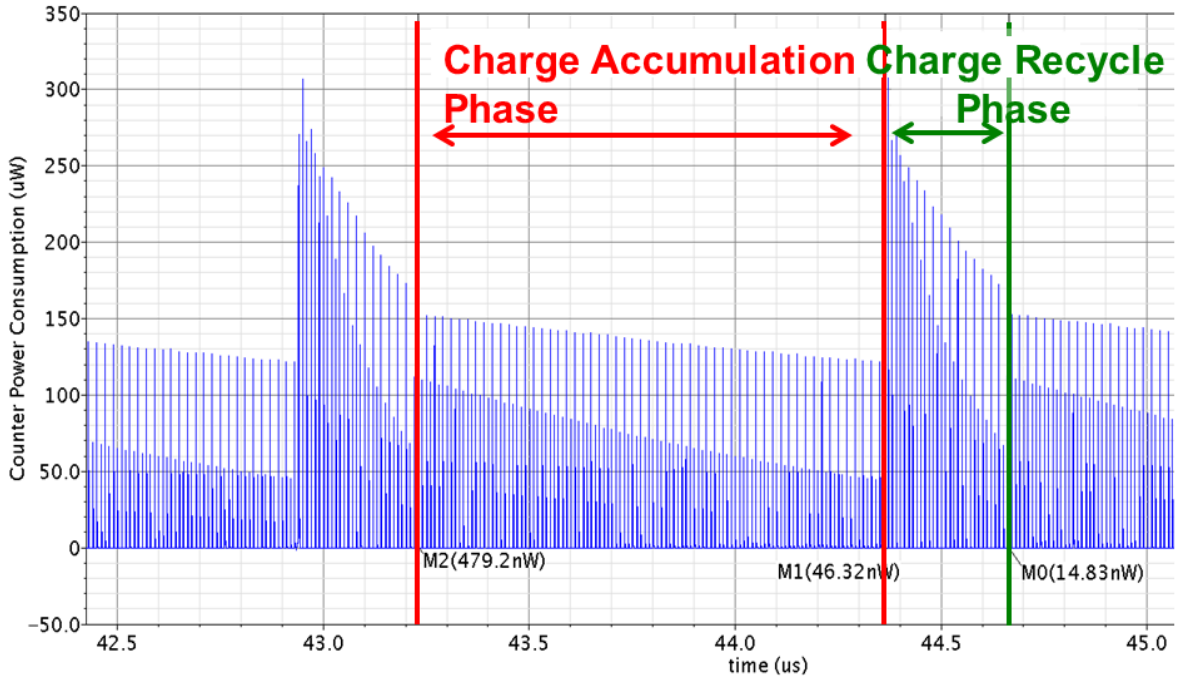
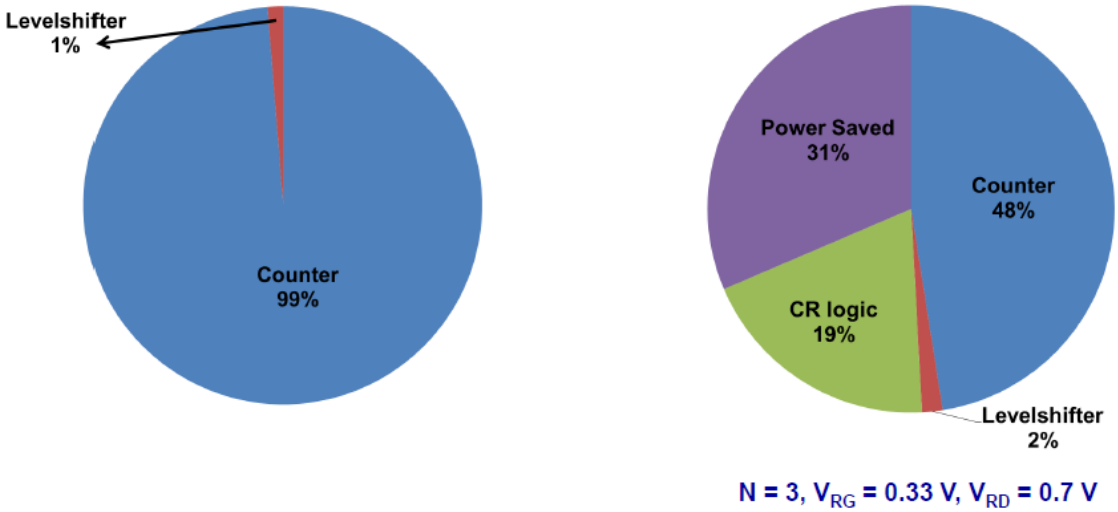


Figure 3.22 Simulated power consumption of the CR Gray-code counter



(a) (b)

Figure 3.23 Power consumption in the 12-bit Gray code counter in 90-nm implementation
(a) counter without charge-recycling (b) counter with charge-recycling

which is very close to the estimated 60% from Figure 3.13 in Section 3.4.2. The losses due to the finite voltage drop across the series switches, and the parasitic top and bottom plate capacitances contribute to the difference between the simulated and estimated values.

The total power saving that includes the power expended by the control logic amounts to 31% in the 90-nm CR counter design. The simulation results of energy consumption and the percentage energy reduction for both the implementations are presented in Table 3.1. The energy saved including the energy dissipated by the control circuitry is close to 30% in both the counter implementations. Since 90-nm process has more leakage current contributions, more charge is recycled and the dynamic V_{DD} reduction also reduces leakage currents and DIBL effect, thus contributing to increased energy savings in the 90-nm design. Furthermore, multiple threshold devices that are available in the 90-nm process were exploited to limit the power consumption of the level-shifters and comparators in the control logic. The comparable energy savings between the two designs verifies that the CR scheme can be employed to efficiently recycle switching-dominated charge as well as charge from leakage currents. The percentage savings can be further improved by minimizing the power dissipation in the comparator and control signals generation.

Table 3.1 Partially Self-Powered Circuit's performance with and without Charge-Recycling at 50 MHz

Gray-Code Counter Design	*Without CR (nJ)*	*With CR (nJ)*	*%Energy Reduction (Counter)*	*%Energy Reduction (incl. Control)*
0.5-µm	15.29	8.19	46%	26%
90-nm	0.241	0.116	52%	31.4%

The energy efficiency using different source and target blocks was also investigated, in the 90-nm design, with the Gray-code counter configured as the source and a different logic block (10-bit binary counter) as the target. Table 3.2 presents a comparison of the percentage energy saved by supplying the power to the Binary counter from the charge recycled in Gray-code counter, and vice versa. The system was simulated for the time required to complete one full cycle of counting at the target block, operating at a frequency of 100 MHz. Since both the counters have similar energy requirements and some of the recycled charge is dissipated at the switches, the charge-accumulation phase lasts longer than the charge-recycle phase. So, the energy reduction at the source block is more than that at the target block. Improving the efficiency of virtual V_{DD} generation would certainly increase the total energy saved at the target counter.

3.6.2 Effect on Circuit's Speed and Delay

Powering digital blocks from virtual V_{DD} and virtual ground introduces variations in the available supply voltage. In this CR scheme, the reduction in the available power supply and the use of body-effect to increase V_{TH}, as a means to reduce leakage currents, would result in increased circuit delay [29]. The propagation delay (t_d) of the counters operating at 50 MHz is presented in Table 3.3. The change in delay is expected due to the variation in power supply during both the charge-accumulation and the charge-recycling phases. It should be emphasized that the increase in delay does not degrade the performance of the counters and there are no missing counts at the output. Since this scheme is targeted for medium-speed low-power circuits, the small increase in delay does not adversely affect the system's performance and operation.

Table 3.2 Energy reduction of system with and without Charge-Recycling at 100MHz (90-nm design)

System Configuration	***Parameter***	***Without CR (pJ)***	***With CR (pJ)***	***%Reduction***
Source: Gray-code Counter Target: Binary Counter	Energy (source)	58.85	35.15	− 40.3%
	Energy (target)	60.84	45.47	− 25%
	Energy (system)	119.69	96.77	− 19%
Source: Binary Counter Target: Gray-code Counter	Energy (source)	243.3	131.4	− 46%
	Energy (target)	235.5	190.6	− 19%
	Energy (system)	478.8	384.2	− 20%

Table 3.3 Propagation delay with and without Charge-Recycling

Gray-Code Counter Design	***Without CR (ns)***	***With CR (ns)***	***Delay increase (ns)***
0.5 µm	2.00	2.66 – 3.13 (Avg: 2.9)	0.90
90 nm	1.11	1.22 – 1.86 (Avg: 1.54)	0.43

3.6.3 Leakage Current Reduction

One of the advantages of implementing a virtual supply and ground is the reduction in leakage currents [26]. The leakage current is dominated by sub-threshold leakage and DIBL currents and is modeled by [33]

$$I_{OFF} = Ae^{\frac{V_{GS}-V_{TH0}-\gamma V_{SB}+\eta V_{DS}}{nv_T}} \cdot \left(1-e^{\frac{-V_{DS}}{v_T}}\right) \tag{3.60}$$

where $A = \mu_0 C_{ox} W/L_{eff} \, v_T{}^2 e^{1.8}$, μ_0 is the zero-bias carrier mobility, C_{ox} is the gate-oxide capacitance, L_{eff} is the transistor effective channel length, W is the transistor width, η is the DIBL coefficient, γ is the linearized body-effect coefficient, n is the transistor sub-threshold swing coefficient and v_T is the thermal voltage (kT/q) [26].

The supply voltage reduction lowers the drain-source voltage and thus reduces the DIBL current. The leakage is also suppressed by the reverse body-bias voltage (V_{SB}). The smaller feature sizes in the 90-nm process node have more leakage compared to the 0.5-µm process. Therefore, the two CR-based designs present good insight to the leakage current reduction by using virtual power supplies in these processes.

3.7 Summary and Conclusions

Charge-recycling has been demonstrated as a viable option to improve the energy efficiency of digital circuits. This chapter presented the design of proposed CR scheme to scavenge charge from the leakage and dynamic load currents that are inherent to digital design. The power-delay tradeoff and energy efficiency analysis of the CR scheme have been examined. The presented design methodology and the energy savings estimation can be effectively reused to implement the CR scheme to cater to the energy requirements of any system.

The novel CR scheme has been designed and implemented for a 12-bit Gray-code counter in 0.5-µm and 90-nm processes. The proposed CR scheme avoids the delay introduced in charge-pump based voltage boosting techniques, and eliminates the need to match the current-consumption in vertically-stacked CR digital blocks. Simulation results demonstrate a total average energy reduction of 31% with this charge-recycling scheme. The average energy of the

counter alone is decreased by 52% by recycling charge. The characterization and measurement results of the 90-nm prototypes are presented in the next chapter.

Chapter 4 Characterization of the Charge-Recycling Gray-code Counter

This chapter presents the measurement results and analysis of the charge-recycling (CR) Gray-code counter design in a 90-nm CMOS process. The goal is to characterize the energy savings realized by employing the CR scheme. The power-performance tradeoffs incurred in this implementation are analyzed. Further, the efficiency of the CR scheme is characterized across changes in frequency of operation and virtual supply voltage variations. The dependency of the CR scheme on process variations is also examined.

4.1 Test Setup

The chip was fabricated in a 90-nm CMOS process that is offered by MOSIS [69] and packaged in a 52-pin Low-profile Quad-Flat (LQF) package. The chips were received in November 2011 and subsequently four test chips were characterized in spring 2012. Figure 4.1 presents the microphotograph of the fabricated die. CadSoft's Eagle layout editor was utilized to design the FR4 printed circuit board (PCB) that was used to characterize the Gray-code counter. Figure 4.2 presents the designed test board that accommodates one test chip. The 52-pin LQFP are soldered directly onto the board in order to reduce the socket parasitics. The test board comprises of four layers of copper planes to provide a quiet ground-return path for the transients inherent to digital circuits. The layer stack-up in the PCB cross-section is illustrated in Figure 4.3. Since most of the components used on the board are surface-mount devices, all the signal routings are on the topmost copper layer of the PCB. Further, as analog buffers are used to probe the virtual V_{DD} and virtual ground nodes, careful power supply distribution is crucial to minimize noise coupling between the analog and digital domains.

4.1.1 Power Supply Generation and Partitions on PCB

Power supply planes and supply partitions are essential to avoid noise coupling and to preserve signal integrity on the test board. The fabricated mixed-signal test chip has individual power supply nodes that are bonded out for ease of power measurements. An analog power

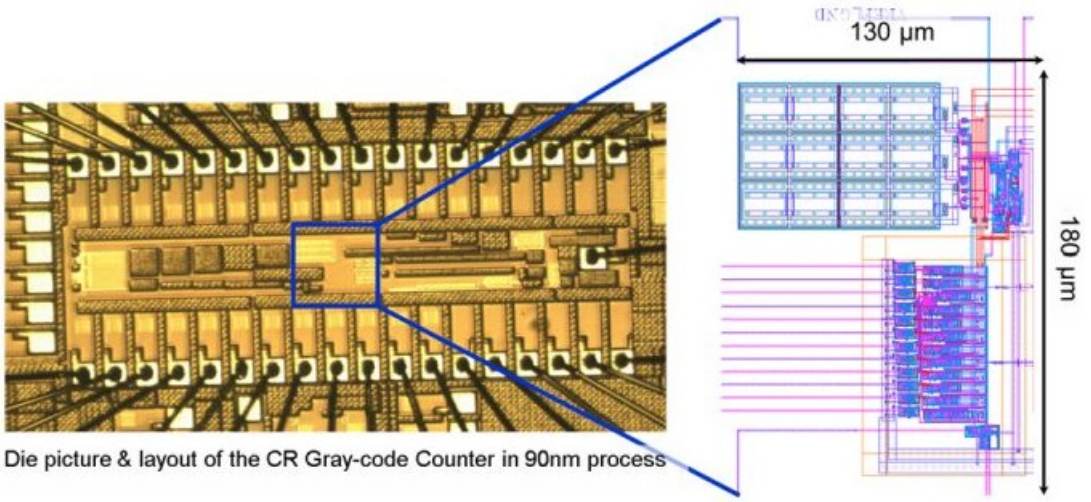


Figure 4.1 Die photo of the charge-recycling Gray-code counter in 90-nm process

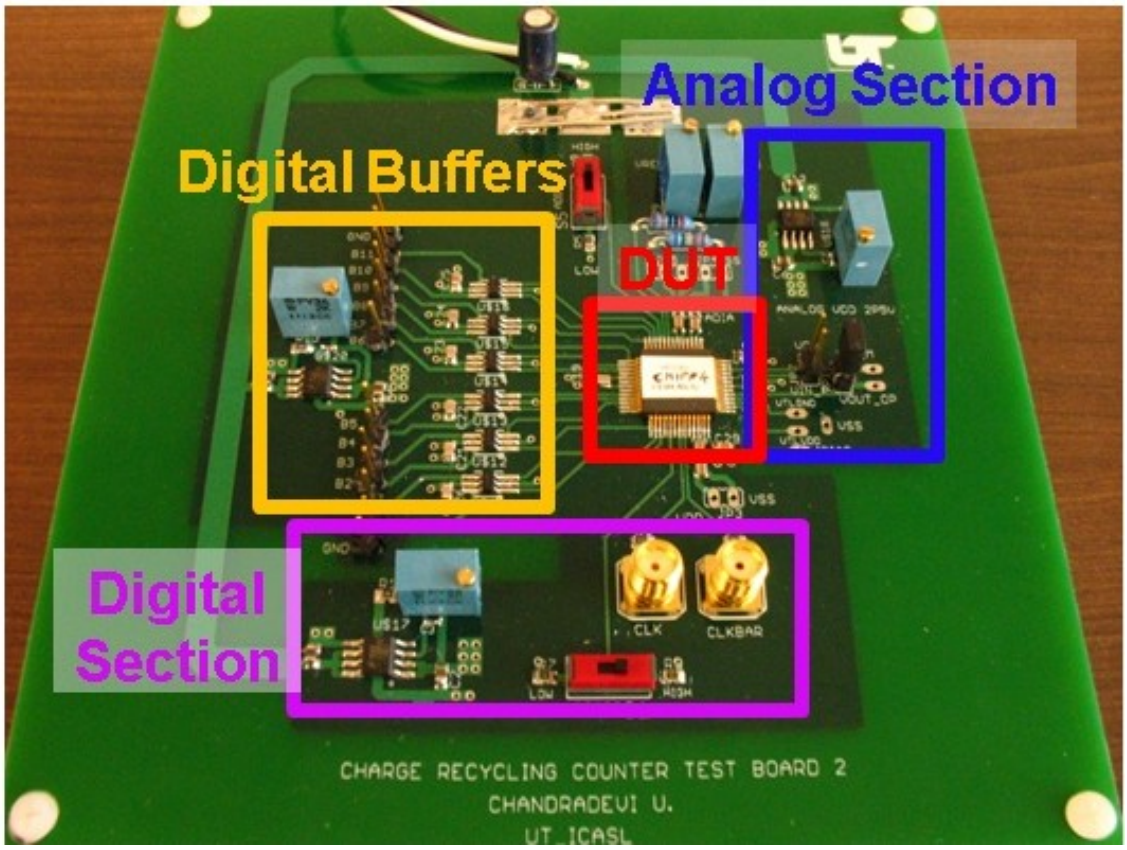


Figure 4.2 Layout of test board to characterize charge-recycling Gray-code counter (90-nm process)

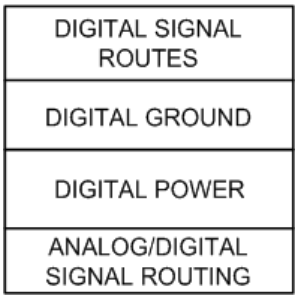


Figure 4.3 Cross-section of the test board showing the layer stack-up

supply of 2.5 V is used while the digital cells are powered up by 1-V supply. To provide a short, quiet return path for current transients during switching events, supply planes are utilized on the board. The inner copper supply layers also act as decoupling capacitors. Additional decoupling capacitors are provided close to the supply pins of the chip and small decoupling capacitors are also provided on-chip.

As highlighted on the test board in Figure 4.2, the board has three supply partitions namely digital buffer, digital supply and analog supply for the test chip. The grounds of the three partitions are connected at only one point on the board in order to eliminate ground-loops. A tight, short ground-plug is used to connect the grounds and thereby eliminate the inductive effects of banana plugs.

4.1.2 On-board Supply Regulators

Onboard voltage regulators are employed to provide stable, low-noise supply voltages to the chip. Linear voltage regulators are preferred over switching regulators due to their low noise capability. A low-dropout, linear voltage-regulator (TI's LP38512) [65] is used in the test board. This regulator provides output voltages in the range of 0.5 V to 4.5 V for an input voltage range of 2.25 V to 5.5 V. In this design, multiple power supply signals from the CR Gray-code counter have been padded out. In order to avoid the use of several power supply regulators, the non-critical power supplies such as pad ESD supply, and digital output pad-drive buffer supply, are supplied by a single regulator. The analog supply of 2.5 V is generated using a separate regulator and the analog ground is isolated from the digital section. Figure 4.4 presents the schematic of the voltage regulator. The required output voltage is realized by varying the ratio of resistors R1 and R2 and is given by

$$V_{OUT} = V_{ADJ}\left(1 + \frac{R_1}{R_2}\right) \tag{4.1}$$

An input voltage of 5 V is applied to the regulators in order to obtain digital and analog power supply voltages of 1 V and 2.5 V, respectively.

4.1.3 Digital Buffers on PCB

The digital output from the Gray-code counter is buffered on the PCB to be able to drive the load presented by oscilloscope cables. The on-board buffers also reduce the effective loading seen by the on-chip pad-drive buffers. This results in lower transient peak currents within the chip and lower noise coupling from bond wire inductances. TI's SN74AUC2G34 dual gate buffer [66] is used in this test board.

4.1.4 Reset signal generation

The fabricated design includes counter enable (active "low") or clock reset signal to disable the chip's operation (i.e. disable counting). Also, in order to measure the computation efficiency of the counter, with and without the charge-recycling scheme, the charge-recycle reset signal has been included to disable only the charge-recycling mechanism while the Gray-code counter is operational. These reset signals are generated on the board using the SPST switches that utilize a make-before-break transition. These signals are derived from the digital power supply voltage of the chip.

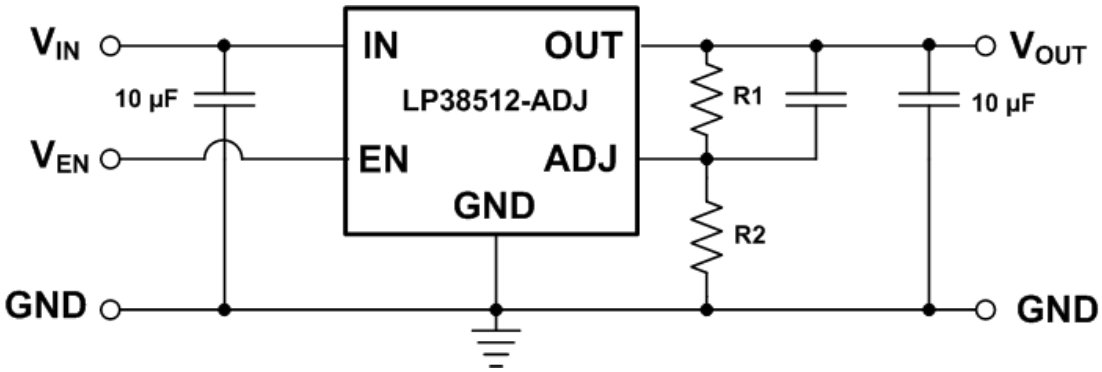


Figure 4.4 Schematic of LDO voltage-regulator circuit on the test board [65]

4.2 Test Procedure

The characterization of the CR counter begins with ensuring that the DUT is supplied with appropriate, stable power supply voltages from onboard regulators, and external power supplies. Before applying power to the Gray-code counter and CR control blocks, the respective reset signals are set HIGH in order to power-up the circuits in the reset mode. Also, the onboard resistive voltage dividers that set the virtual power supply references are verified to be within the operational range of the circuits. The power supply to the Gray-code counter and the CR control block are supplied using Keithley's 2400 Sourcemeter and the current consumed by these circuits is monitored using the Keithley's 2400 Sourcemeter and Keithley's 6485 picoameter. The counter's clock is provided by a LeCroy pulse generator. LabView is also used to interface and control the test equipment.

Once the proper power supply voltages are set, the counter enable signal, and then the counter clock is applied. The 12-bit, Gray-code output bits from the counter are sampled using the Agilent MSO6034A mixed-signal oscilloscope. The sampled data is checked to verify correct operation of the counter. Then, the virtual supply nodes are set with proper reference voltages and the CR scheme is then enabled by releasing the CR reset signal. For this set of virtual supply values, the counter's output is again sampled to verify satisfactory operation without any missing codes. Figure 4.5 presents a picture of the sampled output from the charge-recycling Gray-code counter. Once the counter operation has been verified, the power consumed by the CR counter along with the CR control logic is measured. The efficiency of the CR scheme is accessed using the measured current consumption of the DUT. The power supply to the level-shifting buffers was inadvertently connected to the supply of pad-drive buffers. So, the power expended to perform level-shifting has not been included in the total power reduction calculations. In reality, to keep the power consumption low, the level-shifting operation would be integrated into a flip-flop available in the data path of the system. Since the counter's output bits were padded out for test purposes, a separate level-shifting block is required for this prototype. Furthermore, the simulation results include the level-shifters and they represent less than 2% of the total power dissipated. Although the total measured power reduction reported here presents an optimistic value, the close correlation between the simulation results and the measurement results demonstrates that the accuracy of the measured % energy reduction is within 2%.

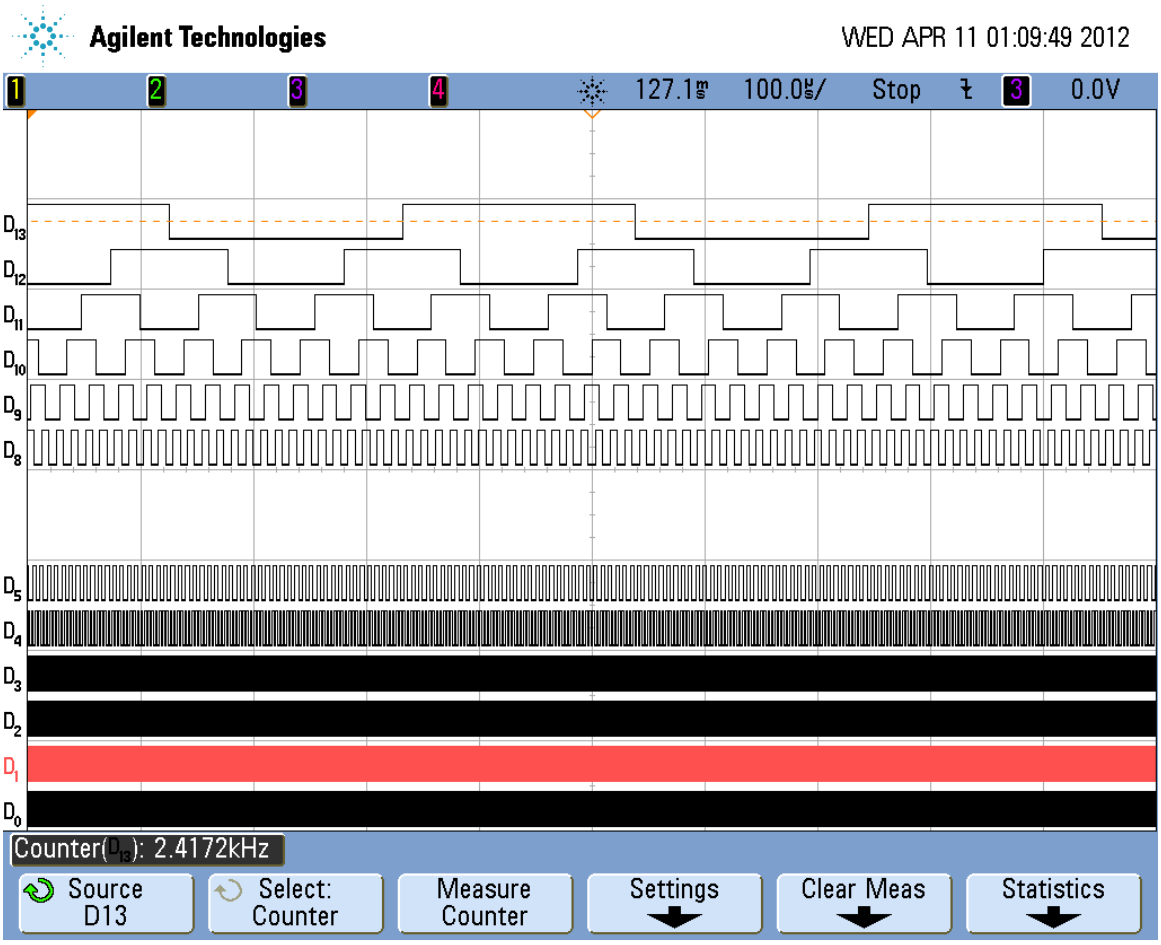


Figure 4.5 12-bit Gray-code output from the charge recycling counter

Figure 4.6 illustrates the transient power consumption of the test chip # 2 when the CR scheme is enabled. The figures also demonstrate the test procedure wherein the counter (without CR) is enabled after startup and is then followed by activating the CR blocks to lower the energy consumption of the circuit. The data was collected from the Keithley instruments using Labview interface. During this test, the counter was operating at a frequency of 35 MHz and the virtual ground and virtual V_{DD} reference voltages (V_{RG} & V_{RD}, respectively) were set at 310 mV and 750 mV, respectively. From Figure 4.6, it can be inferred that CR confers 40% reduction in average power consumption of the counter. The total reduction which includes the power consumed by the CR control logic is about 22%.

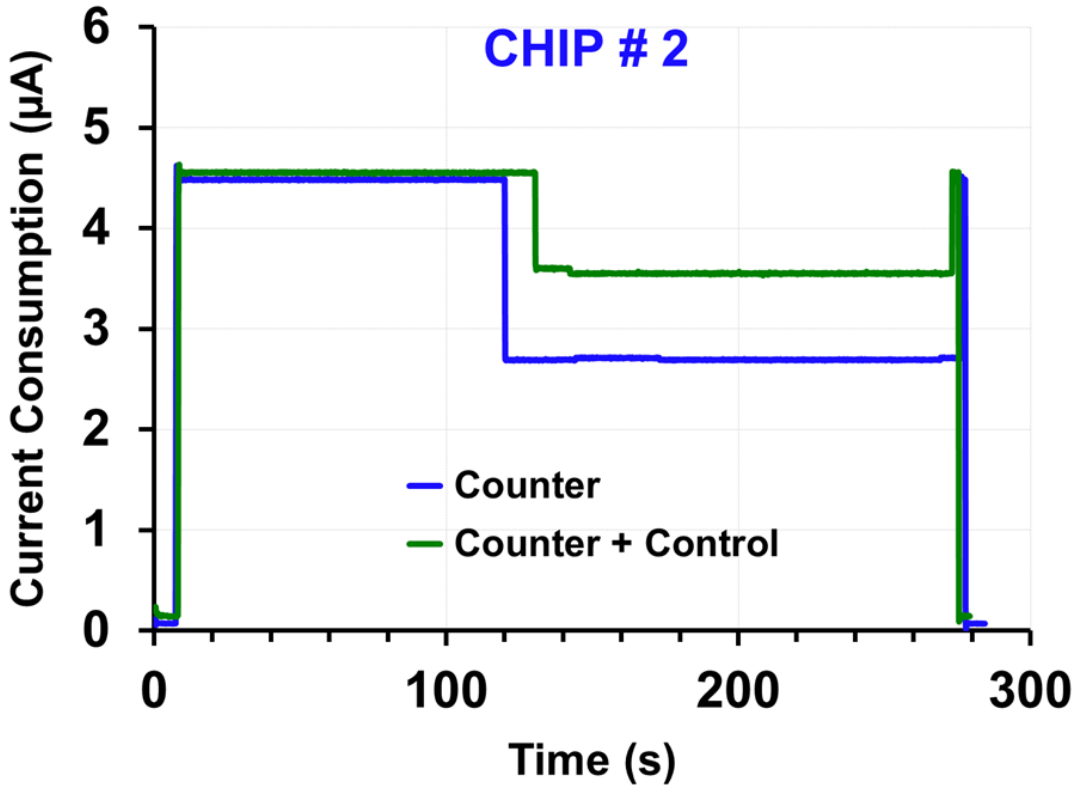


Figure 4.6 Transient measurement results demonstrating power reduction in the counter using the CR scheme (includes counter and CR control)

In order to provide an insight into the charge recycling operation, and to aid in debugging, the virtual power-supply rails (V_{VDD} & V_{VGND}) to the counter are padded-out in the test chips. Analog buffers are employed to shield the virtual supply nodes from the output pad and probe loads. In addition, a copy of the opamp (used in the buffer cell) that is placed close to the two buffers is available to characterize the input offset voltage of the buffer across the power supply range of the counter. Figure 4.7 presents the measured input offset voltage of the opamps across varying input voltages for the four test chips. The measured offset of the analog buffer (i.e. opamp) gives a realistic estimate of the charge recycling operation and also provides an option to compensate for the comparator's offset within the CR control generation circuitry.

Figure 4.8 presents an oscilloscope screenshot of the V_{VDD} and V_{VGND} nodes in the test chip # 2. The figure verifies the operation of the CR scheme where, during the charge-accumulation phase, the ground-bound charges from the circuits are collected by the storage

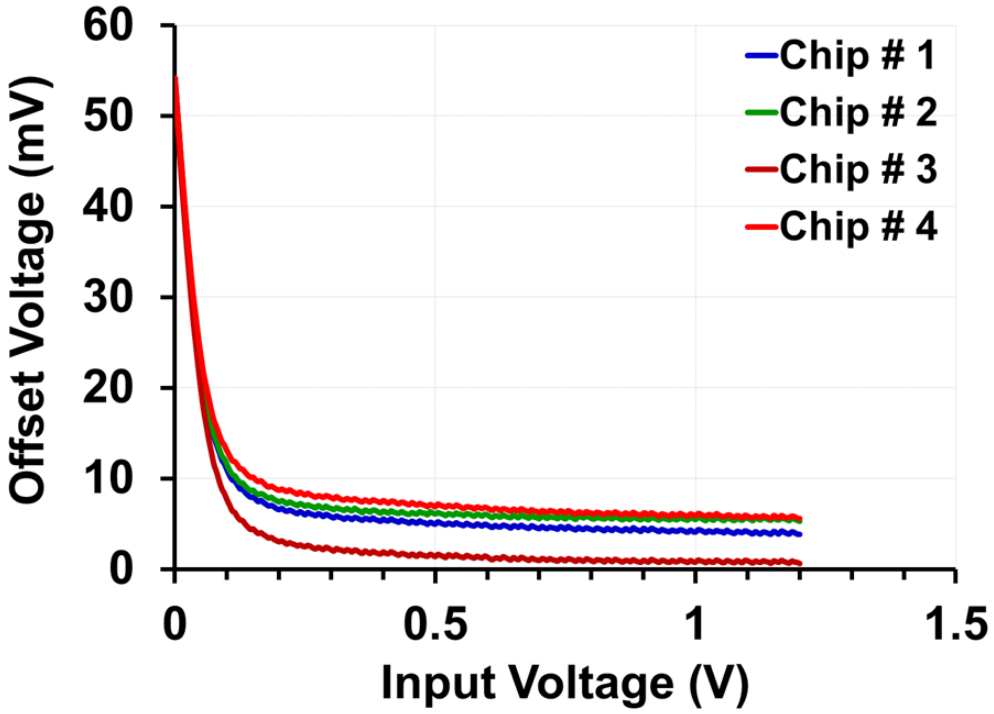


Figure 4.7 Measured input offset voltage of analog buffers

capacitors, as seen in the bottom signal (V_{VGND}) that increases with time, while the V_{VDD} (top signal) is held at a constant V_{DD}. Once the V_{VGND} reaches the reference voltage V_{RG}, the charge-recycling phase begins wherein the V_{VDD} node supplies power to the counter and so it reduces with each clock cycle until it reaches the virtual V_{DD} reference voltage of V_{RD}. During the charge-recycling phase, the offset of the buffer (60 mV at an input of 0 V) masks the actual value of the V_{VGND} which is held at ground. From the varying time period for one full cycle of operation, which includes the charge accumulation (t_{CA}) and charge recycle phases (t_{CR}), it can be inferred that the amount of charge, or the probability of a node discharging to ground, varies with the output of the counter.

4.3 Measurement Results

The test procedure outlined in the previous section was performed on all the four test chips to verify their operation. As discussed in Chapter 3, employing the charge recycling scheme to reduce the energy consumption also increases the propagation delay and thus lowers



Figure 4.8 Transient measurement results illustrating virtual supply rails in the CR counter

the maximum achievable frequency of operation. Thus, it is essential to investigate the power reduction versus propagation delay increase in the Gray-code counter as a result of CR scheme. An accurate measurement of the delay increase in each output bit of the counter is not directly possible since the transient virtual power supply values result in different propagation delays that depend on the phase of the charge-recycling cycle. Further, a very high speed PCI-express data acquisition system of more than 250 MHz data-rate is required to record the high-speed virtual power supply voltage variations. To circumvent the test limitations, the delay increase due to CR scheme was obtained from the measurement of the maximum possible frequency of operation, without any missing counts at the counter output bits. Since the counter's critical delay path determines the maximum frequency of operation, an increase in the propagation delay due to CR, will also reduce the frequency of operation.

Additionally, in order to quantify the efficiency of the proposed charge-recycling scheme, the counter's energy reduction and delay increase were characterized across variation in the frequency of operation, and across different virtual power supply levels. The range of virtual power supply levels was established so as to ensure that the peak V_{VDD} (set by V_{RG}) was always below the maximum rated value of 1.2 V for the 90-nm process. The choice for the minimum V_{VDD} (set by V_{RD}) was governed by the requirement to avoid excessive increase in the propagation delay that brings down the efficiency. Further, the offset of the two comparators that monitor the virtual supply rails to be within the predefined reference voltages, determines the actual power supply voltage realized at the CR counter. Thus, the comparator offset voltage, and the propagation delay from the comparator's output to the switches that control the charge-recycling capacitors, will affect the charge-recycling efficiency. Since an independent comparator was not available for characterization, the offset was estimated from the difference between the maximum virtual ground voltage and the virtual ground reference (V_{RG}), and the deviation of minimum virtual V_{VDD} voltage from V_{RD}. Table 4.1 presents the average offset voltage of the comparators used in the CR logic path.

As discussed in Section 3.3.3, the high-speed comparator topology was chosen with an emphasis to keep its power consumption to a minimum, while trading-off accuracy. The

Table 4.1 Offset voltage of the comparators used in CR control logic

Chip	***Offset at Virtual Ground Comparison (Vtlgnd – V_{RG})***	***Offset at Virtual V_{DD} Comparison (Vtlvdd – V_{RD})***
1	54 mV (late)	15 mV (early)
2	−28 mV (early)	−70 mV (late)
3	40 mV (late)	−40 mV (late)
4	−30 mV (early)	15 mV (early)

measured offset voltages fall within the predicted offset voltage range from the MonteCarlo simulations performed across 3-sigma variations in process and mismatch. The CR scheme's reference voltages can be adjusted to compensate for the comparator offset and thereby achieve higher, reliable efficiency. The measurement results for each CR prototype are presented in this section. Comparison of the measurement results across the four test-chips provides an insight into the CR efficiency across process variations.

4.3.1 Energy Reduction due to Charge-recycling

Figure 4.9 presents the measured energy savings of the Gray-code counter for different charge-recycling voltage levels or virtual power supplies. The corresponding data for the total energy reduction that includes the power dissipated by the CR control logic is illustrated in Figure 4.10. The virtual ground comparator's offset of 54 mV (see Table 4.1) implies that the actual V_{VGND} is 54 mV higher than the virtual ground reference voltage, V_{RG}. So, V_{RG} was limited

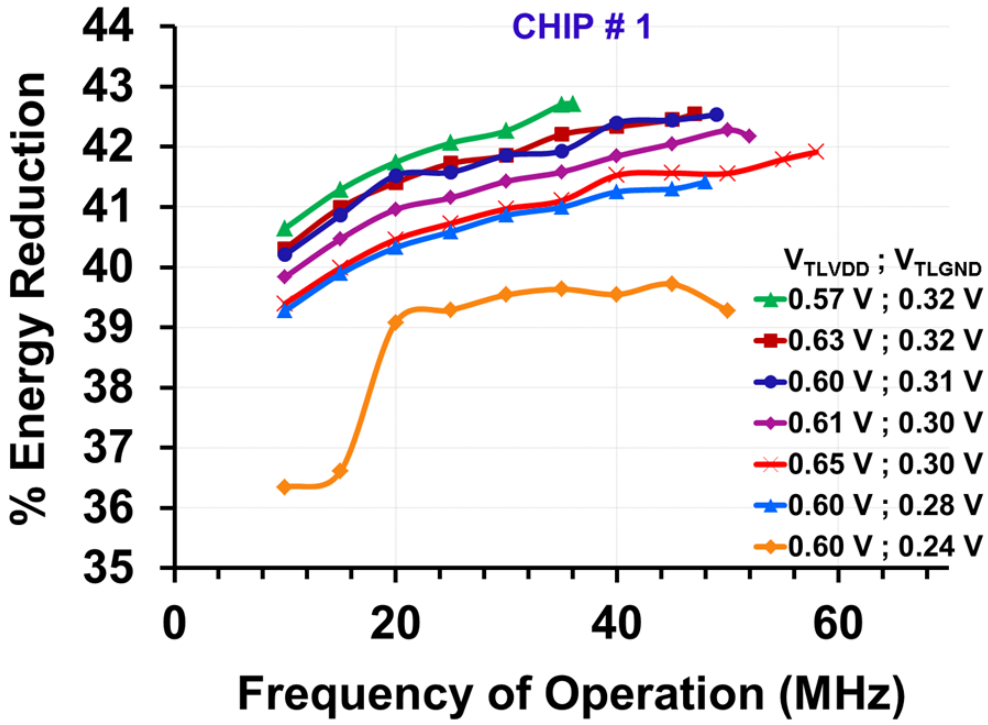


Figure 4.9 Measured energy reduction in the charge-recycling Gray-code counter (Chip # 1)

to a maximum of 0.32 V in order to ensure that the boosted V_{VDD} does not exceed the maximum rated power supply voltage. While the minimum V_{VDD} could be lower than 0.57 V, a very low V_{VDD} would cause large increase in the propagation delay and thereby reduce the efficiency.

As verified by the data in Figure 4.9 and Figure 4.10, for a given frequency of operation, the power or energy consumption can be reduced by decreasing the power supply voltage. For very low V_{RG} of 0.24 V, the charge-storage capacitors accumulate the ground-bound charge to reach a maximum of 0.294 V, including the 54 mV offset of the comparator. However, with the 0.294 V, the maximum boosted V_{VDD} voltage is less than 0.9 V and so the virtual V_{VDD} node discharges to V_{RD} fast. Thus, for low V_{RG} values, both the charge-accumulation phase (t_{CA}) and the charge-recycling phase (t_{CR}) are small and therefore the percentage of energy saved is lower. Further, the V_{RD} voltage is not set at V_{DD}–V_{RG} but is smaller by about 20 mV (after compensating for the comparator offsets) in order to account for the series voltage drops in the charge transfer

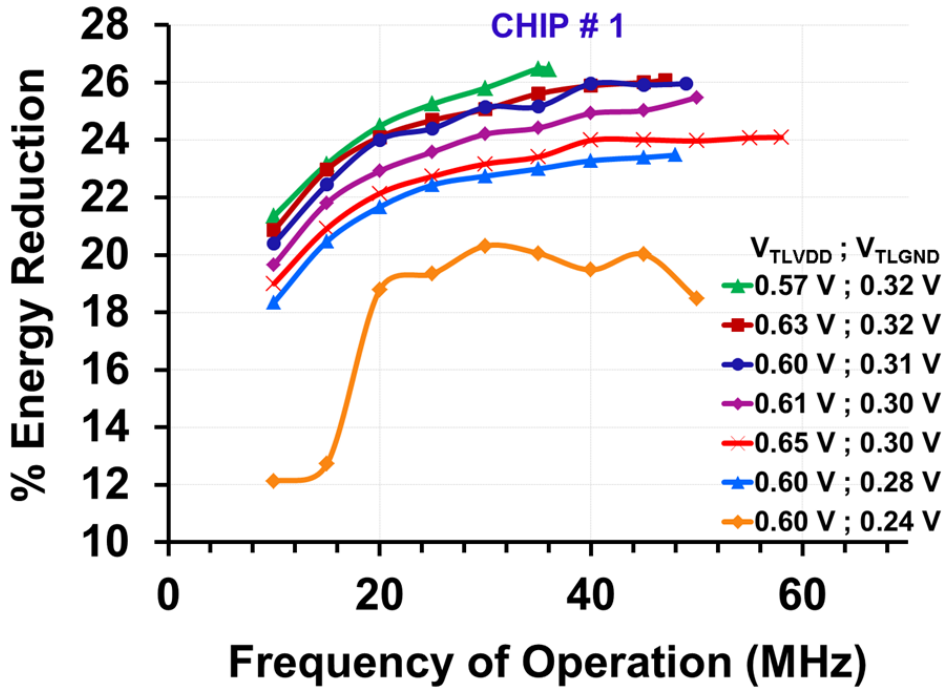


Figure 4.10 Measured energy reduction in the charge-recycling Gray-code counter, including power dissipated by the control logic (Chip # 1)

switches present within the capacitive power supply circuit. Thus, for a reasonable value of V_{RG}, that facilitates charge-recycling, the average power saved in the counter is approximately constant across frequency of operation and is close to 42% for the counter alone, and 24% including the CR scheme's control logic.

Figure 4.11 and Figure 4.12 present the measured energy savings of the Gray-code counter and including control logic, for different charge-recycling voltage levels in chip # 2. Since the virtual ground voltage sensing comparator has a negative offset voltage, the comparator trips at 28 mV below V_{RG} and so the charge-recycling phase starts with a lower V_{VDD}. The virtual V_{DD} comparator triggers the charge-accumulation phase after the V_{VDD} decreases below V_{RD} by 70 mV. Hence, the reference voltages for the virtual supply levels are appropriately chosen to compensate for the offset and thereby achieve good performance. The curve for reference voltages of 0.75 V (V_{RD}) and 0.31 V (V_{RG}) represents the case with uncompensated offset and exhibits close to 37% energy reduction. With offset compensation, similar to chip # 1, this DUT's average energy reduction is 40% for the counter and 23% with the control logic's energy consumption.

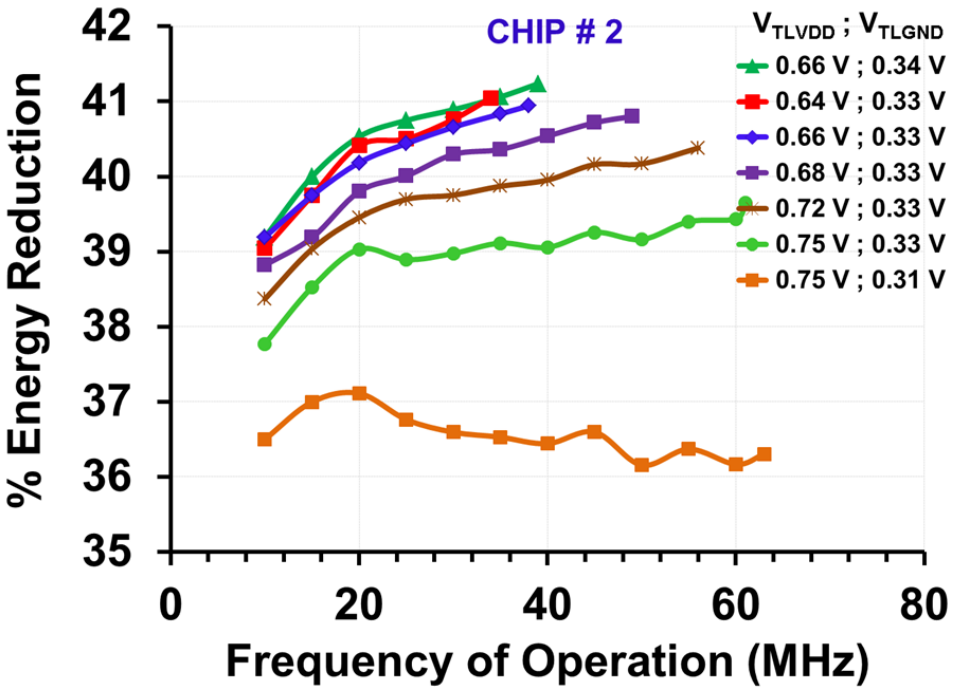


Figure 4.11 Measured energy reduction in the charge-recycling Gray-code counter (Chip # 2)

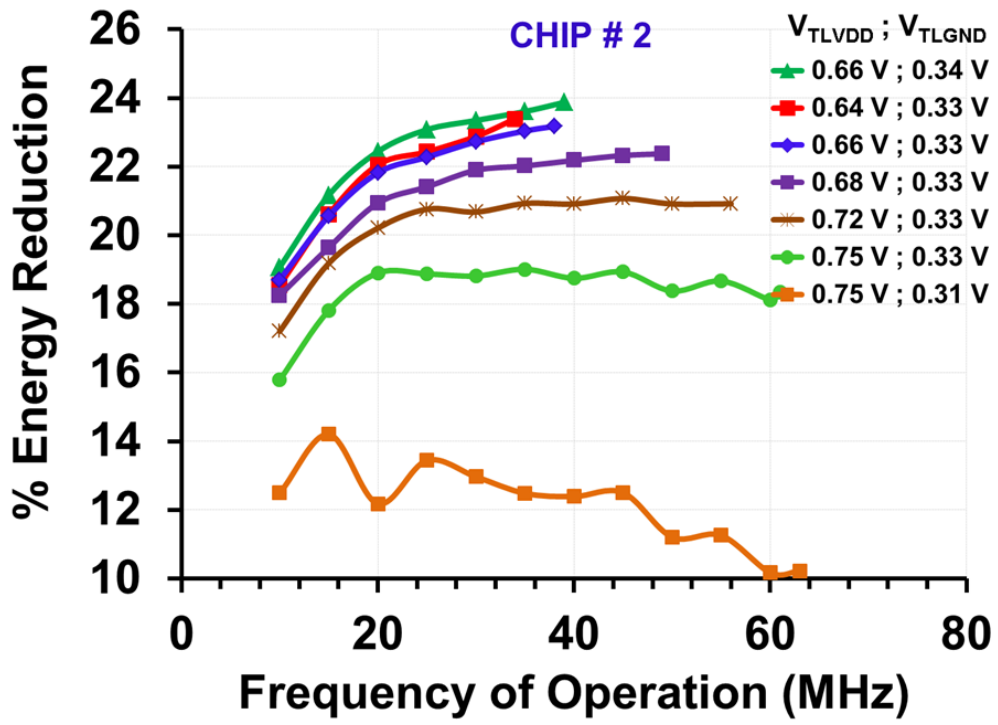


Figure 4.12 Measured energy reduction in the charge-recycling Gray-code counter, including power dissipated by the control logic (Chip # 2)

Figure 4.13 and Figure 4.14 present the respective measured energy savings of the Gray-code counter, and the counter along with control logic, for different charge-recycling voltage levels in chip # 3. The chip # 3 presents the process corner where both the comparators trigger late, i.e. after the input has increased or reduced past the reference voltage. Hence, for an uncompensated reference voltage setting, this process corner would yield the highest energy savings but would also increase the penalty due to increase in propagation delay. With offset compensation, this chip provides an average energy reduction of 41% at the counter and 23% including the control logic's energy consumption. The reduction in power savings at low frequencies, especially below 20 MHz is primarily due to the increase in the losses incurred in the charge-recycling block, primarily due to leakage currents.

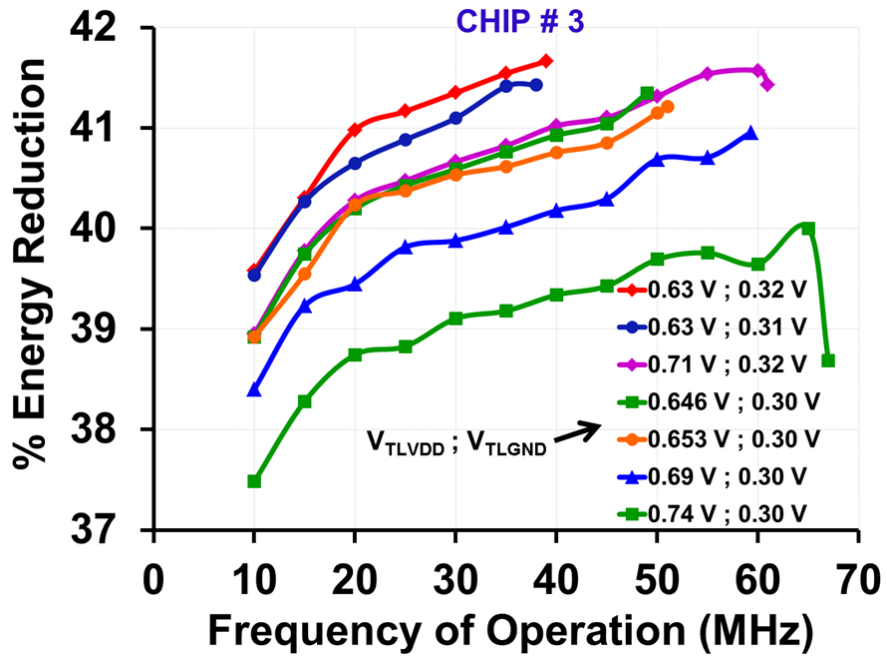


Figure 4.13 Measured energy reduction in the charge-recycling Gray-code counter (Chip # 3)

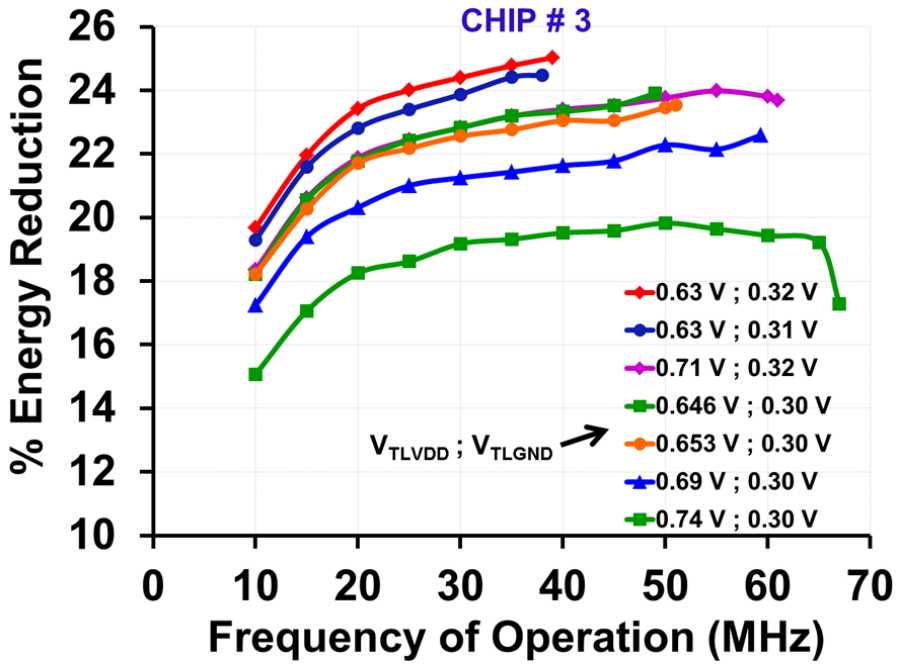


Figure 4.14 Measured energy reduction in the charge-recycling Gray-code counter, including power dissipated by the control logic (Chip # 3)

Figure 4.15 and Figure 4.16 present the measured energy savings data at different charge-recycling voltage levels for chip # 4. The chip # 4 presents the process corner where both the comparators switch their outputs early, i.e. before the virtual supply nodes have reached their reference voltages. Therefore, for uncompensated reference voltages, this process corner represents the worst condition for this CR implementation. With offset compensation, this chip provides an average energy reduction of 40% at the counter and 21 % including the control logic.

In summary, the four tested prototypes demonstrate consistent reduction of more than 40% (counter alone) and 22% (counter and the control logic) in the energy consumption, across the frequency range of interest. The virtual supply's reference voltages can be exploited to adjust for variations in the charge-recycling efficiency due to process and mismatch corners.

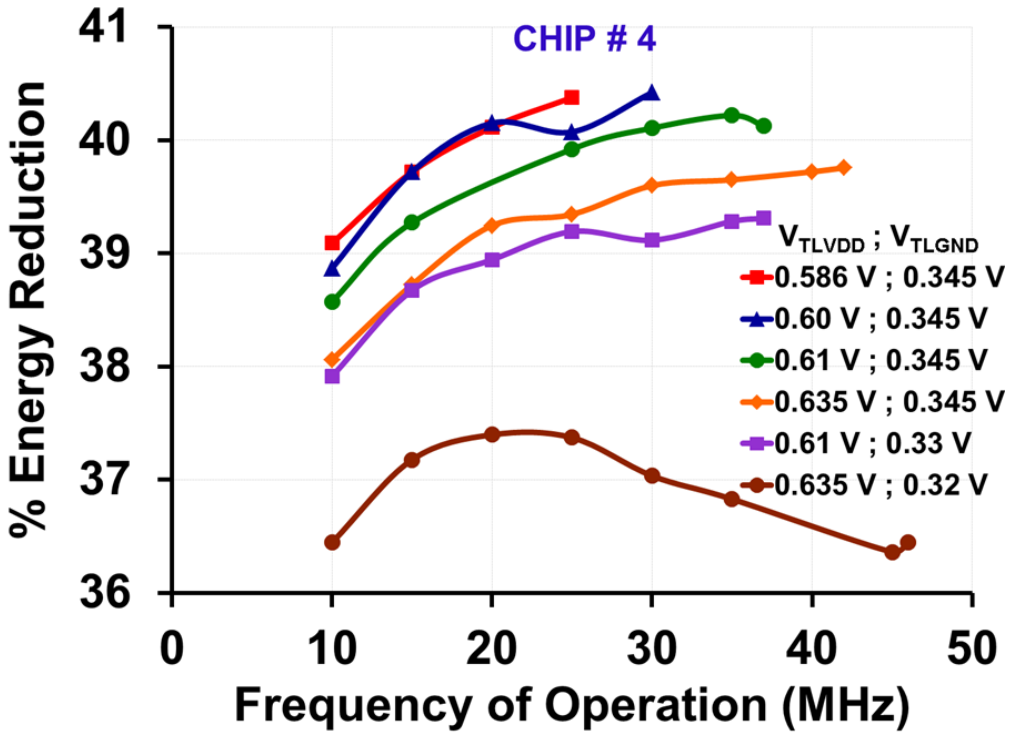


Figure 4.15 Measured energy reduction in the charge-recycling Gray-code counter (Chip # 4)

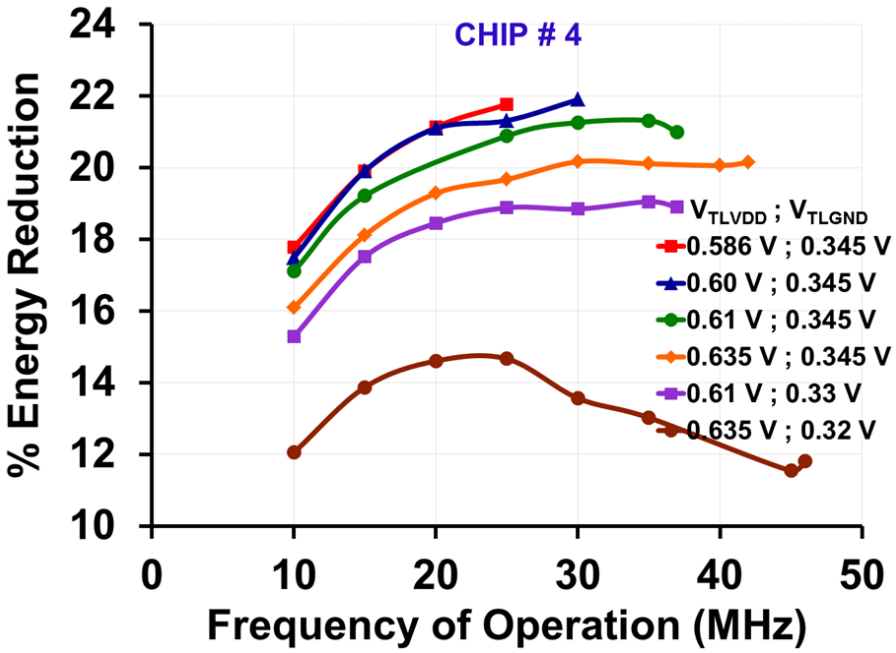


Figure 4.16 Measured energy reduction in the charge-recycling Gray-code counter, including power dissipated by the control logic (Chip # 4)

4.3.2 Efficiency of Charge-recycling scheme

The efficiency of the energy reduction can be deduced by examining the energy-delay tradeoff in the CR scheme. By reducing virtual supply voltage levels, the maximum possible frequency of operation also reduces due to the increase in propagation delay. For a given frequency of operation, energy expended by the counter is normalized to the energy spent by the counter without CR. Figure 4.17 presents the normalized energy versus normalized delay for the counter's operation, across variations in virtual supply voltages for all the four tested samples. Figure 4.18 presents the corresponding normalized energy versus delay results that includes the energy consumption of the CR control logic. As discussed in the previous section, chip # 4 presents the 'slow-slow' process corner and so the delay increase is large in order to attain same energy savings as the other samples. Both these plots, verify that the charge-recycling scheme provides large energy savings, with small performance penalty, for medium-speed digital applications.

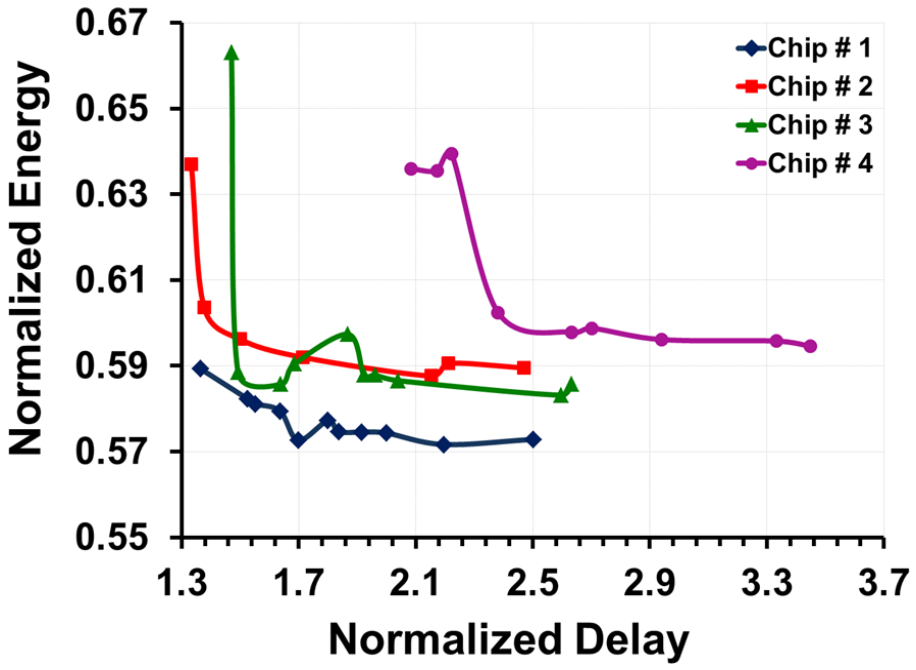


Figure 4.17 Normalized energy in Counter versus normalized delay due to CR scheme

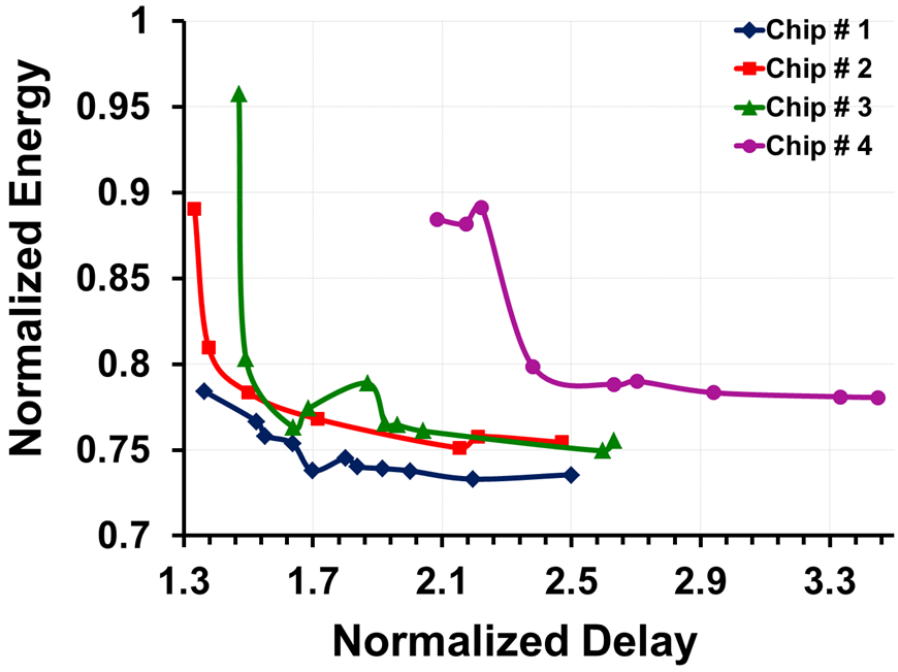


Figure 4.18 Normalized energy (including CR logic) versus normalized delay due to CR scheme

Another measure of the effectiveness of this CR scheme is the comparison to the maximum possible energy reduction that can be achieved with power supply scaling. The energy consumption and the propagation delay of the Gray-code counter were measured across reduction in the power supply voltage. Figure 4.19 presents the measured normalized energy versus normalized delay results of the counter across different V_{DD} levels. As evident in the figure, lowering V_{DD} results in quadratic reduction of the energy consumed per operation in the circuit. The figure also includes the measurement results from the charge-recycling counter of chip #1 in order to facilitate the comparison.

The normalized energy results in Figure 4.19 present the maximum possible energy reduction from supply voltage scaling. The normalized energy per operation for chip # 1's counter which includes the CR logic is close to 0.73 for normalized delay of 2, while those from V_{DD} reduction is about 0.47 for delay of 2. Since the V_{DD} reduction data does not include the

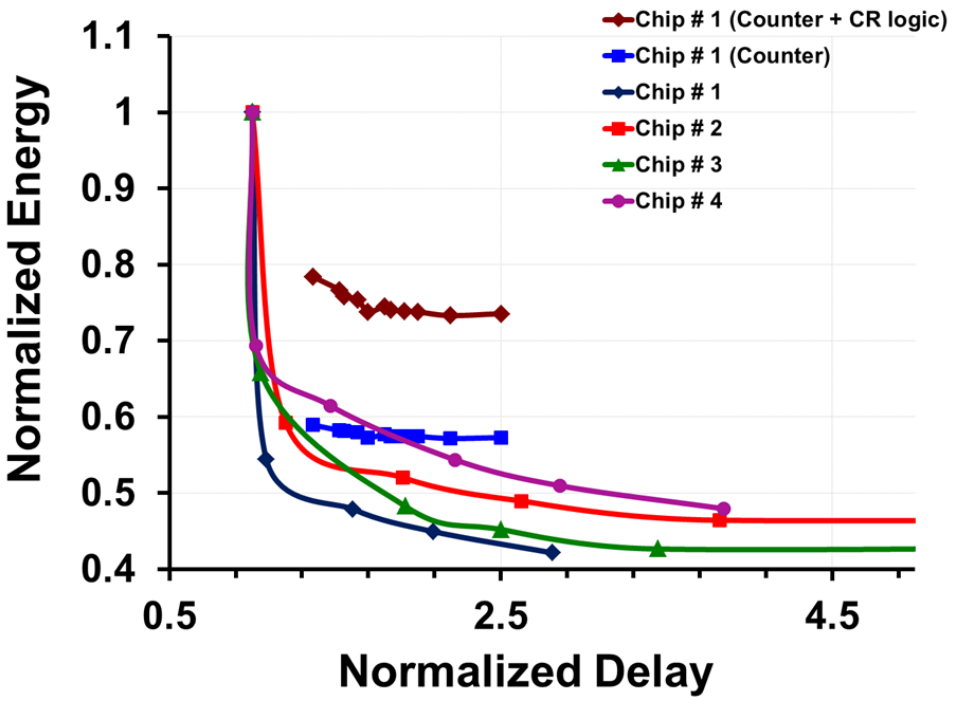


Figure 4.19 Normalized energy versus normalized delay as a result of reduction in V_{DD}

energy consumed by voltage regulators that generate V_{DD}, comparing the energy saving data from just the CR counter would provide a reasonable evaluation of the CR scheme. As seen in the figure, the CR counter's normalized energy of 0.57 is close to that of V_{DD} reductions. The difference in the realized energy reduction is due the fact that the CR scheme has a dynamic virtual power supply level while the V_{DD} reduction methodology operates a fixed V_{DD}. Further, the CR scheme was implemented to realize a partially self-powered circuit which meant the critical path delay was being increased with voltage scaling as a result of charge-recycling. The normalized energy-delay product can be further reduced by implementing the CR scheme on non-critical paths in the system. Another technique to lower the normalized energy expended by the CR counter is to time-multiplex several charge-recycling banks to provide power to the target circuit entirely from recycled charge.

4.4 Techniques to improve the proposed CR scheme

Some enhancements to improve the efficiency and the application of the proposed charge-recycling approach are examined in this section.

Virtual V_{VDD} Generation:

The premise for the selection of current CR topology is to limit the power consumption in the CR logic to a minimum. However, the efficiency of the CR scheme can be improved by reducing the losses within the CR control block. In this CR implementation, the dominant component of power consumption is the switching losses in the digital logic and in the storage or recycling capacitors. The generation of V_{VDD} by stacking the charge-storage capacitors results in charge loss due to charging and discharging the capacitor plates, and the parasitic capacitances from both the top and bottom plates. The switching and charge redistribution losses in this switched capacitor power supply can be reduced by charge-sharing or charge-recycling techniques [38] applied at the bottom plates of capacitors, between the transitions from charge-recycling to charge-accumulation phase when the bottom-plate charges are lost to the ground.

The transitions between the two CR phases are controlled by complementary signals. Therefore, there is a possibility of current flowing from the storage capacitors to the circuit ground, and from the V_{DD} to the CR capacitors, during CR phase transitions. While the loss to ground reduces the amount of recycled charge, the charge from V_{DD} increases the V_{VGND} but

reduces the charge-accumulation time and thus increases the frequency of CR cycle and the power consumption of CR control. Hence, the control of CR capacitors with non-overlapping (NOV) clock phases is desirable. With accurate control of the charge recycling phases, the charge lost during the transitions between the CR phases would be reduced. However, the generation of all the required control signals would also increase the total power consumption of the CR control logic. If the dead-time in the NOV control can be exploited to perform charge-sharing between the capacitors' bottom-plates, the benefits outweigh the increase in power consumption.

Adaptive virtual power-supply reference voltages:

The designed charge-recycling approach to generate virtual power-supply in low-power digital circuits works effectively for a small range of power-supply levels. Across large temperature variations, the changes in the device threshold voltage and mobility limit the amount of recoverable charge (from dynamic switching currents) for a given performance requirement. Further, the virtual ground and virtual V_{DD} reference voltages that offer the best computation efficiency depend on target circuit's topology, required frequency of operation, and the threshold voltage of the devices. As seen in the measurement results, the variation in process parameters affects the comparators' offset voltage and thus the actual power supply voltage that is supplied to the counter. Hence, the reference voltages can be employed to compensate for the variation in performance with process and temperature changes. To this effect, a control loop can be devised that provides dynamic/adaptive virtual V_{DD} and virtual ground voltages by tracking the optimal supply voltage to ensure performance across process and temperature variations.

Simulations were performed on FO4 buffer stages to quantify the optimal variation in the virtual reference voltages in order to guarantee a maximum delay increase of two, across temperature range of –55 ºC to 125 ºC. With dynamic virtual supply rails, the maximum voltage from CR banks ranges from 100 to 300 mV to meet the performance requirement in the buffer at 100 MHz, across –55 ºC to 125 ºC. This range of V_{RG} or maximum V_{VGND} necessitates variable number of storage capacitors and adaptive gain to generate V_{VDD}. Therefore, an ultra-low voltage capable DC-DC converter is essential to boost the voltage from the capacitive storage banks to V_{DD} level. Furthermore, self-starting converters with variable gain ratios facilitate the use of

recycled charge for the voltage boosting operation. Thus self-starting DC-DC converter used in conjunction with the CR scheme would not impose any power overhead to the system. The second part of this dissertation explores the design of very-low voltage capable DC-DC converter.

Time-multiplexed Charge-recycling:

Time-multiplexed charge-recovery banks can be employed to provide constant, uninterrupted power supply to other digital blocks [26]. Depending on the application, time multiplexing can be designed to recycle charge from multiple sources to sustain a single or several target blocks. While time-multiplexed CR offers an attractive method to provide power supply, energy overhead is involved with the generation of control signals to manage several independent, local CR capacitor banks.

4.5 Summary and Conclusion

This research has demonstrated the feasibility of operating digital circuits using the charge scavenged from the leakage and dynamic load currents that are inherent to digital operation. The target application defines the actual implementation of the proposed CR scheme. Time multiplexed CR approach is beneficial in a large system while the partially self-powered approach is the best choice to reduce the power consumption in small independent circuits. The novel charge recycling scheme has been verified on a 12-bit Gray-code counter in 90-nm process technology. The measurement results demonstrate an average energy reduction of 23% with the charge-recycling scheme. The average energy consumption of the counter alone was decreased by 42% by recycling its ground-bound charge.

A comparison of the efficiency of the proposed charge-recycling scheme with the state-of-the-art techniques is presented in Table 4.2. The energy reduction figures achieved in this work show improvement over previously reported CR-based designs of [26], [27] and [28]. Furthermore, the proposed CR scheme avoids the delay introduced in charge-pump based voltage boosting techniques, and eliminates external clocks and the need to match the current-consumption in vertically-stacked CR digital blocks.

Table 4.2 Comparison of the state-of-the-art Charge-recycling based low power techniques

Reference	***% Power Saving***	***Features***	***Comments***
[24]	33 % (V_{DD} stacks) 85 % ($V_{DD}/2$ conversion)	V_{DD} stacks	Current balancing critical
[25]	5 % (dual V_{DD} stacks)	V_{DD} stacks	About 66 % reduction in noise
[26]	10 %	Adiabatic Charge pump	External, multiple phase CP clock required
[28]	25 %*	Single-stage Charge pump	External boost voltage required
This Work, 0.5-µm	26 %*	Capacitive Stack DC-DC conversion	No External CP Clock or Voltage boosting clock
This Work, 90-nm	32 %*; 23 % (Avg.)		

* Based on simulation results

Chapter 5 Design & Analysis of the Ultra-low Voltage DC-DC Converter

This chapter is revised based on the paper published by Chandradevi Ulaganathan et al. [35]:

C. Ulaganathan, B. J. Blalock, J. Holleman, and C. L. Britton, Jr., "An Ultra-Low Voltage Self-Startup Charge Pump for Energy Harvesting Applications," *The 55th Intl. Midwest Symposium on Circuits and Systems,* pp. 206-209, Aug. 2012.

My primary contribution to this paper include (i) identification of the scope of research, (ii) compilation of a literature review of previously published work, (iii) design and analysis of the proposed solution, (iv) implementation and simulation of the circuit, and (v) preparation of the manuscript.

5.1 Introduction and Motivation

The proliferation of portable, battery-operated electronic systems has increased the need for highly efficient, low-voltage-capable DC-DC boost converters. Further, the emerging niche classes of wireless, sensor-based electronic products such as smart sensors, biomedical implants, etc., necessitate power-autonomy to provide essential operations for several years without the need for battery replacement. In these systems, power-autonomy is realized by harvesting or scavenging energy from the surroundings using transducers such as thermoelectric generators (TEG), photovoltaic cells (PV), and piezoelectric sensors. However, due to variations in the operating conditions, these transducers do not generate a constant output. For instance, the output voltage from a PV cell could range from 100 mV to 500 mV due to variations in the incident light [36].

For "on-the-body" applications, as the core body temperature is regulated at 37 °C, there exists a temperature difference between the muscle temperature and the skin surface temperature. TEGs are employed to harvest energy from this temperature gradient that is readily available across the low thermal-conductive fat layer which is sandwiched between the muscles and the

epidermis (skin). However, the temperature differences vary significantly depending on the sensor's position on the body, ambient environment and physical activities [37]. The nominal temperature difference perceived by the TEGs range from 1-5 degree Kelvin and depends on the thickness of the fat layer. Hence, state-of-the-art TEGs require at least 1000 thermocouples (occupying area of 1.3 cm^2) to convert the temperature difference of 5 K into an output voltage of 1 V that can provide 100 μW of power to the load [37]. While increasing the number of thermocouples offers more power output, the power-density from the TEG-cell is independent of the number of couples. Hence, efficient energy harvesting can be realized with minimum sensor area by employing DC-DC converters that transform the very-low sensor output voltage to useful power supply voltage levels in circuits.

In order to guarantee efficient, uninterrupted energy harvesting and thereby achieve complete power-autonomy, energy harvesting systems need to operate across a wide range of input voltages that includes ultra-low voltage regime. The state-of-the art energy harvesters employ power management circuits (PMC) to facilitate the power autonomy. The critical components of PMC include DC-DC converter and the control-clock generator that enables the converter's startup and operation. The PMCs work as an interface between the energy harvesters and the load (application) in order to provide either a regulated output voltage or to ensure maximum power transfer (MPT) to the load [39]-[41], [44]-[49]. This is accomplished by varying the converter's DC-DC gain to provide a constant output voltage or by varying the frequency of operation to guarantee MPT. Therefore, it is essential that the circuits in the power management block are capable of reliable operation across the entire range of transducer's output voltage.

The charge recycling scheme proposed in Chapter 3 can be considered as a type of energy harvester that is capable of enabling power autonomy to a different circuit within the same chip. As discussed in Section 3.3, the charge available for recycling varies with the circuit's frequency of operation, the threshold voltage of the devices and the circuit's power supply voltage. Hence, adopting a CR topology with multiple charge-collection banks (Figure 3.15) could result in variable input levels to the voltage booster. Further, temperature changes would also necessitate adjustment to the charge collection threshold so that the circuit's performance can be maintained across T. For instance, in a CMOS inverter, allowing a

maximum delay increase of 2 times, the available charge-bank voltage would range from 100 mV to 300 mV across –55 °C to 125 °C, in the 90-nm process. Hence, a CR system that adapts to input voltage variations across PVT and multiple capacitor banks would truly augment its application.

Thus, solving the problem of reliable DC-DC conversion across a variable input voltage range, which extends down to very-low input voltages, is critical to energy harvesting applications and as well as improves the energy efficiency of the CR scheme. Hence the design of low voltage, self-starting DC-DC converter presents an attractive challenge with many applications. The goal of this research is to design a low-voltage-input capable converter that does not require external excitation or post-fabrication processing for startup. Furthermore, a switched-capacitor topology that enables on-chip integration without the need for external components, and with adaptable number of gain stages is preferred. Ideal target applications include ultra-low-energy products such as real-time clocks and wrist watches.

5.2 Literature Review

DC-DC converters can be broadly classified into inductor-based and switched-capacitor (SC) based converters. Inductive boost converters are capable of efficiently boosting ultra-low input voltages in the order of few tens of millivolts [39], [40]. However, to avoid the high area-overhead associated with realizing on-chip inductors and to facilitate integrated multiple charge-recycling banks (as in Fig 3.x), switched-capacitor based DC-DC converters are explored in this research.

This section starts with brief introduction to the voltage boosting mechanism in charge pumps (CP) and is followed by a discussion on the losses that affect the conversion efficiency. Then, the operation and challenges of state-of-the-art low-voltage converters and their ability to self-start are studied.

5.2.1 Switched Capacitor Charge Pump topologies

Several CP topologies have been published in literature, each designed to meet specific requirements such as high gain, high drive capability, high efficiency, and small area [42]. The differences in the architectures lie primarily in the mechanisms employed to transfer charge

between the pumping stages and the implementation of the charge transfer switches (CTS). This section discusses the operation and control of the most commonly employed CP topologies.

5.2.1.1 Linear Charge pump (LCP)

The most widely used LCP topology is based on the scheme published by Dickson in 1976 [43] and has been extensively studied since then to improve its performance. Figure 5.1 presents a simplified schematic of a three-stage LCP with each CP stage comprising of a pumping capacitor, C_{Pi}, and a charge transfer switch (CTS), S_i. The load is represented by a DC current sink, I_L, and a load capacitor, C_L. Figure 5.1 (a) to (c) illustrate the commonly employed implementations of CTS in charge pumps. For this discussion, let us consider the switches to be ideal and the clocks Φ_1 and Φ_2 as complementary phases with voltage swing equal to the CP's input voltage i.e. V_{DD}.

During the first cycle of operation, switches S_1 and S_3 are closed while S_2 and S_4 are open. The capacitor C_{P1} is charged to V_{DD}, while charge is transferred from C_{P2} to C_{P3}, charging C_{P3} to approximately $3V_{DD}$ (in steady state). At the output node, the load current is supplied by C_L which slowly reduces the output voltage by $I_LT/2C_L$, where T is the clock's time period. During the subsequent cycle, switches $S2$ and S_4 are closed while S_1 and S_3 are open. Since the bottom plate of C_{P1} is pushed up to V_{DD}, node N_1 is increased from V_{DD} to $2V_{DD}$ which results in charge transfer to C_{P2} through the closed switch S_2. Similarly, node $N3$ is pumped to $4V_{DD}$ and charge lost by C_L during the previous phase is replenished from C_{P3}. Additionally, charge of $I_LT/2$ is transferred from C_{P3} to sustain the load current during this phase. Hence in each clock period, a charge equal to I_LT is transferred between adjacent capacitors towards the direction of the load [61]. The output voltage slowly increases towards the final asymptotic steady-state value of [61]

$$V_{OUT,SteadyState} = (N+1)V_{DD} - N\frac{I_L \cdot T}{C_P} \tag{5.1}$$

where, N is the number of pumping stages. The second term in (5.1) represents the reduction in output voltage due to charge redistribution loss due to charge transfer from the input to the DC load. For the case without load current I_L, the steady state output approaches the ideal value of

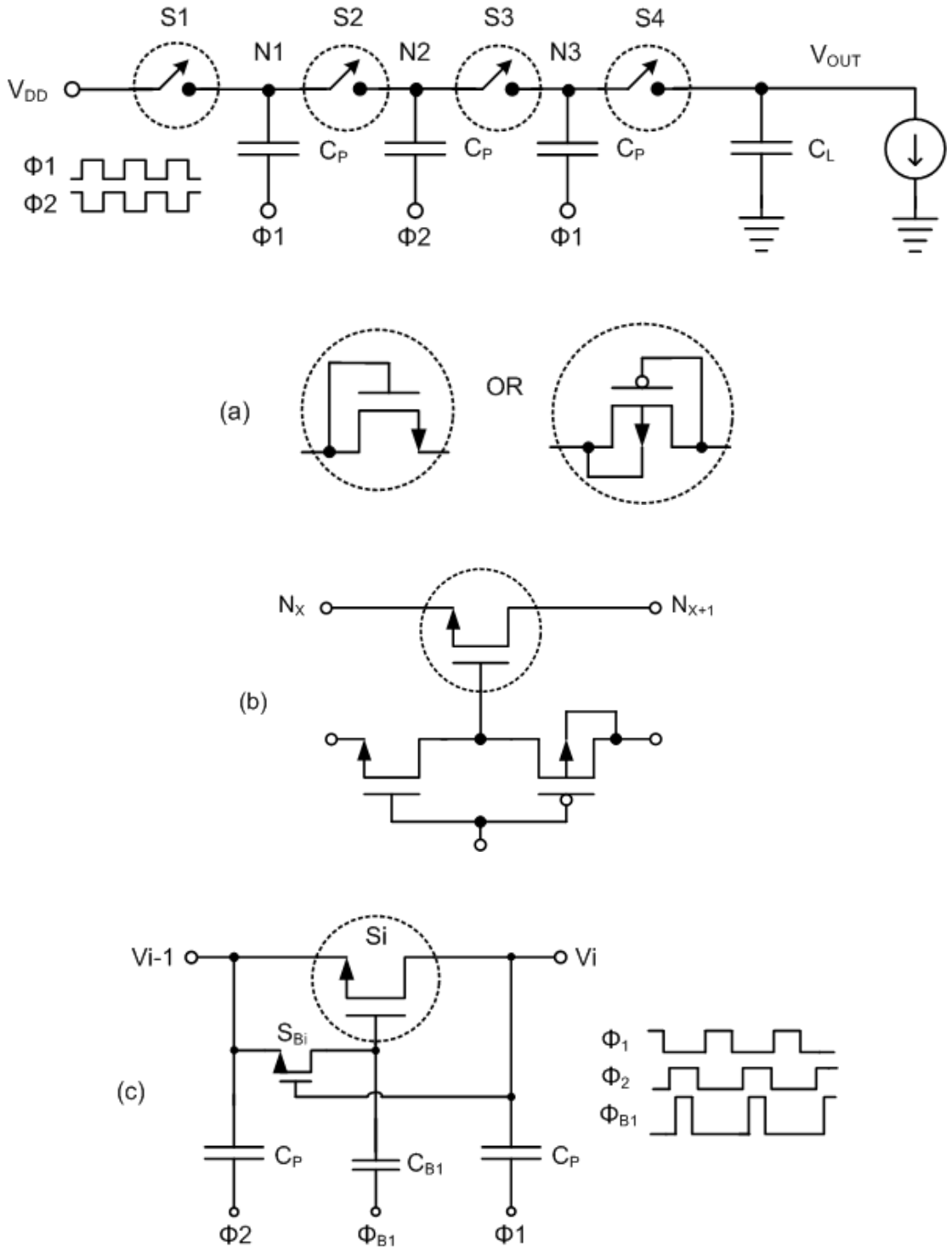


Figure 5.1 Simplified schematic of a three-stage linear charge pump with charge transfer switch (CTS) implementations (a) CMOS diode CTS (b) CTS with gate control generator and (c) Bootstrapped CTS.

$(N+1)\cdot V_{DD}$. Thus, a charge pump extracts charge from the input source and pumps this charge through the different pumping capacitors to a higher voltage at the output. This voltage boosting is accomplished in a linear manner from one stage to the next in the LCP topology.

Variations in the LCP topology can be realized by different implementations of the CTS and control clocks. Figure 5.1 (a) illustrates the case where the CTS is realized as a MOS diode. This topology eliminates the need for switch control generation but results in a lower output voltage due to the presence of a threshold voltage drop in each CP stage. This threshold voltage drop across each stage renders this topology unsuitable for low-voltage applications. Figure 5.1 (b) shows a NMOS CTS and its associated gate control (GC) signal generation circuit [59] that employs dynamic level shifters using the pumped node voltages from different CP stages. The challenge with this approach lies in the choice of appropriate level-shifting voltages and their relative phase transitions. Depending on the relative phase of control signal used for the pumping capacitors, reverse current paths could exist between these CP capacitors. Also, dynamic switching loss in the form of short-circuit current might result due to signal transitions at different phases at the level-shifter rails. Hence, careful implementation and analysis are essential to take advantage of this topology for low-voltage operation. This topology is further discussed in detail during the design of the proposed CP.

Figure 5.1 (c) presents the bootstrap capacitor based implementation of CTS along with the non-overlapping (NOV) control signals. To understand the operation, consider the case when switch S_i is open, Φ_1 is *HIGH* (at V_{DD}), Φ_2 and Φ_{B1} are *LOW* (at ground). The bootstrap switch S_{Bi} is closed ($V_{GS,SBi} = 2V_{DD}$) and the capacitor at S_i's gate node is charged to the previous stage's node voltage (V_{i-1}). During the next clock phase, the Φ_2 is *HIGH* (at V_{DD}), Φ_{B1} is also *HIGH* (but at $2V_{DD}$) while Φ_1 is *LOW* (at ground). The bootstrap switch S_{Bi} is open since its V_{GS} is zero. The top-plate of the bootstrap capacitor is at high impedance and so the voltage at S_i's gate increases to $V_{i-1} + 2V_{DD}$ when Φ_{B1} is at $2V_{DD}$. This sets a V_{GS} of V_{DD} at the charge transfer switch S_i and turns it *ON* for charge redistribution. To eliminate the $2V_{DD}$ amplitude required for Φ_{B1}, four-clock-phase control methodology has been developed in [52], wherein the smaller bootstrap capacitor C_{Bi} charges to $V_{i-1} + V_{DD}$ for a very short period time before the Φ_{B1} goes *HIGH* to V_{DD}. This provides a V_{GS} of V_{DD} at S_i to enable the charge redistribution to the next stage's C_P. Thus the bootstrapped topology is well suited for low voltage operation but requires complex four-

phase clock signal generation which is power hungry and also, larger area due to the bootstrap capacitors [61].

5.2.1.2 Fibonacci Charge Pump (FCP)

The Fibonacci charge pump presented in Figure 5.2 produces a boosted output voltage equal to the $(N+3)^{th}$ number in the Fibonacci sequence. For instance, the three-stage topology would have a gain of 5 V/V which is the 4^{th} number in the sequence 0, 1, 1, 2, 3, 5. As shown in Figure 5.2 (a), during the Φ_1 phase (i.e. *HIGH*), the odd-stage pumping capacitors are charged to their steady-state values while the even-stage capacitors are connected in series to boost their top-plate voltage so as to charge the next stage capacitor. In the next phase (presented in Figure 5.2 (b)), the odd-stage capacitors are connected in series, while the even-stage capacitors are replenished with charge to reach their steady-state values. Thus, with a series-parallel connection between the adjacent CP stages, higher conversion gains than the LCP can be achieved. The improvement in gain is more significant with increase in the number of pumping stages. The main disadvantage with this topology is the considerable reduction in output voltage, compared to the ideal value, due to parasitic capacitances with increasing number of stages.

5.2.1.3 Exponential Charge Pump (ECP)

The exponential CP topology has gained importance in low-voltage applications where large conversion gains are needed with tight area constraints. Figure 5.3 presents a simplified schematic of a three-stage ECP that provides an ideal voltage gain of 8 V/V (which corresponds to 2^3). The operation of the CP can be readily understood by referring to the steady state operation shown in Figure 5.3 (a) for the case when Φ_1 is *HIGH* and Φ_2 is *LOW*. In this phase, the pumping capacitors in the top branch are connected in series and provide the steady-state output voltage of $8V_{DD}$. The capacitors in the bottom branch are connected to the charge replenishing nodes from the top capacitors, and thereby charge up to V_{DD}, $2V_{DD}$ and $4V_{DD}$ respectively. As illustrated in Figure 5.3 (b), during the next phase (Φ_2 is *HIGH)*, the capacitors interchange their roles to sustain the steady state output voltage of $8V_{DD}$ and to refill the charge depleted by the load current.

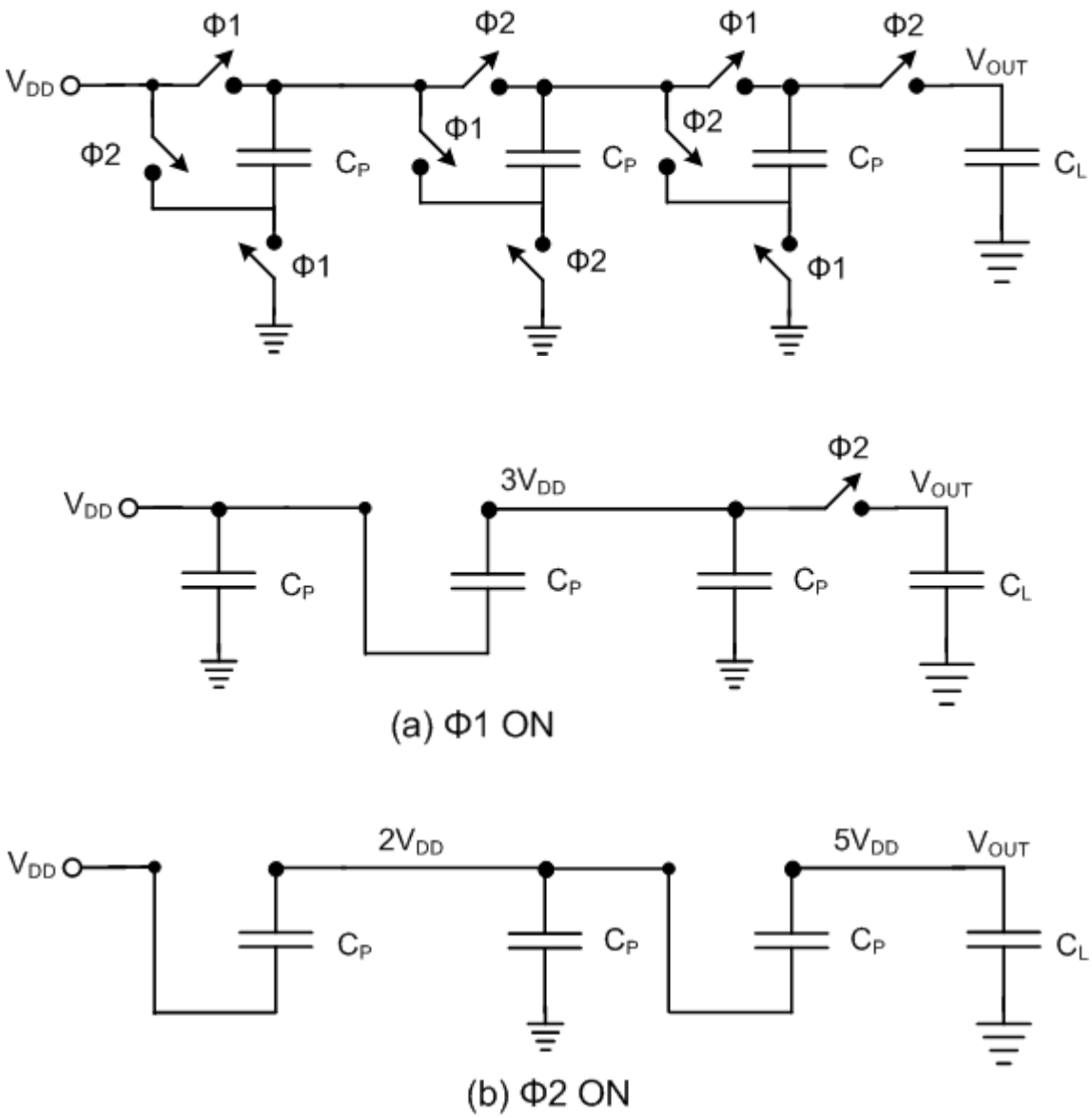


Figure 5.2 Simplified schematic of a three-stage Fibonacci charge pump (a) Φ_1 is active (b) Φ_2 is active.

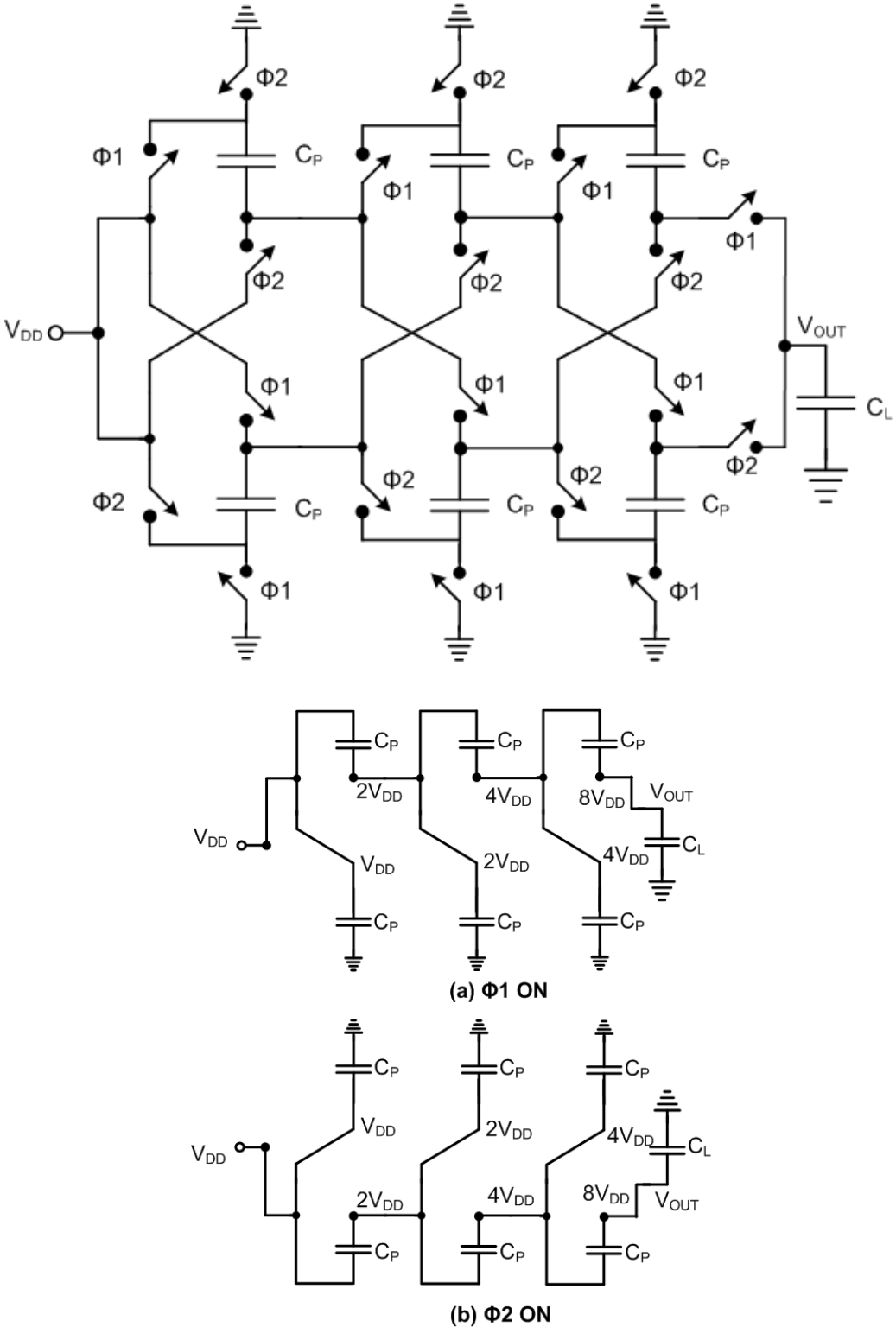


Figure 5.3 Simplified schematic of exponential charge pump (a) Φ_1 is active (b) Φ_2 is active

The main disadvantage with this topology is the higher output resistance when compared to the LCP and FCP topologies. Hence, the series voltage drop across the CTS increases with the output load current and thus the performance of the CP is reduced [42]. Further, since the pumping capacitors are connected in series, the presence of parasitic bottom plate capacitances deteriorates the maximum possible output voltage.

5.2.1.4 Operational Losses in CPs

The efficiency of CP's voltage boosting operation is reduced by the operational losses incurred during the process of transferring charge from the CP's source to the load. Thus, a study of the different mechanisms of loss is essential to improve the efficiency of the CP topologies.

Switching loss

The current required to charge and discharge the bottom plate capacitance of the charge pump capacitors, and also the gate capacitance of the charge transfer switches contributes to the switching loss. Additionally, topologies that employ gate control circuits to generate the control signals for CTS contribute to additional losses due to short-through (or short-circuit) current that can flow between the CP nodes used as supply rails during switching transients. Reducing the CP's operating frequency would reduce the switching losses but the CP's output voltage would experience a large voltage droop that increases with slow clocking. Hence, the solution to lower switching losses is to operate the CP at an optimal frequency that produces an acceptable output ripple voltage, and to size the CP capacitors and CTS for optimal performance.

Conduction loss

The finite "on" resistance of the CP's charge transferring switches results in small voltage drop in each stage and thus causes the CP's conduction loss. The switch's "on" resistance is given by

$$R_{ON} = \frac{1}{\mu C_{OX} \frac{W}{L}\left(V_{GS} - V_{TH}\right)} \tag{5.2}$$

where μ is the mobility, C_{OX} is oxide capacitance, W/L is the CTS device size, V_{TH} is the threshold voltage and V_{GS} is the gate-to-source voltage. This series resistance results in a voltage

drop that depends on the amount of charge transferred by the CP. One way to mitigate this loss is to increase the width of the MOS switch and thereby reduce R_{ON} and the series voltage lost during conduction. However, very large devices introduce significant increase in parasitic capacitances such as gate-to-diffusion, gate-to-body capacitances that require more current for their charge and discharge during switching. Thus, an optimal switch size is required to keep the sum of the conduction and switching losses to a minimum in the CP.

Reversion loss

Reversion loss occurs when reverse currents flow from the later stages to the previous stages in a charge pump i.e. current flowing in the direction opposite to the CP's charge transfer. The most common cause for this reverse current is the controlling of adjacent CTS gates with complementary clock phases. As illustrated Figure 5.4, during switching transitions, when switch S_2 is being opened and, S_1 and S_3 are being closed, a brief period of time exists when both the switches are conducting. This results in the flow of reverse current from the higher potential at node N2 to node N1 and thereby causes loss of charge in the direction opposite to the power transfer in the CP. Reversion loss can be eliminated by implementing the adjacent CTS with a 'break-before-make' action wherein a switch is first opened before closing the adjacent switches for charge redistribution. This can be accomplished by employing non-overlapping clock signals to control the switches in the adjacent CP stages.

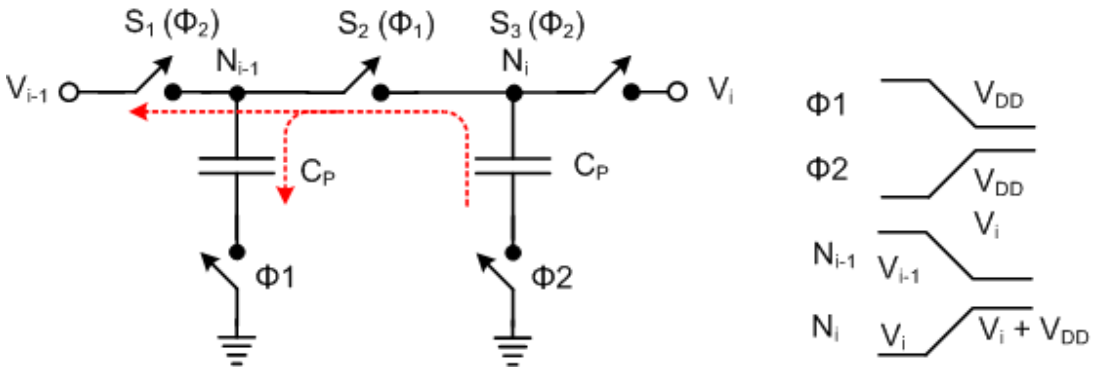


Figure 5.4 Simplified schematic of linear charge pump's stage illustrating reverse current loss.

Charge Redistribution loss

Redistribution loss is due to the transfer of charge between the charge pump capacitors. Charge redistribution loss is independent of the "on" resistance and is proportional to the frequency of operation and the load current. Maintaining low ripple voltage results in smaller charge redistribution between the CP stages and thus lowers charge redistribution loss component in the charge pump.

Equipped with this brief introduction to the operation and losses in charge pump topologies, the rest of this section discusses the state-of-the-art DC-DC converters that are pertinent to ultra-low voltage, energy harvesting applications.

5.2.2 Low voltage self-startup in converters

The self-startup feature denotes the unique capability of the converter to generate all the required control signals and thus enables autonomous operation as long as a valid input is available for conversion. Several self-starting converters for energy harvesting applications have been published in literature [39]-[41], [44]-[50] . A significant number of these designs have demonstrated autonomous operation when the input voltage is above a certain threshold level called the startup voltage. However, these designs do not operate unaided at very-low input voltages. The low-voltage startup aids in these designs include external excitation, such as a battery [47], mechanical vibrator [39], or transformer [41]. External battery initiated startup is the most commonly used methodology at low voltages as it avoids the need for interface circuits required in vibrators.

Of the few designs that eliminate start-up aids, post-fabrication threshold voltage (V_{TH}) tuning is performed in [44] to ensure low voltage startup, whereas [45] uses forward body-biasing to lower the device threshold voltages in the SC charge pump. These designs offer low startup voltages of 100 mV and 180 mV respectively. The energy harvester presented in [49] is a standalone, low-voltage, self-starting DC-DC converter that is targeted for energy harvesting from photovoltaic cells and is capable of boosting inputs as low as 270 mV without any external excitation. A recently published work [41] exploits white noise to trigger oscillations in a transformer-capacitor start-up circuit. The transformer based converter is capable of ultralow startup voltage of 20 mV in a 130-nm process. The research in [50] employs an exponential

charge pump (ECP) to achieve a very low startup voltage of 150 mV in a 65 nm process. The Table 5.1 presents a comparison of the state-of-the-art ultra-low voltage DC-DC converters and their startup characteristics.

5.2.3 Ultra-low voltage SC converters

This section discusses in detail the SC-based converter designs of [49], [50] and [45] that do not require any external excitation for starting, and operate at very low input voltages.

An ultra-low voltage, four-stage linear charge pump [46] that works down to 0.7 V of input voltage is illustrated in Figure 5.5. This CP employs cross-coupled branches to reduce the output ripple voltage. During each clock phase, the CTS are controlled such that one branch (top or bottom) pumps charge towards the load while the capacitors in the other branch replenish their

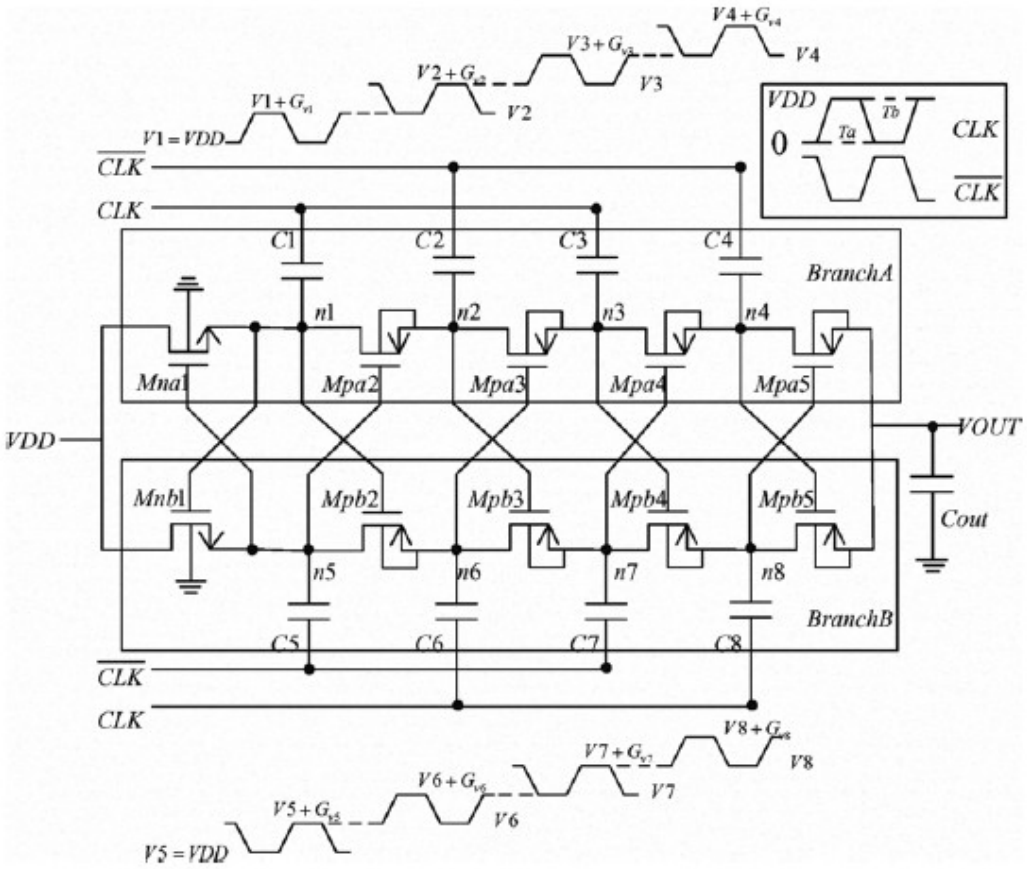


Figure 5.5 Schematic of the low-voltage charge pump in [46]

charge to reach the respective steady state levels. Controlling the two symmetric CP branches with complementary clock phases facilitates the use of symmetric nodes from the opposite branch to generate the CTS gate-control. The main disadvantage of this CP is the presence of reverse current paths across all the pumping stages. This significantly reduces the maximum achievable output voltage. Furthermore, for self-startup topologies where the clock signals would have to be generated from the low input voltages, reverse current loss would drastically increase due to slower clock transitions and thereby impede CP startup.

Figure 5.6 presents the low-voltage capable charge pump published in [45]. The 3-stage charge pump employs cross-coupled, voltage doubler cells [57] that are connected in series to achieve the required gain. Similar to [46], employing complementary clock signals to control the cross-coupled branches helps in the generation of CTS control signals. Additionally, the CP incorporates forward body biasing (FBB) to reduce the threshold voltages of the serially connected charge transferring switches. The body-bias voltage for the PMOS is derived from the input of the previous stage while the NMOS body is biased by the output of the next stage. An extra CP stage with small pumping capacitors that does not contribute to the output voltage, is

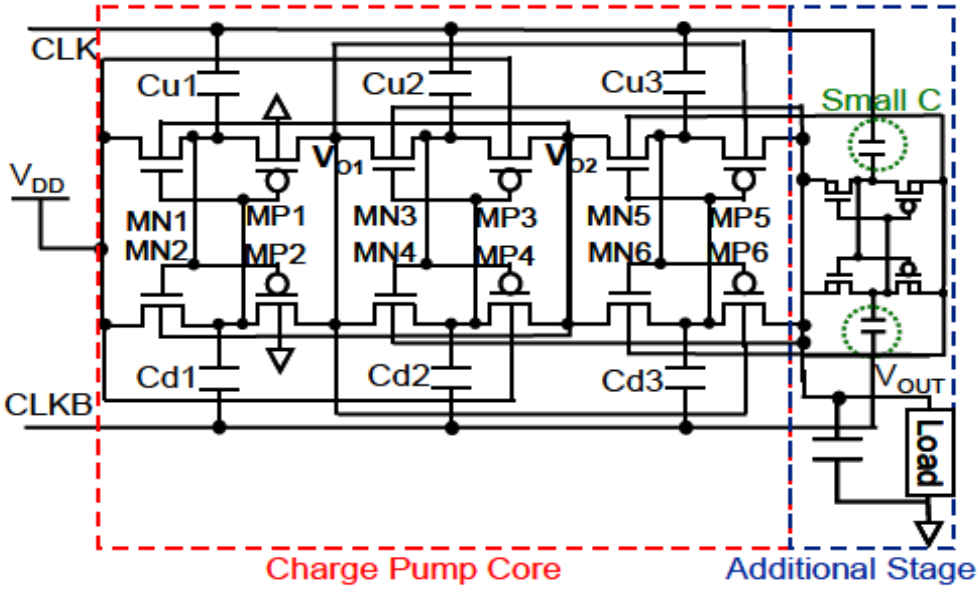


Figure 5.6 Simplified schematic of the low-voltage charge pump in [45]

required to generate the third-stage NMOS device's body bias voltage which is higher than V_{OUT} of the CP. This charge pump design was employed to boost a 180 mV input to a 0.5 V output that drives the clock generation circuitry to control the inductor-based boost converter.

Since this topology includes two series switches in each CP stage, the switches have to be sized large enough to limit the conduction loss. Further, as the body biasing for the CTS is derived from the pumping nodes, charge is lost in the process of charging and discharging the body (diffusion well). Another significant loss mechanism exists during the switching transitions when there is a possibility of all the switches being ON for a brief period of time and large reverse current could flow from the output to the source. Thus, the efficacy of this CP is eclipsed by the existence of several loss mechanisms.

The simplified schematic of the low-voltage charge pump implemented in [49] is shown in Figure 5.7. The charge pump uses two parallel charge-transfer switches (CTS) in each stage to provide efficient charge transfer across a wide range of input voltages (V_{in}). The components M_{AX}, M_{BX}, C_{bx}, and C_{px} form the conventional four-phase Dickson CP cell [52] that is controlled by boosted gate voltages derived from V_{in}. The gate controls for the S_x switches are derived from the output voltages. At very low input voltages, the output voltage is also low so the charge

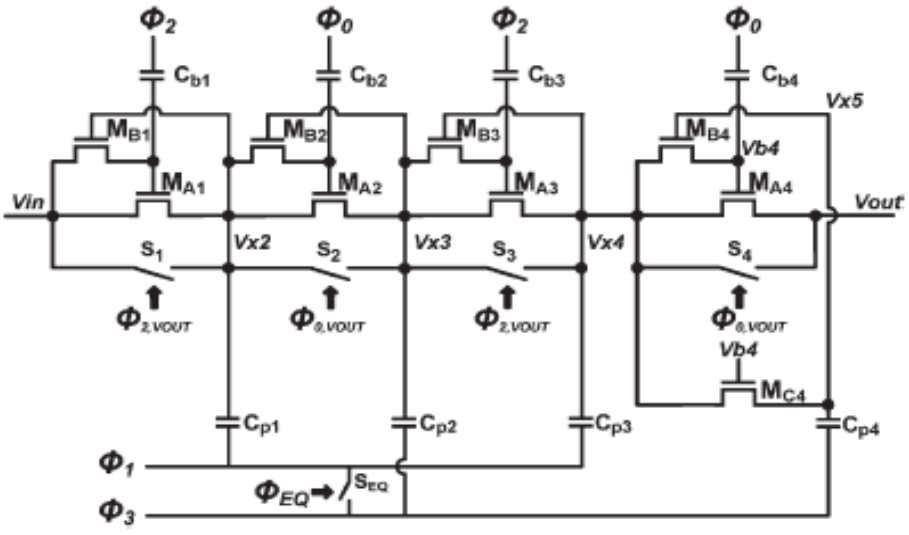


Figure 5.7 Simplified schematic of the low-voltage charge pump in [49]

transfer to the subsequent stage is achieved by the boosted gate control switches M_{AX}. For high input voltages, the switches with gate control derived from V_{out} dominate the charge transfers.

This self-starting converter, designed in 130 nm process technology, employs four-stage, four-phase SC charge pump (CP) to provide a regulated output voltage of 1.4 V at 58% efficiency for a low input of 450 mV. The output voltage from the CP is regulated to within 23 mV of 1.4 V by comparing a scaled version of the output with an on-chip bandgap voltage reference. Also, this work uses the input voltage to power up the clock and phase generation circuits and thereby eliminates the need of an external start-up voltage [49]. The system clock is synchronized (latched) with a comparator such that charge transfers along the CP stages are enabled only when the output voltage drops below the permissible ripple voltage range. The unregulated converter starts at a low voltage of 270 mV while providing 3 times gain. Thus, this self-starting converter is well suited for low voltage photovoltaic cell applications but not for conducive for ultra-low voltage TEG systems.

An ultra-low voltage exponential charge pump (ECP)-based converter capable of 150 mV startup voltage has been recently published [50]. The schematic of the CP core is shown in Figure 5.8. Since the two-phase (Φ_1, Φ_2) clock generator is powered from the input voltage, the ECP requires bootstrapped switches to control charge redistribution between the CP stages. The CP was implemented in a 65nm process with total on-chip capacitance of 5nF. With an input of 150 mV, simulation results illustrate an output of 850 mV at 1 μA of DC load current with an efficiency of 30% [50]. This CP renders itself well to low-voltage energy harvesting applications but the problem with ECP lies in the generation of the CTS control signals and the inability to provide multiple conversion gains.

The Table 5.1 summarizes the characteristics of these converters along with other state-of-the-art ultra-low startup designs. The designs of [39], [40], [47], [48], [41], and [68] (first six rows in the table) that employ external or assisted startup are included in this table to provide a comprehensive review of state-of-the-art converters. Even though the inductor-based converters are capable of boosting ultra-low input voltages (20 mV), it is to be noted that they require external, startup control signals that have large duty cycle requirements. Hence, inductor-based

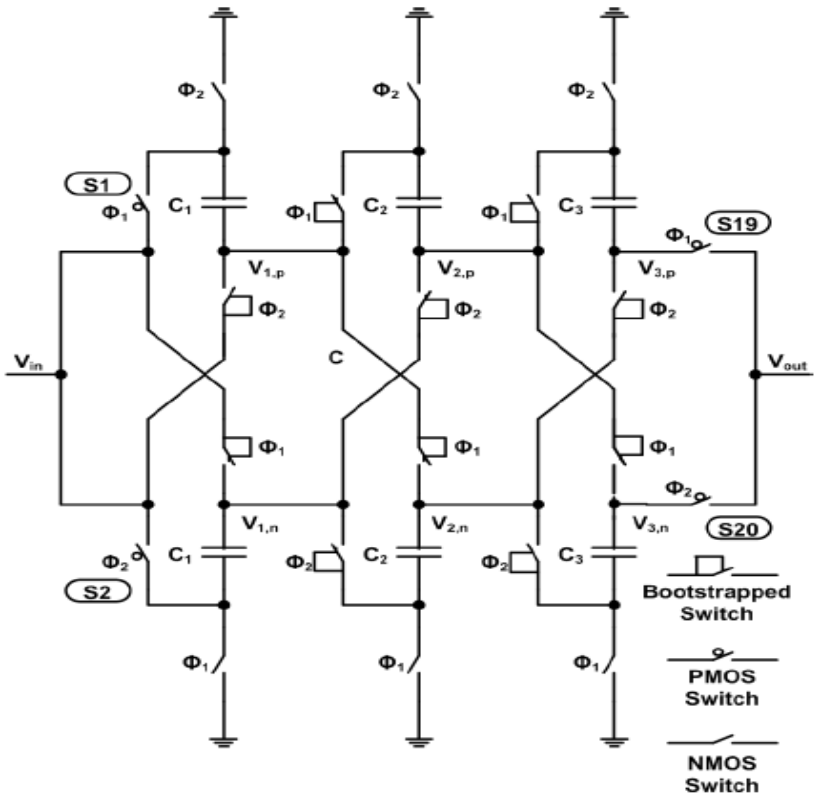


Figure 5.8 Simplified schematic of the low-voltage exponential charge pump in [50]

converters represent efficient but expensive DC-DC conversion. Charge pump based solutions offer the possibility of cheap designs that are capable of self-startup. However, innovative control of the CP stages is required to improve the efficiency of these SC-based boost converters.

From the study of these SC converters, it can be inferred that efficient low-voltage operation is highly dependent on the CTS implementation and its control strategy. For example, in a linear charge pump topology, the unassisted minimum startup voltage published in literature is 270 mV (130 nm process) [49], while the V_{TH} tuning using forward body-biasing reduces the startup voltage to 180 mV in a 65 nm process [45]. Even though the design in [50] does not state a self-startup feature, the exponential CP design can operate with input voltages as low as 150 mV, provided the control signals are available. Furthermore, the CTS implementation in these topologies and their relative phases at the adjacent CP stages determine the reverse current component that deteriorates the maximum attainable output voltage. Thus, an optimal solution

Table 5.1 Summary of the state-of-art low-voltage DC-DC converters with startup mechanisms

Reference	***Startup mechanism***	***Startup voltage***	***Converter Topology***	***Input voltage***	***Output Voltage***	***% Efficiency***	***Process***
[39]	Mechanical switch	35 mV	Inductive	50 mV	1.8 V	58 %	350-nm
[40]	External battery	650 mV	Inductive	20 mV	1 V	75 %	130-nm
[47]	External battery	2 V	LCP	0.6 V	2 V	70 %	350-nm
[48]	Hybrid (External inductors, CP)	200 mV	Inductive	0.2 V	1.2 V	36 %	180-nm
[68]	undescribed	20 mV	Transformer	20 mV	2.35 -5 V	40 %	undescribed
[41]	White noise into transformer, cap	40 mV	Transformer	40 mV	1.2 V	37 %, 61 % (pk.)	130-nm
[44]	Charge pump with V_{TH} tuning	95 mV	Inductive, Ext. CP cap	100 mV	0.9 V	72 %	65-nm
[45]	Forward body biased charge pump	180 mV	CP (Doubler stages)	180 mV	0.7 V	N/A	65-nm
[49]	Charge pump	270 mV	LCP	450 mV	1.4 V	58%	130-nm
[50]	Charge pump	150 mV	ECP	150 mV	0.85 V	30 to 80%	65-nm

that minimizes the operational losses in the CTS control would significantly improve the efficiency and the startup voltage in low-voltage charge pumps.

In conclusion, the literature study of the different low-voltage CP topologies has clearly emphasized the need for a voltage converter that offers both ultra-low voltage operation, and is truly autonomous i.e. self-starting without the need for external excitation. Further, a switched-capacitor based converter that eliminates the need for external components, and facilitates adaptable number of gain stages would greatly improve the efficiency of energy harvested using transducers.

5.3 Design of the proposed low-voltage, self-starting DC-DC converter

The proposed low-voltage DC-DC converter is intended for energy harvesting applications, and as well as for extending the application of charge recycling scheme to operate efficiently across process, voltage and temperature variations. The design goals for the DC-DC converter include:

- Ultra-low voltage operation in the 100 mV range to minimize the amount of wasted energy from transducers and the recycled charge across PVT variations.
- Unassisted self-startup ability to enable power autonomy in harvesters and to reduce the energy overhead on the charge recycling system.
- Easily variable conversion gain that adapts to change in input voltage.
- Area efficient, on-chip integration of the converter to facilitate multiple charge-recycling systems in a single chip and thereby increase energy efficiency by the virtue of dynamic voltage scaling (DVS).

5.3.1 Architecture of the Converter

The block level schematic of a power management circuit (PMC) that includes the proposed self-starting converter is presented in Figure 5.9. The low output voltage (V_{IN}) from energy scavengers is boosted by the charge pump to either meet the power supply requirements of the target application, or, to be stored in the buffer for later use. The control signals required for the CP operation are generated by the five-stage ring oscillator (RO) and the phase generator

(PG) circuits. These circuits are powered directly from V_{IN} in order to enable power-autonomy in the converter. An output control block is employed in the PMC to provide maximum power transfer (MPT) from the CP to the load by controlling the number of conversion stages in the CP [47] or by varying the frequency of operation [40].

At the startup, the system clock and the CP control signals are generated as soon as the harvested voltage (V_{IN}) reaches the minimum power supply voltage (V_{DDMIN}) required by the RO. V_{DDMIN} is limited by the current matching in the PMOS-NMOS devices, the V_{TH}, and the variation in device characteristics across process corners. Additionally, since the circuits operate in subthreshold region at low startup voltages, the device characteristics are more sensitive to process & mismatch variations. Hence, low-threshold voltage (LVT) devices with proper device sizing (as in [51]) are essential to minimize variation in the inverter's switching point (i.e. PMOS-NMOS I_D and V_{TH}) and thus to guarantee oscillation at low startup voltages.

A conventional non-overlapping (NOV) phase generator is employed to produce the clock phases for the different stages in the CP. The NOV clocks minimize the reduction in output voltage due to reverse currents flowing from subsequent stages to previous stages along the CP. The charge pump performs the voltage boosting operation to provide the system power to the application. This remainder of this section discusses the design details of the RO, phase generator and the proposed low-voltage CP circuits.

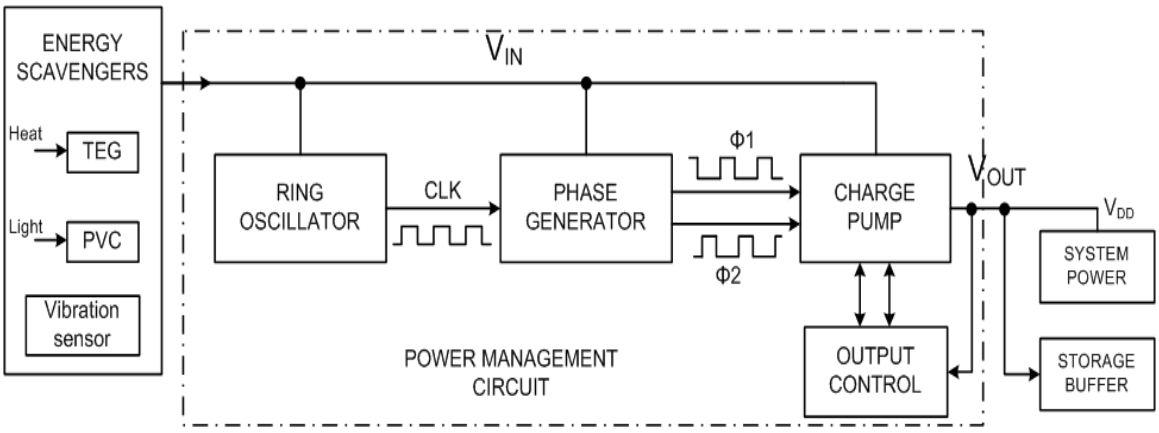


Figure 5.9 Topology of the proposed self-starting converter

5.3.2 Choice of CP topology

SC charge-pumps provide a boosted output voltage by phased charge-transfer from the input source to the output load through the CP stages. The conversion ratio depends on the number of CP stages and the topology of CP cell employed in each stage. This section investigates the suitability of linear CP (LCP), voltage doubler, Fibonacci CP (FCP), and exponential CP (ECP) to autonomous, low-voltage operation.

High conversion gain with fewer number of CP stages than in LCP designs can be realized by cascading voltage doubler cells [57]. This topology doubles the voltage at each CP stage by driving the bottom plate of the CP capacitor with clock amplitude equal to the top plate's steady state voltage. Hence, the main disadvantage of this approach is the requirement to generate the CP clock with different voltage swings that depends on the stage in the CP. This can be accomplished by bootstrapped clock generation from the previous stage's output, or can be derived from the output voltage of the CP's last stage. However, these clock generation techniques add to the parasitic charge losses and thus degrade the efficiency. At low-voltage operation, larger pumping capacitors in each stage and bigger switch sizes are required to reduce the "on" resistance and thereby improve the efficiency of the pump.

FCP & ECP based converters also provide higher boost ratios with lower number of CP stages when compared to the LCPs and thus makes them desirable in low-input voltage, high-gain conversion requirements as demonstrated in [50]. Both the FCPs and ECPs implement series-parallel connections between the CP stages in order to realize the required gain. The most challenging part in the design of these charge pumps is the control generation for the CTS. Bootstrapped switches are required to control these switches. The main drawback in these topologies is that the number of stages cannot be easily adjusted to obtain multiple conversion ratios with dynamically varying input voltages. Also, in the presence of parasitic capacitors, LCPs perform better than FCP and ECP to achieve the highest output voltage [58].

The LCP topology facilitates autonomous operation as a constant clock voltage swing of V_{IN}, across all the CP stages, is sufficient to provide a linear boost of V_{IN} for each stage. Further, since the CP is intended for use with low-voltage, low-power applications, the maximum number of stages is about 5 to 6 which is not very high to introduce significant loss in efficiency. Hence,

a three-stage LCP that provides a theoretical gain of 4 V/V is adopted in the proposed DC-DC voltage converter.

5.3.3 Design of Ring Oscillator

The simplified schematic of an inverter-based ring oscillator topology is shown in Figure 5.10. According to Barkhausen stability criterion, the necessary conditions for oscillations in a feedback loop are:

- The loop gain should be equal to unity, and
- The total phase shift in the feedback loop should be a multiple of 2π.

The feedback loop in a RO with identical inverter cells implies that each stage would provide a phase shift of $2\pi k/N$ at the frequency of oscillation, where k is an integer and N is the number of inverter stages. Since an inverter has an inherent phase shift of π, the stability criterion is met in a RO with a phase shift of $\pi + \theta$ at each stage. Further, in order to generate high frequency of oscillation at low power consumption, the number of inverter stages in the RO is kept as small as possible. As shown in Figure 5.13, this implies that $N.\theta=\pi$ and results in

$$Phase\ \ shift, \theta = \pm\pi / N \tag{5.3}$$

for each stage [53]. This sets the practical, minimum number of stages in a single-ended RO as 3. With even number of stages in a RO, there exists a possibility that the loop might settle at a dc condition and not produce any oscillations.

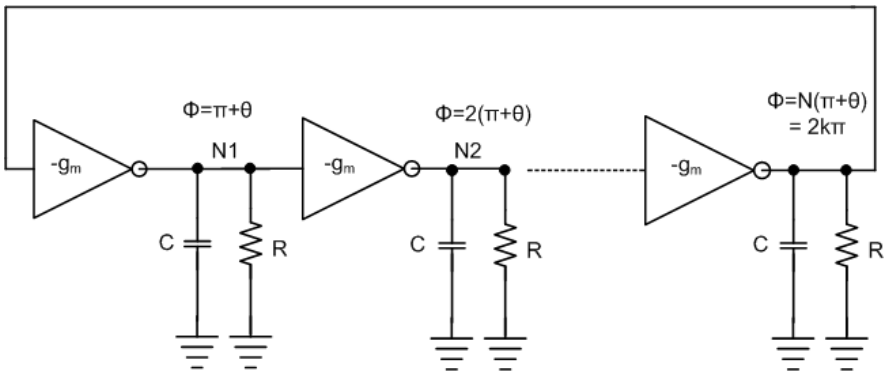


Figure 5.10 Model of inverter-based ring oscillator

For sustained oscillations, the gain requirement should also be satisfied and this entails

$$\left|A(j\omega)\right|^N = 1 \tag{5.4}$$

where $A(j\omega)$ is the transfer function of each stage and can be approximated as

$$A(j\omega) = \frac{-g_m \cdot R}{1 + RCj\omega} \tag{5.5}$$

where g_m is the transconductance of the stage, R and C represent the resistive and capacitive loads for each stage. At the frequency of oscillation, the phase of the transfer function in (5.5) is given by [53]

$$\angle A(j\omega) = -\tan^{-1}(RC\omega_0) \pm \pi = -(\theta + \pi) \tag{5.6}$$

which gives the frequency of oscillation as

$$\omega_0 = \frac{\tan\theta}{RC} \tag{5.7}$$

The gain criterion can be derived from (5.5) as

$$g_m \cdot R \geq \frac{1}{\cos\theta} \tag{5.8}$$

which is 2 for a three-staged RO and 1.24 with five-inverter stages. Equation (5.8) shows that it is easier to meet gain criterion with long inverter chains due to the smaller gain requirement from each stage. This result is important especially for low voltage, subthreshold operation regimes where the gain can be very low. Hence, a five-stage inverter ring is adopted in this design. Furthermore, a 5-stage topology keeps the power consumption low when compared to higher N and also allows for a good range of tuning of the oscillation frequency.

The frequency of the generated clock is dependent on the power supply voltage which is the input voltage from the transducer. For the RO in Figure 5.13, the load resistance R in (5.7) is the "on" resistance of the device and is dependent on the applied V_{DD}. The RO frequency can also be written in terms of the inverter's delay time as

$$f_0 = \frac{1}{(t_{dr} + t_{df})N} \tag{5.9}$$

where t_{dr} and t_{df} are the propagation delays for the rising and falling transitions in each stage, and N is the number of stages. In this research, capacitive delay cells have been included at the output of each stage in order to be able to control the output frequency for a given input, V_{IN}. A 3-bit decoder is employed to add or remove delay cells so as to tune the frequency of the generated CP clock.

5.3.3.1 Low-voltage startup in Ring Oscillators

The ring oscillator's startup voltage defines the minimum possible input voltage that can be boosted by the charge pump. Hence, it is critical to ensure that the RO is capable of providing stable system clock even at very low supply voltages. The design methodology adopted here is to set the sizing ratio of the CMOS devices to facilitate subthreshold operation [51].

The RO's startup voltage is determined by the current matching in the PMOS-NMOS devices, the V_{TH}, and the variation in device characteristics across process corners. The sizing ratio of PMOS-to-NMOS device widths can be used as a soft tool to make small alterations to the inverter's switching threshold voltage, V_M. In ROs, the inverter's switching threshold voltage establishes the duty cycle of the generated clock. Hence, setting the switching threshold at $V_{DD}/2$ results in a 50% duty cycle, maximizes the noise margin, and achieves symmetrical characteristics. The required PMOS-NMOS ratio can be determined by equating the CMOS subthreshold currents at the switching threshold voltage, i.e. $V_{IN}=V_{OUT}$, which gives

$$I_0 \cdot e^{\left(\frac{|V_{GS}|-|V_{TH,p}|}{nV_T}\right)} = I_0 \cdot e^{\left(\frac{V_{GS}-V_{TH,n}}{nV_T}\right)} \tag{5.10}$$

where the gate-to-source voltage (V_{GS}) is set by the input V_{IN}, V_{TH} is the device threshold voltage, V_T is the thermal voltage given by $kt/q \approx 26$ mV, n is the subthreshold slope factor, and I_0 is the technology dependent drain current when $V_{GS}=V_{TH}$ and is given by [54]

$$I_0 = \mu_0 C_{OX} \frac{W}{L}(n-1)\cdot V_T^2 \tag{5.11}$$

Substituting (5.11) in (5.10) and equating for the device ratio gives

$$\frac{(W/L)_P}{(W/L)_N} = \frac{\mu_n}{\mu_p} \cdot \frac{e^{((V_{DD}/2 - V_{TH,N})/nV_T)}}{e^{((V_{DD}/2 - |V_{TH,P}|)/nV_T)}} \tag{5.12}$$

For the 130-nm process used here, the subthreshold slope of 82 mV/decade [55]. Substituting the nominal values of mobility μ, V_{TH}, and V_{DD} of 100mV in (5.12) results in an optimal device ratio of 3.4 to obtain a switching threshold of $V_{DD}/2$.

Equation (5.12) illustrates the exponential dependence of the PMOS-NMOS sizing ratio on the power supply and threshold voltages. Further, changes in the device mobility and V_{TH} values with process variations also affect the optimal device ratio. Hence, to ensure reliable operation at low voltages, the RO was simulated across process corners to determine the optimal device sizing for this application. The startup voltage of the RO is defined as the supply voltage at which the RO's output swing is at least 10% to 90% of the supply voltage. Figure 5.11 shows the RO's startup voltage as a function of device sizing for the nominal process corner. For large device ratios, the size of PMOS can get large such that the PMOS leakage current becomes comparable to the drain current of NMOS and result in weak pull-down i.e. higher than 10% of V_{DD}. So, there is an increase in the minimum required V_{DD} to establish output swing of less 10% of V_{DD}. Similarly, for small PMOS sizes, the pull-up network is weak such that the output cannot

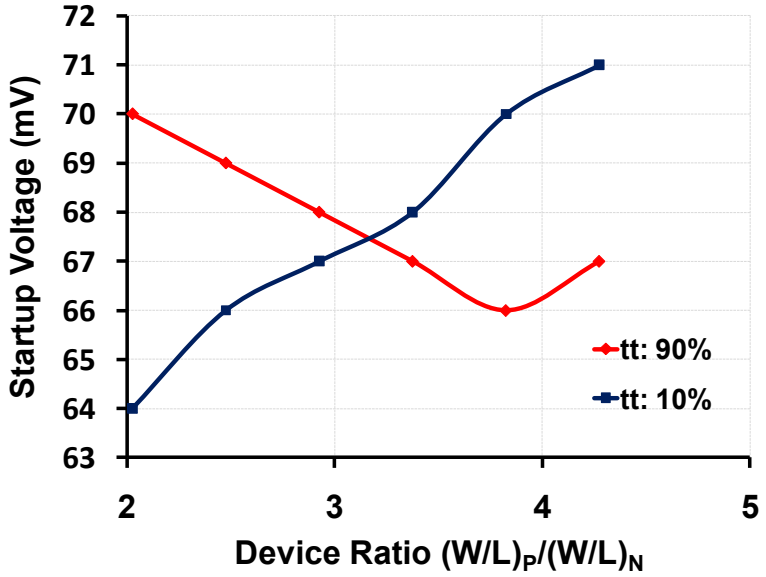


Figure 5.11 RO's startup voltage across device ratio for typical process corner

reach 90% of V_{DD} and thereby increases the minimum V_{DD}. The inequality in the minimum V_{DD} for 10% and 90% implies that the current in the inverter is not matched and so the switching threshold is not centered at *mid*-V_{DD}. The device ratio of about 3.2 which ensures equal minimum V_{DD} presents the best possible device ratio and also closely matches with the hand calculated value of 3.4 from (5.12).

The worst case startup scenario is represented by the *fast-slow* (*fs*) and *slow-fast* (*sf*) process corners. Figure 5.12 present the corresponding plots of RO's startup voltage for the worst-case process corners. As expected, the *fast-slow* case, which represents a strong PMOS device and a weak NMOS, requires larger V_{DD} to provide output low swing of less than 10%·V_{DD}. Similarly, the *slow-fast* corner representing weak PMOS with strong NMOS, needs larger V_{DD} to attain a maximum output voltage of at least 90%·V_{DD}. Similar to the nominal corner, the device ratio of close to 3.2 presents the optimal size for low startup voltage. In the final design, the smallest possible device ratio of 3 which guarantees a low voltage startup voltage across all corners was chosen. The decision to use the small device ratio helps to improve the energy efficiency by minimizing the switching loss and also facilitates high frequency clock output.

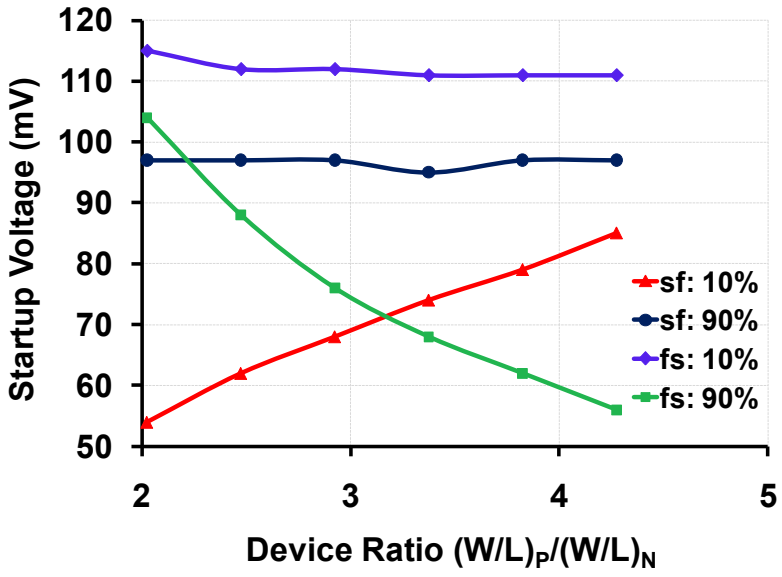


Figure 5.12 RO's voltage across device ratio for worst-case process corners

Load capacitance based delay network has been added at the output of each inverter stage in the RO so as to provide an option to control the oscillator's output frequency. The delay network is controlled by a 3-to-8 bit decoder that connects different set of delay capacitors to obtain the required output frequency with an approximate 50% duty cycle. Figure 5.13 shows the implemented RO along with the device sizing.

5.3.4 Design of Non-Overlapping (NOV) phase generator

The non-overlapping clock phases that control the charge pump are generated from the ring oscillator's output using a conventional phase generator circuit [29]. The schematic of the NOV phase generator which is implemented with NAND gates and delay cells is shown in Figure 5.14. Similar to the ring oscillator design, the CMOS device ratios are adjusted to ensure low-voltage operation. For instance, the NAND device sizing is different from the inverter in order to compensate for the loss in the NMOS drive strength due to stacked devices in the NAND topology. An added advantage of stacked devices is the reduction in leakage current due to increase in V_{TH} as a result of body effect. The delay cell used for the non-overlapping phase generator incorporates a 64fF vertical natural capacitor (vncap) formed between metal1 and metal 3 to generate dead-time of about 0.67 μs at 100 mV input voltage, and 0.36 μs at 125 mV of power supply voltage .

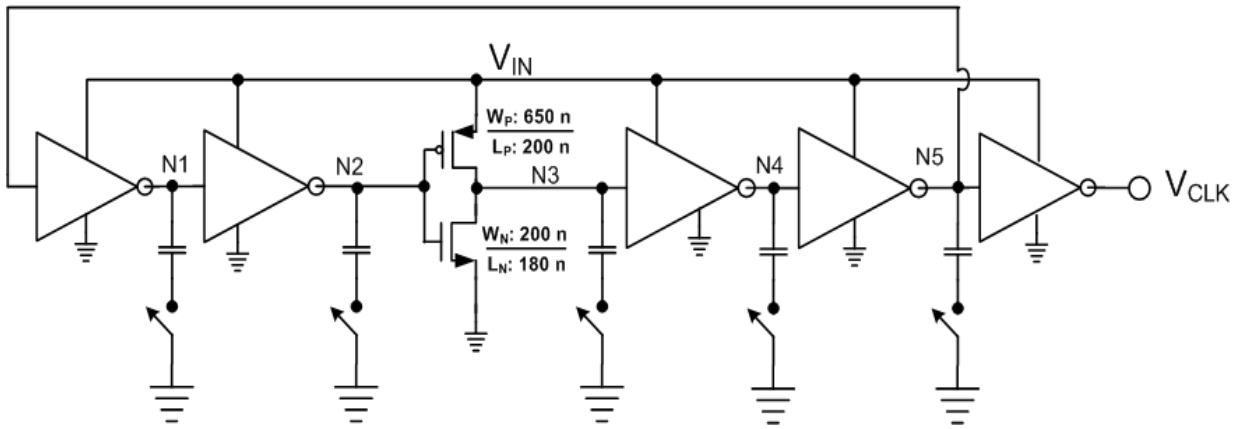


Figure 5.13 Schematic of the 5-stage ring oscillator

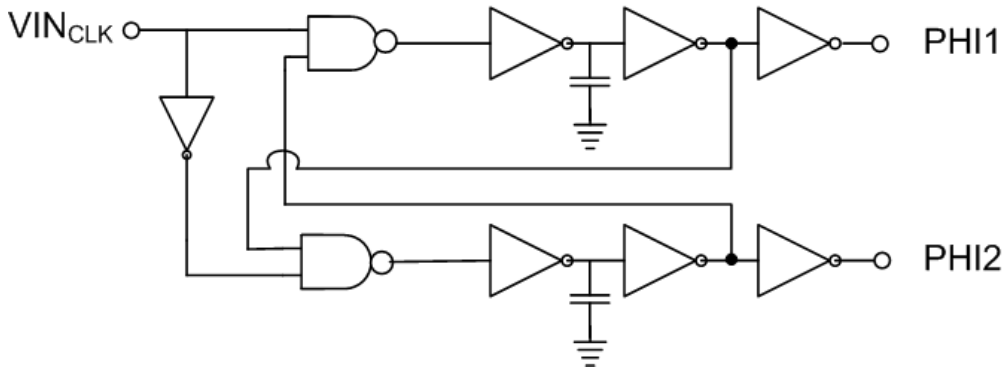


Figure 5.14 Schematic of the non-overlapping phase generator

5.3.5 Design of the Proposed Linear Charge Pump (LCP)

As discussed in Section 5.3.2, a linear charge pump topology offers the best choice for ultra-low-voltage DC-DC conversion with adaptable conversion gains. This work exploits a cross-coupled LCP topology that comprises of two similar charge pump branches that operate at complementary clock phases to provide the output voltage. The cross-coupled stages reduce the output ripple voltage and thereby allow lower frequency operation to achieve the same performance. Further, the reduction in output ripple voltage implies lower charge redistribution loss between the charge pump capacitors. Once the RO's clock is available, the charge transfer switches (CTS) between each pumping stage and their gate control (GC) circuits determine the actual startup voltage of the charge pump. Hence the design, implementation, and control of the CTS play a critical role in the performance of the CP. This section describes the design and implementation of the various CP components.

5.3.5.1 Charge transfer switches

The requirement to design for low-voltage operation determines the type of CTS used for each CP stage. When compared to PMOS, the NMOS switches offer smaller device size, thus smaller parasitic capacitance, for the same *ON* resistance of the switch. However, NMOS devices suffer increase in threshold voltage with increase in the source-to-body voltage due to body-effect. This results in higher CTS threshold along the CP stages. For low-voltage operation, this increase in CTS threshold would severely constrain the minimum achievable startup voltage and CP efficiency. The 130-nm process used in this work offers triple-well NMOS devices but the

choice of PMOS switches presents lower parasitic capacitances at the pumping nodes which is crucial for efficient voltage boosting along the CP stages.

The ease of gate control generation is another factor to be considered in the CTS design. A CTS implemented with PMOS would need a gate voltage that is lower than its source and drain voltage to allow charge transfer when the switch is *ON*. During the *OFF* state, the gate voltage could be equal to the source i.e. $V_{GS}=0$ or a higher gate voltage could also be derived from subsequent stages. Whereas the NMOS switch requires a higher gate voltage than its source and drain to remain *ON* and a lower gate voltage for the *OFF* state. Obtaining a higher voltage is essential for the charge transfer in NMOS switches and this necessitates boot-strapped capacitor gate control especially for the last couple of stages in the CP.

As illustrated in Figure 5.1(c), bootstrapped switch control comprises of a small bootstrap capacitor (C_B) that is charged to the steady state voltage of the previous CP stage. Driving the bottom plate of C_B with a clock generates the required gate control for the CTS. The disadvantage of adopting a bootstrap switch control is the need for additional clock phases to control the bootstrap capacitor. Furthermore, the operational losses incurred to charge and discharge the C_B and the associated switches reduce the efficiency on the CP. Hence, this work employs PMOS switches for the transfer of charge along the CP stages.

Figure 5.15 presents a simplified schematic of the proposed 3-stage CP along with the CTS and the boosted node voltages. The first stage of the CP uses NMOS charge transfer switches (CTS) for ease of switch control generation and also to take advantage of the lower NMOS threshold voltage. The charge-transfer switches from the second stage onwards are implemented using PMOS transistors to avoid increase in device threshold voltage due to body effect. As illustrated in Figure 5.15, the switches were sized to keep the conduction loss due to finite R_{ON} and CTS gate-drive's switching losses as low as possible for the required load drive capability. The simulated ON resistance of the CTS is 25 KΩ at 125 mV input. As the node voltages on each side of the charge-transfer switches change with the CP's phase of operation and with the CP stage, the gate control (GC) voltages that control the CTS operation need to be generated locally for each stage. Further, as the required GC voltages are not directly available

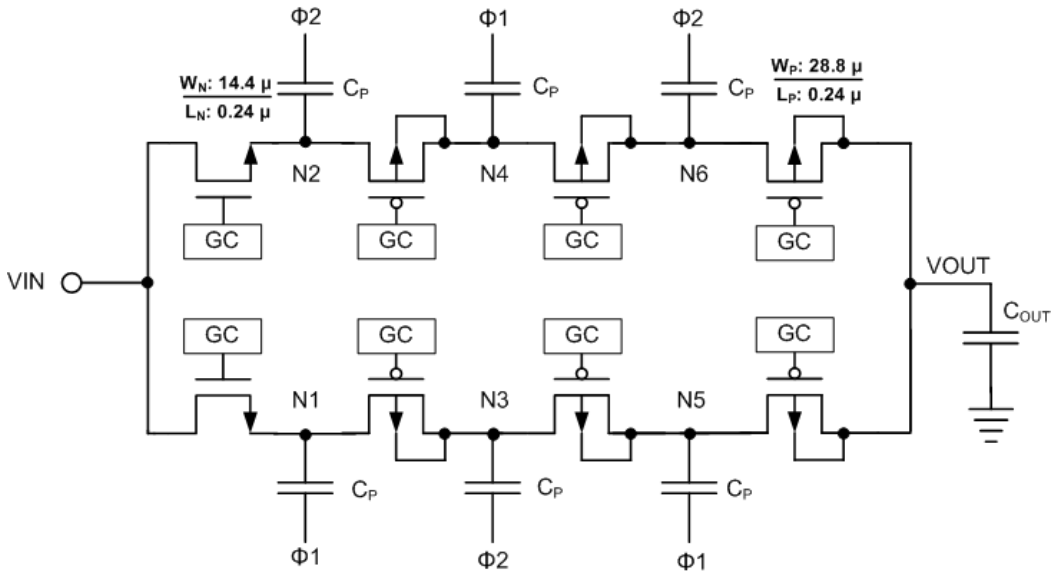


Figure 5.15 Simplified schematic of the proposed LCP

from the pumping nodes, an interface that generates the appropriate control voltages is necessary.

5.3.5.2 Gate Control (GC) Generation

The CTS gate control generation is one of the critical components in the CP design as it establishes and controls the transfer of power from the input to the CP's output. The challenge with GC generation is the need to generate precise voltage levels and relative phase relationship between the GC signals of the CP. To ensure effective charge transfer, the GC signals must provide gate-to-source bias voltages that clearly define the *ON* and *OFF* states of the CTS. Further, the CTS' node voltages increase with the CP stage, thus necessitating the generated gate control voltages to scale along the CP stages. Furthermore, the relative phase difference between the adjacent CP stages determines the amount of reverse current loss. Thus, the GC generation circuitry greatly impacts the pumping efficiency and the achievable gain of the CP.

As two CTS are connected to either side of the pumping capacitors in each stage, a break-before-make action is commonly employed in these switches to avoid reverse current flow.

Numerous GC implementation techniques that improve the efficiency of CPs, have been studied and demonstrated in literature [44]-[50], [56]-[59]. The most commonly adopted methods generate the required control signals using the relative voltage difference between the different CP stages. Bootstrapped gate control methodology uses the voltage from the previous stage [49] while level-shifter based techniques [56], [58], [59] use voltages from both the previous and subsequent stages of the CP. In this work, the gate control signals are derived from the complementary cross-coupled stages using level-shifters. Some of the gate control strategies for efficient charge pumps from [59] are adapted to this low-voltage design. Specifically, the level-shifter based technique has been optimized to ensure operation at low voltages.

Figure 5.16 presents the inverter based CMOS level-shifter (LS) that is employed in this CP. Level-shifting of the CP's clock phases (Φ) is achieved by varying the V_{DD}, V_{SS} and V_G voltages in order to obtain the required signal levels that control CTS operation. The CMOS LS devices are sized for low voltage operation as discussed in section 5.3.3.1. Further, low-threshold voltage devices with a threshold of 230 mV have been employed for CTS and the GC circuits.

Figure 5.17 presents the proposed 3-stage CP along with the level-shifter circuits for GC generation. The top CP branch shows the required gate control voltage levels for the CTS, while the bottom CP branch illustrates the LSs employed to obtain the GC signals. The CTS in the top CP branch employ level-shifters similar to those in the bottom branch. The node voltages of the different CP stages in the top and the bottom branches are enumerated in the figure as (V_X, V_Y)

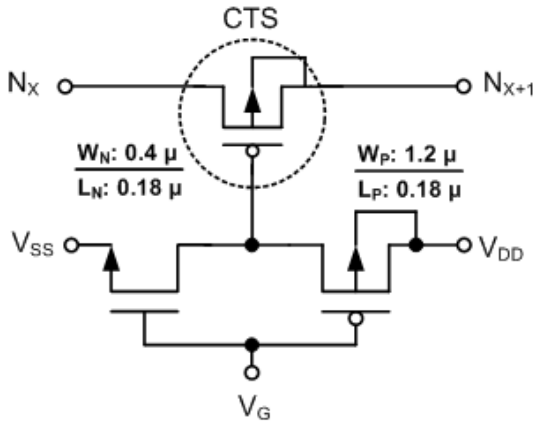
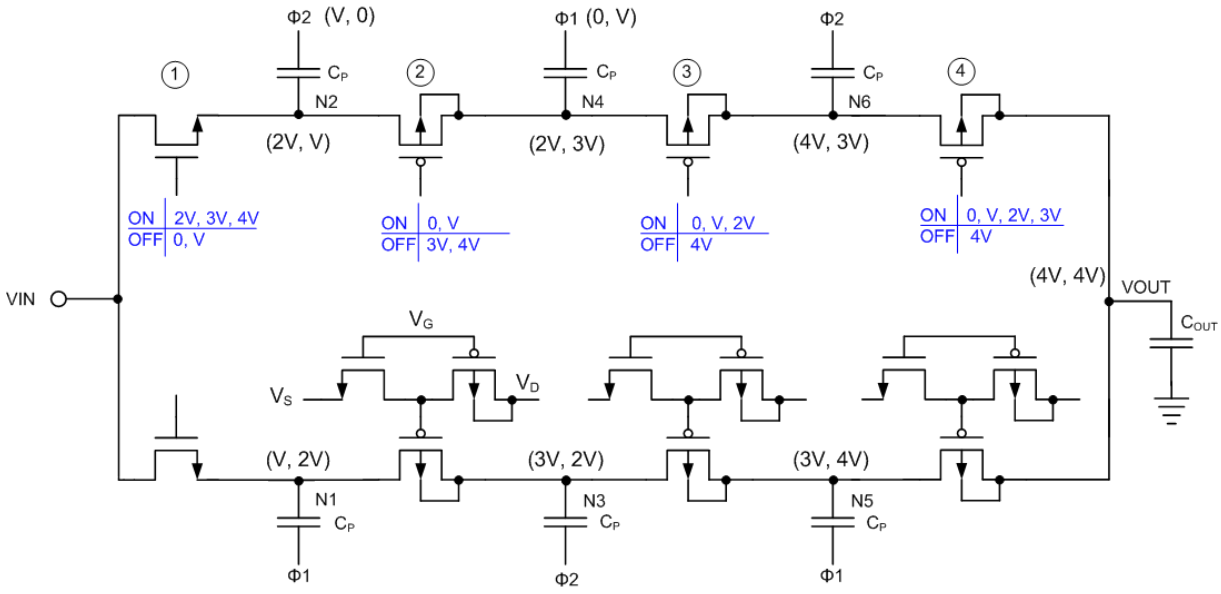


Figure 5.16 Schematic of the level-shifter used to generate the CTS control in the proposed LCP



CTS 2	V_G at CTS 2	V_G (LS)	V_S (LS)	V_D (LS)
ON	0	V, 2V, 3V, 4V	0	$\leq V_G$
ON	V	2V, 3V, 4V	V	$\leq V_G$
OFF	3V	0, V, 2V	$\geq V_G$	3V
OFF	4V	0, V, 2V, 3V	$\geq V_G$	4V

CTS 3	V_G at CTS 3	V_G (LS)	V_S (LS)	V_D (LS)
ON	0	V, 2V, 3V, 4V	0	$\leq V_G$
ON	V	2V, 3V, 4V	V	$\leq V_G$
ON	2V	3V, 4V	2V	$\leq V_G$
OFF	4V	0, V, 2V, 3V	$\geq V_G$	4V

CTS 4	V_G at CTS 4	V_G (LS)	V_S (LS)	V_D (LS)
ON	0	V, 2V, 3V, 4V	0	$\leq V_G$
ON	V	2V, 3V, 4V	V	$\leq V_G$
ON	2V	3V, 4V	2V	$\leq V_G$
ON	3V	4V	3V	$\leq V_G$
OFF	4V	0, V, 2V, 3V	$\geq V_G$	4V

Figure 5.17 Simplified schematic of the proposed LCP along with the GC generation

where, V_X corresponds to the CP phase when Φ_1 is at "0" (LOW) and Φ_2 is at "1" (HIGH) , while V_Y corresponds to the complementary state with Φ_1 HIGH and Φ_2 LOW. In this design, the level-shifter's V_{DD}, V_{SS} and input voltages are chosen from the existing CP nodes to enable self-sustained voltage boosting by the CP.

The first stage of the CP uses NMOS switches to benefit from lower V_{TH} than PMOS switches. This necessitates a voltage higher than V_{IN} to turn *ON* the NMOS switch. With the complementary cross-coupled topology, $2V_{IN}$ voltage is readily available at the cross-coupled node, thereby eliminating the need for extra circuitry in GC generation. Hence, the first CP stage utilizes a conventional voltage-doubler topology as published in [60]. The CTS switches from the second stage onwards use PMOS switches and require individual GC generation to guarantee good pumping efficiency. As PMOS switches do not need a control voltage that is higher than that CP node, the GC voltage can be easily generated using the available CP node voltages. The tables included in Figure 5.17 present the voltages required at the level-shifter nodes in order to generate the appropriate GC signal levels for the switches.

Large voltage swings on GC signals would result in strong ON and OFF switch states but, it would also deplete charge from the pumping capacitors and thus reduce the CP's maximum achievable V_{OUT}. Hence, in order to keep the switching losses due to GC generation at a minimum, the level-shifters are biased with a maximum of $2V_{IN}$ voltage swing (V_{DD} to V_{SS}). Based on this design condition, the permissible voltage levels that are employed in the CTS control are highlighted in the table included in Figure 5.17. From the Figure 5.17, it can be inferred that the level-shifter's ground node can be connected to the complementary branch's CP node of previous stage, the V_{DD} can be connected to the current branch's next stage, while the gate voltage is controlled by the same branch's previous stage. The effect of the phase relationships between these node transitions determine the reverse current loss and will be discussed in detail in the next section.

The gate control voltage for the *i*-th stage PMOS CTS is designed to swing from $(i-1)\cdot V_{IN}$ to $(i+1)\cdot V_{IN}$ (i.e. $2V_{DD}$) in two steps in order to control the transfer of charge to the subsequent stage. During startup, the voltage difference between the adjacent stages is much smaller than V_{IN}. This results in deep subthreshold region of operation until the CP reaches a steady state

operation with a $V_{IN} - \Delta V$ increase in voltage at each CP stage. Hence, it is vital that the level shifters are sized to operate at very low voltages.

The full schematic of the proposed 3-stage cross-coupled LCP is illustrated in Figure 5.18. The proposed CP accomplishes linear voltage boosting of V_{IN} by utilizing just two NOV clock phase signals that are generated by the phase generator. The NMOS only and PMOS only charge transfer switches reduce the switching losses, and are optimized for low voltage startup and operation. The generation of GC using internal CP nodes facilitates extension to any number of CP stages so as to meet the gain requirements of the target application. In the Figure 5.18, Φ_1 and Φ_2 represent two non-overlapping clock phases that are distributed along the CP stages such that, two adjacent CP stages are controlled by NOV clocks in order to mitigate losses during switching transients. Once the CP reaches steady-state operation, the voltage at the output of the N-th stage is approximately $(N+1)V_{IN} - \Delta V$ where ΔV represents losses due to voltage drop across the switches due to finite "on" resistance, parasitic and leakage currents. The dotted lines for the ground connection in 2nd stage's level-shifter represent an alternate connection.

As discussed in 5.2.3, similar LCP topologies have been utilized for low-voltage operation as in [45] and [46]. This work reduces the considerable reverse current loss inherent in [45], [46] and also eliminates the need for two series switches for each charge transfer stage as in [45]. Low-threshold voltage devices with a threshold of about 230 mV have been employed for the entire CP design including the charge-transfer switches (CTS) and the control generation.

5.3.5.2.1 Design for low-voltage operation

To ensure low-voltage operation, the proposed LCP topology has been designed to minimize the losses associated with the CTS. Furthermore, LVT devices have been used for all the CT switches to facilitate low-voltage operation and to offer lower resistance in the charge transfer path.

To investigate the efficiency of the proposed CP, a detailed study of the various operational losses is required. As discussed in Section 5.2.1.4, the power losses associated with LCP topologies include the conduction loss, redistribution loss, reversion loss, and switching loss. Conduction loss is due to the finite "on" resistance of the CTS, while redistribution loss is

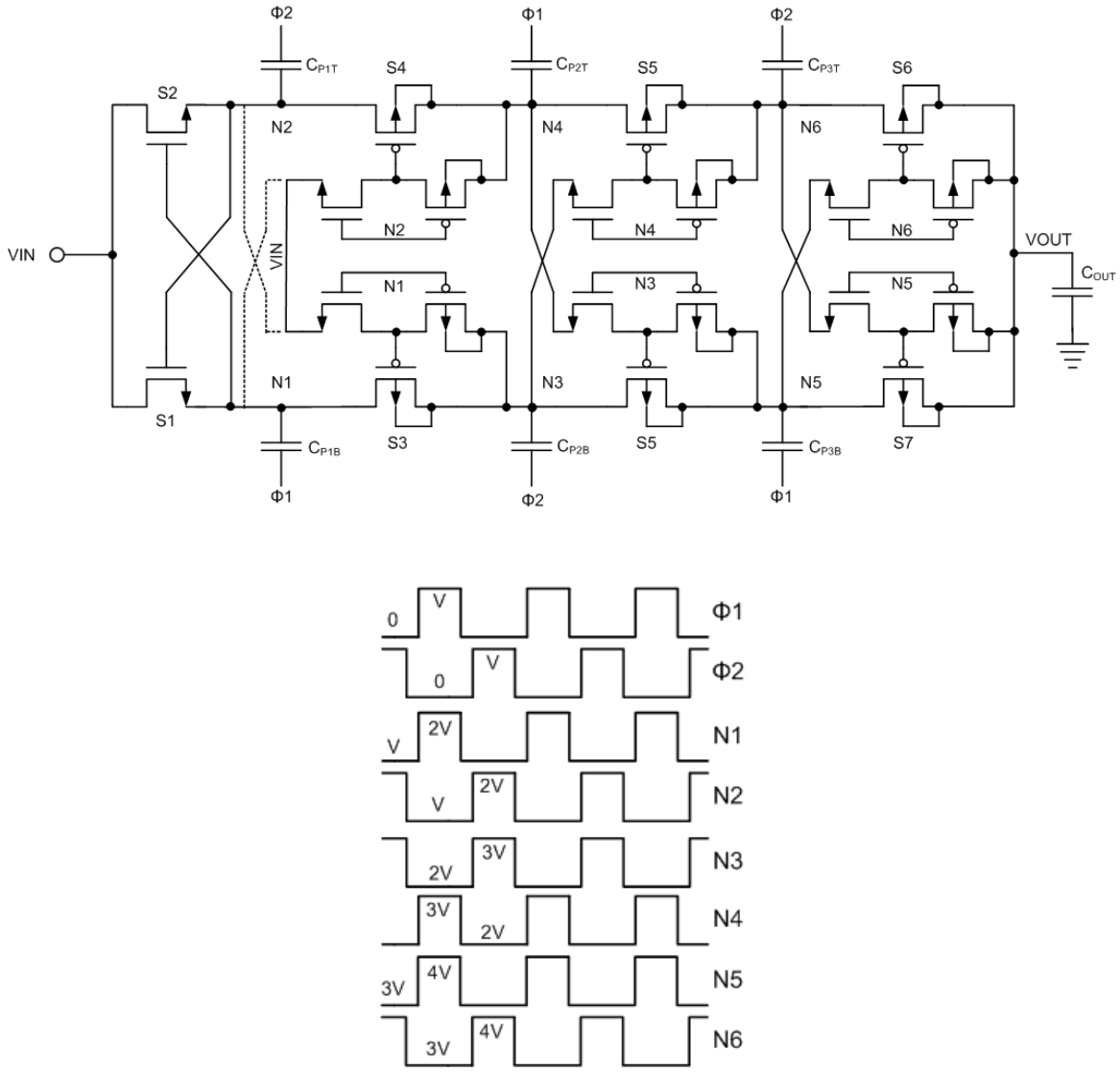


Figure 5.18 Schematic of the proposed self-starting linear charge pump

caused by the transfer of charge along the CP capacitors. Reversion loss occurs when a reverse current flows from the later stages to the previous stages in the CP. The current required to charge and discharge the bottom plate of CP capacitors and the gate-source capacitance of the switches contribute to the switching loss. With optimal sizing of the switches, the total conduction and switching losses have been reduced, while the redistribution loss is lowered with low output-ripple voltage [60].

Influence of GC Signals on Reverse Current Loss

The relative phase-transitions of gate-control signals at adjacent CP stages determine the reversion loss. Employing NOV clock phases for controlling adjacent stages is the most effective methodology to minimize undesirable current paths in a single-branch LCP. However, utilizing CP node voltages from cross-coupled nodes introduces complexity in the GC generation and entails careful design. With the aid of the CP's timing diagram derived from Figure 5.18, the different reverse current components will be studied. While the following discussion is based on the CP's bottom branch operation, the symmetrical topology of this charge pump makes this pertinent to the top branch as well.

Charge transfer from V_{IN} to Stage 1 of the Charge Pump

The designs in [45], [46] employ complementary clock phases to control adjacent CP stages. To investigate the possibility of reverse currents in complementary phase control, consider the first CP stage in Figure 5.19, which is similar to the designs in [45], [46]. If $\Phi 1$ and $\Phi 2$ were complementary signals, during a clock transition, when the voltage at node N1 transitions from V_{IN} to $2V_{IN}$, the node N2 would also transition from $2V_{IN}$ to V_{IN}. During this transition, the NMOS switch connecting to N1 is not completely switched OFF and provides a path for current to flow from N1 back to source V_{IN}. This reverse current reduces the effective charge transferred to the next CP stage and also limits the low-voltage operation. Hence, NOV clock phases have been employed in this proposed LCP.

With NOV clocks, when the node N1 transitions from V_{IN} to $2V_{IN}$, the node N2 remains at V_{IN} and thus the NMOS switch (S1) remains completely OFF. Switch S2 is turned ON with the

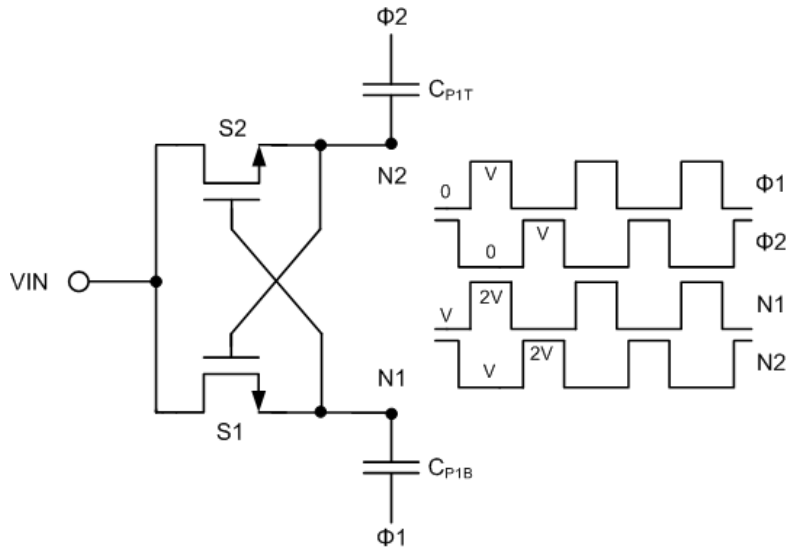


Figure 5.19 Schematic illustrating control signals and charge transfer in the first stage of LCP

increase in V_{GS} from 0 to V_{IN} and results in charge transfer from input to CP_{1T}. Similarly, the switch S2 which is controlled by N1 (*Φ1)* remains completely switched OFF during N2's (*Φ2*'s) rising edge transition while, S1 is turned ON. Thus, NOV clock control eliminates reverse current paths from the first stage of the CP to the input source.

Charge transfer from Stage 1 to Stage 2 of the Charge Pump

The gate-control generation from the second stage onwards uses signals derived from both *Φ1* and *Φ2* and therefore NOV switch control can be realized. To study the GC operation and to examine the existence of leakage current paths in the CP's second stage, let us refer to Figure 5.20 which illustrates the transient node voltages at N1, N2, G3, and N3. The switch S3 is ON during the charging phase (*Φ1 HIGH*) which results in charge transfer from the first stage pumping capacitor (CP_{1B}) to the second stage capacitor (CP_{2B}) in order to replenish the charge lost in CP_{2B}. In the discharge phase (*Φ2 HIGH*), S3 is switched OFF and node N3 is boosted from $2V_{IN}$ to $3V_{IN}$ to transfer charge (i.e. discharge CP_{2B}) to the next stage, while CP_{1B} is charged to V_{IN}.

As shown in Figure 5.20, the gate control voltage (G3) swings from V_{IN} to $3V_{IN}$ to dictate

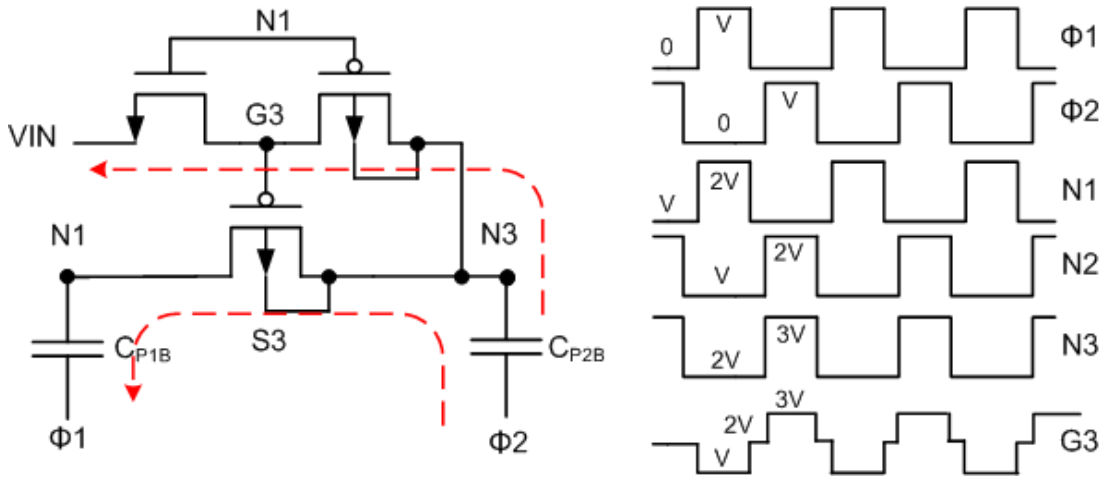


Figure 5.20 Schematic illustrating control signals and charge transfer in the second stage of LCP

the switch's ON and OFF states, respectively. During the dead-time between the charge and discharge phases, G3 is maintained at $2V_{IN}$, with a V_{GS} of 0 V to ensure an OFF state. A reverse current path from CP_{2B} to CP_{1B} is possible only when the switch S3 conducts when the node voltage at N3 is higher than that at N1. This is possible when N3 transitions from voltage of $3V_{IN}$ to $2V_{IN}$, while N1 is at V_{IN}, or, when N1 changes from $2V_{IN}$ to V_{IN} when N3 is at $2V_{IN}$. Since the CTS control signal G3 is in-phase with $\overline{\phi 1}$ and node voltage at N3 is controlled by NOV phase *Φ2*, switch S3 is never ON or changing state when N3 transitions. However, after the charge phase, when N1 transitions from $2V_{IN}$ to V_{IN}, S3 is being switched OFF with V_{GS} at 0 V while N3 (*Φ2)* does not change. With the level-shifter's threshold set at $V_{DD}/2$, node N1 has to change to $1.5 \cdot V_{IN}$ before the CTS's gate voltage is pulled up to $2V_{IN}$ to switch S3 OFF. So, there exists a possibility of small amount of reverse current flow from CP_{2B} to CP_{1B} during this transition. Note that during the transition of N3 from $2V_{IN}$ to $3V_{IN}$, the CTS gate voltage follows N3 and so only a small insignificant amount of charge is used up to ensure S3 remains OFF during the discharge phase.

Since the level-shifter (LS) is biased from the charge pump nodes, the effect of short-circuit currents during switching transients need to be analyzed. Short-circuit current can flow from V_{DD} to V_{SS} when the LS's output changes, or when the rail voltages change with CP's phase of operation. During one full cycle of operation, the LS's output voltage transitions from V_{IN} through $2V_{IN}$ to $3V_{IN}$. The input (N1) transitions between V_{IN} and $2V_{IN}$ node voltages cause one

of the LS devices to switch *OFF*, while the other is being switched *ON*. This transition could result in a short-through or short-circuit current to flow from N3 (V_{DD}) to N2 (V_{SS}) for the brief period of time when both the LS devices are ON. However, during the transition from $2V_{IN}$ to $3V_{IN}$, the pull-up device (PMOS) remains ON and follows the change in its source voltage (N3) and so short-circuit current cannot flow in this case.

Charge transfer from Stage 2 to Stage 3 of the Charge Pump

As illustrated in Figure 5.21, the gate-control generation for the CP's third stage is similar to that of second stage. The CTS switch S5 conducts in-phase with $\overline{\phi 2}$ to charge CP_{3B} to $3V_{IN}$. Similar to the second stage, the switching transients in the level-shifter could result in short-circuit current from N5 (V_{DD}) to N4 (V_{SS}) of the complementary CP branch. Also, there exists a possibility of reverse current flow from N5 to N3 when switch S5 is being switched OFF after the charging phase.

Charge Transfer from Stage 3 to Load Capacitor of Charge Pump

The last stage's CTS control signals of G7 and G8 differ from those of previous stages due to the relatively constant V_{OUT} that is used to bias the LS's V_{DD} rail. Hence, as shown in Figure 5.22, the G7 (G8) voltage swings from $3V_{IN}$ to $4V_{IN}$ to control the S7's (S8's) ON and OFF states respectively. Similar to the previous discussion, reverse current components exist

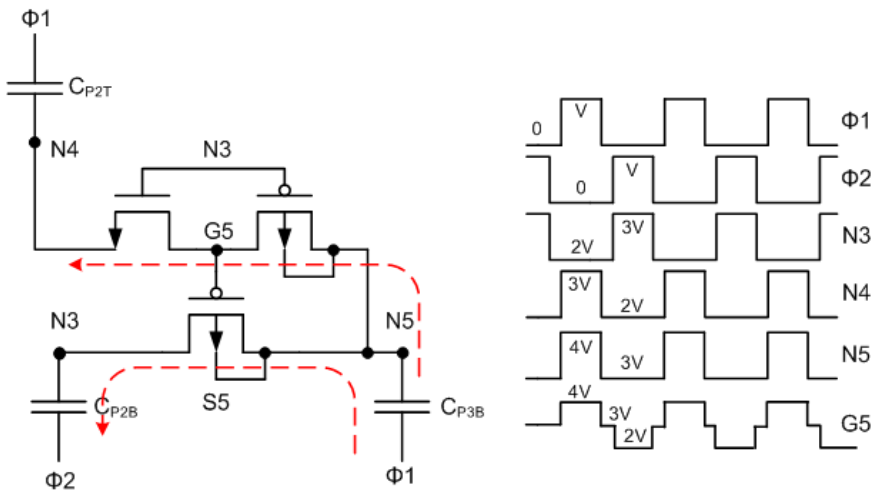


Figure 5.21 Schematic illustrating control signals and charge transfer in the third stage of LCP

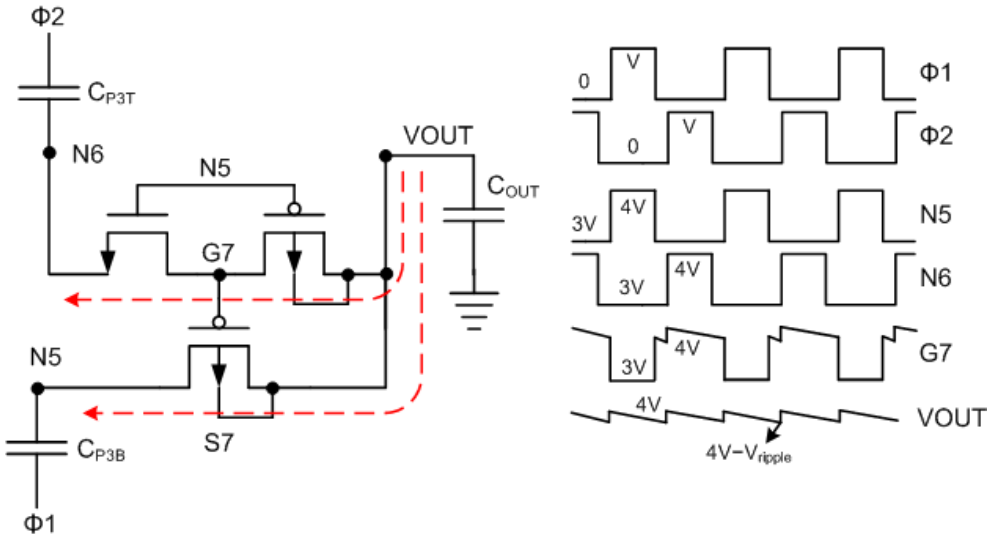


Figure 5.22 Schematic illustrating control signals and charge transfer in the last stage of LCP

during the switching OFF transition of CTS which could degrade the charge pumping efficiency in this stage.

In summary, there exists a possibility for reverse current flow during switching transients from one stage to its previous stage along the same branch and to the complementary branch. However, even at worst case operation with slow transitions, since the CP stages are controlled by NOV clock phases, a reverse current path cannot exist along all the CP stages. Hence, reverse current losses result in a small reduction in the achievable efficiency in this topology as compared to [45] and [46].

5.3.5.3 Improved Version of the Proposed Linear Charge Pump – Version 2

The proposed LCP introduced in the previous section, henceforth referred to as LCP V1, demonstrates lower losses when compared to existing low-voltage LCP designs of [45], [46] by eliminating reverse current paths along the CP stages. However, the existence of short-through or short-circuit current paths could result in reverse current to the previous CP stage. Although this reverse current flows only to the previous stage and never from the load capacitor to the CP input, the loss of charge would result in lowered CP output voltage and increased startup voltage in the CP.

Efforts were taken to mitigate this reversion loss and to improve the startup capability of the CP. Figure 5.23 presents the improved version of the proposed LCP that will be referred to as LCP V2 hereafter. The LCP V2 topology comprises of the same CTS and GC implementations as in LCP V1. The difference lies in the method of controlling the adjacent stages along the CP branches. In contrast to LCP V1 where NOV signals were employed across all adjacent stages, in the LCP V2, complementary clock signals control adjacent CP stages in a branch, while the corresponding stage in cross-coupled branch is managed by NOV clock signals. Since the control signals to the level-shifter-based GC generation define the charge transfer between the CP stages, NOV control can still be realized in the LCP V2. The improvement in CP efficiency is accomplished primarily by reducing the reverse current losses between adjacent CP stages.

5.3.5.3.1 Low-voltage operation in LCP V2

To guarantee low voltage operation, the design methodologies described in Section 5.3.5.2.1 were followed in this design as well to minimize the losses due to switching, conduction, and charge redistribution components. This section examines the CTS control logic and the associated reverse current paths in the CP topology. Figure 5.23 illustrates the timing sequence of the control signals and the node voltages in the LCP V2 design.

Charge Transfer from V_{IN} to Stage 1 of the Charge Pump

The control signals in the first stage of the CP is the same in both the CP versions, so, as demonstrated in the previous discussion (see Figure 5.19 and Figure 5.23), the NOV clock control eliminates reverse current paths from the first stage of the CP to the input source. Furthermore, to aid in the CP start-up, a dynamic-threshold MOS (DTMOS) diode is included in parallel to the CTS in the first stage. During startup, the subthreshold current flowing through the diode charges the CP capacitors in the first stage. Once the NMOS CTS transistors have enough gate-source voltage, the diode is bypassed from the CP action. Thus, the diodes provide assistance for very-low voltage operation. However, the presence of the DTMOS diode adds to the parasitic capacitance at node N1 and thereby slightly reducing the efficiency of this stage.

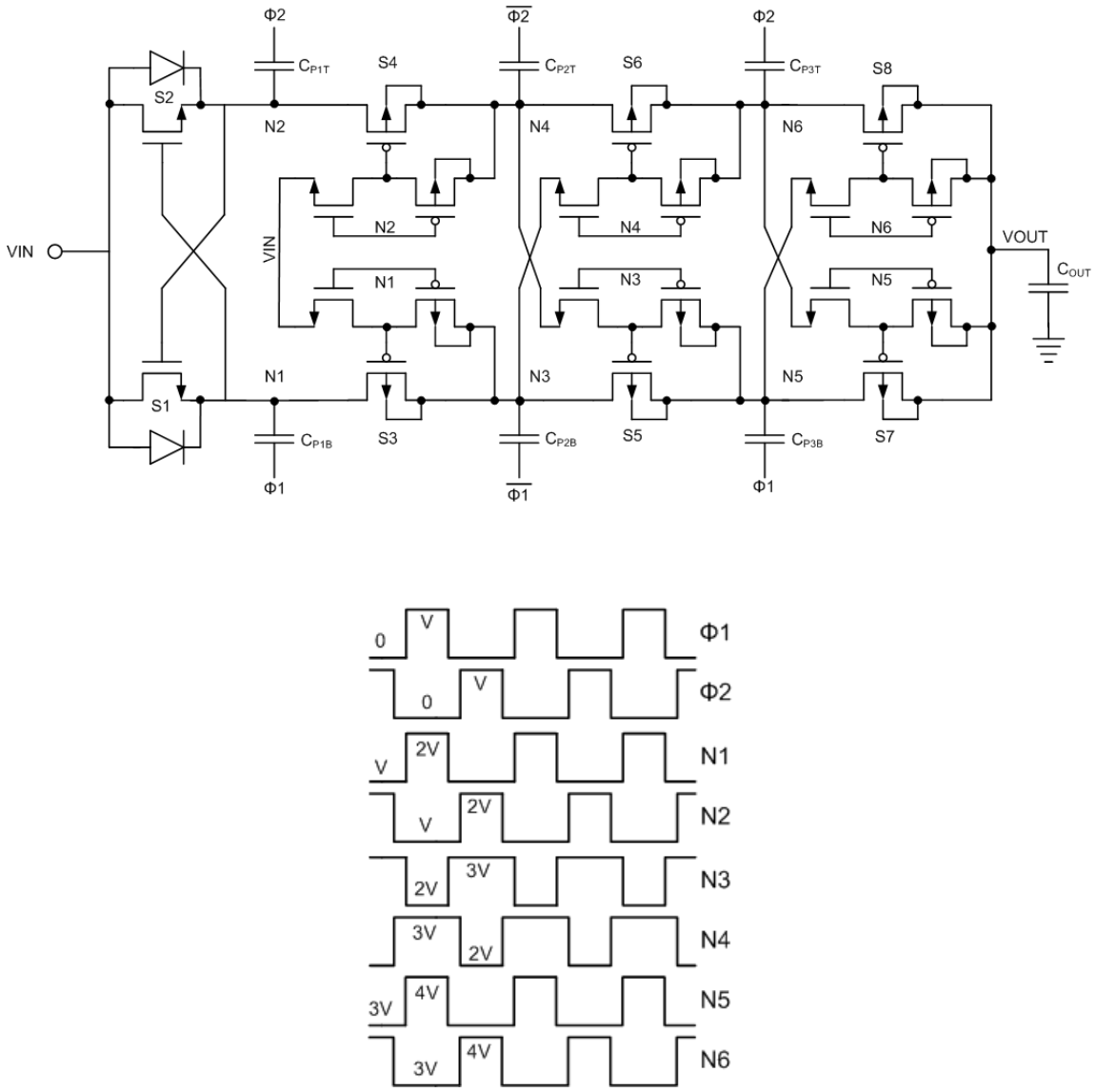


Figure 5.23 Schematic of the proposed improved self-starting charge pump - version 2

Charge Transfer from Stage 1 to Stage 2 of the Charge Pump

The gate-control generation for the lower CP branch's second stage is derived from *Φ1,* $\overline{\phi 1}$ and *Φ2*. Figure 5.24 presents the transient node voltages at N1, N2, G3, and N3. The switch S3 is ON during the charging phase (*Φ1 HIGH*) to replenish the charge lost in the second stage capacitor, CP_{2B}. In the discharge phase ($\overline{\phi 1}$ *HIGH*), S3 is switched OFF and node N3 is pumped from $2V_{IN}$ to $3V_{IN}$ to transfer charge to CP_{B3}, while CP_{1B} is charged to V_{IN}.

As shown in the Figure 5.24, the gate control (G3) signal's transition between V_{IN} and $3V_{IN}$ is dictated by the node voltage at N1 (*Φ1)*. So, the level-shifter's ground rail connection to NOV phase at N2 does not influence the CTS's (G3) control. Hence, the ground connection can be safely tied to V_{IN} and thereby avoid adding parasitic capacitance at N2. Since the source and drain terminals of the CTS are controlled by complementary signals, and the gate G3 is also synchronized with *Φ1*, reverse current can flow from CP_{2B} to CP_{1B}. When CTS S3 is being switched ON, N1 increases from V_{IN} to $2V_{IN}$, N3 decreases from $3V_{IN}$ to $2V_{IN}$, while G3 voltage decreases from $3V_{IN}$ to V_{IN}. For the switch S3 to conduct, the gate voltage (G3) needs to be lower than the source (N3) and since the level-shifter's switching threshold is set at mid-rail, G3 starts to decrease from $3V_{IN}$ only when N1 and N3 have completed more than 50% of their respective transitions. Further, since the level-shifter's positive rail voltage (i.e. N3) decreases while the

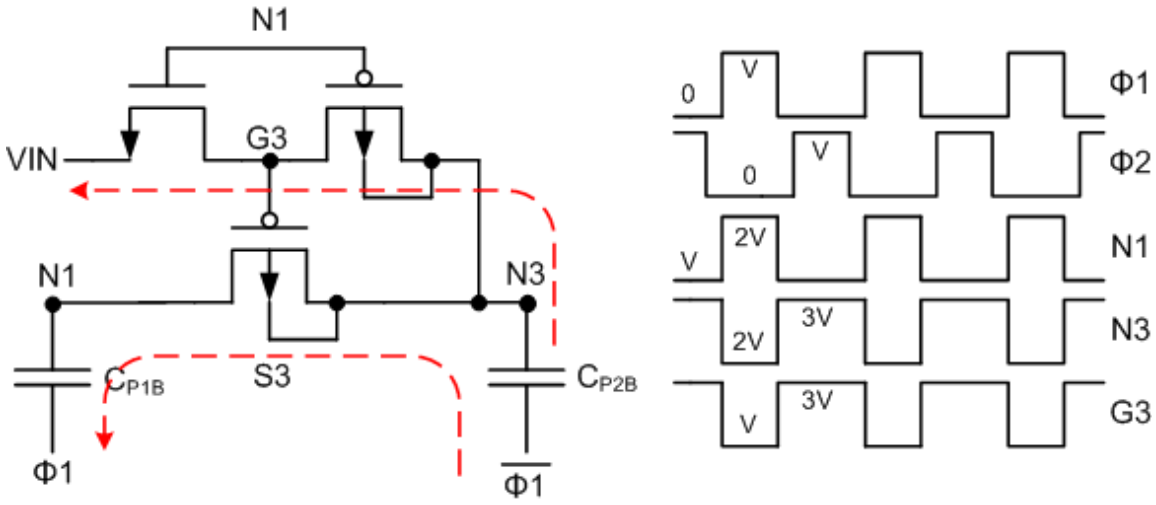


Figure 5.24 Schematic illustrating control signals and charge transfer in the second stage of LCP V2

input voltage (N1) increases, the LS's PMOS device is switched OFF at a faster rate and minimizes the short-circuit component of reverse current from CP_{2B} to V_{IN}. Hence, during the CTS S3's ON transition, reverse current losses from CP_{2B} to CP_{1B} or V_{IN} is very small.

Consider the S3's switching OFF transition, when the node N1 decreases from $2V_{IN}$ to V_{IN}, N3 increases from $2V_{IN}$ to $3V_{IN}$, while G3 voltage increases from V_{IN} to $3V_{IN}$. When this switching transition begins, the switch is conducting and reverse current could flow from N3 to N1 until the switch is turned OFF. The transitions in the opposite direction at the level-shifter PMOS device's gate (N1) and source (N3) voltages accelerates the rise in G3 voltage to follow N3, and thus to switch OFF the CTS. Short-circuit current path from N3 to VIN is again minimized by the fast PMOS switch ON. Thus, the reverse current loss, though finite, is restricted by the fast transition to turn OFF the leakage path. It is to be emphasized here that symmetrical matched routing for the complementary signals is critical to ensure efficient operation.

Charge Transfer from Stage 2 to Stage 3 of the Charge Pump

The gate-control generation for the bottom CP branch's third stage is derived from *Φ1,* $\overline{\phi 1}$ and $\overline{\phi 2}$ signals. In this improved version of the LCP, close to ideal charge transfer can be achieved by proper NOV control of the CTS. The transient sequence of operation is illustrated in Figure 5.25. Consider the steady-state operation where, the charge in CP_{3B} is being discharged to next stage i.e. C_{OUT} (*Φ1 HIGH*), CP_{2B} is being charged to $2V_{IN}$, and the CTS (S5) is switched OFF with its V_{GS} at 0 V. The next transition is triggered by the change in *Φ1* signal to *LOW* which results in the N3 transition from $2V_{IN}$ to $3V_{IN}$ and N5 changing from $4V_{IN}$ to $3V_{IN}$ while N4 remains at $3V_{IN}$. The output of the level-shifter is at high impedance state with the charge from PMOS parasitic capacitors redistributing back to CP_{3B} and the CTS S5 remains in the OFF state. Thus, the finite reverse current component that exists in the previous stage's transition from discharge to charging phase is completely eliminated here.

After a brief dead-time period, the $\overline{\phi 2}$ goes *LOW* which lowers the level-shifter's ground rail (N4) from $3V_{IN}$ to $2V_{IN}$ and thereby switches ON the NMOS device to lower the G5 node voltage to $2V_{IN}$. Since the PMOS device in the LS remains OFF during this transition, there is no

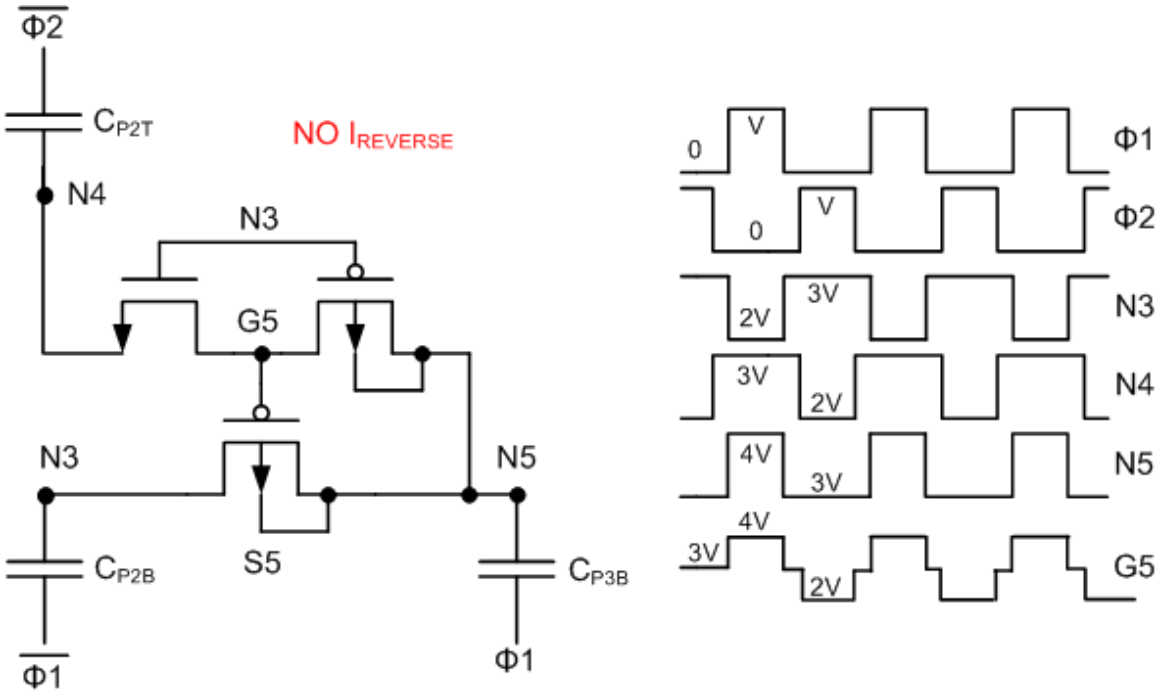


Figure 5.25 Schematic illustrating control signals and charge transfer in the 2nd-to3rd stage of LCP V2

possibility of short-circuit current from N5 to N4. Furthermore, when switch S5 turns ON, the nodes N3 and N5 are already at steady state voltages of $3V_{IN}$ and $3V_{IN}$-ΔV respectively, and thus removing any chance of reverse current flow. After this charging phase, the clock phase $\overline{\phi 2}$ goes *HIGH* which increases the level-shifter's ground rail to $3V_{IN}$ with the NMOS being switched OFF. This transition is again devoid of without any short-circuit current as the LS's PMOS remains OFF throughout this operation. Since the node voltages at N3 and N5 remain equal during S5's switching-OFF event, there is no reverse current at this stage.

The final transition to be considered is when the *Φ1* signal goes *HIGH* to initiate the discharge phase. An increase in N5 only increases the gate voltage at S5 to follow N5 with the CTS staying switched-OFF, so any reverse current flow from N5 to N3 due to the delay in G5 to keep-up with N5 is negligible. Thus, in the LCP V2, the alternate CP stages do not suffer from losses due to reverse currents.

Charge Transfer from Stage 3 to the Load Capacitance of the Charge Pump

The gate-control generation for the final set of CTS is derived from *Φ1, Φ2* and V_{OUT}. The CTS control signals of G7 and G8 are generated in a similar manner to those at G3 and G4, with the only difference being the LS's V_{DD} rail is biased by the constant V_{OUT} voltage. As presented in the LCP V1 design (see Figure 5.22), the G7 (G8) voltage swings from $3V_{IN}$ to $4V_{IN}$ to control the S7's (S8's) ON and OFF states respectively. Similar to the LCP V1 discussion, reverse current components could flow during the switching OFF transition of S7 (S8) and this could degrade the charge pumping efficiency in this stage.

In summary, the LCP V2 improves the efficiency by completely eliminating the short-through currents in the level-shifters and reverse current paths in the alternate CP stages. However, this improvement comes with a small penalty of the very small amount of reverse current between every other alternate CP stages. It is emphasized that every small enhancement is especially significant in ultra-low voltage subthreshold regime of operation and thus offers better CP performance.

5.3.5.4 Adiabatic Gate Control of the Charge-transfer Switches

The energy required to charge or discharge a node can be approximated as $(1/2)\cdot CV^2$ where C and V are the respective capacitance and voltage at that node. Adiabatic switching techniques reduce the dissipated energy by reducing the voltage swing [14]. In this LCP, the gate control signal's voltage is switched in two steps of V_{IN} to control the ON or OFF state. As shown in Figure 5.18 and Figure 5.23, the gate-source voltage of PMOS switch P3 is switched from $-V_{IN}$ during ON, to zero, and then to $+V_{IN}$ for hard-OFF state. This step-wise charging and discharging reduces the peak current required for switching and thus halves the energy dissipated due to switching.

5.3.5.5 Capacitor size calculations

The design of the charge pump involves the estimation of optimum values of the CP parameters such as the CP capacitors (C_P), frequency of operation (f), output capacitor (C_{OUT}) and the number of stages N for a given V_{IN}. The output voltage for an N-stage CP can be approximated as [61]

$$V_{OUT,SteadyState} = (N+1)V_{IN} - N\frac{I_L}{C_P \cdot f} \tag{5.13}$$

where I_L is the load current of the charge-pump. The first term in (5.13) is the ideal voltage gain that can be obtained with an N-stage LCP, and the second term represents the charge-redistribution voltage loss due to the presence of load current. For given N and I_L, the values of C_P and f determine the maximum attainable V_{OUT}. In order to reduce the switching losses, it is desirable to operate the CP at frequencies as low as possible. Since the frequency determined by the RO has only a tuning small range, the value of C_P is maximized for the available area in the chip. In this design, dual-mim capacitors, available in the 130-nm process node, are used to realize the on-chip capacitors. The capacitance per unit area for dual-mim capacitors is 4.1fF/μm^2, and the ratio of bottom-plate parasitic capacitance to the actual capacitance is about 2.6% [62]. With an area of 35,000 μm^2, the total dual-mim capacitance that can be realized, including area for routing is about 100 pF. For the 3-stage LCP ($N=3$), with complementary cross-coupling branches, the CP capacitance for each CP stage is about 16 pF.

The required frequency of operation can be determined from (5.13) for a given load current. In this self-starting CP, the frequency of the clock generated by the ring oscillator depends on the applied input voltage. In order to accommodate a small range input voltages, the clock frequency from the RO can be tuned using delay cells, controlled by a 3-bit decoder, in order to maximize the efficiency of the conversion. For an input voltage of 125 mV, the RO oscillates at a frequency of 360 KHz. With a 100 mV input, the frequency reduces to about 200 KHz.

The required value of C_{OUT} is determined by the load current, frequency of operation, and the acceptable ripple voltage, which is given in [49], [61] as

$$C_{OUT} > \frac{I_L}{f \cdot V_{Ripple}} = \frac{C_{Total}}{V_{Ripple}} \frac{\left((N+1)V_{IN} - V_{OUT}\right)}{N^2} \tag{5.14}$$

where C_{Total} is the total CP capacitance which is 96 pF (=16·3·2 pF). For a ripple voltage of 15mV, V_{IN} of 150mV, V_{OUT} of 500mV, the value of C_{OUT} needs to be greater than 75 pF. A 100 pF dual-mim capacitor with 0.05 mm^2 area is employed in this design.

5.4 Efficiency of the Proposed Charge Pump

The operational losses determine the maximum achievable efficiency of the proposed LCP. The efficiency of the charge pump can be given as

$$\eta = \frac{V_{OUT} \cdot I_L}{V_{IN} \cdot I_{IN}} \tag{5.15}$$

where I_{IN} is the current drawn by the CP from the input source, V_{IN}, in order to sustain a load current of I_L at a boosted output voltage of V_{OUT}. To determine the efficiency of the proposed CP, the CP's output voltage (V_{OUT}) and the current consumption from the input source (I_{IN}) are derived at steady-state operating conditions. The charge redistribution, conduction, and reverse current loss components that reduce the output voltage of the CP are integrated in the V_{OUT} calculation, while the switching loss is included in the I_{IN} equation. The charge-balance analysis discussed in [58] is employed in this work to derive the output voltage of the charge pump.

5.4.1 Output voltage of the Charge Pump

The output voltage of CP can be derived based on the charge balance law which states that *"In a system of capacitors, the sum of all charges leaving a node at any instance of charge transfer is equal to zero."* [58]. This law is based on the charge conservation principle which establishes that the total charge in the system before and after any charge transfer is always equal.

The ideal output voltage level of $(N+1)\cdot V_{IN}$ can never be realized in a charge pump because of the charge redistribution loss that is inherent in switched-capacitor circuits. Charge redistribution loss results due to the sharing of charge when two capacitors with different initial voltages are connected together. Since the voltage boosting action is realized by phased charging and discharging between the CP capacitors, charge redistribution loss occurs along each stage of the CP.

The top-plate parasitic capacitance of the CP capacitors along with the parasitic capacitances due to charge transfer switches, and the level-shifters connected to the charge pump nodes (N1 to N6) consume charge during the CP operation. This contributes to additional loss of charge along the CP stages and reduces the attainable V_{OUT}. The simplified schematic (see Figure

5.18 and Figure 5.23) of the proposed three-stage CP, used in the V_{OUT} derivation, includes the parasitic capacitors in the CP nodes as a factor (γ) of CP capacitor. The factor γ is given by

$$\gamma = \frac{\alpha \cdot C_P + C_{GS,CTS} + C_{GS,LS} + C_{SB,NMOS,LS}}{C_P} \tag{5.16}$$

where, $\alpha \cdot C_P$ is the top plate parasitic capacitance of the charge pump capacitor, $C_{GS,CTS}$ and $C_{GS,LS}$ are the gate-drive capacitance of the CTS and LS respectively, and $C_{SB,NMOS,LS}$ is the source-to-body parasitic capacitance from the LS's NMOS device. The charge redistribution and parasitic loss are included in the V_{OUT} derivation, while the conduction and reverse current loss components will be added at the end. Further, since the NOV dead-time is much smaller than the time period (T), the charge pump's charging and discharging phases are assumed to be equal i.e. $T/2$.

The Figure 5.26 illustrates the node voltages across the CP capacitors during the CP operation. The voltage V_x represents the voltage across the CP capacitor. The Φ_C and Φ_D represent the charging and discharging phases, where the i-th stage CP capacitors are charged to $V_{i-1}+V_{IN}$ and discharged to the steady-state value of V_i. During the charging phase, both the C_P and $\gamma \cdot C_P$ are charged to $V_{i-1}+V_{IN}$ voltage from the previous stage CP capacitor. When the control signals transition to the discharging phase, the C_{Pi} capacitor's bottom plate is raised to V_{IN} which results in transfer of charge from the top plate to charge the parasitic capacitance (at the CP node), and also discharge to the next stage CP capacitor. After the discharge phase, the bottom plate is brought back to ground, while the top plate voltage is at steady-state of V_i. During this transition, the charge redistribution occurs from the parasitic capacitors back to the top plate of CP capacitor.

Equating the charge before and after the transfer, gives

$$\begin{aligned} &\left(C_i + \gamma C_i\right) \cdot \left(V_{i-1} + V_{IN}\right) + C_{i+1}\left(1+\gamma\right) \cdot \left(V_{i+1} + \frac{\gamma}{1+\gamma} V_{IN}\right) = \\ &C_i\left(1+\gamma\right) \cdot \left(V_i + \frac{\gamma}{1+\gamma} V_{IN}\right) + C_{i+1}\left(1+\gamma\right) \cdot \left(V_i + V_{IN}\right) \end{aligned} \tag{5.17}$$

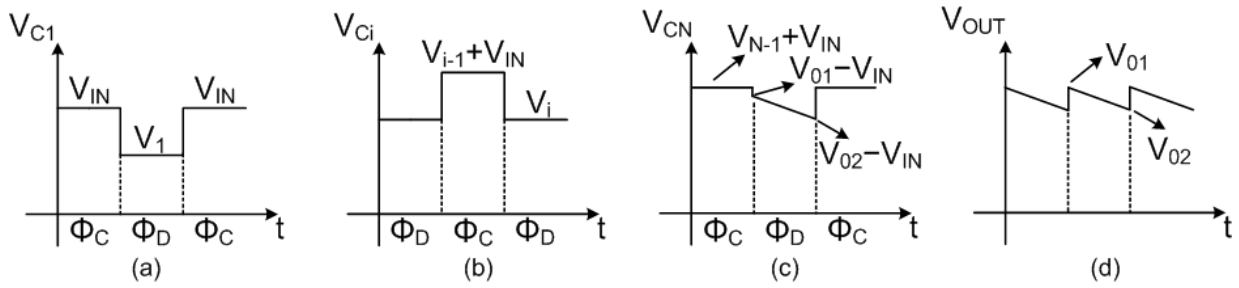


Figure 5.26 Voltage across charge pump capacitors during charging (Φ_C) and discharging (Φ_D) phase of operation for (a) First stage CP capacitor, (b) *i*-th stage CP capacitor, (c) Last or *N*-th stage CP capacitor, and (d) the output capacitor

In the cross-coupled CP topology, charge redistribution at the last stage results in transfer of charge from capacitor (C_N) to replenish the output capacitor (C_{OUT}), and to support the load current. Hence, a total charge of $I_LT/2$ is transferred from C_N during this time period of $T/2$. Therefore, at steady-state of operation, charge of $I_LT/2$ is transferred from one CP stage to the next stage to be able to sustain the load requirements. The charge redistribution equation at the output stage can be written as

$$\left(C_N+\gamma C_N\right)\cdot\left(V_{N-1}+V_{IN}\right)=C_N\left(1+\gamma\right)\cdot\left(V_N+\frac{\gamma}{1+\gamma}V_{IN}\right)+\frac{I_LT}{2} \tag{5.18}$$

Substituting (5.18) in (5.17) and simplifying the equation results in

$$\left(C_i+\gamma C_i\right)\cdot\left(V_i+\frac{\gamma}{1+\gamma}V_{IN}\right)=C_i\left(1+\gamma\right)\cdot\left(V_{i-1}+V_{IN}\right)-\frac{I_LT}{2} \tag{5.19}$$

Equation (5.19) can be rearranged to provide the voltage at *i*-th stage as

$$V_i=V_{i-1}+\frac{V_{IN}}{\left(1+\gamma\right)}-\frac{I_LT}{2\left(1+\gamma\right)C_i} \tag{5.20}$$

Substituting the values of V_{i-1} recursively presents V_i in terms of V_1, V_{IN} and I_L. At the CP's first stage, during the charging phase C_{P1} is charged to V_{IN}, where $I_LT/2$ is transferred from V_{IN} to

replenish C_{P1} of the charge lost in the previous discharging phase. Hence the charge equation is given by

$$C_1(1+\gamma)\cdot\left(V_1+\frac{\gamma}{1+\gamma}V_{IN}\right)+\frac{I_L T}{2}=(C_1+\gamma C_1)V_{IN} \tag{5.21}$$

The resulting V_1 equation is

$$V_1=\frac{V_{IN}}{(1+\gamma)}-\frac{I_L T}{2(1+\gamma)C_1} \tag{5.22}$$

Applying the boundary condition from the CP's first stage into (5.20), and using equal CP capacitors (C_P), results in

$$V_i=\frac{i\cdot V_{IN}}{(1+\gamma)}-\frac{i\cdot I_L T}{2(1+\gamma)C_P} \tag{5.23}$$

The output voltage can be obtained using $V_{OUT} = V_{O2} = V_N + V_{IN}$. The output is now

$$V_{OUT}=\frac{(N+1+\gamma)\cdot V_{IN}}{(1+\gamma)}-\frac{N\cdot I_L T}{2(1+\gamma)C_P} \tag{5.24}$$

This CP output voltage of (5.24) is equal to that derived in [58], where the charge redistribution after the discharge phase from parasitic capacitors to CP capacitors was not accounted for. The two V_{OUT} equations do not differ since the amount of charge redistribution from parasitic back to CP capacitors is very small.

The V_{OUT} equation (5.24) includes the voltage reduction from charge supplied to the load, the average output voltage can now be written as

$$\overline{V_{OUT}}=\frac{(N+1+\gamma)\cdot V_{IN}}{(1+\gamma)}-\frac{N\cdot I_L T}{2(1+\gamma)C_P}+\frac{I_L T}{4(1+\alpha)(C_P+C_{OUT})} \tag{5.25}$$

where the 3rd term represents the average ripple voltage at the charge pump output, and α is the top plate parasitic capacitance factor for this process. The equation (5.25) gives the CP's average output voltage that accounts for the charge redistribution loss and the loss due to parasitic capacitances associated with the gate drive of CTS and level-shifter circuits. As seen in (5.25), the output voltage is always lower than the ideal output of $N+1$ times V_{IN} even when the load

current is not present. Similarly, without parasitic losses, the output voltage reduces with increase in load current.

Conduction loss

The conduction loss due to the series voltage drop in the CTS of each pumping stage will degrade V_{OUT}. The charge transfer switch's "ON" resistance is given by

$$R_{ON} = \frac{1}{\mu C_{OX} \frac{W}{L}(V_{GS} - V_{TH})} \tag{5.26}$$

For low power application of this LCP, the load current is in micro-Ampere range. Hence with a reasonable R_{ON}, the conduction loss can be designed to be very small. As the number of CP stage increases, the V_{TH} of the LS's NMOS device also increase due to body effect. So, the level-shifter's output-low voltage (i.e. gate control to switch ON the CTS) might not be low enough to provide a $|V_{GS}|$ of at least V_{IN} for the CTS. This would result in an increased R_{ON} of CTS along the CP stages and thus increasing the conduction losses with increasing N. For the proposed three-stage LCP, the output voltage which reflects the conduction loss can be approximated as

$$\overline{V_{OUT}} = \frac{(N+1+\gamma)\cdot(V_{IN} - V_{RON})}{(1+\gamma)} - \frac{N \cdot I_L T}{2(1+\gamma)C_P} + \frac{I_L T}{4(1+\alpha)(C_P + C_L)} \tag{5.27}$$

where V_{RON} represents the series voltage drop due to finite ON resistance in the CTS, and is equal to $I_L R_{ON}$.

Reverse-current loss

As discussed in Section 5.3.5.3, the reverse-current flow that reduces the CP's output voltage can be viewed as charge (ΔQ) that is transferred from CP_i to CP_{i-1}. Since at the steady-state of operation, charge transfer of $I_L T/2$ is necessary to sustain load current, an extra amount of charge proportional to ΔQ needs to be transferred from CP_{i-1} to CP_i. A portion of this extra charge feeds the reverse current component that flows back to the previous stage, thus increasing the loss due to charge redistribution and the total energy dissipation. In order to avoid complicating this analysis, the reverse current loss can be incorporated in V_{OUT} as

$$\overline{V_{OUT}} = \frac{(N+1+\gamma)\cdot(V_{IN}-V_{RON})}{(1+\gamma)} - \frac{N\cdot I_L T}{2(1+\gamma)C_P} + \frac{I_L T}{4(1+\alpha)(C_P+C_L)} - \frac{I_{REV}\, t_{rise}}{(1+\gamma)C_P} \qquad (5.28)$$

where I_{REV} represents the total reverse current in the charge pump, t_{rise} (t_{fall}) is the rise (fall) time of the CTS's gate control voltage, and C_P is the pumping capacitor. The equation (5.28) gives the CP's average output voltage that accounts for the charge redistribution, parasitic losses at CP node, conduction loss, and reverse current loss.

5.4.2 Input current consumption of the Charge Pump

The input current consumed by the CP is made of the charge transferred along the CP stages to support the I_L, and the current required to charge and discharge the bottom plate parasitic capacitances of the charge pump capacitors. As shown in the previous discussion, a charge (ΔQ) of $I_L T/2$ is transferred by one stage of the cross-coupled CP to the next. During the charging phase in the bottom CP branch (i.e. Φ_1 HIGH, see Figure 5.23), ΔQ charge is transferred from input to C_{P1B}, and C_{P2B} to C_{P3B}, while the top CP branch is in the discharging phase where C_{P1T} transfers ΔQ to C_{P2T}, and C_{P3T} transfers to C_{OUT} and load. Thus, for one half-cycle (T/2) of operation, we have $(N+1)\cdot\Delta Q$ charge transferred across the CP. For full-cycle of operation, the total charge transferred and thus the total current flowing in the CP branches is given by [63]

$$I_{IN} = (N+1) I_L \qquad (5.29)$$

Equation (5.29) presents the current drawn from input source to support I_L, but does not include the switching current loss. This loss can be incorporated into I_{IN} as

$$I_{SW} = \frac{2NC_{bottomplate,par}\cdot V_{IN}}{T} = 2N\cdot\alpha\cdot C_P\cdot f\cdot V_{IN} \qquad (5.30)$$

where the bottom plate parasitic capacitance, $C_{bottom\ plate,par}$ is proportional to pumping capacitance C_P by a factor α that depends on the process technology. The frequency of CP operation is f, with time period T. Since the individual pumping-capacitors in a cross-coupled CP are half the size of those in a single-branch CP, the total switching current loss is the same in both these topologies. Hence, the total current consumption is

$$I_{IN} = (N+1)I_L + 2N \cdot \alpha \cdot C_P \cdot V_{IN} f \tag{5.31}$$

5.4.3 Conversion Efficiency of the Charge Pump

The conversion efficiency of the charge pump can be derived from the output voltage and the input current consumption using (5.15) as

$$\eta = \frac{\overline{V_{OUT}} \cdot I_L}{V_{IN} \cdot I_{IN}} \tag{5.32}$$

In order to simplify η, the input current consumption I_{IN} can be expressed in terms of I_L by substituting the value of pumping capacitor (C_P) from (5.28). To estimate C_P, the series voltage loss in the CTS (V_{RON}), the reverse current (I_{REV}) and ripple voltage terms are assumed to be very small. Thus, the CP can be approximated from the output voltage as

$$C_P = \frac{N \cdot I_L T}{2\left[(N+1+\gamma)V_{IN} - (1+\gamma)V_{OUT}\right]} \tag{5.33}$$

Substituting C_P into (5.31) gives

$$I_{IN} = \left[(N+1) + \frac{N^2 \cdot \alpha}{\left[(N+1+\gamma) - (1+\gamma)\frac{V_{OUT}}{V_{IN}} \right]} \right] \cdot I_L \tag{5.34}$$

Using (5.34) to calculate η results in

$$\eta = \frac{V_{OUT} / V_{IN}}{(N+1) + \frac{N^2 \cdot \alpha}{\left[(N+1+\gamma) - (1+\gamma)\frac{V_{OUT}}{V_{IN}} \right]}} \tag{5.35}$$

Thus, the efficiency of the linear charge pump can be approximated from the voltage gain (V_{OUT}/V_{IN}), the number of CP stages (N), and the process-dependent factor γ which is given by (5.16). The η equation of (5.35) includes the conduction loss, switching loss and reverse current

losses in the output voltage term. Further approximation of equation (5.35) with $\gamma=0$ results in the commonly used estimate for LCP efficiency as reported in [63] which is

$$\eta = \frac{K}{(N+1)+\dfrac{N^2 \cdot \alpha \cdot I_L}{[(N+1)-K]}} \tag{5.36}$$

where, the factor K is the voltage gain V_{OUT}/V_{IN}.

5.5 Implementation of the DC-DC Converter

The two versions of the cross-coupled, self-starting, low-voltage linear charge pump with three-stages were implemented in a 130-nm CMOS process. The total charge pump capacitance is 196 pF with individual pumping capacitor size of 16 pF and load capacitance of 100 pF. The charge pumps occupy an area of approximately 0.1 mm^2 each and the layouts with highlighted blocks are presented in Figure 5.27 and Figure 5.28. In the ultra-deep submicron processes (UDSM), the threshold voltage of the devices placed near N-well edges increases. For this process technology, a distance of at least 2 µm is required from the active diffusion edge to the N-well edge to avoid V_{TH} increase due to N-well proximity effect. As low-voltage operation is critical to this design, all devices follow the rule to avoid increase in V_{TH}. Furthermore, since the efficiency of the charge transfer across the various CP stages depends on the relative phase of the

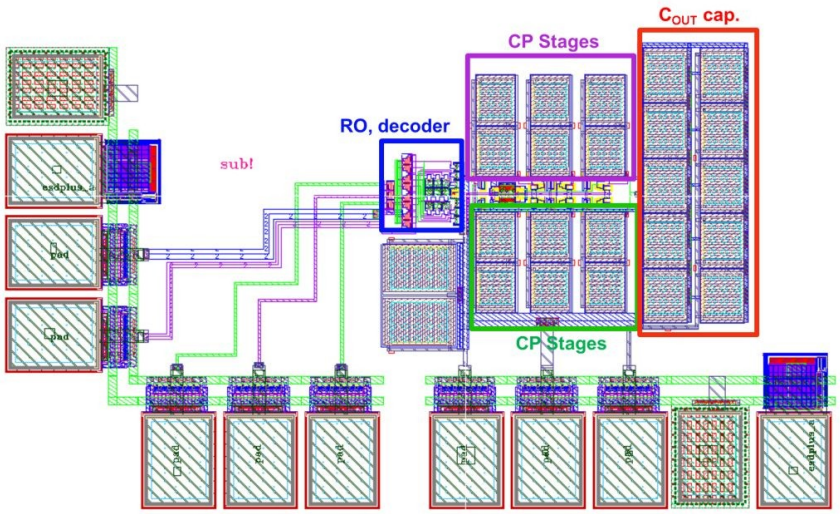


Figure 5.27 Layout of the low-voltage charge pump V1 in 130-nm process

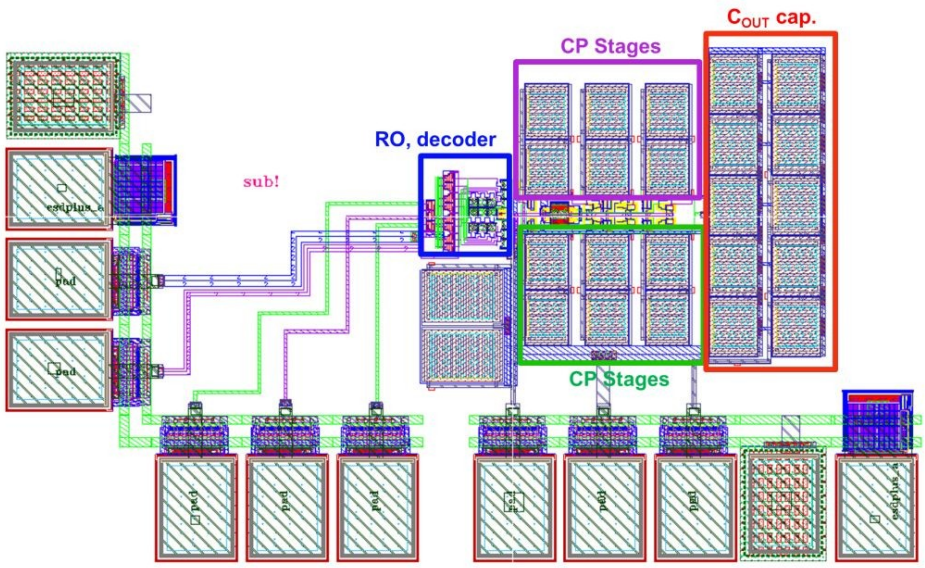


Figure 5.28 Layout of the low-voltage charge pump V2 in 130nm process

control signals distributed to CP capacitor and charge-transfer switches, extra care has been taken to ensure symmetrical routing to match the delay in clock signals. The decoder is powered by a separate power supply and operates at the nominal V_{DD}. This ensures that the switches for the delay cells in the RO have low ON resistance and are not affected by the low-voltage constraint of the input. Decoupling the decoder's power from the CP also facilitates measurement of the CP input current and the efficiency of the CP.

5.6 Simulation Results

The charge pump circuits were simulated from the schematic, as well as with the parasitic capacitances and resistances from the layout extraction. The simulation results characterizing the LCP designs will be presented in this section. The results from ring oscillator and the NOV blocks will be presented first as they are common to both the LCP versions. Since the converter is powered by the input voltage, any change in V_{IN} results in variations in the ring oscillator's output clock frequency, and the dead-time in the NOV phase generator's output. Figure 5.29 presents the change in ring oscillator's output frequency across variations in V_{IN}. The delay networks along with the decoder offer an option to adjust the RO's output frequency. The ability to tune the CP's clock frequency provides a technique to maximize the conversion efficiency for a given load condition. Figure 5.30 illustrates the output frequency range that can be obtained for

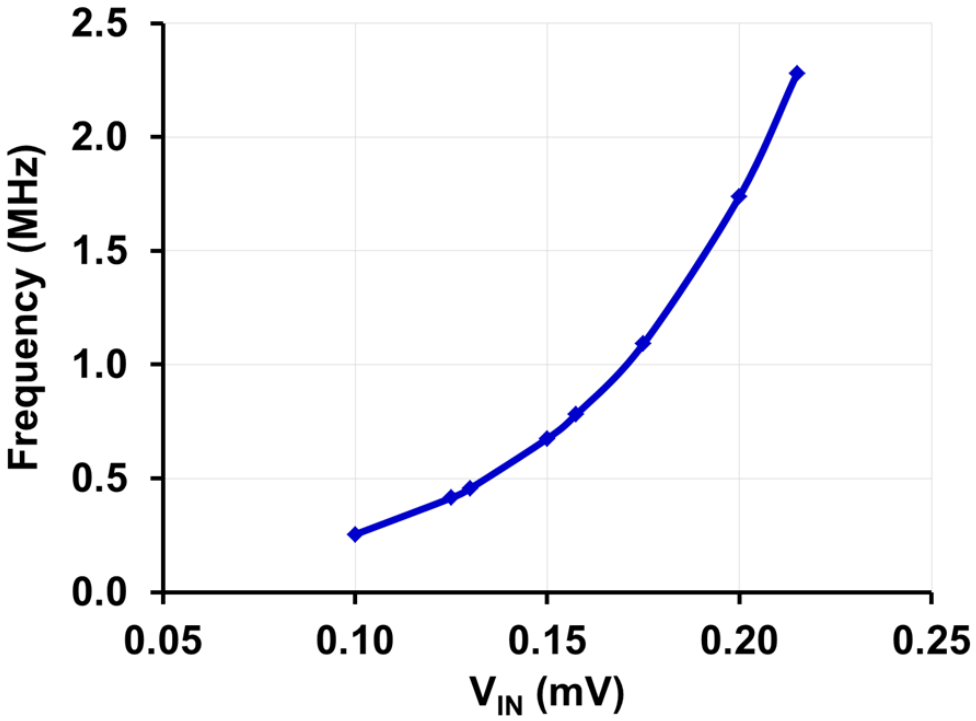


Figure 5.29 Ring oscillator's output frequency across input voltage variations

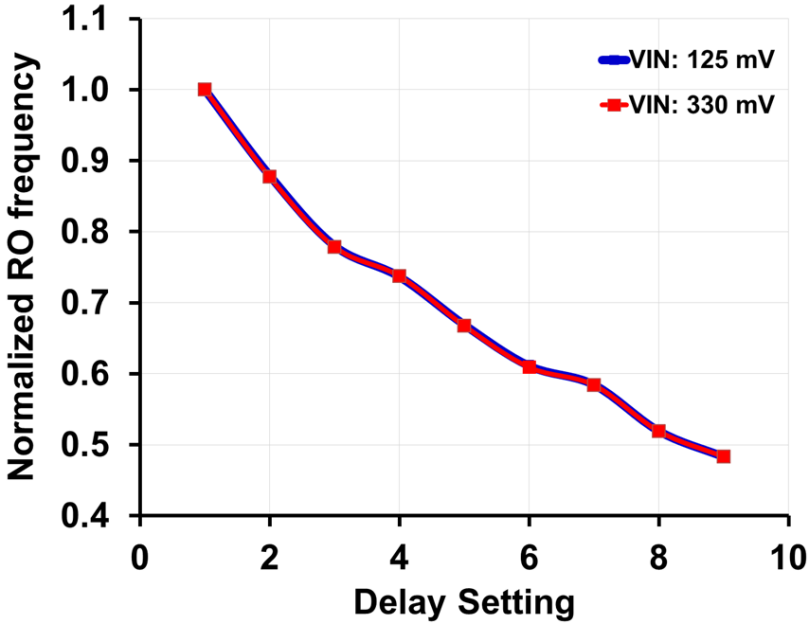


Figure 5.30 Ring oscillator's output frequency control with delay network

various delay settings in the RO. The nominal dead-time introduced by the NOV generator at V_{IN} of 125 mV is 360 ns.

5.6.1 LCP simulation results

The proposed LCP designs were simulated to characterize their startup voltages, conversion gains and efficiencies at different load conditions. The simulations were performed at the free-running frequency mode of the ring oscillator wherein, the delay cells in the RO were not employed. The startup voltage of the CP was characterized based on the CP's output voltage and conversion efficiency at a given V_{IN}.

For an input voltage of 100 mV, the control system, including the RO and NOV generator, was able to generate the required clock signals for the CP's startup and operation. The generated clock frequency from the RO was at 200 KHz. The CP's clock and the output voltage demonstrating the startup behavior of the LCP V1 and LCP V2 designs, at an input voltage of 100 mV, are presented in Figure 5.31 and Figure 5.32, respectively. For the no-load condition, the output voltage reaches a steady-state value of 234 mV in LCP V1 while LCP V2 provides 250 mV output within 1 ms. The figures also illustrate the zoomed-in view of the outputs with details on the RO's output swing of about 95% V_{IN} and the CP's output ripple voltage of less than 1.2 mV for both the designs.

Figure 5.33 and Figure 5.34 present the 3-stage charge pumps' output voltages and conversion gains for low input voltages and across different DC current loads. It is evident from the figures that, above the startup voltage, both the charge pumps provide a linear increment in the output voltage with increase in V_{IN}. Above the startup voltage, the improvement in the output voltage of the LCP V2 when compared to the LCP V1 is clearly visible in the conversion gain plots of Figure 5.34.

At 100 mV input voltage, although the RO provides the necessary control clocks to the charge pumps, the output voltage and conversion gain are low due to weak drive strengths in deep subthreshold regime of operation, and also increased losses along the pumping stages. Hence, the usable range of V_{IN} starts from about 125 mV, where the conversion gain is 3.25 V/V for no-load, and about 2.5 to 2.75 V/V for 0.1 μA load. The output voltage reaches its steady-

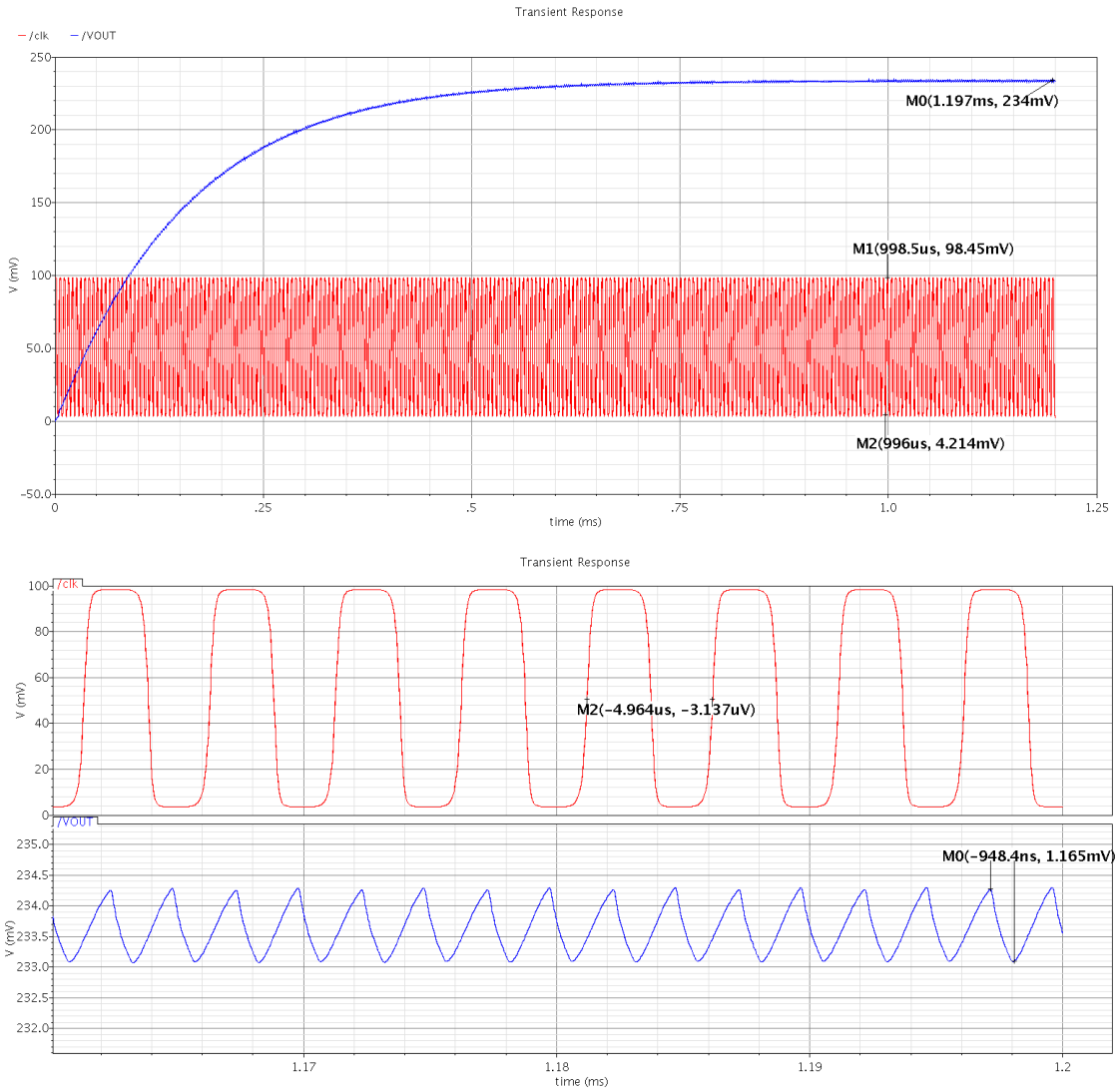


Figure 5.31 Post-layout simulation showing startup of the LCP V1

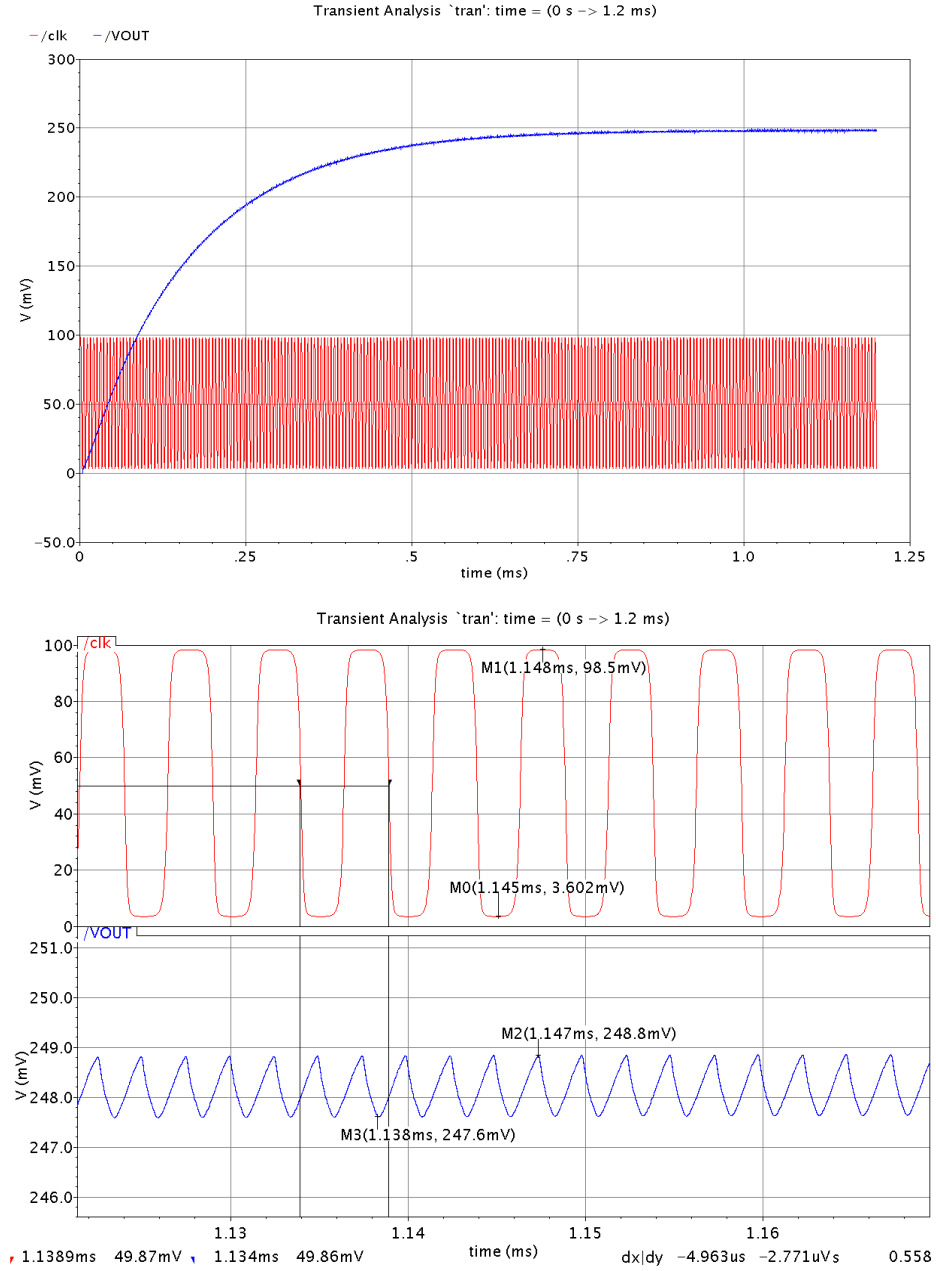


Figure 5.32 Post-layout simulation showing startup of the LCP V2

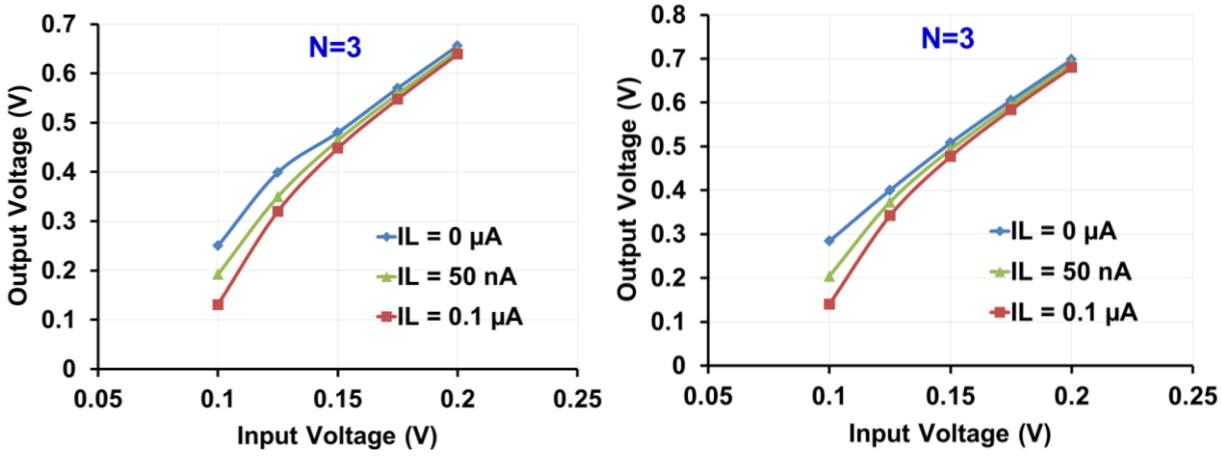


Figure 5.33 Plot of LCP's output voltage across varying input voltages for different load conditions

(a) LCP V1, (b) LCP V2

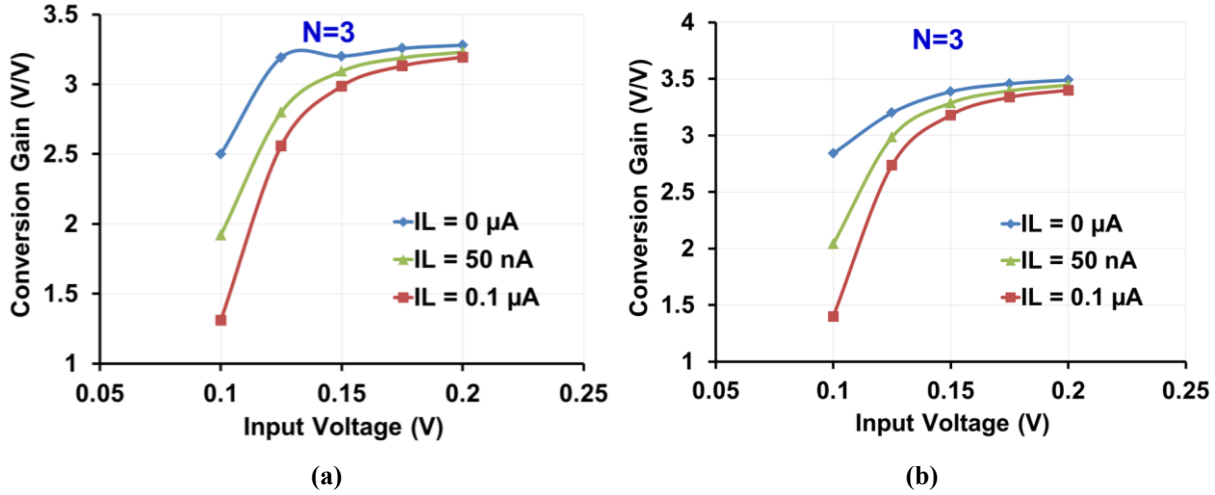


Figure 5.34 Plot of LCP's conversion gain across varying input voltages for different load conditions

(a) LCP V1, (b) LCP V2

state value in less than 1ms for both the CP versions. At V_{IN} of 125 mV, the RO oscillates at 360 kHz and the output ripple voltage is 1.2 mV for a DC load current of 0.1 µA.

The conversion efficiency of the LCP can be approximated as (5.36) [63]

$$\eta_p = \frac{I_L \cdot V_{OUT}}{I_{Power} \cdot V_{IN}} = \frac{K}{N+1+\alpha \frac{N^2}{N+1-K}} \tag{5.37}$$

where K is the gain factor, V_{OUT}/V_{IN} and α is a technology dependent parameter which is the ratio of bottom-plate parasitic capacitance to CP capacitance, $C_{Par,P}/C_P$. Thus the efficiency of the CP depends on the number of CP stages, the value of CP capacitance and the frequency of operation [61]. With the simulated conversion gain, the efficiency of the CP can be estimated for α of 3% in the 130-nm process node [62]. Figure 5.35 presents the estimated efficiency of the charge pumps from simulation results, across varying input voltages and load conditions. As indicated by the low gain ratio, the CP's efficiency at 100 mV input is at 34% and increases to above 65% for input voltages above 125 mV at 0.1 µA DC current load. At no load condition, η_p of less than 100% is due to the switching losses and losses in the charge transfer switches in each stage of the charge pump. As evident in the Figure 5.35, the LCP V2 version provides an improvement in the conversion efficiency for inputs above 125 mV (i.e. startup voltage).

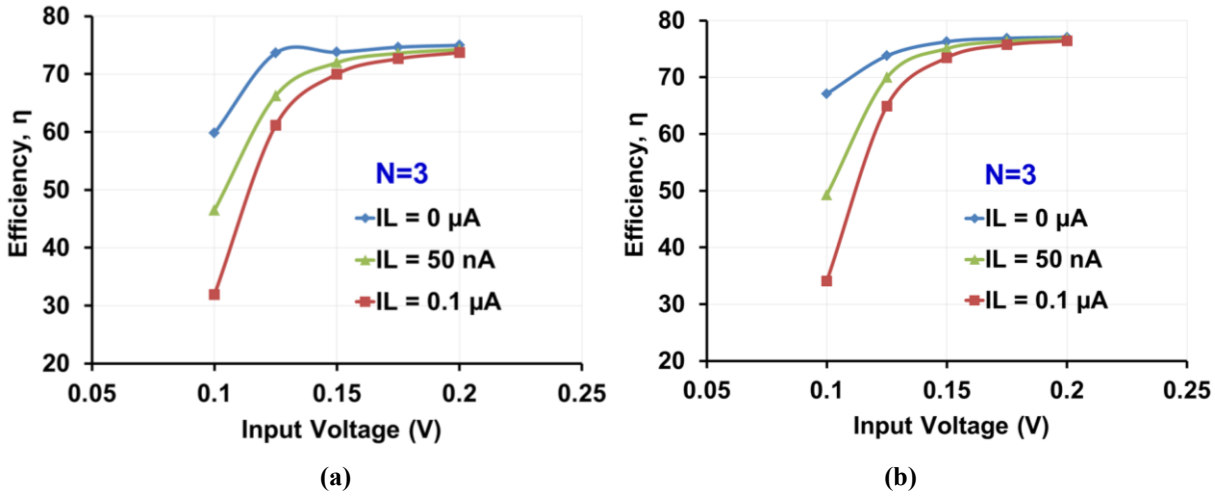


Figure 5.35 Plot of charge pumps' efficiency across varying input voltages and different load conditions (a) LCP V1, (b) LCP V2

5.6.2 Performance of the Proposed CP topology with increase in number of CP stages

In order to demonstrate the ease of gate control generation that facilitates extension of the number of CP stages, the proposed LCP topology was simulated with seven charge pump stages. Figure 5.36 and Figure 5.37 present the output voltage and estimated efficiency for the 7-stage CP topology. The CP boosts the 125 mV input to 745 mV at a maximum efficiency of 69%.

Further, the CP was designed with different number of stages (N) to study the topology's startup and conversion features as a function of pumping stages. Figure 5.38 and Figure 5.39 present the output voltage and estimated efficiency as a function of the number of cascaded pumping stages. The input voltage is varied from 125 mV to 200 mV with a constant load of 0.1 µA. The output voltage increases linearly with increase in the number of CP stages (N). The LCP characteristic reduction in η_p at higher N is due to the increase in conduction, parasitic, and charge redistribution losses due to the CP stages.

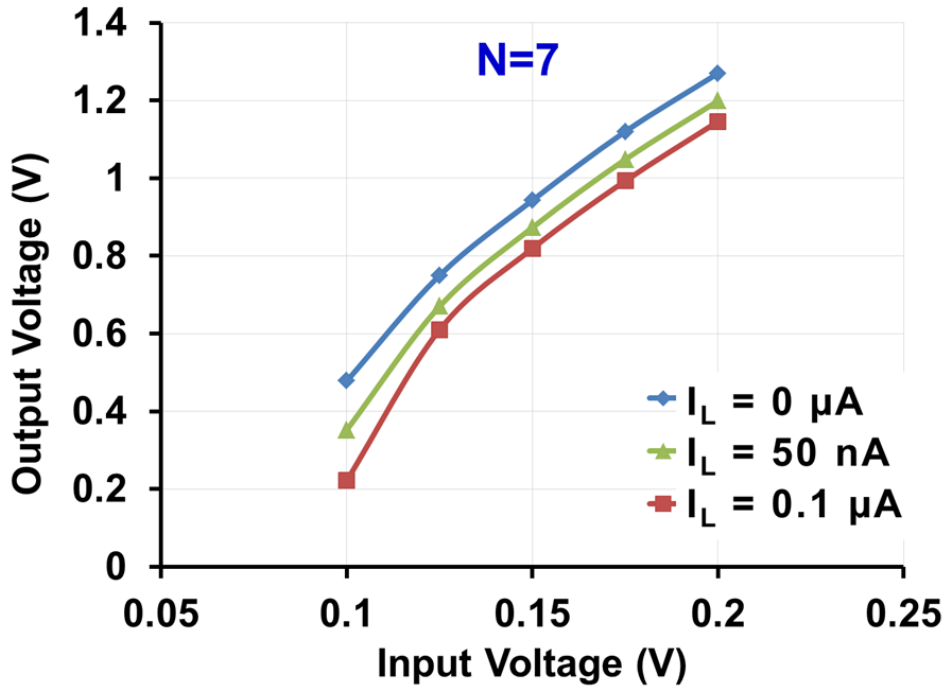


Figure 5.36 Seven-stage LCP V2's output voltage across varying input voltages for different load conditions

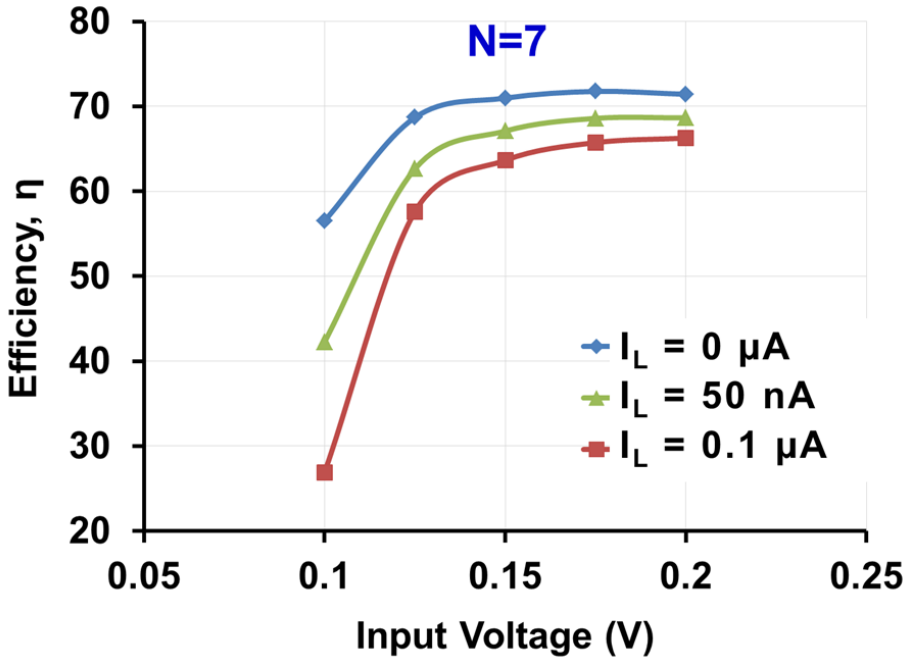


Figure 5.37 Seven-stage LCP V2's efficiency across varying input voltages and different load conditions

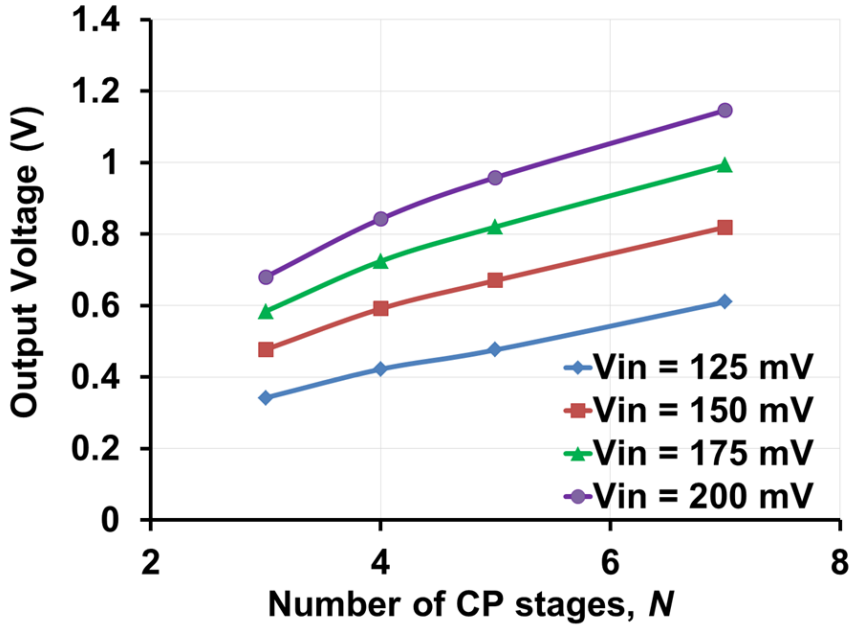


Figure 5.38 Plot of LCP V2's output voltage across varying number of pumping stages (*N*) for different input voltages

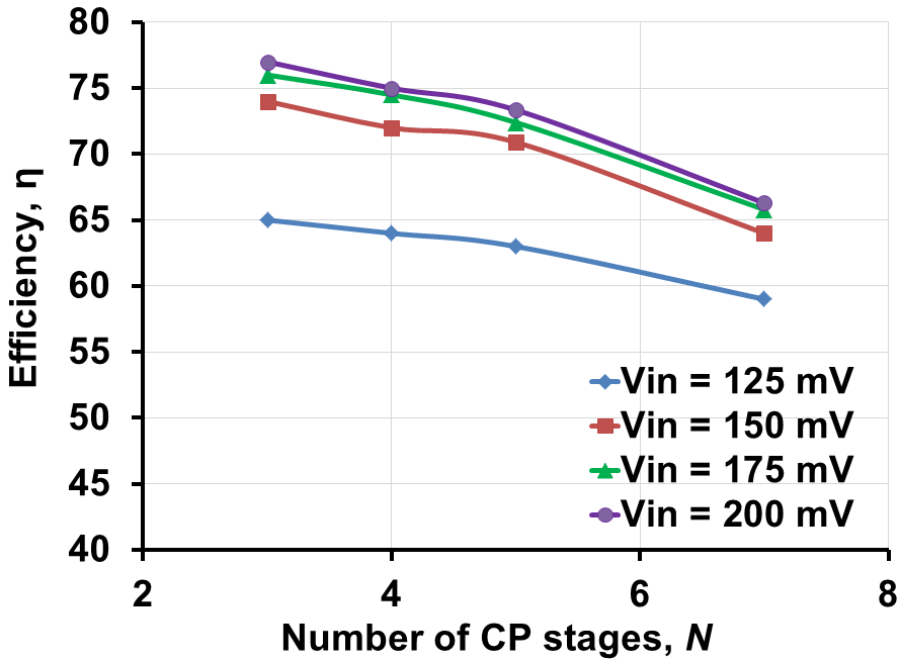


Figure 5.39 Plot of LCP V2's efficiency across varying number of pumping stages (*N*) for different input voltages

5.7 Summary

A low-voltage capable, self-starting charge pump has been designed and implemented in the 130-nm process node. This charge pump topology with increased number of stages and drive strength is targeted to be used as the core component in a DC-DC boost converter design to facilitate charge-recycling based low-power digital design. The self-starting feature renders this charge-pump's use in energy harvesting systems as well. Low-voltage DC-DC converters are essential for energy harvesters that operate from various ultra-low voltage input, low-power sensors such as thermoelectric generators (TEG), photovoltaic cells etc. The measurement results and characterization of the two charge pump designs are presented in the next chapter.

Chapter 6 Characterization of Low-Voltage Self-startup Charge Pump

This chapter presents the measurement results and analysis of the low-voltage self-starting charge pump (CP). The primary goal is to characterize the startup voltage of the charge pump across different DC load current conditions. This is accomplished by measuring the charge pump's output voltage for various input voltages and by evaluating the conversion gain across the input range. Further, comparing the measurement results between the two versions of the CPs would illustrate the improvement realized by reducing the losses due to reverse currents. Correlating the measurement data with simulation results offers a better understanding of the circuit performance across process variations.

6.1 Test Setup

The chip was fabricated in the IBM 8RF CMOS process through MOSIS [69] and packaged in a 64-pin LQFP (Low-Profile Quad Flat Package) for testing. The chips were received and tested in June 2012. A microphotograph of the fabricated die, with highlighted circuit blocks is shown in Figure 6.1. Eagle layout editor was used to design the four-layer FR4 PCB to characterize the charge pumps. Figure 6.2 presents the designed test board which accommodates all the 3 chips that were tested. The layer stack-up in the PCB cross-section is illustrated in Figure 6.3. The majority of the signal routings are on the topmost layer of the PCB, while the inner copper planes enable quiet power supply and ground connections. The inner copper supply layers also act as power supply decoupling capacitors. Additional decoupling capacitors are added close to the supply pins of the chips and small decoupling capacitors are also provided on-chip.

6.1.1 Power Supply Partition & Generation on the PCB

Power supply planes and their partitions are essential to avoid noise coupling and to preserve signal integrity, especially for low-voltage operation. The fabricated chip has two

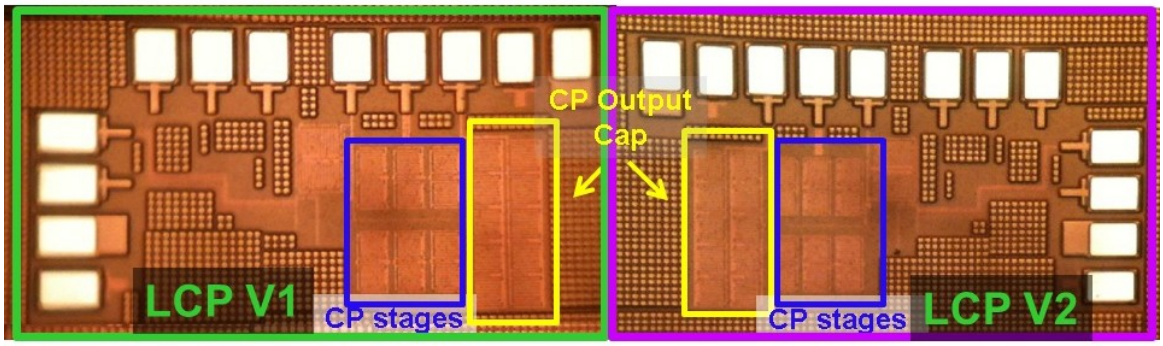


Figure 6.1 Microphotograph of the fabricated die

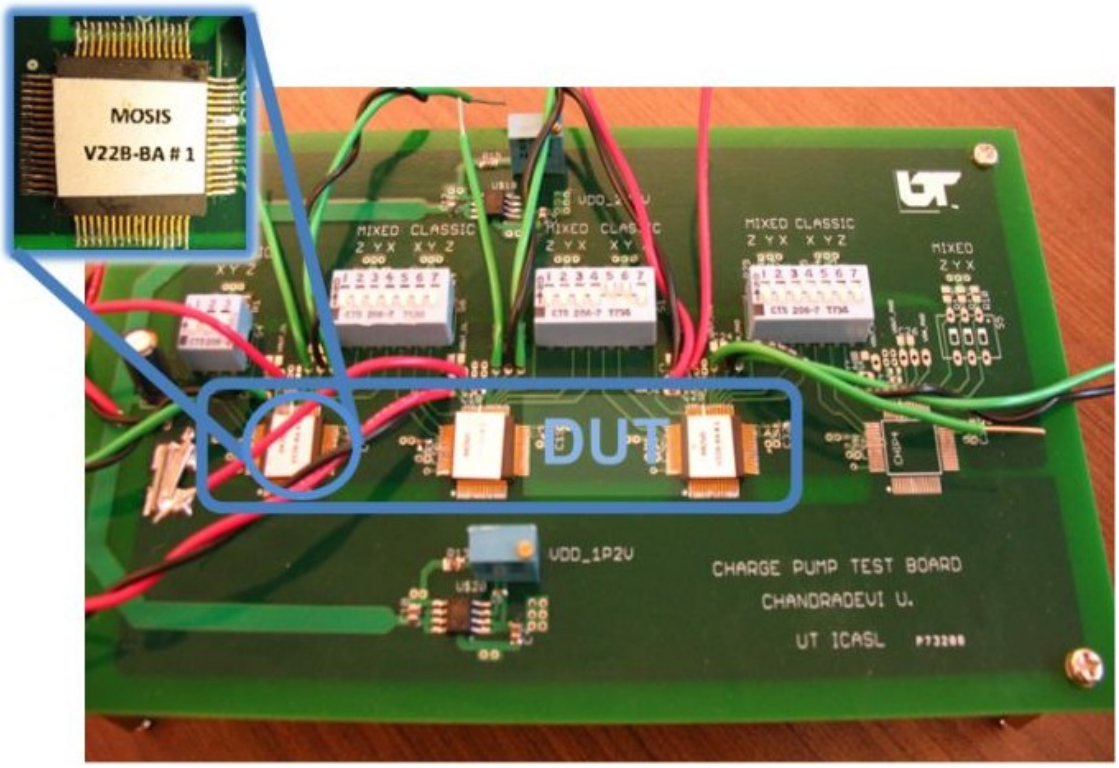


Figure 6.2 Test board to characterize low-voltage charge pumps

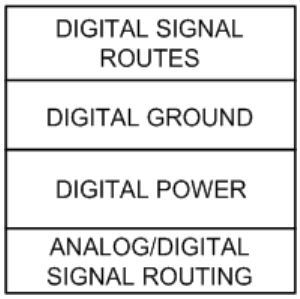


Figure 6.3 Cross-section of the test board showing the layer stack-up

different supply voltage requirements of 2.5 V and 1.2 V. The decoder that is used to control the ring-oscillator's (RO) frequency of operation and its pad frame use 2.5-V power supply since they employ thick-oxide CMOS devices. The pad ring for the core charge pump circuit is powered by a 1.2-V supply voltage. The bond-pads were positioned such that the pins on the chip's top side are powered by 2.5 V, while the 1.2-V power supply is required by pins on both sides of the chip. The pad (signal) placement and the corresponding bonding diagram facilitate power plane partition on layers 2 & 3.

Onboard voltage regulators are employed to provide stable, low-noise supply voltages to the chip. Linear voltage regulators are preferred to switching regulators due to their low noise capability. A low-dropout, linear voltage regulator (TI's LP38512) [65] is used in this design. This regulator provides output voltages in the range of 0.5 V to 4.5 V for an input voltage range of 2.25 V to 5.5 V. The schematic of the voltage regulator is presented in Figure 6.4. The required output voltage is realized by varying the ratio of resistors R1 and R2, and is given by

$$V_{OUT} = V_{ADJ}\left(1+\frac{R_1}{R_2}\right) \tag{6.1}$$

An input voltage of 5 V is applied to the regulators and the ratio of resistors is set to obtain output voltages of 1.2 V and 2.5 V. The grounds of the two supply partitions are connected at only one point on the board in order to eliminate ground-loops. A tight, short ground-plug is used to connect the grounds and thereby eliminate the inductive effects of banana plugs.

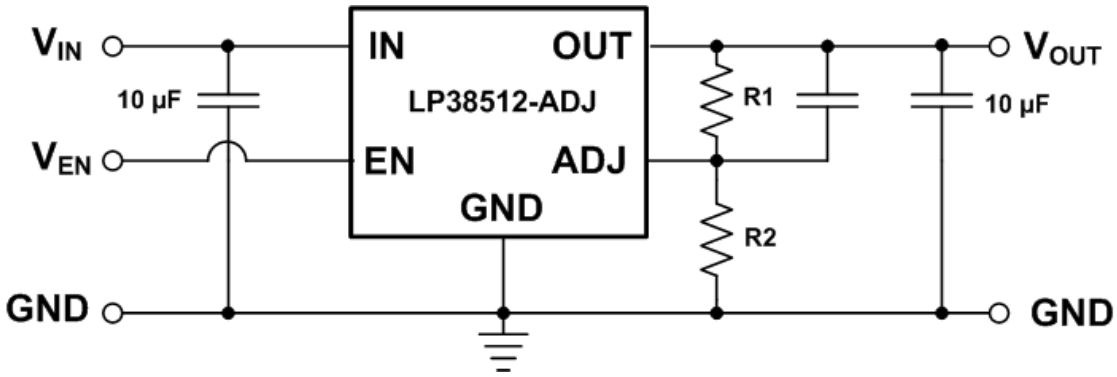


Figure 6.4 Schematic of LDO voltage-regulator circuit on the test board [65]

6.1.2 Ring Oscillator control signal generation

A 3-to-8 decoder is included on-chip in order to vary the ring oscillator's delay setting and thereby provide a means to control its output frequency. The test board includes single pole, single throw (SPST) switches to generate the three-bit control signal for each charge pump.

As illustrated in Figure 6.1, the fabricated chip includes both the versions of the charge pump circuits. The three test chips were directly soldered on to the test board to reduce socket parasitics. However, during soldering, the power supply pin to the CP version 1 in chip # 2 was damaged. So, the CP testing was limited to two prototypes for the LCP V1 design, while three circuits of the LCP version 2 were available for characterization.

6.2 Test Procedure

The low-voltage charge pump characterization begins with ensuring stable, onboard power supply voltages for the test chips. Then, an input voltage is applied using the Keithley 2400 sourcemeter to the CP-under-test while the DC load current is drawn out of the output node using another Keithley 2400 sourcemeter. The boosted CP output voltage is measured using a digital multimeter and the current supplied by the input voltage is also monitored in order to determine the CP efficiency. An output voltage close to the expected value from the three-stage CP verifies the functionality of the charge pump, the associated ring oscillator, and phase generator circuits. Once the charge pump startup and operation are ascertained, the control bits to the decoder are changed to vary the frequency of the CP control signals. For a fixed load

condition, the change in frequency of CP control signals would directly influence the input current consumption and the output voltage and thus the CP efficiency. The switch setting that corresponds to the maximum output voltage and maximum efficiency is determined for various input voltage and output load conditions. With the appropriate control bits to the decoder, the CP is then characterized across different input voltages and load conditions.

6.3 Prototype Characterization

6.3.1 Ring Oscillator

Figure 6.5 presents the CP output voltage across different frequencies of operation, obtained by varying the delay in ring oscillator, for an input voltage of 0.33 V and DC load of 0.1 μA. Figure 6.6 presents the normalized efficiency of the CP designs obtained across different delay settings in ring oscillator for the same setup conditions as in Figure 6.5. The plots show only a small variation in the output voltage and efficiency for both the CP versions across frequency. On examination of the final fabricated design, it was found that the decoder circuit which is required to output a thermometer-code was erroneously designed to not do so. The fabricated design is a 3-to-8 binary decoder with only one active (high) output that depends on the input bits. Figure 6.7 (a) illustrates the delay network designed to control the ring oscillator's output frequency. The Figure 6.7 (b) and (c) also highlight the difference in the realized delay and the desired delay, for each switch setting. From Figure 6.7 it is evident that the fabricated frequency control circuit does not achieve the maximum possible range of frequency variations, and is constrained to approximately 3 different frequency settings. Figure 6.8 presents the simulated RO frequency variations, normalized to free-running case for both the thermometer-code and binary decoder controlled delay settings. The thermometer decoder provides at least 2X frequency variation, while the binary decoder offers less than 20% change. This explains the lack of variation in the CP's measured performance across delay variations in Figure 6.5 and Figure 6.6.

As seen in Figure 6.6, the best CP performance that corresponds to a maximum output voltage and minimum input current (i.e. maximum efficiency), is achieved at the switch setting of "110" for both the CP versions and across all chips. Hence, all characterizations were

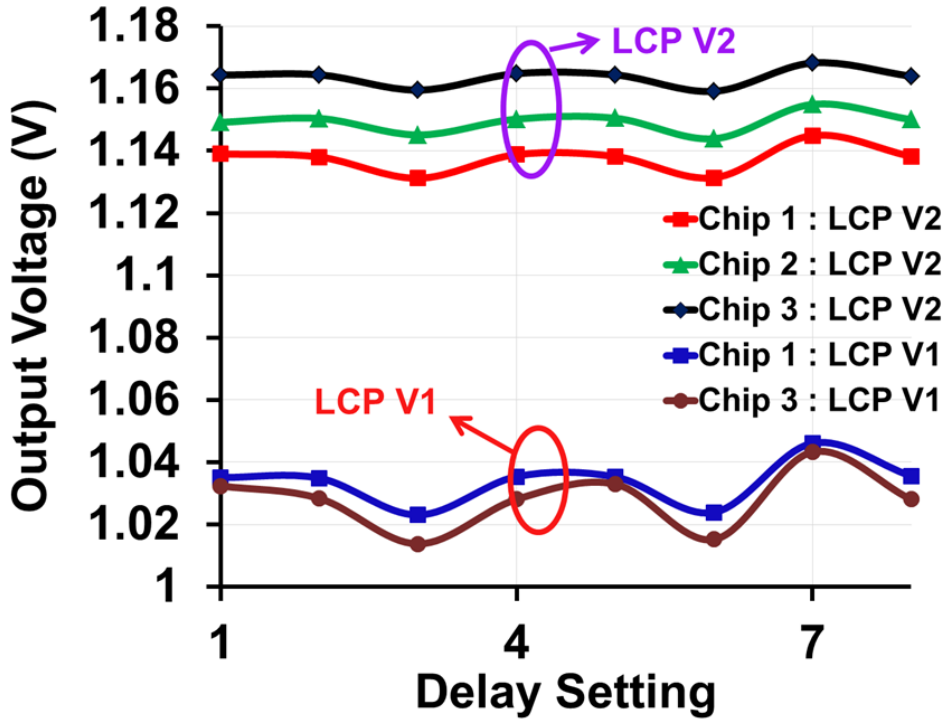


Figure 6.5 Measured charge pump output voltage across frequency of operation (V_{IN} at 0.33 V)

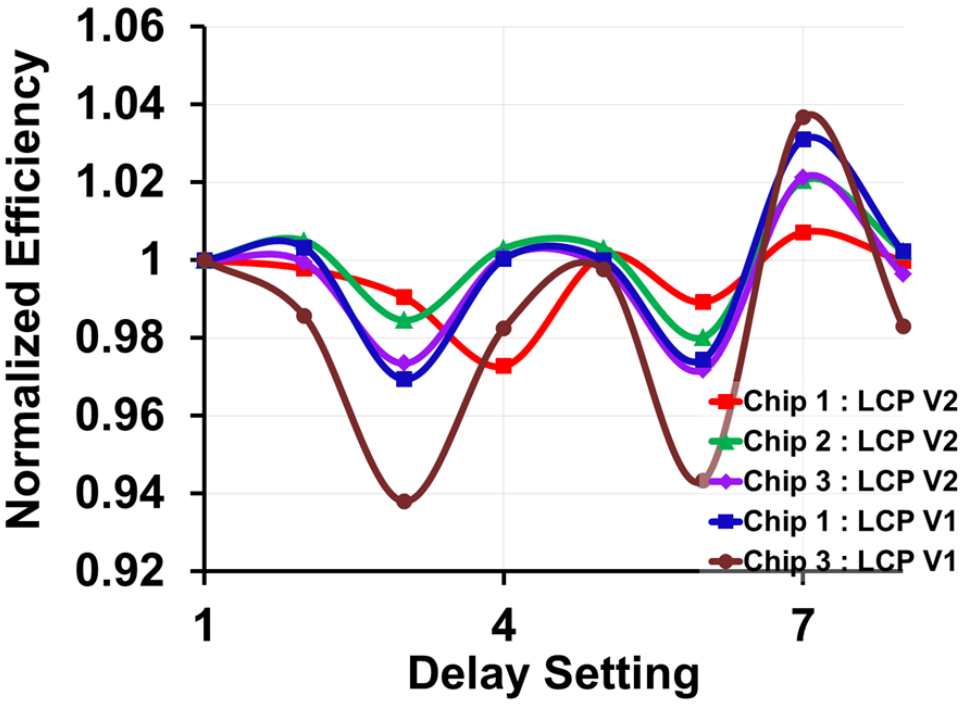


Figure 6.6 Measured charge pump efficiency across frequency of operation, normalized to free-running RO's efficiency (V_{IN} at 0.33 V)

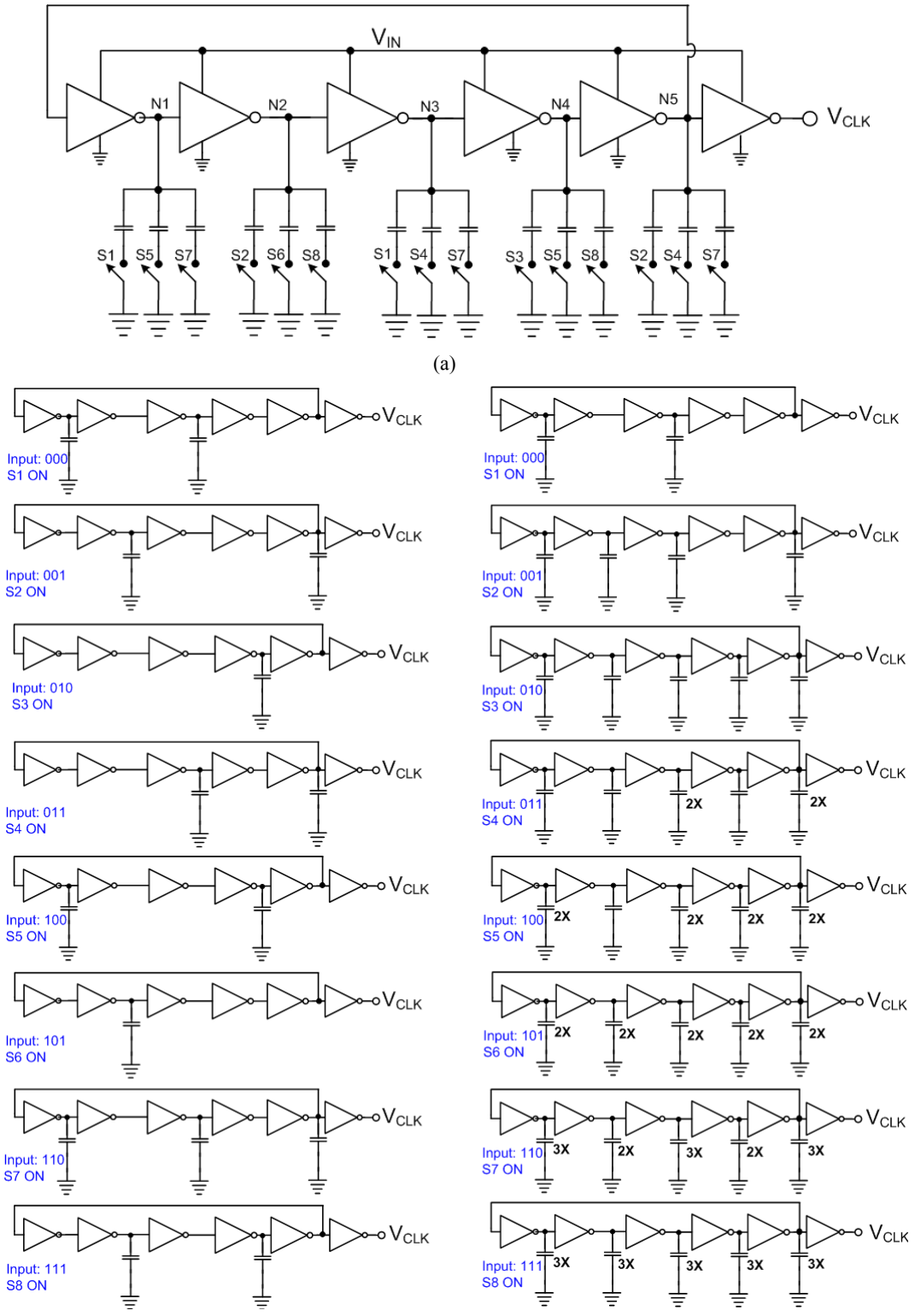


Figure 6.7 Frequency tuning in ring oscillator (a) simplified schematic of RO illustrating delay cells, (b) Realized RO schematic, and (c) Required RO schematic, across different delay (switch) settings

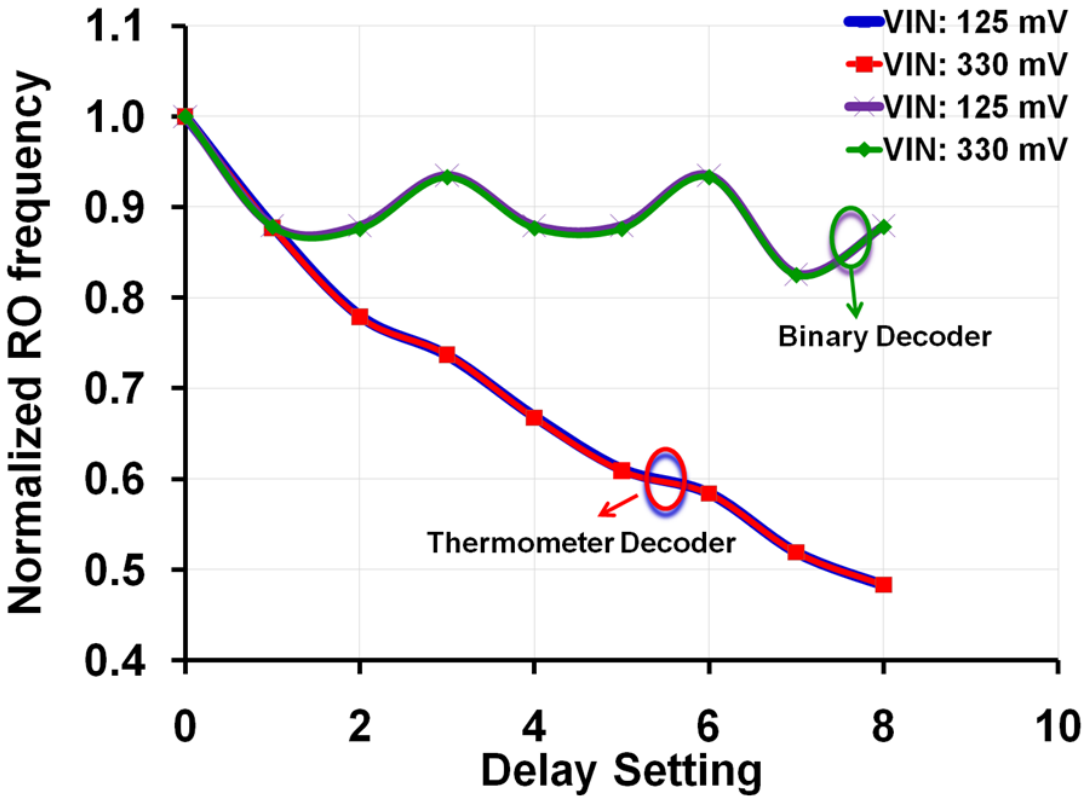


Figure 6.8 Simulated RO's output frequency, normalized to the free-running frequency, across delay settings for V_{IN} at 0.125 V and 0.33 V.

performed with this switch (delay) setting that provides the best possible conversion efficiency for the charge pumps. Further, note that an input of "110" to the decoder corresponds to the smallest frequency (maximum delay) in the ring oscillator. Thus, the measured CP efficiency could be further improved with a lower frequency of operation, depending on the load conditions.

6.3.2 Charge Pump Output Voltage

The output versus input voltage characteristics across different load conditions is compared between the two versions of the CPs in Figure 6.9 to Figure 6.11. The input voltage is varied such that, at the maximum input, the CP's output extends to the maximum nominal supply voltage for this process (i.e. 1.2 V). The improved LCP version 2 reduces the reverse-current losses between the CP stages and thus delivers a higher output voltage than the LCP version 1 which is based on conventional non-overlapping clock phase technique.

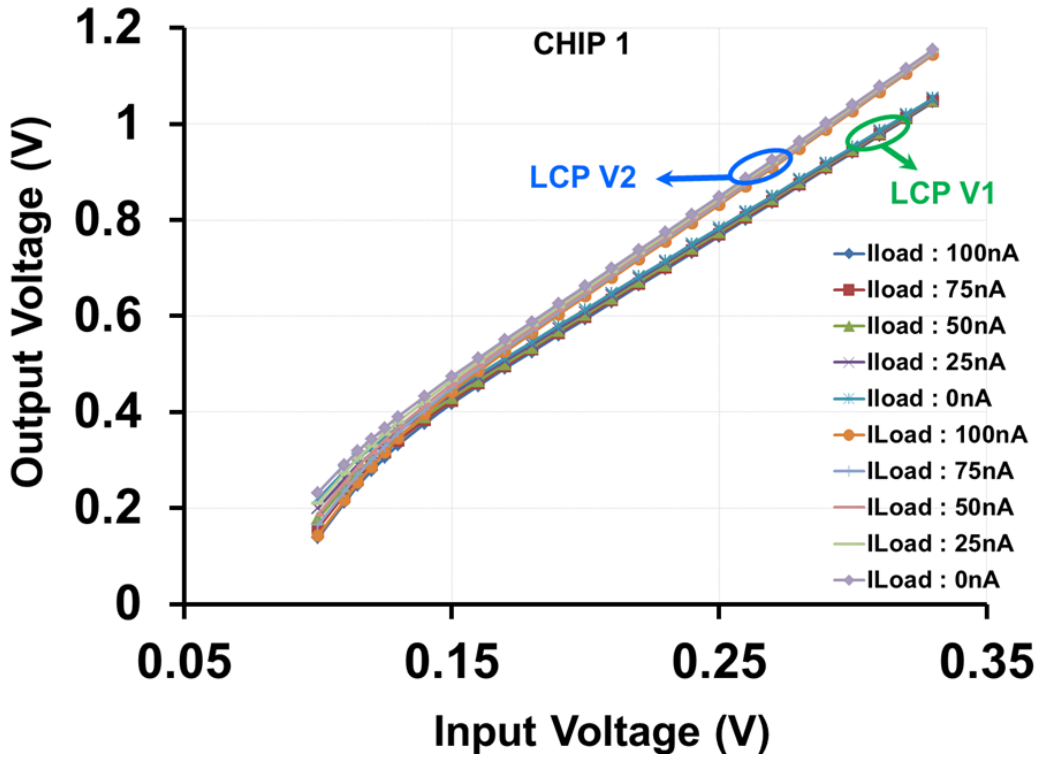


Figure 6.9 Measured charge pump output voltage across variations in input voltage and DC load current for Chip 1

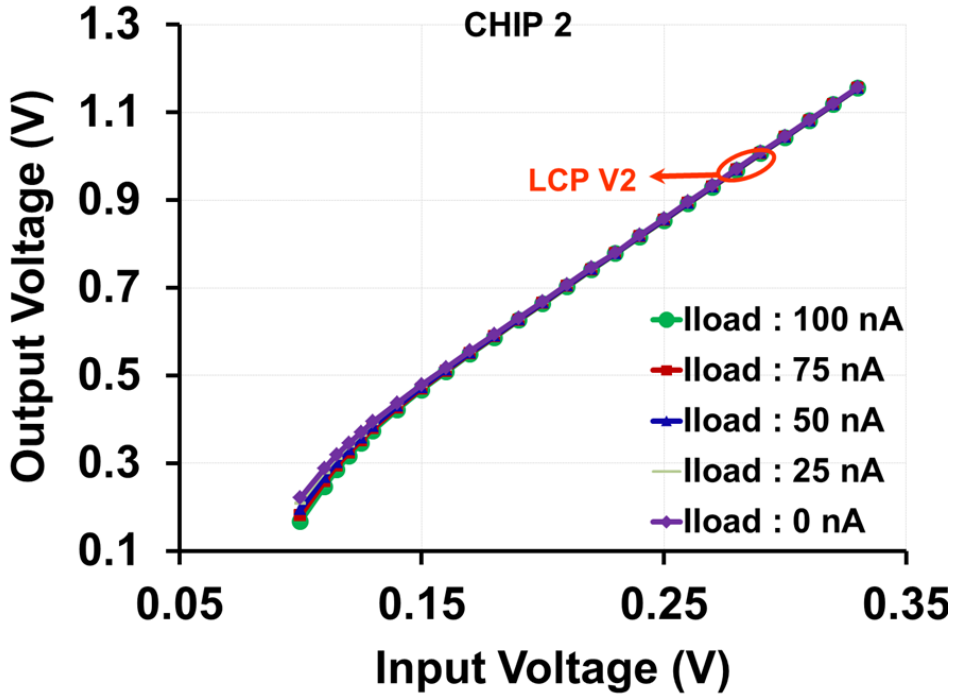


Figure 6.10 Measured charge pump output voltage across variations in input voltage and DC load current for Chip 2

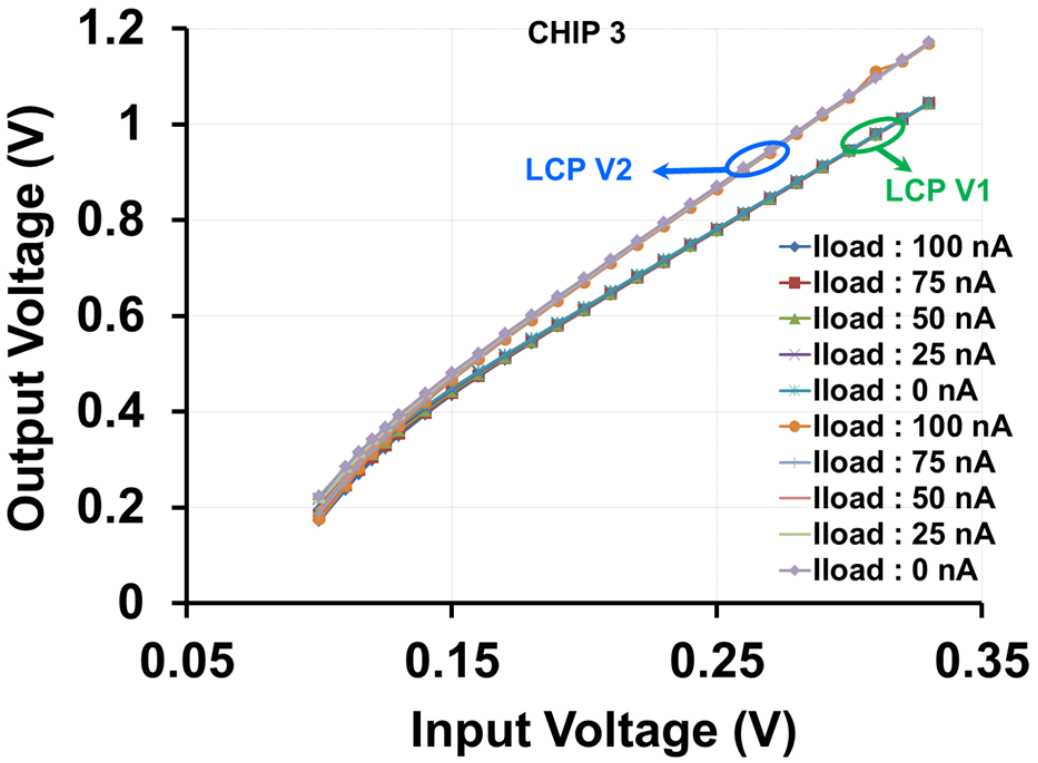


Figure 6.11 Measured charge pump output voltage across variations in input voltage and DC load current for Chip 3

Also, note that the difference in the output voltages increases with the input and is evident for inputs above 0.2 V in Figure 6.9 and Figure 6.11. This sizeable difference in the output voltages between the two CPs is due to the increase in the amount of reverse current and switching losses with increase in the frequency of operation at higher input voltages.

Figure 6.12 to Figure 6.14 present a closer look at the low-voltage startup and operation of these charge pumps. From the plots, it can be observed that even at very low voltages, the LCP V2 performs better than the LCP V1. At low voltages, the charge transfer switches and the CP control generation circuits operate in sub-threshold regime and thus have slow transition edges. As described in Section 5.3.5.2, these slow edges result in increased reverse current losses in the odd pumping stage of the LCP V2 and thus the output voltages of both the CP versions start to converge at very low input voltages i.e. around startup voltage.

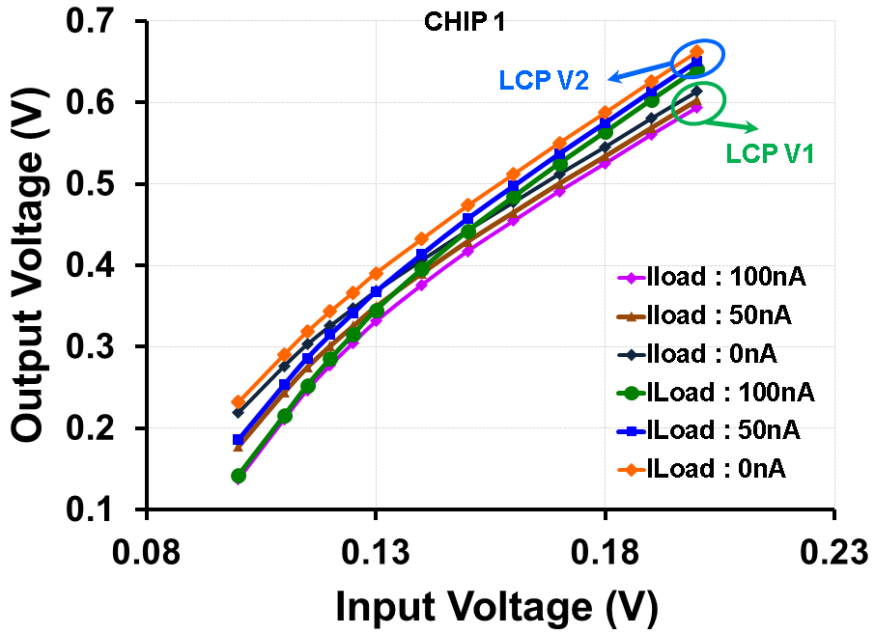


Figure 6.12 Measured charge pump output voltage across low input voltages at different DC load current conditions for Chip 1

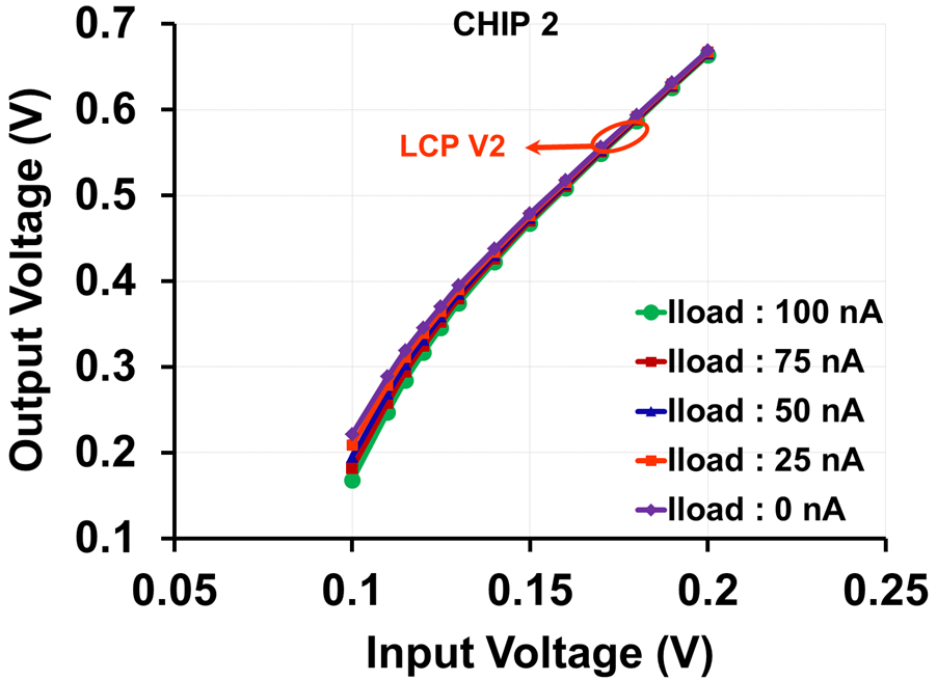


Figure 6.13 Measured charge pump output voltage across low input voltages at different DC load current conditions for Chip 2

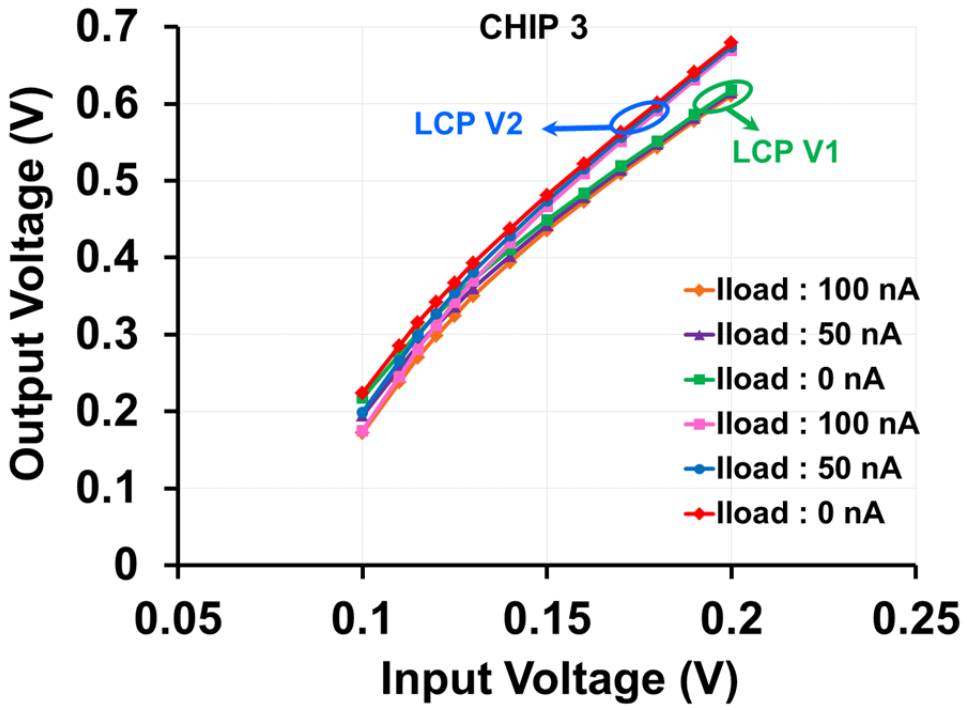


Figure 6.14 Measured charge pump output voltage across low input voltages at different DC load current conditions for Chip 3

6.3.3 Charge Pump Startup Voltage

The conversion gain characteristics of the LCPs across input voltages are employed to quantify the CP's startup voltage. The CP conversion gains across input voltage range for no-load and 0.1 μA load conditions are illustrated in Figure 6.15 and Figure 6.16. Even though the CPs can furnish output at very low voltages, the gain and thus the efficiency of operation start to drop steeply with reduction in input voltage beyond a certain point. From the gain plots, it can be inferred that the practical startup voltage is approximately around the knee of the curves, below which the conversion gain degrades sharply. The startup voltages for the CP versions are tabulated in Table 6.1 for different load conditions. The LCP V2 has lower-voltage startup capability due to the DTMOS diodes in the first pumping stage (Section 5.3.5.3) that provide a path for the pumping capacitors to start charging at low voltages. Also, note that the startup voltage depends on the CMOS threshold voltages and thus is process dependent. In this small sample of test chips, the threshold voltages of the devices in chip 1 are higher than those of other samples. Hence, the LCP designs in chip 1 require a higher startup voltage when compared to

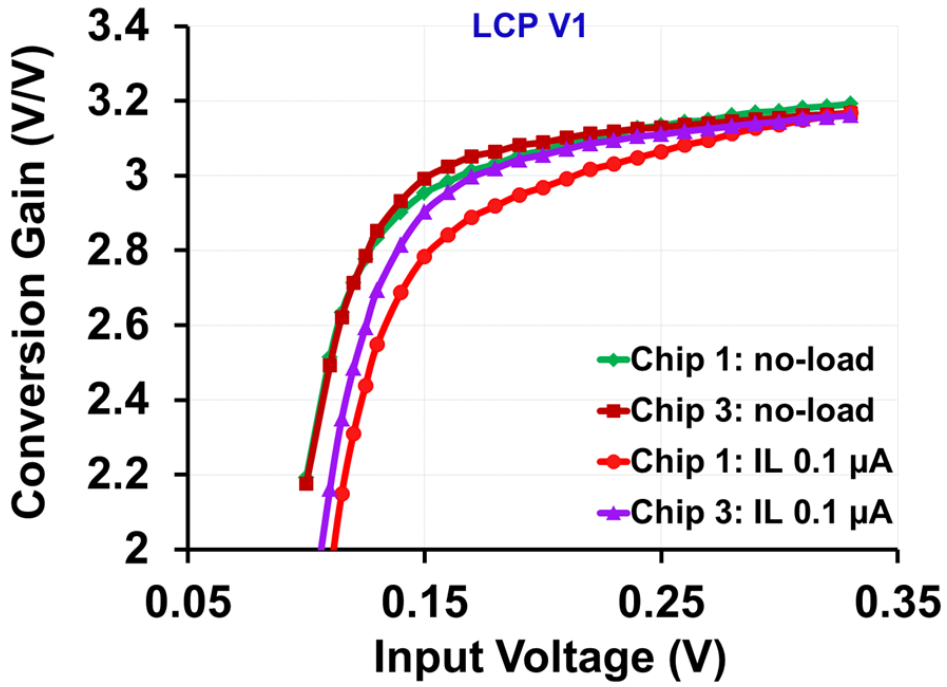


Figure 6.15 LCP V1's conversion gain across low input voltages and load conditions

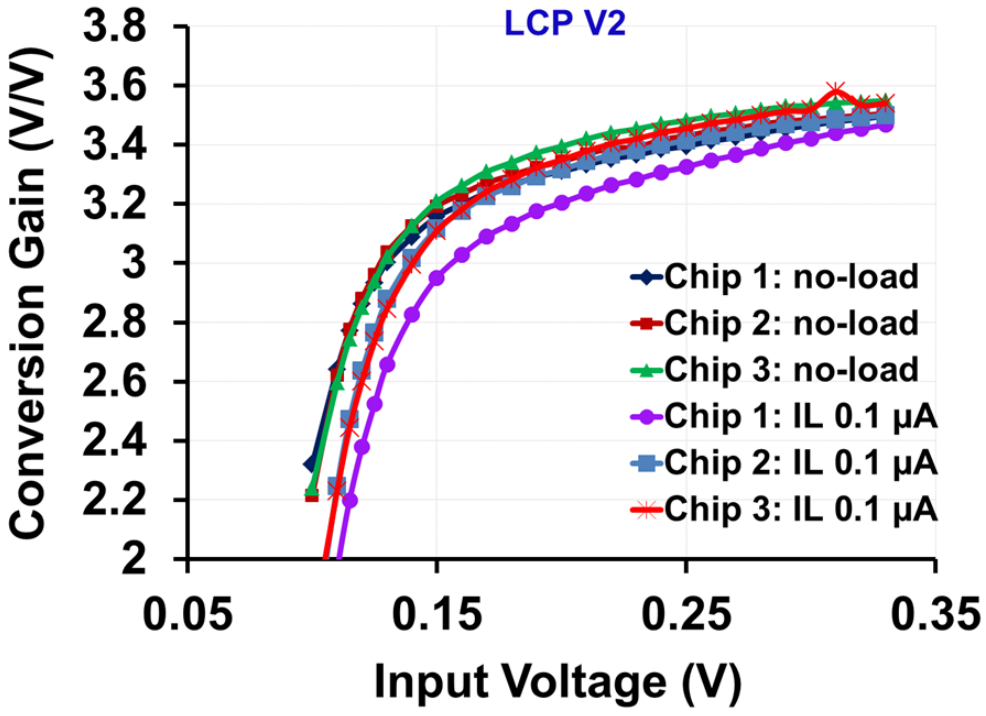


Figure 6.16 LCP V2's conversion gain across low input voltages and load conditions

Table 6.1 Charge pump startup voltage across different load conditions

DC Current load (μA)	*Startup Voltage (mV)*				
	LCP V1		*LCP V2*		
	Chip 1	*Chip 3*	*Chip 1*	*Chip 2*	*Chip 3*
No load	150	140	130	125	130
0.05	155	150	140	130	135
0.1	170	160	150	140	140

those in other chips. Both the linear charge pump versions exhibits a startup voltage variation of approximately 10 mV across the tested prototypes at 0.1 μA DC load current. A larger number of test samples are required to quantify the actual variation in the startup voltage.

6.3.4 Charge Pump Drive Capability

Figure 6.17 to Figure 6.19 illustrate the load driving capability of the charge pump designs. For a fixed frequency of operation (*f*), the output voltage reduces with increased load current due to the increase in losses associated with the CP operation. The CP's output voltage can be approximated as

$$V_{OUT,SteadyState} = (N+1)V_{IN} - N\frac{I_L}{C_P \cdot f} \tag{6.2}$$

where the second term represents the reduction in output voltage due to charge-redistribution loss incurred to sustain the load current. For input voltages close to the startup voltage, the charge pumps are able to sustain 0.2 μA of DC load current. They can support 0.5 μA loads at input voltages above startup. As seen in the plots, for inputs above the startup voltage, the LCP V2 clearly surpasses the LCP V1 design. However, near the startup voltage, LCP V2 is only marginally better at low current loads, while the outputs merge at high load currents. As in

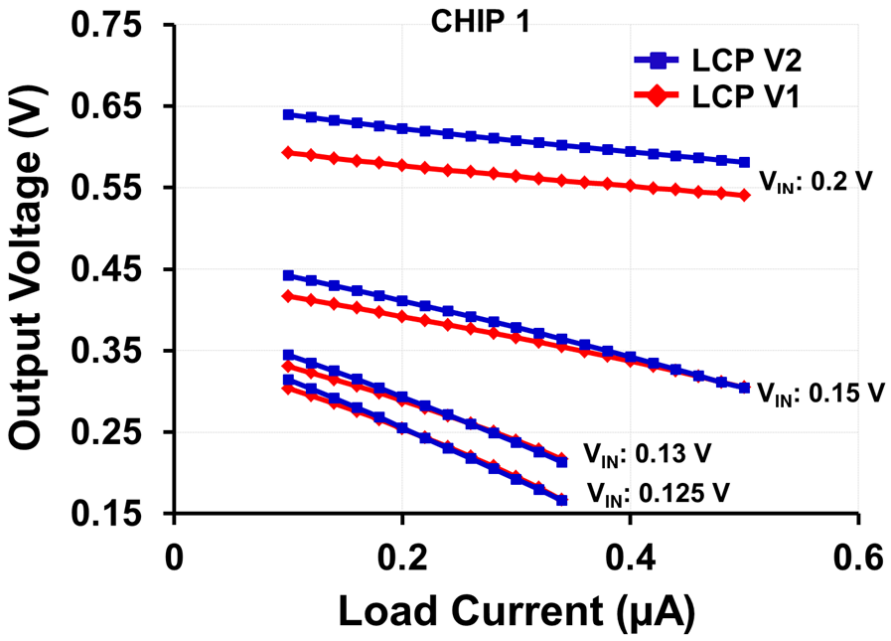


Figure 6.17 Output voltage of LCP across varying load conditions for chip 1

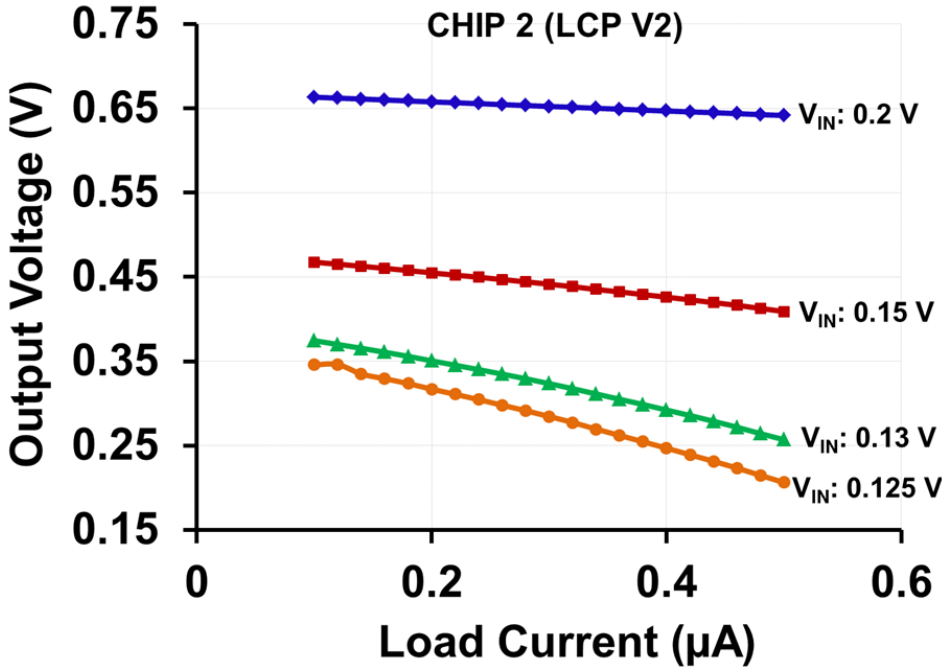


Figure 6.18 Output voltage of LCP across varying load conditions for chip 2

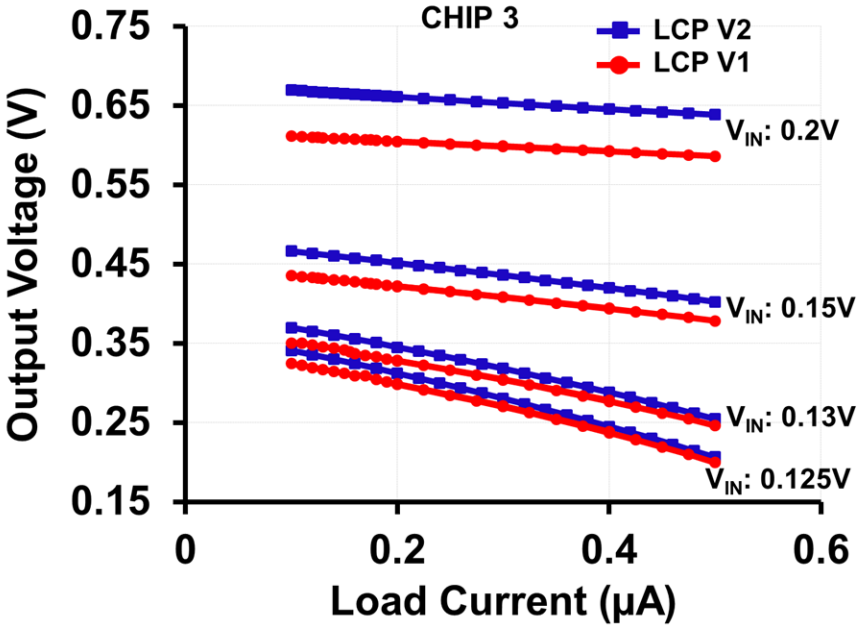


Figure 6.19 Output voltage of LCP across varying load conditions for chip 3

Figure 6.12 to Figure 6.14, for very low input voltages, the increase in reverse current losses in the odd number stages of the LCP V2 diminishes the improvement gained in the even stages at very low input voltages, so LCP V2's output is only slightly better than that of LCP V1 at very low voltages. For high load currents at very low input voltages, both the LCP designs were not designed to sustain large DC load currents, consequently the outputs merge together and drop steeply. Also, since the frequency of operation was not changed during this test, the measured output voltages do not reflect the maximum possible efficiency to drive the DC load current.

6.3.5 Charge Pump Efficiency

The CP's efficiency to boost the input voltage is given by

$$\eta = \frac{I_L \cdot V_{OUT}}{I_{Power} \cdot V_{IN}} \tag{6.3}$$

where I_{Power} is the power supply current consumed by the CP to provide the load with an output voltage (V_{OUT}) and load current of I_L, for an input voltage of V_{IN}. Due to space constraints, the input pad to the CP had to be shared with the power supply pin to the ring oscillator and the phase generator circuits in order to minimize chip area. Hence, the measurement results represent

the end-to-end converter efficiency which includes the power consumed by the ring oscillator, phase generator, the charge pump, and leakage currents in the ESD diodes. Figure 6.20 to Figure 6.21 present the end-to-end efficiency of the converter designs at the startup voltage, across load current variations. At the startup voltage, the CP designs provide comparable conversion efficiency to drive DC load currents. As seen in the previous characterization results, LCP V2 provides a lower startup voltage than LCP V1 and better performance for inputs just above the startup voltage. During this measurement, the capacitive delay network within the RO was maintained at a fixed maximum value that corresponds to the switch setting of *"110"* (Section 6.3.1) across the input voltage range. Since the tuning of RO's output frequency was constrained by the error in decoder implementation, the measured output voltages do not reflect the maximum possible efficiency that can be achieved to drive the DC load current for the input range.

With a thermometer decoder-based control of the RO's delay, the tuning range of the RO's output frequency can be further increased to provide optimal performance of the CP designs across variation in input voltage and load currents. Figure 6.22 illustrates the

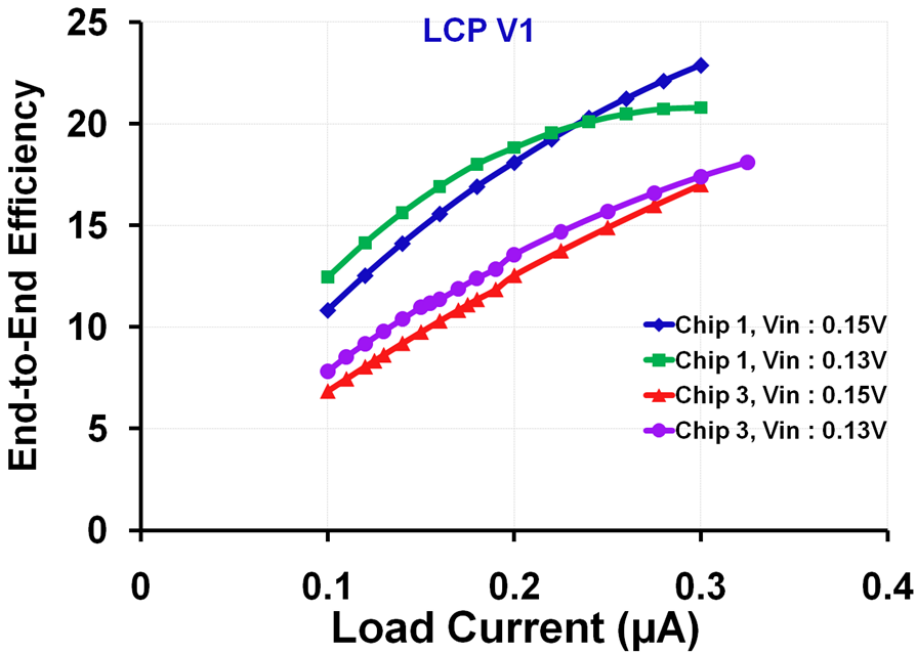


Figure 6.20 Measured end-to-end efficiency of the DC-DC converter (LCP V1) across varying load conditions

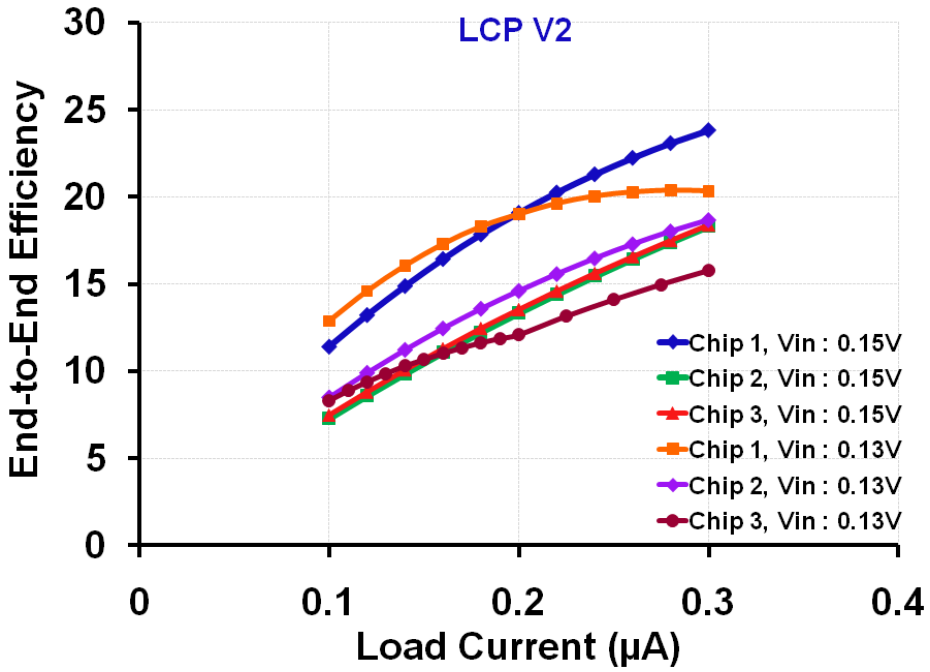


Figure 6.21 Measured end-to-end efficiency of the DC-DC converter (LCP V2) across varying load conditions

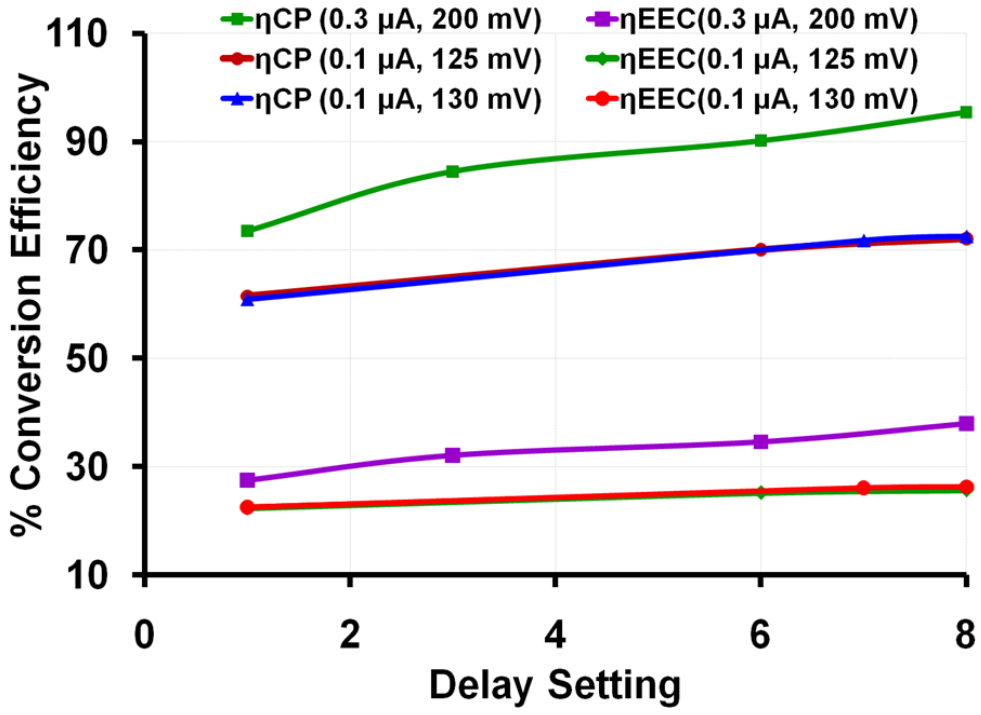


Figure 6.22 Simulated LCP V2 efficiency and end-to-end converter efficiency (LCP V2) across varying load conditions and input voltages

improvement in the simulated efficiency of the charge pump, η_{CP} (LCP V2) and the end-to-end conversion efficiency (η_{EEC}) at startup voltage, across different delay settings from the thermometer decoder. For inputs close to the startup voltage of 130 mV, the end-to-end conversion efficiency increases from 22% to 27%, while the efficiency of the charge pump ranges from 62% to 73% for variations in the RO's output frequency. The efficiency at 200 mV input voltage, well above the startup voltage, is also included to illustrate the higher efficiency capability of the charge pump ($\eta_{CP} \approx 90\%$ & $\eta_{EEC} \approx 40\%$) for inputs above startup voltage. Thus, from simulation results, the maximum conversion efficiency is obtained at the lowest frequency setting for both charge pumps.

From the efficiency measurement plots of Figure 6.20 and Figure 6.21, the improvement in the measured end-to-end efficiency with increase in load current confirms that the conversion efficiency can be improved by reducing the frequency of operation, with respect to very low input voltage and load conditions. Furthermore, as seen in startup voltage measurements, chip 1 has a process corner with higher threshold voltage and so the ring oscillator's output frequency is lower than that in the other chips. This results in a higher efficiency when compared to the other samples. Thus, from the examination of the measurement results, it can be inferred that the measured conversion efficiency can be enhanced by tuning the frequency of operation with respect to the operating conditions.

In micro-energy harvester applications, low startup voltage is the critical requirement, while the end-to-end efficiency of 25% is not as important. For instance, the charge pump could be integrated into a power management system where it is used as a low-voltage multiplier that supplies reference or bias levels to other circuits. Hence, the ultra-low voltage startup demonstrated in this self-starting linear charge pump renders itself indispensable in micro-energy applications. For applications that necessitate high charge pump efficiency at low input voltages, this charge pump topology can be adopted without the self-starting feature and thereby achieve efficiencies close to 75%, based on simulation results.

6.4 Techniques to improve efficiency

Reducing the losses incurred in the charge pump stages is the most effective method to improve the efficiency of a linear charge pump. The switching losses due to charging and

discharging the bottom plate of CP capacitors, and the gate-drive loss at the charge transfer switches, form a significant percentage of the total losses in the linear charge pump topologies. Some of the techniques that can be adopted to improve CP's efficiency include adaptive frequency control and charge recycling schemes.

6.4.1 Adaptive Frequency control

The switching losses can be reduced by lowering the frequency of the charge pumping operation. However, the reduction in operating frequency also results in increased output ripple and increase in charge redistribution loss. Therefore, there exists an optimum frequency of operation that corresponds to maximum efficiency in the CP for a given input and load conditions. This work aimed at variable-delay based frequency control to maximize conversion efficiency. With proper implementation of the delay control logic, the frequency of operation can be tuned across a large range to accommodate variation in input voltage and load conditions. Further, adaptive frequency control can also be realized by varying the frequency of operation by monitoring the CP's output ripple voltage [67].

6.4.2 Charge Recycling

Charge-recycling based methodologies reduce the switching loss at the CP bottom plates by recycling the charge at the end of the discharge phase. The common implementation is to employ the non-overlapping dead-time between the charge and discharge phases of CP, to redistribute charge among the bottom plates of adjacent CP stage capacitors [38], [67].

6.5 Summary and Conclusion

From the measurement results, it can be concluded that the proposed CP topologies are capable of very-low voltage operation with self-startup capability. It has been demonstrated that reducing the losses associated with the linear charge pump topologies improves the performance, even under very-low voltage operation. Since the charge pumps operate at ultra-low voltage regime, the startup voltage is dependent of the CMOS device threshold voltage and can therefore be sensitive to process variations. Of the three tested samples, the variation in startup voltage due to process corners is within 10 mV, but more samples are required to quantify the percentage

Table 6.2 Performance comparison of the proposed charge pump with state-of-the-art converters

Reference	*Startup mechanism*	*Startup voltage*	*Converter Topology*	*Ideal CP Gain*	*Input voltage*	*Output Voltage*	*% Efficiency*	*Output Ripple*	*Area (mm^2)*	*Process*
[44]	Charge pump with V_{TH} tuning	95 mV	Inductive, Ext. CP cap	N/A†	100 mV	0.9 V	72 %	N/A	0.17 & Ext. CP cap	65-nm
[45]	Forward body biased charge pump	180 mV	CP (Doubler stages)	4	180 mV	0.7 V	N/A	N/A	0.29	65-nm
[49]	Charge pump	270 mV	Linear CP	4	450 mV	1.4 V	58%	15 mV	0.42	130-nm
[50]	Charge pump	150 mV	Exponential CP	8	150 mV	0.85 V	30 % (sim.)	N/A	N/A	65-nm
This work LCP V1	Charge pump	150 mV	Linear CP	4	150 mV	0.43 V (0.1 µA)	23 %* (meas) 70 % (CP, sim)	1.5 mV	0.15	130-nm
This work LCP V2	Charge pump	130 mV	Linear CP	4	130 mV	0.38 V (0.1 µA)	20 %* (meas) 73 % (CP, sim)	1.5 mV	0.15	130-nm

* End-to-end converter efficiency
† Not Available

variation.

A comparison of the performance of the proposed CP designs with the state-of-the-art low voltage, CP-based self-starting converters is provided in Table 6.2. It is to be noted that this self-starting CP outperforms the state-of-the-art charge pump based converters with respect to low startup voltage. The very high efficiency of the standalone charge pump proposed in this work is achieved at ultra-low startup voltage, without the need for external excitation, external components, or post-fabrication trims. Furthermore, the charge pumps with total capacitance of 200 pF occupy a very small area of 0.15 mm^2.

The very-low startup voltage capability renders this CP suitable for ultra-low voltage energy harvesting systems such as TEGs. Also, this CP could be employed in kick-start applications for boost converters, and in battery-recharging systems from energy harvesters.

Chapter 7 Conclusion

The feasibility of charge-recycling based low-power digital operation has been demonstrated in this work. The proposed CR scheme has been designed and implemented to improve the energy-efficiency of a 12-bit Gray-code counter. This CR technique advances the state-of-the-art CR designs by eliminating the delay incurred in charge-pump based voltage boosting, and removing the need for current-balancing between vertically-stacked digital blocks. Additionally, the proposed scheme makes it possible to conceive partially self-powered circuits that reuse the recycled power harvested from their own operation. For a 2X reduction in the maximum frequency of operation, the proposed scheme offers 41% energy reduction in the source block while the total energy savings, including the control logic, aggregates to 25%, per cycle of operation. The energy reduction accomplished by the proposed scheme is more than that of other CR schemes reported in literature. Furthermore, this CR implementation realizes the 25% energy reduction without the need to generate multiple, regulated power supply voltages. Thus, the proposed CR methodology clearly improves the energy efficiency in medium speed, digital systems, and advances the current state-of-the-art CR techniques.

The second part of this research presents the design of an ultra-low voltage, switched-capacitor based charge pump that broadens the application of the charge-recycling scheme to compensate for process, voltage and temperature (PVT) variations. The unassisted, self-startup capability in the ultra-low voltage regime renders this charge pump indispensable to energy harvesting applications. Further, the proposed low voltage, self-starting charge pump can be employed to kick start a boost converter and thereby improve the efficiency of micro-energy harvesters.

The CR scheme in conjunction with the proposed self-starting, low-voltage charge pump facilitate harvesting of energy from digital circuits. The characterized prototypes validate the effectiveness of the proposed design methodologies to enable highly energy efficient operation. In summary, this research has demonstrated successful design and implementation of key components required to realize highly energy-efficient mixed-signal systems.

7.1 Original contributions

The original contributions of this work include

- A novel charge-recycling approach to lower power consumption in medium-speed digital circuits.
- Analysis of the amount of energy-reduction that can be achieved using CR techniques in conjunction with dynamic voltage scaling.
- A methodology to implement charge-recycling in existing digital circuits. The absence of delay in the voltage boosting path facilitates the application of the proposed scheme in low-power systems such as portable electronics, and sensor based systems that have intermittent operation spread within long idle states.
- Design of a self-starting, ultra-low voltage, charge pump that extends the application of the CR methodology to compensate for PVT variations and enables tracking of maximum performance.
- A self-starting charge pump that can operate autonomously from the recycled charge or from the energy harvested from digital circuits.
- Investigation of the various losses incurred in the proposed low-voltage charge pump topology.
- Successful design and characterization to demonstrate the effectiveness of the proposed CR methodology and the ultra-low voltage self-startup charge pump.

7.2 Directions for future work

There are several interesting, open-ended problems that can be solved in order to improve the energy efficiency of low power circuits. A few directions to enhance the effectiveness and application of this work are included here.

7.2.1 Charge recycling based low power digital operation

- The efficiency of the virtual V_{DD} generation can be improved by charge-sharing or charge-redistribution from the bottom plates of the CR capacitors.
- The offset of the comparators employed to monitor the virtual ground and virtual V_{DD} voltages affects the overall efficiency of the CR scheme. Hence, a

compromise can be made with power consumption of the comparator in order to increase the accuracy and thus improve the efficiency across PVT variations.

- Comprehensive characterization can be performed on the CR prototype to include the effect of temperature variations on the CR efficiency.
- The CR reference voltage generation circuitry can be integrated within the control logic. This facilitates the generation of dynamic virtual power supply levels that adapt with process and temperature variations so as to guarantee consistent performance across varying operating conditions. Furthermore, this also enables tracking of the maximum energy efficiency point across PVT variations.
- The proposed CR scheme can be implemented on a digital system that allows for multiple supply levels of operation. Furthermore, time-multiplexed CR approach can be explored to enhance the energy efficiency of the system.

7.2.2 Charge pump

- The efficiency of the proposed linear charge-pump can be improved by recycling the charge from the bottom plates of the pumping capacitors. Charge redistribution techniques presented in [38] can be adopted to share the charge in the bottom plates of the capacitors during the dead-time in between the charging and pumping phases.
- The application of the ultra-low voltage charge pump can be further broadened by increasing the drive strength of the charge pump.
- The prototype can be characterized to examine the change in the startup voltage and efficiency across variation in the temperature.
- The ultra-low voltage charge pump can be decoupled from the self-startup circuits in order to characterize the maximum efficiency of the charge-pump as a function of the frequency of operation, for different input and load conditions.

Finally, the low-voltage self-startup charge pump can be integrated into a charge-recycling mixed-signal system in order to realize an autonomous energy harvester that operates entirely from the recycled charge.

References

[1] International Technology Roadmap for Semiconductors, 2010, http://www.itrs.net/Links/2010ITRS/Home2010.htm

[2] International Technology Roadmap for Semiconductors, Design Chapter 2010, http://www.itrs.net/Links/2010ITRS/Home2010.htm

[3] Anantha P. Chandrakasan et al., "Low-Power CMOS Digital Design", IEEE JSSC, vol. 27, no. 4, pp. 473–483, Apr. 1992.

[4] Rahul Sarpeshkar, *Ultra Low Power Bioelectronics: Fundamentals, Biomedical Applications and Bio-inspired Systems*, Cambridge University Press, New York, 2010.

[5] Neil H. E. West and David Harris, *CMOS VLSI Design, A Circuits and Systems Perspective*, 3rd Edition, Pearson Education Inc., Boston, 2005.

[6] Wai-Kai Chen, *The Electrical Engineering Handbook*, Academic Press, 2004.

[7] Dejan Markovic et al., "Ultralow-Power Design in Near-Threshold Region," *Proc. of the IEEE*, vol.98, no.2, pp. 237–252, 2010.

[8] J. Rabaey, "Low Power Design Essentials," *Series on Integrated Circuits and Systems*, DOI 10.1007/978-0-387-71713-5_4, Springer Science + Business Media, 2009.

[9] J.-M. Chang and M. Pedram, "Energy Minimization using Multiple Supply Voltages," *IEEE Transactions on VLSI Systems*, vol. 5, no. 4, pp. 436–443, Dec. 1997.

[10] J. Cai *et al.*, "Supply Voltage Strategies for Minimizing the Power of CMOS Processors," Symposium on VLSI Technology, pp. 102–103, 2002.

[11] Vincent R.von Kaenel et al., "Automatic Adjustment of Threshold & Supply Voltages for Minimum Power Consumption in CMOS Digital Circuits," *IEEE Symposium on Low Power Electronics*, pp. 78–79, 1994.

[12] Sami Kirolos and Yehia Massoud, "Supply Voltage Adaptive Low-Power Circuit Design," *IEEE Workshop on Design, Applications, Integration and Software*, pp. 131–134, 2006.

[13] Yibin Ye and Kaushik Roy, "Low-Power Circuit Design Using Adiabatic Switching Principle," *IEEE Midwest Symposium on Circuits and Systems*, pp. 1189–1192, 1995.

[14] W. C. Athas, L. Svensson, J. Koller, N. Tzartzanis, and Y.-C. Chou, "Low-power digital systems based on adiabatic-switching principles," IEEE TVLSI, vol. 2, pp.398–407, Dec. 1994.

[15] John S. Denker, "A Review of Adiabatic Computing," *IEEE Symposium on Low Power Electronics*, pp. 94–97, 1994.

[16] Suhwan Kim, Conrad H. Zeisler, and Marios C. Papaefthymiou, "Charge-Recovery Computing on Silicon," IEEE Transactions on Computers, vol.54, no. 6, pp.651–659, 2005.

[17] Yong Moon, and Deog-Kyoon Jeong, " An Efficient Charge Recovery Logic Circuit," *IEEE JSSC*, vol. 31, no. 4, pp.514–522, Apr. 1996.

[18] Bo Zhai et al., "Extended Dynamic Voltage Scaling for Low Power Design," *Proc. of Int. SOC Conference*, pp. 389–394, 2004.

[19] A. Chakraborty et al., "Implications of Ultra Low-Voltage Devices on Design Techniques for Controlling Leakage in NanoCMOS Circuits," *IEEE Int. Symposium on Circuits and Systems*, pp. 33–36, 2006.

[20] Kyung Ki Kim, and Yong-Bin Kim, "Novel Adaptive Design Methodology for Minimum Leakage Power Considering PVT Variations on Nanoscale VLSI Systems," *IEEE Transactions on VLSI Systems*, vol. 17, no. 4, pp.517–528, 2009.

[21] M. Nomura et al., "Delay and power monitoring schemes for minimizing power consumption by means of supply and threshold voltage control in active and standby modes," *IEEE JSSC*, vol. 41, no.4, pp.805–814, Apr. 2006.

[22] S. Rajapandian, X. Zheng, and K. L. Shepard, "Charge-recycling voltage domains for energy-efficient low-voltage operation of digital CMOS circuits," *Proc. Int. Conf. Computer Design,* pp. 98–102, 2003.

[23] S. Rajapandian, Z. Xu, and K. L. Shepard, "Energy-Efficient Low-Voltage Operation of Digital CMOS Circuits Through Charge-Recycling," *Symposium on VLSI Circuits Digest of Technical Papers*, pp. 330–333, 2004.

[24] S. Rajapandian et al., "Implicit DC-DC Downconversion Through Charge-Recycling", *IEEE JSSC*, vol. 40, no. 4, pp. 846–852, Apr. 2005.

[25] Jie Gu and Chris H. Kim, "Multi-Story Power Delivery for Supply Noise Reduction and Low Voltage Operation," *ISLPED*, pp. 192–197, 2005.

[26] K. Keung, V. Manne and A. Tyagi, "A Novel Charge Recycling Design Scheme Based on Adiabatic Charge Pump," *IEEE Trans. Very Large Scale Integr. (VLSI) Syst.*, vol. 15, no. 7, pp.733–745, Jul. 2007.

[27] V. Manne and A. Tyagi, "An Adiabatic Charge Pump Based Charge Recycling Design Style," *PATMOS 2003, Lecture Notes in Computer Science*, vol. 2799, pp.299–308, 2003.

[28] K. Keung, and A. Tyagi, "SRAM CP: A Charge Recycling Design Schema for SRAM," *PATMOS 2006, Lecture Notes in Computer Science*, vol. 4148, p.95–106, 2006.

[29] J. M. Rabaey, A. Chandrakasan and B. Nikolic, *Digital Integrated Circuits*, 2nd ed., Pearson Education, Delhi, 2004.

[30] B. Razavi and B. A. Wooley, "Design Techniques for High-Speed, High-Resolution Comparators," *IEEE Journal of Solid-State Circuits*, vol. 27, no. 12, pp. 1916–1926, Dec. 1992.

[31] David Harris *et al.*, "The Fanout-of-4 Inverter Delay Metric," http://www3.hmc.edu/~harris/research/FO4.pdf

[32] C.Ulaganathan, C. L.Britton Jr., J. Holleman, and B. J. Blalock, "A Novel Charge Recycling Approach to Low-Power Circuit Design," *Intl. Conference on Mixed Design of Integrated Circuits and Systems*, pp.208–213, May 2012.

[33] K. Roy and S. C. Prasad, *Low-Power CMOS VLSI Circuit Design,* Wiley, New York, 2000.

[34] N.Nambiar *et al.*, "SiGe BiCMOS 12-bit 8-channel low power Wilkinson ADC," *Midwest Symposium on Circuits and Systems*, pp. 650–653, Aug. 2008.

[35] C.Ulaganathan, B. J. Blalock, J. Holleman, and C. L.Britton Jr., " An Ultra-Low Voltage Self-Startup Charge Pump for Energy Harvesting Applications," *Accepted for publication at The 55th Intl. Midwest Symposium on Circuits and Systems,* pp. 206-209, Aug. 2012.

[36] Nathan Bourgoine, "Harvest Energy from a Single Photovoltaic cell," *Journal of Analog Innovation, Linear Technology*, vol.21, no. 1, Apr, 2011.

[37] Alic Chen, "Thermal Energy Harvesting with Thermoelectrics for Self-powered Sensors: With Applications to Implantable Medical Devices, Body Sensor Networks and Aging in Place," *Ph.D. Dissertation, University of California, Berkeley*, 2011.

[38] Hye-Won Hwang, Jung-Hoon Chun, and Kee-Won Kwon, "A Low Power Cross-Coupled Charge Pump with Charge Recycling Scheme," *IEEE Intl. Conference on Signals, Circuits and Systems*, pp. 1–5, 2009.

[39] Y. K. Ramadass and A. P. Chandrakasan, "A battery-less thermoelectric energy harvesting interface circuit with 35 mV startup voltage," *IEEE Journal of Solid-State Circuit*, vol. 46, no. 1, pp. 333–341, Jan. 2011.

[40] E. Carlson, K. Strunz, and B. Otis, "20 mV input boost converter for thermoelectric energy harvesting," *IEEE Symp. VLSI Circuits Dig.Tech. Papers*, pp. 162–163, Jun. 2009.

[41] J.-P. Im *et al,*"A 40 mV transformer-reuse self-startup boost converter with MPPT control for thermoelectric energy harvesting," *Proc. IEEE ISSCC Dig. Tech. Paper*, pp. 104–106, Feb. 2012.

[42] L. Gobbi, A. Cabrini, and G. Torelli, "A Discussion on Exponential-Gain Charge Pump," *ECCTD*, pp. 615–618, Aug. 2007.

[43] J. F. Dickson, "On-chip high-voltage generation in NMOS integrated circuits using an improved voltage multiplier technique," *IEEE Journal of Solid-State Circuit*, vol. 11, no. 3, pp. 374–378, Jun. 1976.

[44] P.-H. Chen *et al.*, "A 95 mv-startup step-up converter with VTh-tuned oscillator by fixed-charge programming and capacitor pass-on scheme," *Proc. IEEE ISSCC Dig. Tech. Papers*, pp. 216–218, Feb. 2011.

[45] P.-H. Chen *et al.*, "0.18-V Input Charge Pump with Forward Body Biasing in Startup Circuit using 65nm CMOS," *IEEE CICC*, pp. 1–4, 2010.

[46] J. Che, C. Zhang, Z. Liu, Z. Wang, and Z. Wang, "Ultra-low-voltage low-power charge pump for solar energy harvesting systems," ICCCAS, pp. 674–677, 2009.

[47] I. Doms, P. Merken, R. Mertens, and C. Van Hoof, "Integrated capacitive power-management circuit for thermal harvesters with output power 10 to 1000 μW," *Proc. IEEE ISSCC Dig. Tech. Papers*, pp. 300–301, Feb. 2009.

[48] Anna Richelli, Luigi Colalongo, Silvia Tonoli, and Zsolt M.Kovacs-Vajna, "A 0.2–1.2 V DC/DC Boost Converter for Power Harvesting Applications," *IEEE Trans. on Power Electronics*, vol.24, no.6, pp.1541–1546, Jun. 2009.

[49] Yi-Chun Shih and Brian P. Otis, "An Inductorless DC-DC converter for Energy Harvesting With a 1.2–μW Bandgap-Referenced Output Controller, *IEEE Trans. on Circuits and Systems–II: Express Briefs*, vol.58, no.12, pp. 832–836, Dec. 2011.

[50] M. AbdElFattah, A. Mohieldin, A. Emira, and E. Sanchez-Sinencio, "A Low-Voltage Charge Pump for Micro Scale Thermal Energy Harvesting," *IEEE Intl. Symposium on Industrial Electronics*, pp. 76–80, 2011.

[51] A. Wang, B. H. Calhoun, and A. P. Chandrakasan, "Sub-threshold design for ultra-low power systems," *Springer*, pp. 75–102, 2006.

[52] A. Umezawa *et al.*, "A 5 V -only operation 0.6-μm Flash EEPROM with row decoder scheme in triple-well technology," *IEEE Journal of Solid-State Circuits*, vol. 27, no. 11, pp. 1540–1546, Nov. 1992.

[53] Y. A. Eken, "High Frequency Voltage Controlled Ring Oscillators in Standard CMOS," *Ph.D. Dissertation, Georgia Institute of Technology*, Nov. 2003.

[54] C. Enz, F. Krummenacher, and E. Vittoz, "An Analytical MOS Transistor Model Valid in All Regions of Operation and Dedicated to Low-Voltage and Low-Current Applications," *Special issue of the Analog Integrated Circuits and Signal Processing Journal on Low-Voltage and Low-Power Design*, vol. 8, pp. 83–114, Jul. 1995.

[55] CMOS 8RF Design Manual, http://www.mosis.com/vendors/view/ibm/8rf-dm, 2010.

[56] A.Richelli *et al.*, "Charge Pump Architectures Based on Dynamic Gate Control of the Pass-Transistors," IEEE Transactions on Very Large Scale Integration Systems, vol. 17, no. 7, pp. 964–967, Jul. 2009.

[57] Y. Nakagome et al., "An experimental 1.5V 64Mb DRAM," *IEEE Journal of Solid-State Circuits*, pp.465–472, Apr. 1991.

[58] Wing-Hung Ki, Yan Lu, Feng Su, and Chi-Ying Tsui, "Design and Analysis of On-Chip Charge Pumps for Micro-Power Energy Harvesting Applications," *IEEE Intl. Conference on VLSI and System-on-Chip*, pp.374–379, 2011.

[59] Feng Su, Wing-Hung Ki, and Chi-Ying Tsui, "Gate Control Strategies for High Efficiency Charge Pumps," *IEEE Int. Symposium on Circuits and Systems*, pp. 1907–1910, 2005.

[60] L. Su and D. Ma, "Design and optimization of integrated low-voltage low-power monolithic CMOS charge pumps," *IEEE SPEEDAM*, pp.43–48, 2008.

[61] G. Palumbo and D. Pappalardo, "Charge Pump Circuits: An Overview on Design Strategies and Topologies," *IEEE Circuits and Systems Magazine*, First Quarter, pp. 31–45, 2010.

[62] IBM Microelectronics Division, "CMOS8RF Design Manual," Nov. 2010.

[63] G. Palumbo, D. Pappalardo, and M. Gaibotti, "Charge-Pump Circuits: Power-Consumption Optimization", *IEEE Transactions on Circuits and Systems–I*, vol. 49, no. 11, Nov. 2002.

[64] Wing-Hung Ki, Feng Su, and Chi-Ying Tsui, "Charge Redistribution Loss Consideration in Optimal Charge Pump Design," *IEEE Int. Symposium on Circuits and Systems*, pp. 1895–1898, May 2005.

[65] Texas Instruments Datasheet, "LP38512-ADJ 1.5A Fast Transient Response Adjustable Low-Dropout Linear Voltage Regulator," http://www.ti.com/product/lp38512-adj , Feb. 2009.

[66] Texas Instruments Datasheet, "SN74AUC2G34 Dual Buffer Gate," http://www.ti.com/lit/ds/symlink/sn74auc2g34.pdf , Nov. 2003.

[67] Y. K. Ramadass, "Energy Processing Circuits for Low-Power Applications," *Ph.D Dissertation, Massachusetts Institute of Technology*, Jun. 2009.

[68] Linear Technology Datasheet, "LTC3108 Ultralow Voltage Step-up Converter and Power Manager," http://cds.linear.com/docs/Datasheet/3108fb.pdf, 2010.

[69] MOSIS, http://www.mosis.com/products/ic-fabrication.

Vita

Chandradevi Ulaganathan was born in Pondicherry, India. She attended the St. Joseph of Cluny Higher Secondary school. She obtained a Bachelor of Technology degree in Electronics and Communication Engineering from Pondicherry University, India in May 2001. She worked as a Software Engineer in Infosys Technologies for two years before moving to United States to further her education. She obtained a Master of Science degree in Electrical Engineering from the University of Tennessee, Knoxville in May 2007.

Since June 2007 Chandradevi has been pursuing the Doctor of Philosophy degree in Electrical Engineering at UT, under the supervision of Dr. Benjamin J. Blalock. In June 2012, she joined Texas Instruments, Knoxville, Tennessee, where she works in the Home Audio Amplifiers group.